



UNIVERSITÀ DEGLI STUDI DI MILANO
CORSO DI DOTTORATO IN
SCIENZE DELLA TERRA

Dottorato di Ricerca in Scienze della Terra
Ciclo XXVI

Rock Mass Characterization and
Spatial Estimation of Geomechanical Properties
through Geostatistical Techniques

Ph.D. Thesis

Federica Ferrari
Matricola R08991

Tutore
Prof.ssa Tiziana Apuani

Co-tutore
Prof. Gian Paolo Giani

Anno Accademico
2012-2013

Coordinatore
Prof.ssa Elisabetta Erba

*If you don't make mistakes,
you're not working on
hard enough problems,
and that's a big mistake.*

Frank Wilczek

INDEX

| | |
|--|------------|
| 1. INTRODUCTION | 5 |
| 1.1 Basic principles of geostatistics | 8 |
| 1.1.1 Exploratory Spatial Data Analysis | 9 |
| 1.1.2 Semivariogram analysis..... | 13 |
| 1.1.3 Estimation..... | 20 |
| 1.2 Geostatistics and rock mechanics: state of art | 29 |
| 2. VALCHIAVENNA CASE STUDY..... | 35 |
| 2.1 Geographical, geological and structural settings | 35 |
| 2.2 Geomechanical surveys..... | 41 |
| 2.3 Geostatistical analyses | 50 |
| 2.3.1 Horizontal intercept..... | 51 |
| 2.3.2 Rock Mass Rating..... | 64 |
| 2.3.1 Volumetric Joint Count | 80 |
| 2.4 Conclusions..... | 88 |
| 3. GRIMSELPASS CASE STUDY | 91 |
| 3.1 Geographical and geological settings | 92 |
| 3.2 Exfoliation joints | 98 |
| 3.2.1 Features and generations of exfoliation joints near Grimselpass | 99 |
| 3.3 Photogrammetric models of outcropping rock masses at Grimsel..... | 104 |
| 3.4 Data collection of geometric features of exfoliation joints | 107 |
| 3.4.1 Orientations | 112 |
| 3.4.2 Trace lengths and terminations..... | 114 |
| 3.4.3 Rock bridge lengths..... | 131 |
| 3.4.4 Sinuosity Index..... | 132 |
| 3.4.5 Spacing | 133 |
| 3.5 Geostatistical analysis of some properties of exfoliation joints..... | 137 |

| | | |
|------------|--|------------|
| 3.5.1 | Real trace lengths | 138 |
| 3.5.2 | Mean spacing..... | 145 |
| 3.5.2.1 | Comparison with in situ surveys | 153 |
| 3.5.3 | Orientations: difference between slope and exfoliation joint dip angle | 168 |
| 3.6 | Statistical analyses of tectonic joint sets..... | 180 |
| 3.6.1 | Orientations | 182 |
| 3.6.2 | Trace lengths and terminations..... | 186 |
| 3.6.3 | Rock bridge lengths..... | 193 |
| 3.6.4 | Sinuosity Index | 194 |
| 3.6.5 | Spacing | 194 |
| 3.7 | Geostatistical analyses of tectonic joint sets | 196 |
| 3.7.1 | Real trace length..... | 197 |
| 3.7.2 | Spacing | 201 |
| 3.8 | Conclusions..... | 204 |
| 4. | GENERAL CONCLUSIONS AND FINAL REMARKS | 207 |
| 5. | REFERENCES | 210 |
| 6. | APPENDIXES..... | 224 |
| 6.1 | Appendix 1 - Papers about rock mechanics and geostatistics..... | 224 |
| 6.2 | Appendix 2 - Summary of data collected in Chiavenna Valley | 226 |
| 6.3 | Appendix 3 - Recapitulatory sheet of geomechanical survey..... | 229 |
| 6.4 | Appendix 4 - Summary of exfoliation joints data collected at Grimselpass. | 230 |
| 6.5 | Appendix 5 - Summary of tectonic joints data collected at Grimselpass..... | 232 |

1. INTRODUCTION

This thesis deals with geostatistics, which is a branch of statistics focusing on spatial or spatiotemporal datasets, and explores its possible application to rock mechanics, with particular reference to wide areas, located in the Alpine context. The final objective of this work is the estimation (i.e. the prediction), through geostatistical techniques, of the geomechanical parameters determining the quality of rock masses, starting from punctual and scattered sampling locations.

A rock mass is composed by rock matrix and some fractures, which can be arranged into sets of discontinuity. The mechanical behaviour of the rock mass depends on both rock matrix and, especially, fractures behaviours, as well as from their interaction. Generally, the presence of discontinuities has a remarkable impact on the mechanical behaviour of rock mass, reducing both the strength and deformability of the rock mass.

While the rock material, at the scale of the rock mass, can be homogenous or heterogeneous and isotropic or anisotropic, the rock mass is always heterogeneous and anisotropic, which means that its physical properties change with the considered direction. While the rock matrix has own physical characteristics and mechanical properties which can be easily and quite cheaply directly measurable in situ or in lab, the discontinuities are extremely difficult and expensive to sample and test. The rock mass, being discontinuous and heterogeneous and having anisotropic features, has mechanical features depending on different parameters, which are mostly related to the properties of discontinuities.

The characterization of the rock masses consists in describing those properties that allow to derivate the mechanical behaviour of the rock mass, which is very important to investigate because it governs the stability of the rock mass, as well as its possible response if subjected to engineering works.

The geomechanical properties of rock masses can be measured through direct or indirect investigations, the former consists in measurements taken directly on the rock masses or on rock samples, the latter in deriving the properties from measurements carry out without the contact with the rock mass, such as geophysical investigations and photogrammetric surveys. Although the discontinuities affect enormously the rock mass behaviour, they are very difficult to sample and test. The most common and economic method to investigate directly the rock masses, paying attention especially to the fractures, which are the main responsible of rock mass quality, is the geomechanical survey. It relies on an orderly set of quantitative measurements and qualitative observation, which are carried out in order to obtain the geomechanical parameters of the rock mass (Clerici, 2000), with particular reference to its mechanical behaviour. During a geomechanical survey, it is necessary to describe the sizes of both outcrop and of main blocks dislocated by fractures, intercept, the geological features of rock matrix, as well as the following properties of the main discontinuity set affecting the rock masses: kind, orientation, spacing, persistence (i.e. continuity), roughness, undulation, aperture, infillings, strength, weathering, and humidity conditions. The geomechanical surveys, as well as the in situ

and in laboratory tests, aim to obtain the quality index of rock mass, which describes its mechanical behaviour, through quantitative parameters. The main drawback of this kind of measures of rock mass features is that they give punctual values. Obviously, especially in mountainous areas, it is not possible to sample the rock masses and so to measure the geomechanical properties everywhere, due to logistic, but also economic constrains.

Far from sampling points, the properties of rock masses can be deducted and estimated, using geostatistics (the bases of geostatistics have been summarized in the paragraph 1.1). Geostatistics can be defined as the branch of statistical sciences that studies spatial/temporal phenomena and capitalizes on spatial relationships to model possible values of variable(s) at unobserved, unsampled locations (Caers, 2005). In the past the geostatistics was called the theory of regionalized variables (Matheron, 1971), because it deals with variables distributed in space, investigating their spatial structures of correlation. Geostatistics is able to incorporate these spatial structures, which mean spatial dependence of regionalized variable at different location in space.

Geostatistics has been originally developed in mining operation, to predict the probability distributions of ore grades (Krige, 1951). Nowadays, geostatistics is successfully applied in several disciplines, especially those related to geography, with particular reference to those ones involving the spread of diseases (epidemiology), the practice of commerce and military planning (logistics), and the development of efficient spatial networks. Geostatistics is currently applied also in agriculture, soil science, landscape ecology, environmental sciences, forestry, geography, geo-metallurgy, geochemistry, oceanography, hydrogeology, meteorology, hydrology and geology.

In the past the application of geostatistics to problems in geology concerned especially with mining and hydrology. Today, beyond the control and mapping of the evolution of contaminated soils and waters (both in space and in time), the main application of geostatistics in the geological field deals with the petroleum geology: the main objective is the characterization of reservoir heterogeneities that influence the amount, position, accessibility, and flow of fluids through the reservoir. Three-dimensional description at the required resolution is generally difficult because of the sparse sampling yielded by traditional methods of data acquisition. Thus, geostatistical methods are applied in order to estimate (i.e. to predict) geological, geophysical, and petro-physical properties between the sampling points (e.g., wells and seismic lines) and establish potential variabilities. The resulting reservoir models can be used in a variety of ways, for example, serving as a common database, for oil in place calculation, flow simulation, well placement optimization, and visualization purposes (Seifert & Jensen, 1999). Geostatistics in petroleum geology, which is in continuous development, focuses on reservoirs, thus porous and fractured rock formations, especially sediments. The application of geostatistics to hard rock (and their properties), especially in mountains areas, is of course a less developed topic, even if it would be very useful to be able to predict the variation of mechanical properties of rock mass in space.

Sometimes geostatistics has been already applied to the rock mass characterization (as it will be treated in the paragraph 1.2), especially for mining purposes, but always focusing on specific problems and so on very small areas. The capability to investigate and predict values of rock mass quality on wide areas (from dozens to hundreds of square kilometres), which is a big potentiality of the geostatistical tool, would be very useful, because the knowledge of geomechanical properties is an important prerequisite in any design of civil engineering and mining activities. In particular, the estimation of geomechanical properties, outside from the sampling points, in extended areas can be very important, useful in different fields of geosciences, and geo-engineering. In particular, the spatial distribution of rock fractures must be known in solving hydro-geological problems of fracture-affected flow channels, in resource exploration activities for vein-type mineral deposits and fluids in fractured reservoirs (National Research Council, 1996; Adler & Thovert, 1999), but also in slope stability evaluation, as well as in planning underground excavations. Therefore, the reproduction of the spatial variability of geomechanical properties in a whole area can be a very useful tool, especially during the pre-feasibility and feasibility planning phases, particularly to individuate critical points.

The possibility to estimate the fracture properties of rock masses in a whole area can be done using geostatistical techniques (Isaaks & Srivastava, 1989; Villaescusa & Brown, 1990; Giani, 1992), and although this approach seems to be very promising, the topic deserves to be deepened.

This thesis is a contribute in assessing how the rock mass features, in the Alpine geological context, can be regarded as regionalized variables, and the geostatistical tool can be used to foresee the spatial structure of rock masses. The main topic regards the estimation of rock mass properties, and their associated variations, at regional scale, through geostatistical techniques. The estimation consists in forecasting the behaviour and the values of a regionalized variable, in an area, starting from punctual and scattered measures.

The main challenge is to understand if the geostatistical techniques, applied so successfully to local and specific problems, can be applied also at regional scale (i.e. considering very wide portion of territory), finding the best method useful to make estimation of that scale. Actually to have a tool able to predict the rock mass parameters at regional scale can be very useful in areas interested by the planning and construction of large-scale engineering works. The study areas, chosen to verify the applicability of geostatistical methods at regional scale, are both located in the Central Alps: the first is the Italian Alpine Valley named Valchiavenna (SO), while the second is in Switzerland, near the Grimselpass. The main innovative aspects of this thesis, respect to the previous works, are:

- the area involved in the estimations: very wide areas have been considered in order to verify if geostatistics give good results also at regional scale;
- the geology of the site: hard rock masses outcropping on two different location of the Alpine chain have been investigated: the first one is in the Italian Central Alps and the second one in the Swiss Alps;

- the starting measurements: data have been collected in situ using both direct and indirect measurements (i.e. geomechanical survey in Valchiavenna, combined with photogrammetric analysis at Grimsel test site).

1.1 Basic principles of geostatistics

Geostatistics is the study of phenomena that vary in space and/or time (Deutsch, 2002); geostatistics can be regarded as a collection of numerical techniques that deal with the characterization of spatial attributes, employing primarily random models in a manner similar to the way in which time series analysis characterizes temporal data (Olea, 1999). Geostatistics is the tool that helps us to characterize the spatial variability and uncertainty resulting from imperfect characterization of that variability (Bohling, 2005).

Geostatistics concerns with spatial data: each data value is associated with a location in space and there is at least an implied connection between the location and the data value. The term location has at least two meanings: one is simply a point in space and secondly with an area or volume in space. For example, a data value associated with an area might be the average value of an observed variable, averaged over that volume. In the latter case, the area or volume is often called the *support* of the data. This is closely related to the idea of the support of a measure.

Let x, y, \dots be points (not just coordinates) in 1, 2, or 3 dimensional space and $Z(x), Z(y), \dots$ denote observed values at these locations. Now suppose that t is a location that is not sampled. The objective then is to estimate (i.e. to predict) the value $Z(t)$. If only this information is given then the problem is ill posed: it does not have a unique solution. One way to obtain a unique solution is to introduce a model into the problem. There are two ways to do this: one is deterministic and the second is stochastic or statistical. Both approaches must somehow incorporate the idea that there is uncertainty associated with the estimation/prediction step. The value at the unsampled location is not itself random, but our knowledge of it is uncertain. One approach then is to treat $Z(x), Z(y), \dots$ and $Z(t)$ as being the values of random variables. If the joint distribution of these random variables were known then the best estimator (best meaning unbiased and having minimal variance of the error of estimation) would be the conditional expectation of $Z(t)$ given the values of the other random variables. However data consist of only one observation of the random variables $Z(x), Z(y), \dots$ and none of the random variable $Z(t)$, hence it is not possible to estimate or model this distribution using standard ways of modelling or fitting probability distributions. The geostatistical approach, which relies on the autocorrelation principle, is more suitable. The autocorrelation is the correlation between elements of a series and others from the same series separated from them by a given interval.

Geostatistics relies on the semivariogram, a graph that allows to individuate the spatial correlation among the data, plotting the distance among pair of sampling points, on x-axis, against their variance, on y-axis. The principle is very simple: closer the two sampling points are, more similar they are. Going far away the variance increases until a distance, called the range, beyond which the points are no more correlated. The

experimental semivariogram can be fitted by several theoretical models, which are used to perform the estimation (i.e. the prediction in unsampled locations).

Basically, geostatistics consists of three main steps:

1. Exploratory spatial data analysis;
2. Semivariogram analysis: it allows the characterization of spatial correlation;
3. Estimation: the prediction is usually performed through the kriging technique (which is the optimal interpolation, generating the best linear unbiased estimate at each location) or the stochastic simulations (which generate multiple equiprobable images of the variable). Both techniques employ the semivariogram model.

1.1.1 Exploratory Spatial Data Analysis

Geostatistical methods are optimal when data are normally distributed and stationary (i.e. mean and variance do not vary significantly in space). The Exploratory Spatial Data Analysis –ESDA– is useful to check the frequency distribution of data and if the stationarity and ergodicity properties are respected. Actually, significant deviations from normality, stationarity and ergodicity can cause problems, so it is always best to begin by looking at a histogram or similar plot to check for normality and a posting of the data values in space to check for significant trends.

The first step of ESDA consists of calculation of the main statistical parameters of the variable, in order to understand its frequency distribution. These main statistical parameters can be subdivided into: local tendency, dispersion and shape parameters.

The local tendency parameters, also called location parameters, include:

- the arithmetic mean: it is often simply called mean of a sample, and is the sum of the sampled values divided by the number of items in the sample;
- the median: it is the numerical value separating the higher half of a data sample, a population, or a probability distribution, from the lower half;
- the mode: it is the value that appears most often in a set of data;
- the mid-range, which is the arithmetic mean of the maximum and minimum values in a data set;
- the quartiles, which are the three points of a ranked set of data values that divide the data set into four equal groups, each group comprising a quarter of the data. A quartile is a type of quantile. The first quartile (Q_1) is defined as the middle number between the smallest number and the median of the data set. The second quartile (Q_2) is the median of the data. The third quartile (Q_3) is the middle value between the median and the highest value of the data set;

- the interquartile mean (IQM): it is also called midmean and is a truncated mean, it is computed discarding the lowest and the highest scores, and calculating the mean value of the remaining scores.

The dispersion parameters, called also scale parameters, are:

- the range, which is the difference between the largest and smallest values;
- the interquartile range (IQR): it is also called the midspread or middle fifty is a measure of statistical dispersion, being equal to the difference between the upper and lower quartiles. The IQR is the 1st Quartile subtracted from the 3rd Quartile:

$$IQR = Q_3 - Q_1 \quad (1)$$

- the variance: it measures how far a set of numbers is spread out (a variance of zero indicates that all the values are identical). A non-zero variance is always positive: a small variance indicates that the data points tend to be very close to the mean (expected value) and hence to each other, while a high variance indicates that the data points are very spread out from the mean and from each other. The variance of a random variable X is its second central moment, the expected value of the squared deviation from the mean $\mu = E[X]$:

$$Var(X) = E[(X-\mu)^2] \quad (2)$$

- the standard deviation: it is the square root of variance;
- the standard error: it is the standard deviation of the sampling distribution of a statistic. The term may also be used to refer to an estimate of that standard deviation, derived from a particular sample used to compute the estimate. In practical applications, the true value of the standard deviation (of the error) is usually unknown;
- the coefficient of variation (CV): it is a normalized measure of dispersion of a probability distribution or frequency distribution. The coefficient of variation is defined as the ratio of the standard deviation to the mean.

The shape of the distribution can be described by the following shape parameters:

- the skewness: it is a measure of the extent to which a probability distribution of a random variable leans to one side of the mean. The skewness value can be positive or negative, or even undefined. The qualitative interpretation of the skew is complicated. For a unimodal distribution, negative skew indicates that the tail on the left side of the probability density function is longer or fatter than the right side, without distinguishing these shapes. Conversely, positive skew indicates that the tail on the right side is longer or fatter than the left side. In cases where one tail is long but the other tail is fat, skewness does not obey a simple rule. For example, a zero value indicates that the tails on both sides of the mean balance out, which is the case both for a symmetric distribution, and for asymmetric distributions where the asymmetries even out, such as one tail being long but thin, and

the other being short but fat. Further, in multimodal distributions and discrete distributions, skewness is also difficult to interpret. Importantly, the skewness does not determine the relationship of mean and median;

- the kurtosis: it is the measure of the peakedness of the probability distribution of a random variable. There are different ways of quantifying it for a theoretical distribution and there are various interpretations of kurtosis. Generally, big values indicate the presence of a modal sharp peak.

However, a fast qualitative analysis of the kind of distribution can be done, analysing the relationship between the mean and median:

1. if the distribution is symmetric then the mean is equal to the median, and the distribution will have zero skewness;
2. if the mean is greater than (to the right of) the median there is a positive (also called right) non-parametric skew;
3. if the mean is less than (to the left of) the median, it means a negative (or left) non-parametric skew.

The computation of the main statistical parameters is necessary to understand the kind of distribution. Since many geostatistical techniques are more reliable if the variable of interest has a standard Gaussian distribution, it is necessary to verify if the variable has a normal distribution and if not the transformation of data into a standard Gaussian one is essential. It is rare in the modern geostatistics to consider untransformed data. The use of Gaussian techniques requires a prior Gaussian transformation of data and the reconstruction of semivariogram model on these transformed data. This transformation has some important advantages: the difference between extreme values is dampened and the theoretical sill of the semivariogram should be close to the unit (Grigarten & Deutsch, 2001).

The problem is that the most common statistical tests used to verify if the univariate distribution of the data is Gaussian, such as the Shapiro-Wilk, chi-square and Kolmogorov-Smirnov tests, are designed on the assumption that the observations are independent and identically distributed. In geostatistical applications, however, this is not usually the case: if the data are correlated, the standard tests cannot be applied to the probability density function –pdf– or cumulative probability function –cdf– estimated directly from the data. The problem with correlated data arises not from the correlation per se, but from cases in which correlated data are clustered rather than being located on a regular grid (Pardo-Igúzquiza & Dowd, 2004). When preferential sampling occurs, observations that are close together provide partially redundant information that must be taken into account in calculating pdf or cdf. Actually, it is difficult and often impossible to sample geological data using a regular grid, therefore the occurrence of preferential sampling is very frequent. For instance, in this thesis, the sampling locations are obviously dependent on the outcrop positions and, for the Valchiavenna case study, on their accessibility too. Hence, the sampling locations are not dis-

posed on a regular grid. The preferential sampling could lead to the presence of spatial clusters, and subsequent biases. When the sampling is clustered, unbiased estimates of pdf or cdf must first be obtained, by de-clustering, then normality tests can be applied. However, in geostatistics the weighting coefficient assigned to a sample is lowered to the degree that its information is duplicated by nearby, highly correlated samples with little variability (Isaaks and Srivastava, 1999). This helps mitigate the effect of variable sample density (i.e. preferential sampling).

Moreover, in order to perform any type of geostatistical estimation or simulation one requires a decision or assumption of stationarity (Deutsch & Journel, 1998; Chiles & Delfiner, 1999). Any statistical method, including geostatistics, relies on this assumption. Otherwise, estimation of uncertain/random variables would not be possible. The spatial stationarity property implies the absence of systematic trends, which can be verified representing the magnitude of variable along different directions in the space. Implicitly, it is assumed that all the values originate from a single population. The population is often referred to as the zone of stationarity, a region that allows pooling information together. Hence, any estimation of statistics such as mean and variance relies implicitly on a decision of stationarity. Such stationarity decision is not only relevant for simple statistics such as histograms, it carries over to higher order statistics (Caers & Zhang, 2004). The semivariogram, for instance is a statistical measure of order two, since it describes the dissimilarity between the same (or different) variables at two spatial locations. Hence, variogram calculations rely on a decision or assumption of stationarity.

The geostatistical approach relies also on the ergodic hypothesis, being the computation of the variogram based on the Mean Ergodic Hypothesis (Papoulis & Pillai, 2002) that permits the substitution of the stochastic mean value with the mean value of all the couples of measurement points that are approximately at a given distance apart. This implies that the process is regular or statistically homogeneous to ensure that, from a unique realization of the process, there is a representation of all possible values. Actually, the mean value of the regionalized variable does not depend on its spatial position, but on the distance from the realizations. In other words, a random function is mean-ergodic if the process has finite variance: the process may be assumed distribution-ergodic if the indicator covariance function tends to zero for a distance known as the (practical) range of the covariance, and this distance is much smaller than the maximum distance inside the considered domain. It follows that the semivariogram must reach a sill, within a finite distance (Pardo-Igúzquiza & Dowd, 2004). This condition can be used to check experimentally the distribution-ergodic hypothesis. In practice, the process is not observed over an infinite domain but over a finite domain of interest. The ergodicity explains the inevitable fluctuations of statistics and their consequences on modelling. These ergodic fluctuations are due to the limited, finite extent of the spatial domain being simulated. Simulation on an infinitely large domain will result in statistics of a realization that exactly match the model statistics. Therefore, when simulating on a finite domain, some statistics have smaller variations than other. Ergodicity therefore plays an important role in both the estimation of model parameters as well as their simulation (Caers & Zhang, 2004). It is typically advised in traditional geostatistical practice not to

use any lag distance information beyond 1/2 the size of the field, since they are not reliable (not enough samples to provide a reliable semivariogram), and this statement has been observed in this thesis.

1.1.2 Semivariogram analysis

The key of geostatistics is the modelling of semivariogram, which is the tool that permits to individuate the occurrence of some spatial structure in the dataset. The semivariogram is the mathematical model that captures the spatial correlation among data. The semivariogram is a measure of variability, it increases as samples become more dissimilar. The semivariogram is defined as the expected value of a squared difference (Isaaks & Srivastava, 1989):

$$2\gamma(\mathbf{h}) = \text{Var}[Z(\mathbf{u}_\alpha) - Z(\mathbf{u}_\alpha + \mathbf{h})] = E\{[Z(\mathbf{u}_\alpha) - Z(\mathbf{u}_\alpha + \mathbf{h})]^2\} \quad (3)$$

Where Z is a stationary random function with known mean m and variance σ^2 , which are independent of location, so $\mu(\mathbf{u}_\alpha) = \mu$ and $\sigma^2(\mathbf{u}_\alpha) = \sigma^2$ for all locations \mathbf{u}_α in the study area, therefore the semivariogram function depends only on the distance \mathbf{h} and so the intrinsic hypothesis occurs.

The semivariogram is therefore a graph (**Figure 1**) that can be obtained plotting the distance among sampling points (called *lag*) on x-axis, versus the associated variance, on y-axis. The semivariogram therefore is the expected squared difference between two data values separated by a distance vector. The semivariogram $\gamma(\mathbf{h})$ is one half of variogram $2\gamma(\mathbf{h})$, to avoid excessive jargon in this paper we simply refer to it with the term variogram.

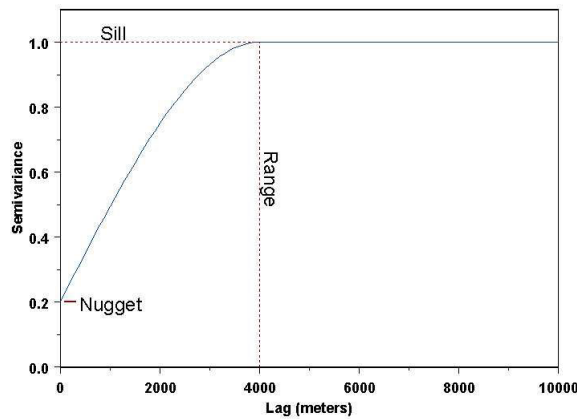


Figure 1 – Semivariogram: x-axis represents distance among pairs of points and y-axis their semivariance (from Bohling, 2005)

If a variable is correlated, initially the variogram increases and then becomes stable beyond a distance \mathbf{h} called *range*. Beyond this distance, the mean square deviation between two quantities $z(\mathbf{u}_\alpha)$ and $z(\mathbf{u}_\alpha + \mathbf{h})$ no longer depends on the distance \mathbf{h} between them and the two quantities are no longer correlated. When the range is different in some directions of space, the examined regionalized variable exhibits a geometric anisotropic structure. The range corresponds to a variance value called *sill*, which corresponds to zero correlation. In theory, the semivariogram value at the origin (0 lag) should be zero. If it is significantly different

from zero for lags very close to zero, then this semivariogram value is referred to as the *nugget effect*, which represents variability at distances smaller than the typical sample spacing, including measurement error.

The variogram quantifies the distance (range) at which samples become uncorrelated from each other, giving an idea of the best and the worst spatial correlation directions among the data. The former occurs where the range is maximum, the latter has been assumed perpendicular to the maximum correlation direction. The variogram is calculated by pooling information at similar lag distances together into a single scatter plot (a bivariate histogram essentially) from which the variogram value is calculated.

The variogram is a measure of variability; it increases as samples become more dissimilar. The covariance is a statistical measure that is used to measure correlation (it is a measure of similarity):

$$C(\mathbf{h}) = E\{[Z(\mathbf{u}_\alpha)Z(\mathbf{u}_\alpha+\mathbf{h})]-\mu^2\} \quad (4)$$

By definition, the covariance at $\mathbf{h} = \mathbf{0}$, $C(\mathbf{0})$, is the variance σ^2 . The covariance $C(\mathbf{h})$ is 0.0 when the values \mathbf{h} -apart are not linearly correlated. Expanding the square in Equation (3) leads to the following relation between the semivariogram and covariance (**Figure 2**):

$$\gamma(\mathbf{h}) = C(\mathbf{0})-C(\mathbf{h}) \quad (5)$$

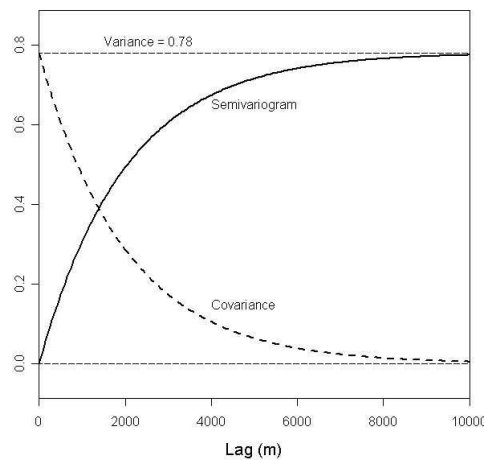


Figure 2 – Example of semivariogram and covariance functions. The x-axis is the distance among pairs of points and the y-axis their semi-variance (from Bohling, 2005)

This relation depends on the model decision that the mean and variance are constant and independent of location. These relations are the foundation for variogram interpretation. That is:

1. the sill of the variogram is the variance, which is the variogram value that corresponds to zero correlation;
2. the correlation between $Z(\mathbf{u}_\alpha)$ and $Z(\mathbf{u}_\alpha+\mathbf{h})$ is positive when the variogram value is less than the sill;

3. the correlation between $Z(\mathbf{u}_\alpha)$ and $Z(\mathbf{u}_\alpha + \mathbf{h})$ is negative when the variogram exceeds the sill.

This is illustrated by **Figure 3**, which shows three **h**-scatter plots corresponding to three lags on a typical semivariogram.

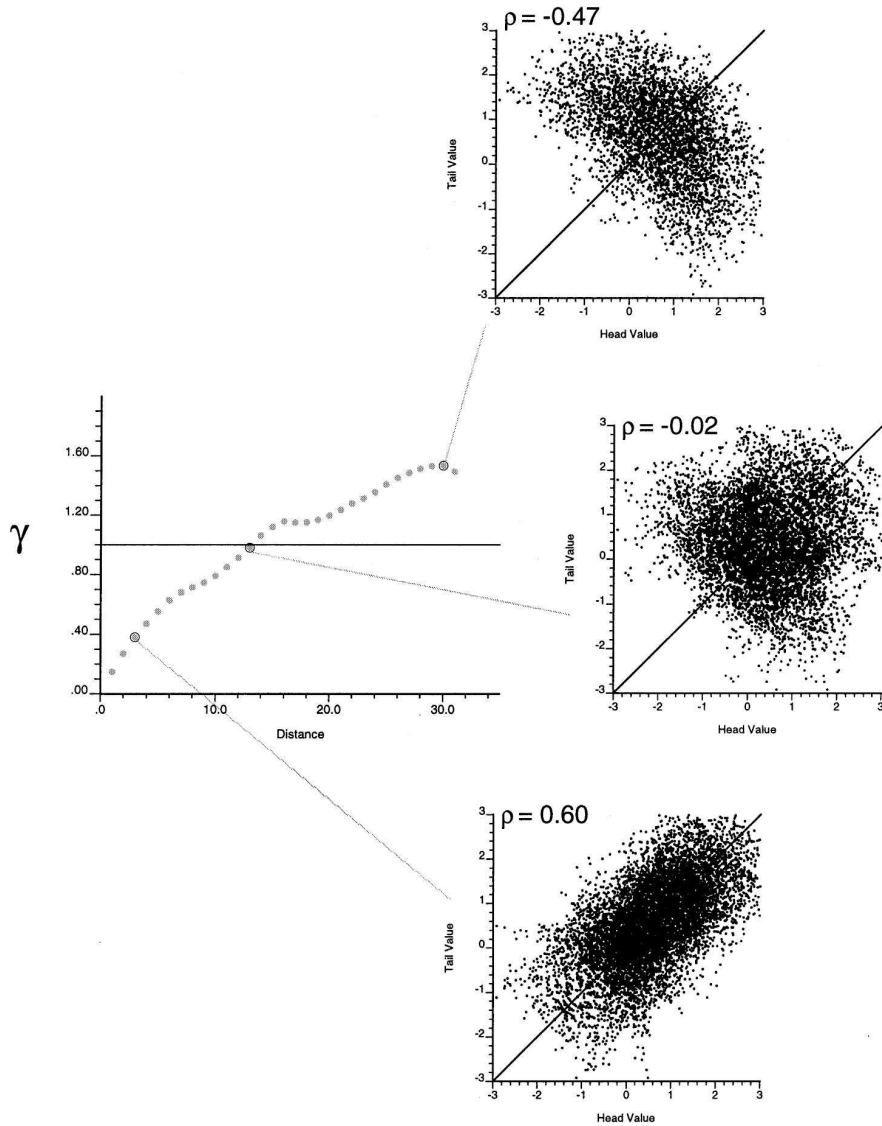


Figure 3 - Semivariogram with the **h**-scatter plots corresponding to three different lag distances. Note that the correlation on the **h**-scatter plot is positive when the semivariogram value is below the sill, zero when the semivariogram is at the sill, and negative when the semivariogram is above the sill (from Grigarten & Deutsch, 2001)

The covariance function and semivariogram provide measures of spatial continuity or variability over the full range of attribute values, they are therefore indicate to work with continuous variables. The pattern of spatial continuity or variability, may however differ, depending on whether the attribute value is small, medium or large (Goovaerts, 1997). Dealing with categorical variables (i.e. characterized by discrete values), the indicator semivariogram approach is preferable. Actually the categorical variable, having the values subdivided in classes (according to the chosen thresholds), cannot be treated such as a numerical, continuous variable. The employment in geostatistics of variables described in classes, requires the indicator ap-

proach, which consists in the evaluation of the conditional cumulative distribution function (ccdf) at selected threshold values z_k (Journel, 1983). The ccdf appears as the conditional expectation of a binary indicator transform of the initial random function $Z(x)$. Therefore, the indicator approach is based on the binary transformation of sample population. Defining indicators for categorical variables would lead to the following non-linear transformation of data value, into either a 1 or a 0:

$$i(\bar{u}_\alpha; z_k) = \begin{cases} 1, & \text{if } z(\bar{u}_\alpha) \leq z_k \\ 0, & \text{otherwise} \end{cases} \quad (6)$$

where $i(\mathbf{u}_\alpha; z_k)$ is the indicator transform at location \mathbf{u}_α depending on the presence of a specified z_k , and $z(\mathbf{u}_\alpha)$ is the observed categorical realization at location \mathbf{u}_α . In other words, using this method, each attribute to be modelled is described through a binary indicator variable that takes the value 1 if that attribute is encountered at a given location, and 0 if not.

The indicator approach allows estimating the probability distribution of a variable within a region (Alli et al., 1990): following the above transformation, at every location \mathbf{u}_α where the observed spacing class $z(\mathbf{u}_\alpha)$ is, a value of 1 (equivalent to a 100% outcome probability) is assigned, every other sample location receives a value of 0 (0% probability). The interpolation of these probability values gives estimators that can be interpreted as the outcome probabilities of the modelled variable.

The indicator approach is very often used, not only for categorical variables, because it is nonparametric in the sense that it does not require any prior hypothesis about either the multivariate or bivariate distribution of the random function $Z(x)$, and does not consist in estimating the parameters of an assumed distributional form for the ccdf. Succinctly no assumptions concerning the distribution of the modelled variable are needed (i.e. the Gaussian distribution of data is not required). Actually, the indicator transformation partitions the overall sample distribution by a number of thresholds, with consequent no need to fit or assume a particular analytically derived distribution model for the data. However, one has to be aware that the indicator transformation always implies a loss of information (Marinoni, 2003). Especially in the case of categorical variables, it does not play a role whether, for instance, in a class a value exceeds lightly or copiously the threshold value: in either case, an indicator of 1 would be assigned to or the extra information about significant small or big value is lost.

Performing the estimation of binary-transformed indicator values requires the knowledge of the spatial correlation, which can be achieved through the semivariogram, called the indicator semivariogram, calculated on the binary-transformed indicator population. The indicator semivariogram is computed as:

$$\gamma(\bar{h}; z_k) = \frac{1}{2N(\bar{h})} \sum_{\alpha=1}^{N(\bar{h})} \left[i(\bar{u}_\alpha; z_k) - i(\bar{u}_\alpha + \bar{h}; z_k) \right]^2 \quad (7)$$

The indicator variogram value $2\gamma(\mathbf{h}; z_k)$ measures how often two z -values separated by a vector \mathbf{h} are on opposite side of the threshold values z_k . In other words, the indicator variogram value measures the transi-

tion frequency between two classes of z -values as a function of h . The greater $\gamma(\mathbf{h}; z_k)$ or $\gamma(\mathbf{h}; z_k)$, the less connected in the space are the small $[z(\mathbf{u}_\alpha) \leq z_k]$ or large values $[z(\mathbf{u}_\alpha) > z_k]$.

Multiple indicator variograms, one for each threshold value, are necessary and they cannot be modelled independently one from on other and must verify a few necessary order relations (Journel & Posa, 1990). These indicator variograms should cover the range of the input data. The main advantage of the computation of indicator variograms, although it is very time-consuming, is the possibility to handle different anisotropies at different cutoffs. Note that if the anisotropy changes too much between adjacent thresholds, the order relations violations become prohibitively large, but if the changes are gradual then the situation depicted can easily be handled (Glacken & Blackney, 1998). Typically, experimental indicator semivariograms at extreme threshold values tend to be a bit erratic; indeed, for such extreme classes, the indicator variogram value depends on the spatial distribution of few data pairs where the two z -values are on opposite side of the threshold z_k .

After the construction of the experimental (or empirical) variogram or indicator variogram, it is necessary to find the theoretical experimental variogram that best fits it: the empirical semivariogram need to be replaced with an acceptable semivariogram model, because the estimation algorithms need access to semivariogram values for lag distances other than those used in the empirical semivariogram. More importantly, the semivariogram models used in the estimation process need to obey certain numerical properties in order for the kriging equations to be solvable. Technically, the semivariogram model needs to be non-negative definite, in order the system of kriging equations to be non-singular. Therefore, geostatisticians choose from a palette of acceptable or licit semivariogram models (**Figure 4**). Using h to represent the lag distance, a to represent the (practical) range, and c to represent the sill, the five most frequently used models are:

- pure nugget: this model represents the discontinuity at the origin due to small-scale variation. On its own it would represent a purely random variable, with no spatial correlation;

$$\gamma(\vec{h}) = \begin{cases} 1 & \text{if } \vec{h} = 0 \\ c & \text{otherwise} \end{cases} \quad (8)$$

- spherical: this model actually reaches the specified finite sill value (c) at the specified range(a), and as the exponential one, exhibits linear behaviour the origin, appropriate for representing properties with a higher level of short-range variability;

$$\gamma(\vec{h}) = \begin{cases} c \cdot \left[1.5 \left(\frac{\vec{h}}{a} \right) - 0.5 \left(\frac{\vec{h}}{a} \right)^3 \right] & \text{if } \vec{h} \leq a \\ c & \text{otherwise} \end{cases} \quad (9)$$

- exponential: this model, like the Gaussian one, approaches the sill asymptotically, with a representing the practical range, the distance at which the semi-variance reaches 95% of the sill value (c);

$$\gamma(\vec{h}) = c \cdot \left[1 - \exp\left(\frac{-3\vec{h}}{a}\right) \right] \quad (10)$$

- Gaussian: this model has a parabolic behaviour at the origin, which represents very smoothly varying properties;

$$\gamma(\vec{h}) = c \cdot \left[1 - \exp\left(\frac{-3\vec{h}^2}{a^2}\right) \right] \quad (11)$$

- power: this model does not reach a finite sill and does not have a corresponding covariance function. Power-law semivariogram models are appropriate for properties exhibiting fractal behaviour;

$$\gamma(\vec{h}) = c \cdot \vec{h}^\omega \quad \text{with } 0 < \omega < 2 \quad (12)$$

Linear combinations of licit semivariogram models are also licit models, so that more complicated models may be built by adding together the basic models described above with different ranges and sill. The resulting model is called nested model.

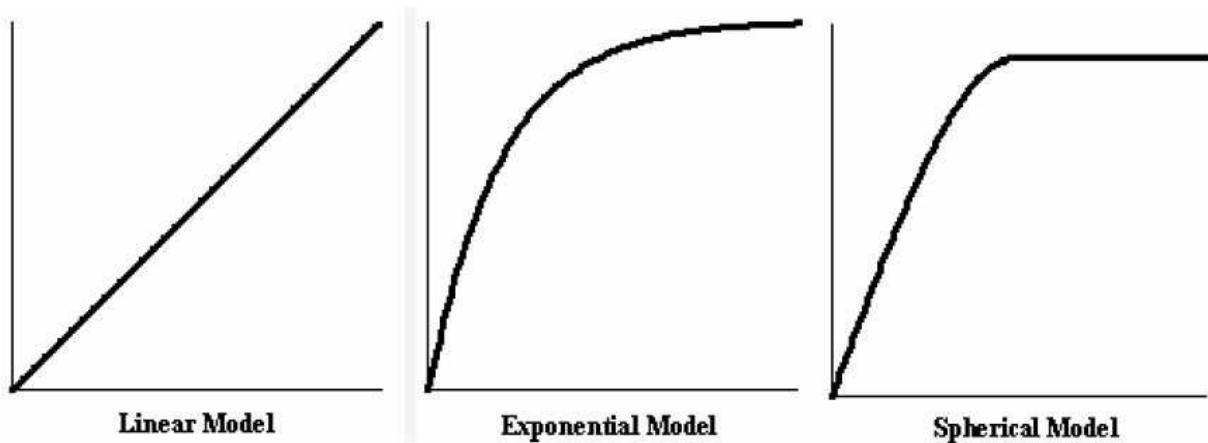


Figure 4 – Examples of some theoretical licit semivariogram models (from Barnes, 2003)

The above discussion has assumed that the spatial correlation structure is the same in all directions, or isotropic. In this case the covariance function, correlogram, and semivariogram depend only on the magnitude of the lag vector, $h=|\vec{h}|$, and not the direction, and the empirical semivariogram can be computed by pooling data pairs separated by the appropriate distances, regardless of direction. Such a semivariogram is described as omnidirectional.

In many cases, however, a property shows different autocorrelation structures in different directions, and an anisotropic semivariogram model should be developed to reflect these differences. The most commonly employed model for anisotropy is geometric anisotropy, with the semivariogram reaching the same sill in all directions, but at different ranges. In geological settings, the most prominent form of anisotropy is a strong contrast in ranges in the (stratigraphically) vertical and horizontal directions, with the vertical semivariogram reaching the sill in a much shorter distance than the horizontal semivariogram. In some set-

tings, there may also be significant lateral anisotropy, often reflecting prominent directionality in the depositional setting (such as, along and perpendicular to channels).

The most common approach to modelling geometric anisotropy is to find ranges, a_x , a_y , and a_z , in three principal, orthogonal directions and transform a three-dimensional lag vector $(\mathbf{h}) = (\mathbf{h}_x, \mathbf{h}_y, \mathbf{h}_z)$ into an equivalent isotropic lag using:

$$\gamma(\bar{h}) = \sqrt{\left(\frac{\bar{h}_x}{a_x}\right)^2 + \left(\frac{\bar{h}_y}{a_y}\right)^2 + \left(\frac{\bar{h}_z}{a_z}\right)^2} \quad (13)$$

To check for directional dependence in an experimental variogram, it is possible to compute semi-variance values for data pairs falling within certain directional band, as well as falling within the prescribed lag limits. The directional bands are specified by a given azimuthal direction, angular tolerance, and bandwidth (**Figure 5**).

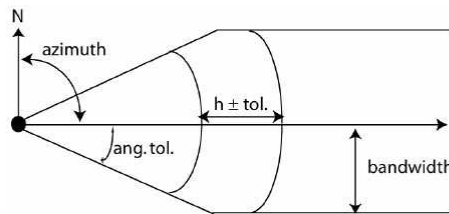


Figure 5 – Parameters used to compute directional semivariograms (from Bohling, 2005)

Obviously, the empirical semivariograms, especially if the directional ones, are often quite noisy, due to the reduced number of data pairs used for estimation; hence, quite a bit of subjective judgment goes into selecting a good model.

Geostatistical modelling generally uses the variogram instead of the covariance (Grigarten & Deutsch, 2001). This is primarily because the semivariogram, which averages squared differences of the variable, tends to filter the influence of a spatially varying mean. Also, the semivariogram can be applied whenever the first differences of the variable, $Z(\mathbf{u}_\alpha) - Z(\mathbf{u}_\alpha + \mathbf{h})$, are second-order stationary. This form of stationarity, referred to as the intrinsic hypothesis, is a weaker requirement than second-order stationarity of the variable itself, meaning that the semivariogram can be defined in some cases where the covariance function cannot be defined. In particular, the semi-variance may keep increasing with increasing lag, rather than levelling off, corresponding to an infinite global variance. In this case, the covariance function is undefined (Bohling, 2005).

The computation of semivariograms is always based on the stationarity and mean ergodic hypotheses. The spatial stationarity property is verified when systematic trends are absent. A trend in the variable occurs when the empirical variogram continues climbing steadily beyond the global variance value, resulting in a

negative correlation between variable values separated by large lags. Three options for dealing with the trend are:

1. to fit a trend surface and work with residuals from the trend;
2. to try to find a trend-free direction and use the variogram in that direction as the variogram for the variable;
3. Ignore the problem and use a linear or power variogram models.

The ergodicity implies that the indicator covariance function tends to zero for a distance known as the (practical) range of the covariance, meaning that experimental variograms should not have a drift effect (i.e. they are not monotone ascending), but present a sill.

1.1.3 Estimation

The existence of a model of spatial dependence allows one to tackle the problem of estimating attribute values at unsampled locations (Goovaerts, 1997). The estimation consists of the interpolation of a variable at an unmeasured location from observed values at surrounding locations. The interpolation is a method of constructing new data points within the range of a discrete set of known data points.

In engineering and science, one often has a number of data points, obtained by sampling or experimentation, which represent the values of a function for a limited number of values of the independent variable. It is often required to interpolate (i.e. estimate) the value of that function for an intermediate value of the independent variable. This may be achieved by classical mathematical interpolation (through curve fitting or regression analysis) or by geostatistical estimation (through kriging or stochastic simulations). The main advantage of the geostatistical approach is that it is the only available techniques that allows dealing with spatial variability (Houlding, 2000), and anisotropies, through the variogram modelling. Moreover, the geostatistical estimation is able to account for random noise: the noisier the sample set, the less the individual samples represent their immediate vicinity, the more they are smoothed and the greater the associated uncertainty (Isaaks & Srivastava, 1989). Finally, the geostatistical estimation predicts not only a value but also a measure of the uncertainty associated with the values, which is an integral part of the estimation results. The measure of uncertainty is also a measure of the goodness or reliability of the estimated vales as well as a measure of its possible variability; a result that other prediction techniques are unable to provide.

The most popular geostatistical estimation technique is kriging, which is the technique that provides the Best Linear Unbiased Estimator of unknown fields (Journel & Huijbregts, 1978; Kitanidis, 1997). Kriging is the optimal interpolation based on regression against observed z values of surrounding data points, weighted according to spatial covariance values.

All the interpolation methods estimate the value at a given location as a weighted sum of data values at surrounding locations. Mathematical algorithms (inverse distance squared, splines, radial basis functions, triangulation, etc.) assign weights according to functions that give a decreasing weight with increasing separa-

tion distance, while kriging assigns weights according to a (moderately) data-driven weighting function, rather than an arbitrary function. However, kriging is still just an interpolation algorithm and will give very similar results to others in many cases (Isaaks & Srivastava, 1989). In particular:

1. if the data locations are fairly dense and uniformly distributed throughout the study area, you will get fairly good estimates regardless of interpolation algorithm;
2. if the data locations fall in a few clusters with large gaps in between, you will get unreliable estimates regardless of interpolation algorithm;
3. almost all interpolation algorithms will underestimate the highs and overestimate the lows; this *smoothing effect* is inherent to averaging.

On the other hand the kriging presents the following advantages:

- it helps to compensate for the effects of data clustering, assigning individual points within a cluster less weight than isolated data points (or, treating clusters more like single points);
- it gives estimate of estimation error (kriging variance), along with estimate of the variable, Z , itself;
- the availability of estimation error provides basis for stochastic simulation of possible realizations of $Z(\mathbf{u})$.

Basically, kriging is a generic name adopted by geostatisticians for a family of least-squared regression algorithms in the recognition of the pioneering work of Krige (1951). All kriging estimators are but variants of the basic linear regression estimator $Z^*(\mathbf{u})$, defined as (Goovaerts, 1997):

$$Z^*(\bar{u}) - m(\bar{u}) = \sum_{\alpha=1}^{n(\bar{u})} \lambda_{\alpha}(\bar{u}) [Z(\bar{u}_{\alpha}) - m(\bar{u}_{\alpha})] \quad (14)$$

where: \mathbf{u} and \mathbf{u}_{α} are location vectors for estimation point and one of the neighbouring data points, indexed by α ; $n(\mathbf{u})$ is the number of data points in local neighbourhood used for estimation of $Z^*(\mathbf{u})$; $m(\mathbf{u})$ and $m(\mathbf{u}_{\alpha})$ are the expected values (means) of $Z(\mathbf{u})$ and $Z(\mathbf{u}_{\alpha})$; λ_{α} is the kriging weight assigned to datum $z(\mathbf{u}_{\alpha})$ for estimation location \mathbf{u} , interpreted as a realization of a regionalized variable –RV– $Z(\mathbf{u}_{\alpha})$. Same datum will receive different weight for different estimation location.

$Z(\mathbf{u})$ is treated as a random field with a trend component, $m(\mathbf{u})$, and a residual component, $R(\mathbf{u})=Z(\mathbf{u})-m(\mathbf{u})$.

Kriging estimates residual at \mathbf{u} locations as weighted sum of residuals at surrounding data points. Kriging weights, λ_{α} , are derived from covariance function or semivariogram, which should characterize residual component. Distinction between trend and residual somewhat arbitrary; it varies with scale.

The goal of kriging is to determine weights, λ_{α} , that minimize the error variance (σ_E^2) of the estimator:

$$\sigma_E^2(\bar{u}) = Var\{Z^*(\bar{u}) - Z(\bar{u})\} \quad (15)$$

under the unbiasedness constraint:

$$E\{Z^*(\bar{u}) - Z(\bar{u})\} = 0 \quad (16)$$

The kriging estimator varies depending on the model adopted for the random function $Z(\mathbf{u})$ itself. The random field –RF– $Z(\mathbf{u})$ is usually decomposed into a residual component $R(\mathbf{u})$ and a trend component, $m(\mathbf{u})$:

$$Z(\mathbf{u}) = R(\mathbf{u}) + m(\mathbf{u}) \quad (17)$$

The residual component is modeled as a stationary RF with zero mean and covariance $C_R(\mathbf{h})$:

$$E\{R(\bar{u})\} = 0 \quad (18)$$

$$Cov\{R(\bar{u}), R(\bar{u} + \bar{h})\} = E\{R(\bar{u}) \cdot R(\bar{u} + \bar{h})\} = C_R(\bar{h}) \quad (19)$$

The residual covariance function is generally derived from the input semivariogram model:

$$C_R(\mathbf{h}) = C_R(\mathbf{0}) - \gamma(\mathbf{h}) = Sill - \gamma(\mathbf{h}) \quad (20)$$

The expected value of the RV Z at location \mathbf{u} is thus the value of the trend component at the location:

$$E\{Z(\bar{u})\} = m(\bar{u}) \quad (21)$$

The three main kriging variants, simple, ordinary, and kriging with a trend, differ in their treatments of the trend component $m(\mathbf{u})$:

- the simple kriging –SK– considers the mean $m(\mathbf{u})$ to be known and constant throughout the study area A :

$$m(\bar{u}) = m \quad \text{known} \quad \forall \bar{u} \in A \quad (22)$$

so that:

$$Z_{SK}^*(\bar{u}) = m + \sum_{\alpha=1}^{n(\bar{u})} \lambda_{\alpha}^{SK}(\bar{u}) [Z(\bar{u}_{\alpha}) - m] \quad (23)$$

This estimate is automatically unbiased, since $E[Z(\mathbf{u}_{\alpha}) - m] = 0$, so that $E[Z_{SK}^*(\mathbf{u})] = m = [Z(\mathbf{u})]$.

The estimation error $Z_{SK}^*(\mathbf{u}) - Z(\mathbf{u})$ is a linear combination of random variables representing residuals at the data points, \mathbf{u}_{α} , and the estimation point, \mathbf{u} :

$$Z_{SK}^*(\bar{u}) - Z(\bar{u}) = [Z_{SK}^*(\bar{u}) - m] - [Z(\bar{u}) - m] = \sum_{\alpha=1}^{n(\bar{u})} \lambda_{\alpha}^{SK}(\bar{u}) R(\bar{u}_{\alpha}) - R(\bar{u}) = R_{SK}^*(\bar{u}) - R(\bar{u}) \quad (24)$$

Using rules for the variance of a linear combination of random variables, the error variance is then given by:

$$\sigma_E^2(\bar{u}) = Var\{R_{SK}^*(\bar{u})\} + Var\{R(\bar{u})\} - 2Cov\{R_{SK}^*(\bar{u}), R(\bar{u})\} \quad (25)$$

The minimization of the error variance, leads to the following system of equations:

$$\sum_{\beta=1}^{n(\bar{u})} \lambda_{\beta}^{SK}(\bar{u}) C_R(\bar{u}_{\alpha} - \bar{u}_{\beta}) = C_R(\bar{u}_{\alpha} - \bar{u}) \quad \alpha = 1, \dots, n(\bar{u}) \quad (26)$$

Because of the constant mean, the covariance function for $Z(\mathbf{u})$ is the same as that for the residual component, $C(\mathbf{h}) = C_R(\mathbf{h})$, so that it is possible to write the simple kriging system directly in terms of $C(\mathbf{h})$:

$$\sum_{\beta=1}^{n(\bar{u})} \lambda_{\beta}^{SK}(\bar{u}) C(\bar{u}_{\alpha} - \bar{u}_{\beta}) = C(\bar{u}_{\alpha} - \bar{u}_{\beta}) \quad \alpha = 1, \dots, n(\bar{u}) \quad (27)$$

This can be written in matrix form as

$$\mathbf{K} \boldsymbol{\lambda}_{SK}(\mathbf{u}) = \mathbf{k} \quad (28)$$

where \mathbf{K}_{SK} is the matrix of covariances between data points, with elements $\mathbf{K}_{i,j} = C(\mathbf{u}_i - \mathbf{u}_j)$; \mathbf{k} is the vector of covariances between the data points and the estimation point, with elements given by $\mathbf{k}_i = C(\mathbf{u}_i - \mathbf{u})$, and $\boldsymbol{\lambda}_{SK}(\mathbf{u})$ is the vector of simple kriging weights for the surrounding data points. If the covariance model is licit (meaning the underlying semivariogram model is licit) and no two data points are collocated, then the data covariance matrix is positive definite and we can solve for the kriging weights using:

$$\boldsymbol{\lambda}_{SK} = \mathbf{K}^{-1} \mathbf{k} \quad (29)$$

Once having the kriging weights, both the kriging estimate and the kriging variance can be computed, as:

$$\sigma_{SK}^2(\bar{u}) = C(0) - \boldsymbol{\lambda}_{SK}^T(\bar{u}) \vec{k} = C(0) - \sum_{\alpha=1}^{n(\bar{u})} \lambda_{\alpha}^{SK}(\bar{u}) C(\bar{u}_{\alpha} - \bar{u}) \quad (30)$$

It finds a set of weights for estimating the variable value at the location u from values at a set of neighbouring data points. The weight on each data point generally decreases with increasing distance to that point, in accordance with the decreasing data-to-estimation covariances specified in the right-hand vector, \mathbf{k} . However, the set of weights is also designed to account for redundancy among the data points, represented in the data point-to-data point covariances in the matrix \mathbf{K} . Multiplying \mathbf{k} by \mathbf{K}^{-1} (on the left) will downweight points falling in clusters relative to isolated points at the same distance.

- the ordinary kriging –OK– accounts for local fluctuations of the mean limiting the domain of stationarity of the mean to local neighbourhood $W(\mathbf{u})$:

$$m(\bar{u}') = m \quad \text{constant but unknown} \quad \forall \bar{u}' \in W(\bar{u}) \quad (31)$$

Therefore the mean is constant in the local neighbourhood of each estimation point, that is that

$m(\mathbf{u}_{\alpha}) = m(\mathbf{u})$ for each nearby data value, $Z(\mathbf{u}_{\alpha})$, used to estimate $Z(\mathbf{u})$. In this case, the kriging estimator can be written as

$$Z_{OK}^*(\bar{u}) = m(\bar{u}) + \sum_{\alpha=1}^{n(\bar{u})} \lambda_{\alpha}^{OK}(\bar{u}) [Z(\bar{u}_{\alpha}) - m(\bar{u})] = \sum_{\alpha=1}^{n(\bar{u})} \lambda_{\alpha}^{OK}(\bar{u}) Z(\bar{u}_{\alpha}) + \left[1 - \sum_{\alpha=1}^{n(\bar{u})} \lambda_{\alpha}^{OK}(\bar{u}) \right] m(\bar{u}) \quad (32)$$

filtering the unknown local mean by requiring that the kriging weights sum to 1, leads to an ordinary kriging estimator of

$$Z_{OK}^*(\bar{u}) = \sum_{\alpha=1}^{n(\bar{u})} \lambda_{\alpha}^{OK}(\bar{u}) Z(\bar{u}_{\alpha}) \quad \text{with } \sum_{\alpha=1}^{n(\bar{u})} \lambda_{\alpha}^{OK}(\bar{u}) = 1 \quad (33)$$

In order to minimize the error variance subject to the unit-sum constraint on the weights, it is necessary to set up the system minimize the error variance plus an additional term involving a Lagrange parameter, $\mu_{OK}(\mathbf{u})$:

$$L = \sigma_E^2(\bar{u}) + 2\mu_{OK}(\bar{u}) \left[1 - \sum_{\alpha=1}^{n(\bar{u})} \lambda_{\alpha}^{OK}(\bar{u}) \right] \quad (34)$$

so that minimization with respect to the Lagrange parameter forces the constraint to be obeyed:

$$\frac{1}{2} \frac{\partial L}{\partial \mu} = 1 - \sum_{\alpha=1}^{n(\bar{u})} \lambda_{\alpha}^{OK}(\bar{u}) = 0 \quad (35)$$

In this case, the system of equations for the kriging weights turns out to be:

$$\begin{cases} \sum_{\beta=1}^{n(\bar{u})} \lambda_{\beta}^{OK}(\bar{u}) C_R(\bar{u}_{\alpha} - \bar{u}_{\beta}) + \mu_{OK}(\bar{u}) = C_R(\bar{u}_{\alpha} - \bar{u}) & \alpha = 1, \dots, n(\bar{u}) \\ \sum_{\beta=1}^{n(\bar{u})} \lambda_{\beta}^{OK}(\bar{u}) = 1 \end{cases} \quad (36)$$

where $C_R(\mathbf{h})$ is once again the covariance function for the residual component of the variable. In simple kriging, it is possible to equate $C_R(\mathbf{h})$ and $C(\mathbf{h})$, the covariance function for the variable itself, due to the assumption of a constant mean. That equality is not valid here, but in practice the substitution is often made anyway, on the assumption that the semivariogram, from which $C(\mathbf{h})$ is derived, effectively filters the influence of large-scale trends in the mean. Actually, the unit-sum constraint on the weights allows the ordinary kriging system to be stated directly in terms of the semivariogram (in place of the $C_R(\mathbf{h})$ values above). In a sense, ordinary kriging is the interpolation approach that follows naturally from a semivariogram analysis, since both tools tend to filter trends in the mean.

Once the kriging weights (and Lagrange parameter) are obtained, the ordinary kriging error variance is given by:

$$\sigma_{OK}^2(\bar{u}) = C(0) - \sum_{\alpha=1}^{n(\bar{u})} \lambda_{\alpha}^{OK}(\bar{u}) C(\bar{u}_{\alpha} - \bar{u}) - \mu_{OK}(\bar{u}) \quad (37)$$

In matrix terms, the ordinary kriging system is an augmented version of the simple kriging system.

- the kriging with a trend model –KT– was formerly known as universal kriging. It considers that the unknown local mean $m(\mathbf{u}')$ smoothly varies within each local neighbourhood $W(\mathbf{u})$, hence over the entire study area A . The trend component is modelled as a linear combination of functions $f_k(\mathbf{u})$ of the coordinates:

$$m(\bar{u}) = \sum_{k=0}^K [a_k(\bar{u}') f_k(\bar{u}')] \quad \text{with } a_k(\bar{u}') \approx a_k \quad \text{unconstant but unknown} \quad \forall \bar{u}' \in W(\bar{u}) \quad (38)$$

The coefficients $a_k(\mathbf{u}')$ are unknown and deemed constant within each local neighbourhood $W(\mathbf{u})$. By convention $f_0(\mathbf{u}') = 1$, hence the case $K = 0$ is equivalent to ordinary kriging (constant but unknown mean a_0).

If the variable of interest does exhibit a significant trend, a typical approach would be to attempt to estimate a “de-trended” semivariogram and then feed this into kriging with a firstorder trend. However, Goovaerts (1997) warns against this approach and instead recommends performing simple kriging of the residuals from a global trend (with a constant mean of 0) and then adding the kriged residuals back into the global trend.

These three methods (SK, OK and KT) are widely applied dealing with continuous variable, but if the variable is categorical the classical approach is the Indicator Kriging (IK), which was introduced by Journel in 1983; since that time has grown to become one of the most widely-applied grade estimation techniques in the minerals industry. Its appeal lies in the fact that it makes no assumptions about the distribution underlying the sample data, and indeed that it can handle moderate mixing of diverse sample populations. However, despite the elegant and simple theoretical basis for IK, there are many practical implementation issues which affect its application and which require serious consideration. These include aspects of order relations and their correction, the change of support, issues associated with highly skewed data, and the treatment of the extremes of the sample distribution when deriving estimates (Glacken & Blackney, 1998). Firstly, it is necessary to settle on a finite number of thresholds that adequately represent the input data distribution shape. There is always a trade-off between the number of thresholds selected and the time available for the required analysis.

The outcome of IK is a conditional cumulative distribution function (ccdf) – in effect a distribution of local uncertainty or possible values conditional to data in the neighbourhood of the block to be estimated.

The primary motivation behind the use of IK in most earth science applications, and one of the main reasons for its introduction, is that it is non-parametric. Moreover, it is one of the few techniques that addresses mixed data populations.

Since IK generates at each point or block a cumulative distribution, this should be non-decreasing and valued between zero and one. These two requirements are sometimes not met, leading to so-called order relations violations. Many methods have been proposed to counteract the order relations issue the most commonly-used involves direct correction of the indicator values (Deutsch & Journel, 1998).

The Multiple Indicator Kriging – MIK – consists in the use of a variogram model for each class (the indicator semivariogram). When anisotropy changes too much between adjacent thresholds, the order relations violations become prohibitively large and the MIK is not applicable; the more common alternative to MIK

consists in using the indicator semivariogram at median threshold values, which may be used to detect pattern of spatial continuity whenever extreme-valued data renders the traditional variogram erratic (Goovaerts, 1997). This approach, which in the estimation is called Median Indicator Kriging, consists in inferring the median indicator variogram (i.e. the variogram for the median of input data) and using this to define the continuity conditions for all indicators, and so it is used for all cut-offs. This approach is very fast, since the kriging weights do not depend on the cutoff being considered. Median Indicator Kriging also necessitates the solution of only one kriging system in contrast to the multiple systems required for Multiple Indicator Kriging (Glacken & Blackney, 1998). This method is a simplified form of MIK, which is frequently used when sample data is sparse and thus it is difficult or impossible to define grade continuity for a full range of indicators (this situation is quite common, for instance in the early stages of a resource project). The median indicator variogram is typically the most robust of all indicators, it tends to have the greatest range of continuity, and it is the easiest to define with some confidence from sparse data. The application of variograms from a single indicator to all thresholds reveals the main assumption associated with the median indicator method: the direction and range of continuity does not vary with changing thresholds. Obviously, the Median Indicator Kriging is not a recommended technique if data permits the full estimation of a set of indicator variograms.

The IK theory has now largely been superseded and improved by the conditional simulation paradigm. Conditional simulation offers all of the advantages of IK and more. The single drawback – still a major issue at most sites – is the quantum leap in processing time and computing power required for the successful implementation of a simulation approach. However, even this is becoming a diminishing problem as computers exponentially increase in speed and memory capacity.

Stochastic simulation is a means for generating multiple equiprobable realizations of the property in question, rather than simply estimating the mean. Essentially, we are adding back in some noise to undo the smoothing effect of kriging. This possibly gives a better representation of the natural variability of the property in question and gives us a means for quantifying our uncertainty regarding what's really down there.

The two most commonly used forms of simulation are: sequential Gaussian simulation –SGS– for continuous variables and sequential indicator simulation –SIS– for categorical variables.

The basic idea of sequential Gaussian simulation (SGS) is very simple. Recall that kriging gives an estimate of both the mean and standard deviation of the variable at each grid node; it is possible to represent the variable at each grid node as a random variable following a normal (Gaussian) distribution. Rather than chooses the mean as the estimate at each node, SGS chooses a random deviate from this normal distribution, selected according to a uniform random number representing the probability level.

So, the basic steps in the SGS process are:

1. to generate a random path through the grid nodes;

2. to visit the first node along the path and use kriging to estimate a mean and standard deviation for the variable at that node based on surrounding data values;
3. to select a value at random from the corresponding normal distribution and set the variable value at that node to that number;
4. to visit each successive node in the random path;
5. to repeat the process, including previously simulated nodes as data values in the kriging process.

The use of a random path avoids artefacts induced by walking through the grid in a regular fashion. The previously simulated grid nodes are included as data, in order to preserve the proper covariance structure between the simulated values.

Sometimes SGS is implemented in a “multigrid” fashion: first simulating on a coarse grid (a subset of the fine grid – maybe every 10th grid node) and then on the finer grid (maybe with an intermediate step or two) in order to reproduce large-scale semivariogram structures. Without this, the “screening” effect of kriging quickly takes over as the simulation progresses and nodes are filled in, so that most nodes are conditioned only on nearby values, so that small-scale structure is reproduced better than large scale structure.

For SGS, it is important that the data actually follow a Gaussian distribution. If they do not, the normal score transformation, also called Gaussian anamorphosis, is required. If the multi-Gaussian assumption is not satisfied with observed data, the Sequential Indicator Simulation –SIS– should be the next priority considered (Goovaerts, 2001). Actually the SIS can be used for the stochastic modelling of non-parametric data (that is without a Gaussian distribution) of both discrete and continuous attributes.

The SIS is very similar to the sequential Gaussian simulation, except that indicator kriging is used to build up a discrete cumulative density function for the individual categories at each case and the node is assigned a category selected at random from this discrete cdf.

SIS is a popular pixel-based simulation method, based on the sequential simulation approach. Considered a set of random variables $z(x')$ for an attribute at n unsampled locations $(x'_1, x'_2, \dots, x'_n)$ in the study area, the objective is to generate a joint realization $\{z(x'_1), z(x'_2), \dots, z(x'_n)\}$ at the unsampled locations. The sequential simulation approach requires simulation of a prior distribution at each unsampled location. In SIS, the IK estimator is used to model the prior conditional cumulative distribution function –ccdf– at each unsampled location. Since modelling the prior CCDF at each unsampled location should use previously simulated values at other unsampled locations, the simulated values for all unsampled locations are referred to as a joint realization (Goovaerts, 1996). A flow chart illustrating the SIS procedure and its steps is shown in

Figure 6.

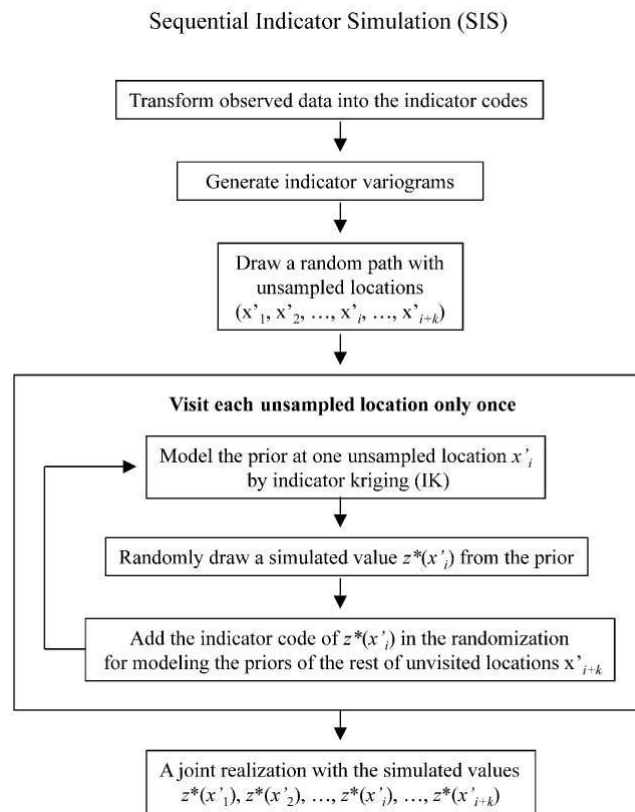


Figure 6 – The flow chart illustrating the procedure of sequential indicator simulation (from Juang et al., 2004)

The SIS algorithm is based on the following steps:

1. to transform the data into the indicator codes (1 or 0) by the indicator function;
2. to obtain one indicator variogram for each cutoff values;
3. to define a random path to unsampled locations;
4. to visit each location to be simulated once only;
5. to repeat the four previous steps to proceed along the random path to obtain a joint realization for unsampled locations.

Many realizations can be generated with various random paths. Each realization given a random path obtains an outcome of the spatial distribution of the variable and thus the uncertainty of mapping can be obtained through many realizations (Juang et al., 2004).

Following a random path through the three-dimensional grid, individual grid-nodes are simulated, one after another, using constantly updated, thus increasing size, conditioning datasets. The conditioning dataset includes the original data and all previously simulated values within a specified neighbourhood. This ensures that closely spaced values have the correct short scale correlation (Seifert & Jensen, 1999). In other words, in this simulation approach, a grid-node is selected randomly and simulated with reference to the original conditioning dataset. In the next step, another grid-node is selected randomly, and the variable is simulated

using the newly generated conditional cumulative distribution function –ccdf–, which is now increased in size by one value. In this way, each node is simulated (Deutsch & Journel, 1992).

1.2 Geostatistics and rock mechanics: state of art

Some authors have already applied the geostatistical approach to problems relative to rock mass fracture-distribution modelling (Long & Billaux, 1987; Chilès, 1988; Gringarten, 1996; Dantini et al., 1999; Meyer & Einstein, 2002; Dowd et al., 2007; Rafiee & Vinches, 2008; Koike et al., 2012) and to the estimation of rock mass specific properties:

- La Pointe (1980) used geostatistics for estimating block ore grade and tonnage in a quarry at Lannion (France). The geostatistical approach allowed indicating the degree of in homogeneity in frequencies and orientation of two distinct joint sets, and estimating the distance to which these properties can be extrapolated. Each joint set was represented by a regional semi-variance function, plus a local oscillatory component corresponding to the average spacing of the most persistent joints.
- After few years, Barla et al. (1987) applied geostatistical analysis to rock mass characterization, at the Masua mine in Sardinia (Italy). These authors looked for spatial correlations and variability of the following rock mass parameters: Rock Quality Designation —RQD—, number of discontinuities for metre, spacings, orientation (in term of dip angle and dip direction), condition of discontinuities, and Rock Mass Rating index —RMR— (Bieniawski, 1989).
- Hoeger & Young (1987) furnished local estimates of discontinuity and rock mass conditions obtained through geostatistics as inputs to geotechnical designs. They used geostatistics for local estimation of rock joint orientation data for slope stability analysis of an open pit mine. Joint orientations were mapped on the surface of the pit slopes, using regular squared cells, with the side of 15 metres. From the entire data set three major sets were indentified and screened from the remainder of the data set. Kriging was used to build a localized block model of rock joint orientations.
- Long & Billaux (1987) investigated the areal fracture density, the orientations, lengths and aperture distributions of fractures, in a uranium mine, located in France. The data were collected in a long section of a drift, mapping the fractures. The data were subdivided into 5 sets. The mean lengths and fracture densities were simulated for each discontinuity set.
- Regarding the orientations of rock joints, Young (1987a; 1987b) evaluated their local distribution, using data from an open pit mine in porphyry deposits. Local estimations of rock fracture orientations was performed by ordinary kriging, as well as by indicator kriging.
- Billaux et al. (1989) used geostatistical simulation methods to reproduce the spatial structure of rock, such as the variation of fracture density, persistence and orientation in space. Data were mapped, along two different sections, at the Fanay-Augères mine in Limousin (France).

- Yu and Mostyn (1993) reviewed concepts and models used for modelling the spatial correlation of joint parameters, including not only the geometric parameters of rock joints, such as orientation (in term of dip and dip direction), trace length, size and spacing, but also their mechanical properties, as strength (cohesion and internal friction angle).
- Taboada et al. (1997) applied geostatistical techniques to the exploitation planning in slate quarries. Geostatistics was used to evaluate the rock mass quality, in term of recovery index, and to plan the mechanical cutting works.
- Tavchandjian et al. (1997) analyzed the spatial distribution of fracture density (calculated in function of the frequency, length and width of fracture trace) in shear zones, using data obtained from the mapping of drift walls at the Henderson mine in Quebec (Canada). The spatial distribution of the fracture density of each set was estimated, through indicator kriging, using three variables: the absence of fracture, the presence of cluster of small fractures with negligible thickness and the presence of fractures with measurable thickness.
- Escuder Viruete et al. (2001; 2003a; 2003b) used the fracture index, or the number of structural discontinuities present by unit length of scanline in the outcrop, to characterize quantitatively the fracture system and the associated spatial variability in the Mina Ratones area, located in the Alcala Gratomic Pluton (Iberian Massif, Spain). They used field data, together with 3D-seismic tomographic data, core and well log structural information. The fracture index was estimated by means of ordinary kriging, sequential Gaussian simulations, using both a bi-dimensional and a tri-dimensional approach.
- Koike et al. (2001) focused on fracture density along a borehole and appearance of relation of azimuths (strike and dips) between a fracture pair considering different scales of analysis. A fracture density map was produced by sequential Gaussian simulation technique, and a direction of each simulated fracture was assigned combining the ordinary kriging with the principal component analysis. Horizontal distribution of fractures and continuities of them were estimated, and the permeability calculated.
- Ozturk & Nasuf (2002) analysed the spatial distribution of rock compressive strength, RQD, Joint wall Compressive Strength —JCS—, and net cutting rate in tunnel route, with the aim to estimate the properties of rock masses and so the required machine performance in sewerage tunnel project in Istanbul (Turkey). The prediction of these mechanical properties was made by means of the kriging technique.
- Gumiax et al. (2003) applied geostatistical methods to the directional data of fracture orientations, calculating the mean principal directions and analysing the variations of data in space. The statistical analysis cannot be made with classical circular data; therefore, their directional cosines were used in the geostatistical estimation, performed through ordinary kriging method.

- Also Einstein (2003) reported the use of geostatistics on RQD values.
- Oh et al. (2004) integrated magneto-telluric resistivity data and borehole information for the spatial estimation of RMR values along a tunnel 2 kilometres long. The mean RMR values, around the borehole sites, were estimated through simple kriging, combined with the non-linear indicator transform method of resistivity data.
- Bastante et al. (2005, 2008) applied several geostatistical techniques in order to evaluate and estimate the resources in an ornamental slate deposit, located in Cabrera (Spain). Data were collected from drill core, subdividing the deposit into exploitable (i.e. useful and saleable) and not exploitable (or not useful) slate. Indicator kriging, sequential indicator simulations and multiple-point statistics were applied, and their results were compared.
- Koike & Ichikawa (2006) studied the fracture distributions and the scaling law of fracture systems, in the Tohoku district (Japan). Fracture systems were investigated over different scales: remotely sensed images from satellites, borehole-fracture data in two drilling directions, and a thin-section of rock core sample. The spatial correlation structures of fractures were clarified by semivariograms, focusing on joint's line density along boreholes, area density of linear features, and directional relations of strikes between a fracture pair to produce semivariograms of densities and cross-semivariograms of the strikes transformed into binary data sets. The same model independent of the scales could approximate the semivariograms of each parameter. The modelling at the borehole-fracture scale involved three steps: generation of fracture-density map by a sequential Gaussian simulation, assignment of strikes to each simulated fracture, and connection of fractures considering distances and differences in strikes between a closely located fracture pair.
- By means of geostatistical techniques, You & Lee (2006) incorporated geophysical exploration, drilling and field data, along a tunnel alignment, located in Korea. They, applying the multiple indicator kriging technique, estimated the RMR classes, before the excavation and at three different construction stages of the tunnel.
- Choi & Lee (2007) and Choi et al. (2009) used the geostatistical approach to characterize rock mass quality along a tunnel alignment, located in Kimhae City (Korea). The RMR values were estimated, by using the three-dimensional anisotropic indicator kriging approach, combining field, borehole and geophysical data. A quantitative method for assessing the uncertainty of the estimated RMR was proposed.
- Stavropoulou et al. (2007) exploited geological and borehole geotechnical data obtained in the exploratory phase of a tunnelling project to reproduce the spatial variability of rock mass quality (in term of RMR). The ordinary kriging was used to estimate the RMR values around the projected twin tunnels, having a total length of 130 metres each.

- Exadaktylos & Stavropoulou (2008) investigated the spatial variability exhibited by RMR during an underground excavation, affronting also the problem of the upscaling of the rock deformability and strength parameters, from the laboratory tests to 3D geological representative volumes. The interpolation of RMR values was performed by the kriging technique.
- Exadaktylos et al. (2008) investigated the rock mass quality, through the RMR and also the Q-system —Q— (Barton et al. 1974) classifications, studying also its effects on the Tunnel Boring Machine —TBM— parameters and the specific energy —SE— of rock cutting. The estimation was based on sampled data referring to rock mass classification indices or TBM related parameters. Kriging was performed in order to make predictions of RMR, Q or SE along the chainage of the tunnel from boreholes at the exploration phase and design stage of the tunnel, and to make predictions of SE and RMR or Q ahead of the tunnel's face during excavation of the tunnel based on SE estimations during excavation. This methodology was applied to several study cases, using data from: a system of twin tunnels in Hong Kong (China), three tunnels excavated in Northern Italy, and a section of the Metro tunnel in Barcelona (Spain).
- An example of geostatistical application to rock mass stability evaluation, related to tunnel and mining activities, is given by Ellefmo & Eidsvik (2009), that, using borehole data, quantified the local and spatial frequency of joints and the associated variability (or uncertainty) at unsampled locations, in the Kvannevan Iron Ore (Norway). Not only the expected RQD values, but also possible values (i.e. RQD ranges) were assessed, and the probability that the joint frequency exceeds five joints per metre was estimated. Three different techniques were applied: kriging with Poisson sampling, turning band method and using a spatially smooth Gaussian prior distribution. By using simulation instead of estimation, a clear picture of possible joint frequency values or ranges, i.e. the uncertainty, was obtained.
- Chiessi et al. (2010) employed geostatistical techniques, combined with the classical deterministic approach, in the rockfall hazard assessment procedure. Geostatistics was applied to the analysis of observations of location and dimension of previously fallen blocks, in order to assess the probability of arrival of blocks due to potential future collapses in the village of San Quirico (Italy). The geostatistical approach revealed to be unquestionably useful, because it gave the best estimation of point-source phenomena such as rockfalls inferred from either on-site observations or rockfall path data. In this study several estimation techniques were employed: ordinary kriging, simple kriging, disjunctive kriging, indicator kriging, and the modified form of indicator kriging, called probability kriging (Sullivan, 1984), which is a non-linear method employing indicator variables. The obtained maps, which highlight areas susceptible to rock block arrivals, are consistent with the recorded field data, especially using the indicator kriging method, which yielded the highest density of the blocks and agreed with field observations.

- Lana et al. (2010) used the indicator kriging for the estimation of potential failure risks in a mine slope, located in Minas Gerais (Brazil). This slope, excavated in quartzite with a maximum height of 200 metres at the time of this study, presented many failure problems involving the sliding of small blocks formed by discontinuities. Geostatistics was applied to estimate potential failure risks in limited areas along this slope. The indicator kriging was employed, subdividing the blocks in stable and unstable, on the basis of orientations of joint discontinuities and slope face.
- Kaewkongkaew et al. (2011) investigated the applicability and limitation of geostatistical methods in predicting rock mass quality, using the RMR index, along tunnel alignments based on drill hole data. They used data coming from two different case studies, both located in Thailand: a pumped storage project, affecting horizontal beds of sedimentary rocks, and a dam site, located in a volcanic rock belt. The prediction, by ordinary kriging, allowed estimating RMR values, which were compared with field observation data available from the excavation of the exploratory tunnels. The first case study gave good results, but not the second one, due to the complex geological setting of the site.
- In addition, Esfahani and Asghari (2012) studied the spatial distribution of rock mass quality, in term of RQD, in an apatite deposit in Iran. The RQD, obtained from drill cores, was estimated through the sequential Gaussian simulation, in order to detect the fractured zones. The domains with low RQD value (below the 20%) were interpreted as fault zones, while the high RQD domains correspond to less fractured areas. The spatial position of fault systems was used for the selection of the excavation method and the estimation of ore reserves.
- Yi et al. (2013) estimated the RMR values along future additional drifts that will be constructed during site redevelopment of Gagok mine, located in the Samcheok area of Gangwon (South Korea). The multiple indicator kriging was applied, using borehole RMR and electrical resistivity tomography data. Two correction methods were proposed to increase the reliability of kriging-based estimation.
- Alikarami et al. (2013) analysed the petro-physical and mechanical properties of sandstone, investigating the distribution of deformation structures, such as fractures and deformation bands, in the Navajo and the Entrada sandstones in the fault core and damage zones of two faults, located in Cache Valley and San Rafael Swell (Utah). These two localities had different degree of calcite cementation. In-situ measurements by Tiny-Perm II and Schmidt hammer were performed in order to examine the distribution of permeability and strength/elasticity of rock, within the damage zone of these faults. The statistical relation between Tiny-Perm II measurements and Schmidt hammer values, permeability and uni-axial compressive strength, and permeability and Young's modulus of deformed rocks were investigated. The correlations between the studied parameters varied with the degree of calcite cementation in mineralogically similar sandstones (quartz sandstone): an exponen-

tial law resulted to be more suitable for non-cemented sandstone, whereas for cemented sandstone these relations were better approximated by a power law.

All these authors concluded that rock mass parameters are successfully estimable in unsampled locations, using geostatistical interpolation methods. All the described geostatistical analyses have been applied to specific problems and on localized sites, never considering a big area.

A summary of papers regarding the estimation of rock mass properties has been reported in **Appendix 1**.

2. VALCHIAVENNA CASE STUDY

2.1 Geographical, geological and structural settings

The first study area is located in the Italian Central Alps, along a glacial valley, called Chiavenna Valley (Province of Sondrio), which is situated between Lake Como and the Splügen Pass (**Figure 7**). The Chiavenna Valley consists of two main valleys: San Giacomo and Bregaglia valleys, which connect Italy to Switzerland.

This thesis focuses on San Giacomo Valley, also called Spluga Valley, whose extension is about 200km² and its morphology results from its structural and glacial evolution.



Figure 7 – Location of study area: the red circle represents Chiavenna Valley

The Central Northern Alps are a fold and thrust system, belonging to the Alpine nappe pile, which created in a subduction zone environment during the closure of the Piemontais and Valaisan oceans. The major thrust sheets developed during the Alpine compressional phase and imbricated from South to North, forming, in the region of interest, the Pennidic Nappe arrangement. In the Pennidic nappes of San Giacomo Valley consist of tabular overlapped bodies, composed by recumbent folds north verging (Sciesa, 1991). These Pennidic units emplaced, by thrusting towards North-east, in the early Tertiary (Froitzheim et al., 1994).

In particular, the research area pertains to the upper Pennidic units which have been considered to be an orogenic wedge consisting of underplated basement and sedimentary slices related to the Valaisan subduction (Marquer et al., 1994). After the onset of continental collision, E-W extension took place along major ductile displacement zones; late folding overprinted and steepened the previous structures. The latest structures are brittle normal faults cross-cutting all the previous structures (e.g. the Forcola fault) and may be coeval with displacements along the Engadine line and the Iorio-Tonale line, which corresponds to the late stage of the Insubric line (Schmid et al., 1987).

In brief, the regional geological setting of San Giacomo Valley is characterized by the emplacement of sub-horizontal gneissic bodies (“Tambò” and “Suretta” basement units) emplaced towards East and separated by a metasedimentary cover unit, called “Spluga Syncline” (Figures 8 and 9).

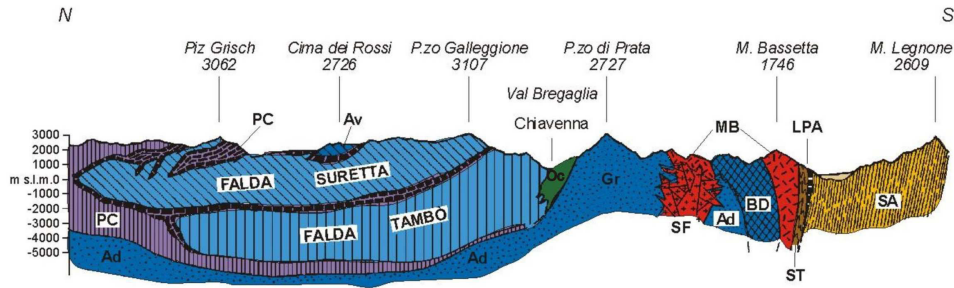


Figure 8 – Geological cross-section of Chiavenna Valley: San Giacomo Valley is to the North of Chiavenna

The tectonic contact between the two main nappes gently dips towards NE. The Tambò and Suretta nappes form thin crystalline slivers, each with a thickness of about 3.5 kilometres, essentially composed of poly-cyclic and poly-metamorphic basement of paragneisses and metagranites, both of pre-Permian age; thin layers of amphibolites and orthogneisses are intercalated within the paragneisses. The lithological features of basements are so almost similar.

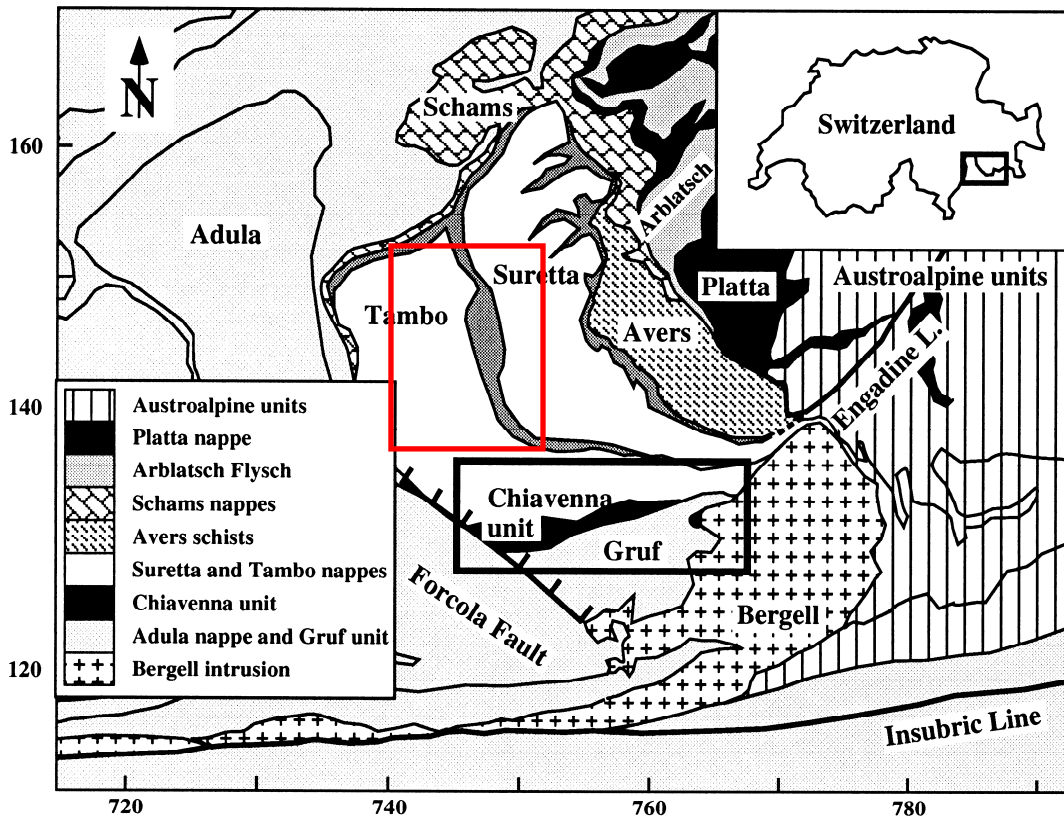


Figure 9 – Tectonic sketch map of the Penninic zone of the Italian Central Alps (or Eastern Swiss Alps). The red rectangular represents San Giacomo Valley, the black one Bregaglia Valley. Numbers refer to the Swiss coordinate grid (from Huber & Marquer, 1998)

The Tambo nappe is derived from the Briançonnais continental domain, which separated the Valais ocean from the Piemont-Liguria Ocean.

The crystalline basement of Tambò nappe, of Hercynian age, covers a very large domain in the study area: it is developed for about 35-40 kilometres, with thickness up to 400 metres. The Tambò basement consists of granitic bodies and the Prealpine embedding crust; it is dominantly composed of paragneisses which already suffered Variscan deformation and to a minor extent of Late Variscan laccolithic granitoid complexes. The basement of Tambò nappe has a complex structure, which has been divided in several zones:

- in the southern part of the study area a lithotype of Permian age, called the Truzzo metagranite, outcrops: it is an augen orthogneiss (i.e. a coarse-grained gneiss), interpreted as resulting from metamorphism of granite, which contains characteristic elliptic or lenticular shear bound K-feldspar porphyroclasts (of several centimetres), within the layering of the quartz, biotite and magnetite bands. It is often associated with migmatites, and rich in inclusions of schist and microgranitic facies (Digonzelli, 1987);
- in the northern part of the study area, the basement of Tambò Nappe includes some units consisting of different rock types of sedimentary origin. The outcrops belong to the Superior Corbet Sequence: it is composed of several lithologies, with sedimentary origin, often interbedded. Paragneiss with muscovite, chlorite and biotite prevails. Nevertheless this sequence includes also garnet-mica schist, gneiss, pegmatites and basic rocks (De Poli, 1987).

The Tambò nappe contains some north verging folds, with axes dipping towards E or NE, with a dip angle ranging from 10 ° to 40 °, attributable to two distinct folding events.

The Tambò nappe is separated from the overlying Suretta nappe by the Tambò cover unit, called Spluga Syncline (or also Splügen zone), a unit comprising Permo-Mesozoic strata. It is interbedded between the basements of the Tambò and Suretta nappes, with tectonic contacts and consists of a series of slivers of metasediments, unstuck from the substrate and overlapped between them. Basal conglomerates, quartzites and dolomitic marbles on top of the Tambo basement are considered as its autochthonous cover, but are overlain by strongly sheared and imbricated allochthonous Triassic carbonatic sequences (Baudin et al., 1993).

The Spluga Syncline shows intensive deformations and great thickness variations: from a few metres up to several hundred metres in thickness (the apparent thickness reaches up to 800 metres). The Spluga Syncline consists of Permo- Mesozoic metasediments, distinguishable in various zones, characterized by different stratigraphic sequences.

The Suretta nappe consists of Briançon-derived crustal slices, which were assembled in a south dipping subduction zone during the Alpine orogenic cycle (Scheiber, 2013). The nappe contains post-Variscan rocks of the Rofna Porphyry Complex and Permo-Mesozoic cover sequences. The overall geometry of the Suretta nappe is the result of two main deformation phases: (1) Eocene top-to-the-NNW directed thrusting

and folding (Ferrera phase), which is overprinted by (2) back-folding and back-shearing (Niemet–Beverin phase).

The basement of the Suretta nappe, as well as the Spluga Syncline, outcrops in continuity along the left hydrographical side of San Giacomo Valley; on the right side they outcrop only near the top of a peak (the Mount Tignoso klippe).

The basement of Suretta nappe, belongs to the Superior Penninic domain, and has a very complex structure, with significant foldings, developed during several distinct deformative phases, which led to the formation of horizontally isoclinal folds.

In the study area, the basement of Suretta nappe lithologically consists of two main units:

- in the southern part, a heterogeneous polymetamorphic rock assemblage named Stella-Timun complex (Gelmetti, 1988) or Timun complex is exposed (Milnes & Schmutz, 1978). It mainly consists of metapelites, semipelites, metagraywackes, paragneisses, micaschistes with garnet and staurolite, with discontinuous interbedded augen orthogneisses of unknown age, and minor lenses of mafic rocks (amphibolites). The metasedimentary rocks locally show migmatitic structures (Wilhelm, 1921; Staub, 1926). This basement was intruded by pre-Alpine magmatic bodies, such as porphyritic orthogneisses of unknown age and a lower Permian subvolcanic intrusion, the Rofna Porphyry Complex. Mineralogical and structural investigations of mafic lenses embedded within the Timun complex led to the distinction of two events in the metamorphic history of the Suretta nappe: a pre-Alpine high-P, high-T subduction-collision event and an Alpine high-P, low-T event of 380-450 °C at about 1 GPa (Ring, 1992a; Biino et al., 1997; Nussbaum et al., 1998; Steinitz & Jäger, 1981);
- in the northern part, a large, variably deformed igneous body is exposed, the Rofna Porphyry Complex (Scheiber, 2013), which in the past was also inappropriately called Rofnaporphyr (Heim, 1891), Rofnagneiss (Schmidt, 1891; Wilhelm, 1929), Rofna gneiss (Hanson et al., 1969), Rofna rhyolite (Marquer et al., 1998) and Rofna metagranite (Nussbaum et al., 1998). The magmatic event emplacing the Rofna Porphyry Complex –RPC– is dated at 268.3 ± 0.6 Ma (Marquer et al., 1998). Preliminary results of measurements on zircons indicate that all members of the RPC most likely represent Permian magmatic rocks. Parts of the intrusion remained unaffected by Alpine deformation. The RPC, forming the frontal part of the Suretta nappe, is intensively folded together with strips of Triassic marbles.

In the lower and interior parts of the Suretta nappe, weakly to undeformed boudins are generally surrounded by L-tectonites indicating WSW–ENE stretching; foliated equivalentes reveal a plane strain deformation state. The upper part of the Suretta nappe, which was strongly affected by back-shearing, shows flattening strain (Scheiber, 2013).

The basements of Tambò and Suretta nappes are unconformably overlain by Permo-Mesozoic sedimentary covers, which show the typical stratigraphy of internal Briançonnais sediments (Baudin et al., 1995). The Permo-Mesozoic cover, from older to younger sediments, is constituted of: conglomerates with quartz pebbles and albite-bearing quartzites, which probably formed from Permian volcano-detritic sediments (Huber & Marquer, 1996). The Mesozoic cover consists of pure quartzites in the Suretta nappe and impure quartzites in the Tambò nappe, with also dolomitic marbles, marbles and schists.

The sedimentary rocks lying on the Suretta basement are Permo-Triassic conglomerates, quartzites, marbles, dolomites and an unconformable thick member of polygenic breccia probably late Cretaceous in age (Baudin et al., 1995). This thin autochthonous sedimentary cover lies unconformably on the already deformed basement of Suretta nappe. These Permo-Mesozoic autochthonous sediments overlie both the Timun complex and the RPC, but they do not outcrop in the study area. No fossils are recorded from these sediments; however, they have to be younger than the RPC.

The Alpine metamorphic grade increases from the top of the Suretta nappe to the bottom of the Tambò nappe and from the North to the South of nappes from greenschist facies to amphibolite facies (Baudin & Marquer, 1993). Alpine pressure-dominated metamorphism did not reach conditions higher than blue-schist facies, and the eclogite facies present in the Upper Pennine Units (Tambò and Suretta) are ascribed to the Pre-alpine metamorphic events.

In order to outline the intricate structural history, the principal deformational events have been recognised. Each event produced various sets of structures under a relatively constant regional stress field and metamorphic type. However, this does not imply that, for instance, D₃ structures can always be clearly separated in time from D₄ structures. The events result from an orogenic evolution that progressed in time and space Ring, (1992b).

In the past, only four main deformational events have been distinguished in the upper eastern Pennine Units (Huber & Marquer, 1988), which are related to: the closure of the Valais Pennine basin, the north-westward thrust structure formation during the Eocene subduction; the Oligo–Miocene collision, accompanied with a syn-collisional E–W extension. Today, the geometry of the Penninic units in this area is interpreted as the result of five superimposed deformation phases (Milnes & Schmutz, 1978; Schmid et al., 1997; Wiederkehr et al., 2008, Scheiber, 2013):

1. The Avers phase (D₁) is considered as an early detachment and thrusting stage, which marks the beginning of a continuous thrusting history during the Paleocene and Eocene. During this phase, the Avers nappe (Piemont-Liguria affinity) is emplaced on top of the Suretta nappe and the Schams nappes are detached from their crystalline substratum (Briançon basement). In the N-Penninic Bündnerschiefer the equivalent Safien phase is held responsible for the stacking of different cover nappes (Grava and Tomül).

2. The Ferrera phase (D_2) represents the major stage of nappe imbrications affecting crystalline basement and, furthermore, the main phase of ductile penetrative deformation. The transport direction is inferred to be to the NNW. Elongated quartz minerals define an ENE–WSW stretching lineation.
3. The Niemet-Beverin phase (D_3) is associated with large scale back-folding and back-shearing of the nappe stack around an ENE-WSW striking fold axis. During the final stages of the Niemet–Beverin phase, vertical shortening of the entire nappe pile was accompanied by localized E-W extension.
4. The Domleschg phase (D_4) is mainly associated with a crenulations cleavage in the N-Penninic units and asymmetric NNW-verging folds at various scales in the Schams nappes. Both structures are related to SSE-NNW directed shortening of the nappe pile.
5. The Forcola phase (D_5) encompasses E-W extension along distinct normal faults, accompanied by the uplift of the Lepontine dome.

Briefly, the second deformation phase induced the most penetrative ductile structures and is responsible of the main regional schistosity which is parallel to the contact between the Suretta and Tambò nappes. Major ductile detachment zones cross-cut the tectonic contact between the nappes. Subsequent deformation structures are related to the late and Post-alpine deformation and are due to the vertical extrusion of crustal block at north of the Insubric lineament and to the brittle–ductile E–W extension parallel to the Forcola line. The two late deformation phases overprinted and steepened the previous structures, and produced an extensive fracturing pattern, dominated by two sets orientated NW-SE and NE-SW, mainly expressed by normal faults which cross-cut all previous structures.

In San Giacomo Valley main structural alignments show the following directions: WNW-ESE, NW-SE, NE-SW and N-S. The first system seems to be related to the regional orientation of the Insubric Line, whilst the second one has the features of the Forcola Line. The NE-SW system is related to the Engadine Line and is characterized by shear component of movements, which are frequently underlined by movement streaks (Mazzoccola, 1994). The last system, parallel to the valley, is not directly connected to any tectonic line of regional significance, but it is represented by a bundle of persistent fractures, including both fractures formed in the post-glacial age, and shear joints, probably attributable to pre-existing tectonic lines, along which the pre-glacial valley developed (Mazzoccola, 1993). In the study area, beyond the main mentioned systems, many others local discontinuities sometimes occur, which have been described during geomechanical surveys.

The San Giacomo Valley, furrowed by the Liro Stream, follows an almost N–S striking tectonic lineament, which is accompanied by minor parallel sub-vertical structural elements responsible for a series of geomorphologic terraces on both sides of the valley. Deep seated flank deformations, structurally controlled, are present especially on the upper portion of the valley, while rockfalls sometimes occur mainly on the left hydrographical side of San Giacomo Valley, characterized by high rock walls.

2.2 Geomechanical surveys

In San Giacomo Valley, geomechanical surveys have been carried out, during several field campaigns, in 97 different sites, mainly located on the left side of the Liro Stream; 78 sampling points involve the Tambò basement, 7 the Spluga Syncline, and 12 the Suretta basement (**Figure 10**). The measurement points are very scattered, because they are strongly affected by the position and accessibility of outcrops.

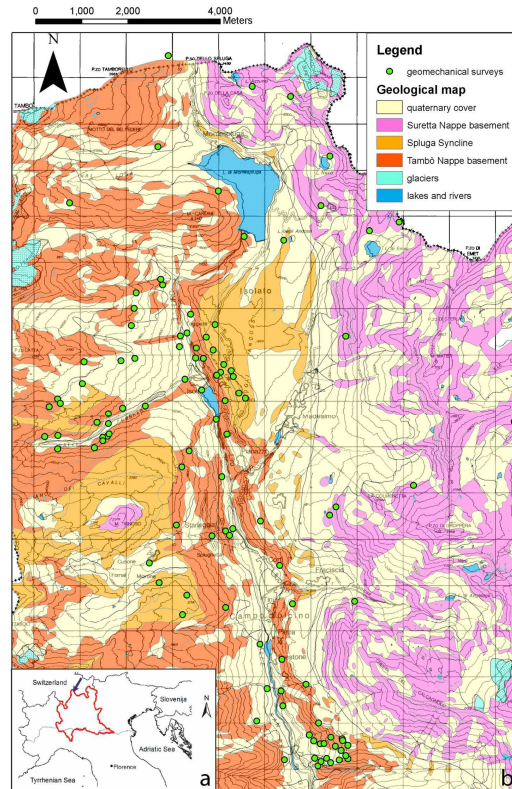


Figure 10 - Research area and sampling points: location of the research area (a) and geological sketch map of study area, circles show the position of geomechanical surveys (b)

Detailed geomechanical field surveys have been performed according to the International Society of Rock Mechanics – ISRM – suggested methods (ISRM, 1978), allowing the characterization of each investigated rock mass, its intact rock and discontinuities, in terms of: number of main joint sets, their representative orientation, vertical and horizontal intercepts, average set spacing, persistence, aperture, degree of weathering, moisture conditions, roughness and joint wall compression strength coefficients, presence and nature of infill.

Using the geomechanical data, all the measurements collected during the surveys, a database has been created. Although the in situ survey have been performed by several people: Claudio Pasqua (CP), Fabio Belloni (FB), Fabio and Marco (FM), Matteo Garzonio (MG), and Calloni & Gritti (CG), Marcello Rossi (RM), Daria Mazzola (DM) and myself (FF), a standard procedure has been followed in the data collection.

Moreover, all the data have been checked and rearranged, in order to have a standardized database, coming from homogenous and uniform measurements.

The database has been organized in a worksheet, containing the list of measurements (**Appendix 2**). For each geomechanical survey the following properties have been reported:

- a code: in order to uniquely identify the surveys, at each of them has been assigned an alphanumeric code consisting of two letters, corresponding to the initials of the name and surname of the sampler, followed by a sequential number;
- date: the day of the survey has been reported;
- geographical coordinates: each survey site has been also geo-referenced, in term of longitude and latitude, using the Gauss-Boaga coordinate system (GB), referred to the ellipsoid Monte Mario 1. This step is crucial and very important in geostatistics, because the spatial analysis can be achieved only if the measurement points are correctly located in space;
- elevation: height above the sea level of the survey location;
- structural unit: the formational unit (basement of Tambò nappe, Spluga Sincline, or basement of Suretta nappe) of each geomechanical survey has been reported;
- lithology: for each outcrop the lithology has been described, in the worksheet the lithological name has been reported using some abbreviations (listed in the **Appendix 2**);
- number of set and name: the number of discontinuity sets of each outcrop has been determined with reference to the measured average orientation (**Figure 11**). In order to uniquely define the orientation of the discontinuity, assumed to be planar. The orientation is the attitude of discontinuity in space (ISRM, 1975). It can be described by the dip direction (i.e. the azimuth, the compass bearing of the steepest line in the plane) and the dip angle (the angle that this steepest line makes to the horizontal plane).

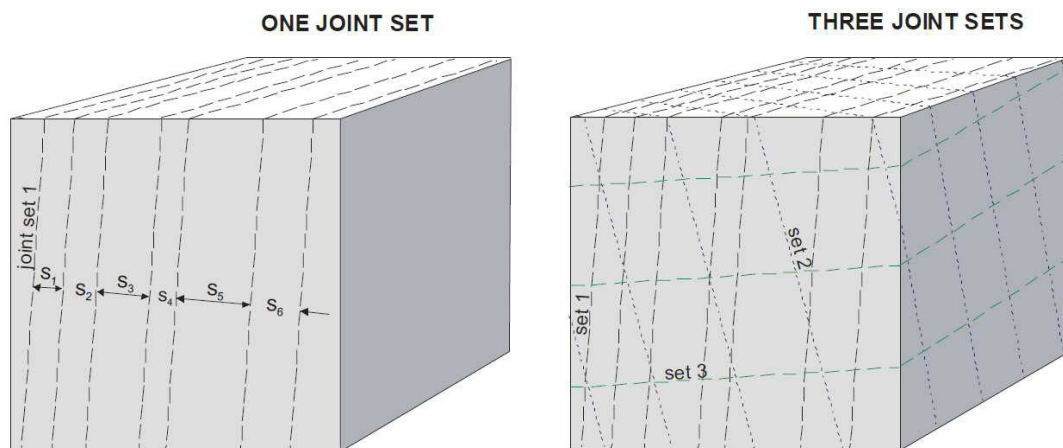


Figure 11 - Joint sets subdivided according to their orientations, S_n indicates spacing values (from Palmström A., 2005)

All the possible orientations, in term of dip direction and dip angle, have been divided in sets, using the stereographical plot, according to a merely geometric criterion, in order to allow the comparison among rock masses. At each discontinuity set a name has been assigned, according to the orientation, except the fractures developed parallel to the layering or foliation, which have been called K1 (i.e. S1), irrespective of their orientation: their average dip direction can range from 0° to 360°, and their dip angle from 0° to 90°. For all the other sets, a name has been assigned according to their mean orientation (). In the entire stereogram 16 sets have been identified, dividing the equal-area stereographic projection into 8 radial wedges of 45° amplitude (dip direction fields), each of them has been divided into three concentric bands (dip angle fields: 0°-36°, 37°-72°, 73°-90°). The intersection among the fields identifies 24 zones. Since the fields having dip angle between 0° and 36° correspond to sub-horizontal discontinuities, they have been grouped, obtaining ranges of variation in dip direction of 90°. As well, the sub-vertical discontinuities (with dip angle between 73°-90°) having opposite dip direction have been considered to belong to the same family. This has led to the determination of the 17 discontinuity sets described in **Table 1**.

| DISCONTINUITY SET | | | | |
|--------------------------|--------------|----------------------|---------------------|---------------------|
| Dip direction | | Dip angle [°] | | |
| | [°] | 0<<36 | 37<<72 | 73<<90 |
| N | 337.5<<22.5 | K14 | K6 | K2 |
| NE | 22.5<<67.5 | | K7 | K3 |
| E | 67.5<<112.5 | K15 | K8 | K4 |
| SE | 112.5<<157.5 | | K9 | K5 |
| S | 157.5<<202.5 | K16 | K10 | K2 |
| SW | 202.5<<247.5 | | K11 | K3 |
| W | 247.5<<292.5 | K17 | K12 | K4 |
| NW | 292.5<<337.5 | | K13 | K5 |

Table 1 – Names attributed to the discontinuity sets, according to their orientation

- dip direction [°]: the mean dip direction of each discontinuity set, measured through the compass, has been reported. At least one hundred measurements have been performed for each geomechanical survey;
- dip angle [°]: the mean dip angle of each discontinuity set, measured through the compass with clinometer, has been reported. At least one hundred measurements have been performed for each geomechanical survey;
- intercept [cm]: it is the mean distance between all fractures in a rock mass, independently from their orientation, measured along a scanline 2 meters long. The horizontal intercept is the average of the intercept values measured along a horizontal scanline, the vertical intercept is the average of

the values measured along the vertical scanline, and the general intercept has been calculated as the average of all the intercept values measured during the survey;

- spacing [cm]: is the perpendicular distance between two adjacent joints, within the same joint set. At least ten measures have been carried out for each set and the resulting average spacing for each joint set has been reported;
- mean spacing [cm]: the average of all set spacing has been reported;
- persistence [%]: is the discontinuity trace length as observed in an exposure. The persistence may give a crude measure of the areal extent or penetration length of a discontinuity inside the rock mass. It can be therefore defined as the ratio between the area of the discontinuity and the total area of the plane, in which that discontinuity is contained. Persistence is related to the size of discontinuities, which in turn is related to the trace length on exposures. The lateral persistence refers to the lateral extent of a discontinuity plane, while the areal persistence to the overall dimensions of the plane. In practice, the persistence has been often estimated by the one-dimensional extent of the trace lengths as exposed on rock surfaces. Termination in solid rock or against other discontinuities reduces the persistence. During the geomechanical surveys, the persistence has been estimated using three classes (**Table 2**);

| <i>PERSISTENCE</i> | <i>Lateral</i> | <i>areal</i> |
|--------------------|----------------|--------------|
| high | >90% | >80% |
| medium | 50-90% | 20-80% |
| low | <50% | <20% |

Table 2 – Classes of persistence

- aperture [mm]: is the perpendicular distance between the adjacent rock surfaces of a discontinuity, in which the intervening space is air or water filled. It is a constant value only for parallel and planar adjacent surfaces, a linearly varying value for non-parallel and planar adjacent surfaces, and completely variable for rough adjacent surfaces. This parameter has mechanical and hydraulic importance, and a distribution of apertures for any given discontinuity and for different discontinuities within the same rock mass is to be expected. Where possible, the aperture has been measured with fessurimetre, executing at least ten measures for each set. If the measurements cannot be performed the aperture has been estimated, according to the aperture classes reported in the suggested methods for the quantitative description of discontinuities in rock masses (ISRM, 1978);
- infilling: is the material that separates the adjacent rock walls of a discontinuity. During the geomechanical surveys, the presence or absence of infillings within the discontinuities has been noted, and the kind of infilling specified;
- Joint Roughness Coefficient (JRC): it describes the roughness of joint surfaces, at centimetric and millimetric scale. Although discontinuities are assumed to be planar for the purposes of orientation

and persistence analysis, the surface of the discontinuity itself may be rough. Discontinuity roughness may be defined either by reference to standard charts or mathematically. From the practical point of view, only one technique has any degree of universality and that is the Joint Roughness Coefficient (JRC) developed by Barton and Choubey (1977). This method involved comparing a profile of a discontinuity surface with standard roughness profiles and hence assigning a numerical value to the roughness. The JRC values vary from 0 (for a very smooth discontinuity) to 20 (for a discontinuity with very high roughness). It can be measured using the profilometre (also called Barton comb), and comparing the resulting profile with the chart of Barton & Choubey, 1977 (Figure 12). Ten profiles, parallel to the dip direction, have been taken for each discontinuity set.

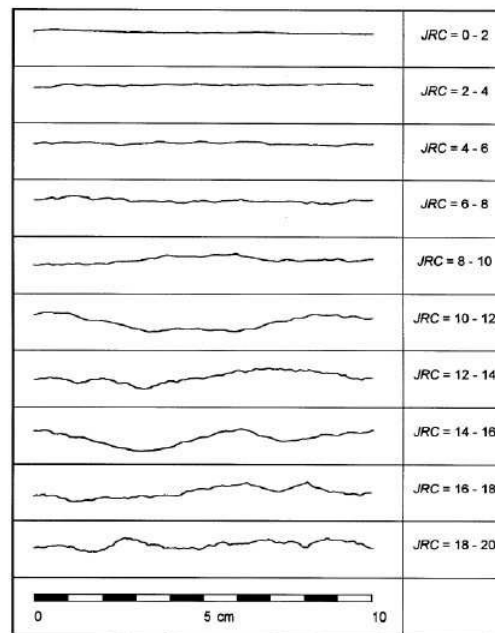


Figure 12 - Roughness profiles and corresponding JRC values (from Barton & Choubey, 1977)

Since the Barton comb, and so the normal JRC, is referred to 10 centimetres of length, the JRC at big scale (i.e. referred to 1m) has been computed, using the following formula (Bandis et al., 1981):

$$JRC_n = JRC_0 \left(\frac{L_n}{L_0} \right)^{-0.02 JRC_0} \quad (39)$$

where: JRC_n is the JRC at big scale, JRC_0 is the JRC at the classical scale of 10 centimetres, L_n is the considered length (in this case equal to 1 metre), and L_0 the length of the sample (equal to the Barton comb: 10cm);

- waviness (or undulation): it describes the roughness of joint surfaces, at decimetric and metric scale; it is limited to descriptive terms which are based on two scales of observation: small scale (several centimetres) and intermediate scale (several metres). The intermediate scale of waviness is divided into three degrees: stepped, undulating and planar, and the small scale of roughness superimposed on the intermediate scale is also divided into three degrees: rough (or irregular), smooth,

slickenside. The waviness has been estimated by visual comparison, according to the nine classes reported in the suggested methods for the quantitative description of discontinuities in rock masses (ISRM, 1975), and reported in **Figure 13**;

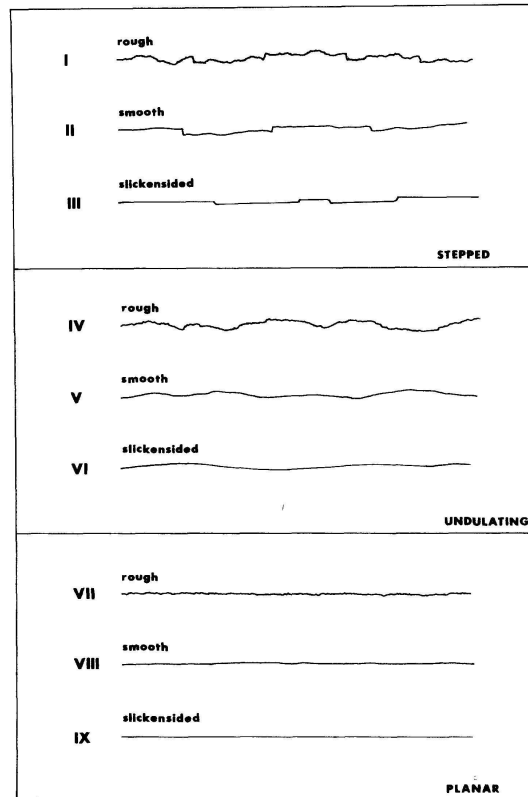


Figure 13 - Waviness profiles and nomenclature. The length of each profile is in the range 1-10 metres (from ISRM, 1978)

- Joint Compressive wall Strength (JCS): is the equivalent compression strength of the adjacent rock walls of a discontinuity. It may be lower than rock block strength, due to weathering or alteration of the walls. The JCS values have been computed from measurements carried out on not abraded (i.e. natural) and abraded discontinuities, using the Schmidt hammer. The rebound valued has been corrected on the basis of the orientation of the hammer. The calculation of JCS had been performed applying the Deere & Miller (1966) formula:

$$JCS = 10^{0.00088\gamma R + 1.01} \quad (40)$$

where: γ is the weight unit of rock material (expressed in kN/m^3), and R the representative rebound, i.e. the mean of five higher measured values on a set of ten measures for each tested discontinuity. The resulting JCS is significant only if the JRC of the tested discontinuity is smaller than 9.

The computed JCS, is referred to the surface of measure (i.e. 10cm for side), therefore the JCS at big scale (i.e. referred to 1 metre) has been computed, using the formula (Bandis et al., 1981):

$$JCS_n = JCS_0 \left(\frac{L_n}{L_0} \right)^{-0.03JRC_0} \quad (41)$$

where: JCS_n is the JCS at big scale, JRC_0 is the JCS at the classical scale (obtained from the Equation 40), L_n is the desiderated length (in this case, as for the JRC, it has been chosen equal to 1 metre), and L_0 is the length of the sample (10 centimeters for side);

- weathering degree: it has been computed as the ration between the JCS measured on the natural surface and the JCS measured on the same, but abraded surface;
- moisture conditions: water seepage through rock masses results mainly from flow through water conducting discontinuities (secondary permeability). During the surveys, the moisture conditions of specific sets exposed in an outcrop, have been assessed according to the following descriptive scheme (ISRM, 1978):

U - Unfilled discontinuities:

- I. the discontinuity is very tight and dry, water flow along it does not appear possible;
- II. the discontinuity is dry with no evidence of water flow;
- III. the discontinuity is dry but shows evidence of water flow (i.e. rust staining, etc.);
- IV. the discontinuity is damp but no free water is present;
- V. the discontinuity shows seepage, occasional drops of water, but no continuous flow;
- VI. the discontinuity show a continuous flow of water.

F - Filled discontinuities:

- I. the filling materials are heavily consolidated and dry, significant flow appears unlikely, due to very low permeability;
 - II. the filling materials are damp but no free water is present;
 - III. the filling materials are wet, with occasional drops of water;
 - IV. the filling materials show sign of outwash, continuous flow of water (in the order of l/min);
 - V. the filling materials are washed out locally, considerable water flow along out-wash channels;
 - VI. the filling materials are washed out completely, very high water pressures experienced, especially on first exposure.
- Volumetric joint count – J_v – [n°/m^3]: is by definition an average measurement for the actual rock mass volume measured, expressing the number of joints occurring in this volume. It is defined as the number of joints intersecting a volume of one m^3 of rock mass. Actually, the J_v has been computed for each geomechanical survey, according to the following formula (Palmström, 1982):

$$J_v = \frac{100}{S_{K1}} + \frac{100}{S_{K2}} + \dots + \frac{100}{S_{Kn}} \tag{42}$$

where S_{K1} , S_{K2} and S_{Kn} are the average spacings for the joint sets (expressed in centimetres).

Since the J_v is based on joint measurements of spacings or frequencies, it can easily be calculated. Random joints are not included, because they do not belong to a particular joint set.

The J_v describes the degree of jointing of a rock mass, which can be: very low ($J_v < 1$), low ($1 < J_v < 3$), moderate ($3 < J_v < 10$), high ($10 < J_v < 30$), very high ($30 < J_v < 60$) or crushed ($J_v > 60$).

- Geological Strength Index –GSI– (Hoek & Brown, 1997): is a quality index of the rock mass, which has been evaluated for each geomechanical survey. The GSI provides a number which, when combined with the intact rock properties, can be used for estimating the reduction in rock mass strength for different geological conditions. This number has been attributed according to **Table 3**.

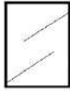





| GEOLOGICAL STRENGTH INDEX FOR JOINTED ROCKS (Hoek and Marinos, 2000) From the lithology, structure and surface conditions of the discontinuities, estimate the average value of GSI. Do not try to be too precise. Quoting a range from 33 to 37 is more realistic than stating that GSI = 35. Note that the table does not apply to structurally controlled failures. Where weak planar structural planes are present in an unfavourable orientation with respect to the excavation face, these will dominate the rock mass behaviour. The shear strength of surfaces in rocks that are prone to deterioration as a result of changes in moisture content will be reduced if water is present. When working with rocks in the fair to very poor categories, a shift to the right may be made for wet conditions. Water pressure is dealt with by effective stress analysis. | | SURFACE CONDITIONS | | | | |
|---|--|--|-----|----|-----|-----|
| STRUCTURE | | DECREASING SURFACE QUALITY → | | | | |
|  | INTACT OR MASSIVE - intact rock specimens or massive in situ rock with few widely spaced discontinuities | 90 | | | N/A | N/A |
|  | BLOCKY - well interlocked undisturbed rock mass consisting of cubical blocks formed by three intersecting discontinuity sets | 80 | 70 | | | |
|  | VERY BLOCKY- interlocked, partially disturbed mass with multi-faceted angular blocks formed by 4 or more joint sets | | 60 | 50 | | |
|  | BLOCKY/DISTURBED/SEAMY - folded with angular blocks formed by many intersecting discontinuity sets. Persistence of bedding planes or schistosity | | | 40 | 30 | |
|  | DISINTEGRATED - poorly interlocked, heavily broken rock mass with mixture of angular and rounded rock pieces | | | | 20 | |
|  | LAMINATED/SHEARED - Lack of blockiness due to close spacing of weak schistosity or shear planes | N/A | N/A | | | 10 |
| | | ← DECREASING INTERLOCKING OF ROCK PIECES ↓ | | | | |
| | | ← SURFACE QUALITY ↓ | | | | |

Table 3 - Characterization of blocky rock masses on the basis of interlocking and joint conditions (Hoek & Brown, 1997)

- Rock Mass Rating –RMR– (Bieniawski, 1989): it is a quality index of the rock mass, which has been computed using the collected data. The Rock Mass Rating (RMR) index accounts for a number of factors influencing the strength of a rock mass, and may be used to quantify the competence of an outcrop or geologic unit. RMR scores range from 0 to 100, with 100 being the most competent rock mass. The final RMR is the sum of the five inputs listed in **Table 4** (Part A), with a rating adjustment for discontinuity orientation (Part B).

| A. CLASSIFICATION PARAMETERS AND THEIR RATINGS | | | | | | | |
|---|--------------------------------------|---|---|--|--|--|--|
| Parameter | | Range of values | | | | | |
| 1 | Strength of intact rock material | Point-load strength index | >10 MPa | 4 - 10 MPa | 2 - 4 MPa | 1 - 2 MPa | For this low range - uniaxial compressive test is preferred |
| | | Uniaxial comp. strength | >250 MPa | 100 - 250 MPa | 50 - 100 MPa | 25 - 50 MPa | |
| | Rating | | 15 | 12 | 7 | 4 | 2 1 0 |
| 2 | Drill core Quality RQD | | 90% - 100% | 75% - 90% | 50% - 75% | 25% - 50% | < 25% |
| | Rating | | 20 | 17 | 13 | 8 | 3 |
| 3 | Spacing of discontinuities | | > 2 m | 0.6 - 2 m | 200 - 600 mm | 60 - 200 mm | < 60 mm |
| | Rating | | 20 | 15 | 10 | 8 | 5 |
| 4 | Condition of discontinuities (See E) | | Very rough surfaces Not continuous No separation Unweathered wall rock | Slightly rough surfaces Separation < 1 mm Slightly weathered walls | Slightly rough surfaces Separation < 1 mm Highly weathered walls | Slickensided surfaces or Gouge < 5 mm thick or Separation 1-5 mm Continuous | Soft gouge >5 mm thick or Separation > 5 mm Continuous |
| | Rating | | 30 | 25 | 20 | 10 | 0 |
| 5 | Groundwater | Inflow per 10 m tunnel length (l/m) | None | < 10 | 10 - 25 | 25 - 125 | > 125 |
| | | (Joint water press/ (Major principal σ) | 0 | < 0.1 | 0.1 - 0.2 | 0.2 - 0.5 | > 0.5 |
| | General conditions | Completely dry | Damp | Wet | Dripping | Flowing | |
| | Rating | | 15 | 10 | 7 | 4 | 0 |
| B. RATING ADJUSTMENT FOR DISCONTINUITY ORIENTATIONS (See F) | | | | | | | |
| Strike and dip orientations | | | Very favourable | Favourable | Fair | Unfavourable | Very Unfavourable |
| Ratings | Tunnels & mines | | 0 | -2 | -5 | -10 | -12 |
| | Foundations | | 0 | -2 | -7 | -15 | -25 |
| | Slopes | | 0 | -5 | -25 | -50 | |
| C. ROCK MASS CLASSES DETERMINED FROM TOTAL RATINGS | | | | | | | |
| Rating | | 100 ← 81 | 80 ← 61 | 60 ← 41 | 40 ← 21 | < 21 | |
| Class number | | I | II | III | IV | V | |
| Description | | Very good rock | Good rock | Fair rock | Poor rock | Very poor rock | |
| D. MEANING OF ROCK CLASSES | | | | | | | |
| Class number | | I | II | III | IV | V | |
| Average stand-up time | | 20 yrs for 15 m span | 1 year for 10 m span | 1 week for 5 m span | 10 hrs for 2.5 m span | 30 min for 1 m span | |
| Cohesion of rock mass (kPa) | | > 400 | 300 - 400 | 200 - 300 | 100 - 200 | < 100 | |
| Friction angle of rock mass (deg) | | > 45 | 35 - 45 | 25 - 35 | 15 - 25 | < 15 | |
| E. GUIDELINES FOR CLASSIFICATION OF DISCONTINUITY conditions | | | | | | | |
| Discontinuity length (persistence) | | < 1 m | 1 - 3 m | 3 - 10 m | 10 - 20 m | > 20 m | |
| Rating | | 6 | 4 | 2 | 1 | 0 | |
| Separation (aperture) | | None | < 0.1 mm | 0.1 - 1.0 mm | 1 - 5 mm | > 5 mm | |
| Rating | | 6 | 5 | 4 | 1 | 0 | |
| Roughness | | Very rough | Rough | Slightly rough | Smooth | Slickensided | |
| Rating | | 6 | 5 | 3 | 1 | 0 | |
| Infilling (gouge) | | None | Hard filling < 5 mm | Hard filling > 5 mm | Soft filling < 5 mm | Soft filling > 5 mm | |
| Rating | | 6 | 4 | 2 | 2 | 0 | |
| Weathering | | Unweathered | Slightly weathered | Moderately weathered | Highly weathered | Decomposed | |
| Rating | | 6 | 5 | 3 | 1 | 0 | |
| F. EFFECT OF DISCONTINUITY STRIKE AND DIP ORIENTATION IN TUNNELLING** | | | | | | | |
| Strike perpendicular to tunnel axis | | | Strike parallel to tunnel axis | | | | |
| Drive with dip - Dip 45 - 90° | Drive with dip - Dip 20 - 45° | | Dip 45 - 90° | | Dip 20 - 45° | | |
| Very favourable | Favourable | | Very unfavourable | | Fair | | |
| Drive against dip - Dip 45-90° | Drive against dip - Dip 20-45° | | Dip 0-20 - Irrespective of strike° | | | | |
| Fair | Unfavourable | | Fair | | | | |

* Some conditions are mutually exclusive. For example, if infilling is present, the roughness of the surface will be overshadowed by the influence of the gouge. In such cases use A.4 directly.

** Modified after Wickham et al (1972).

Table 4 - Rock Mass Rating scheme and guidelines (from Bieniawski, 1989)

An example of final sheet of geomechanical survey has been reported in **Appendix 3**.

From the collected data, some general considerations can be outlined, with the aim to describe analogies and differences in the investigated rock masses, especially about their quality, being the parameter that best summarize the features of the investigated rock masses. The examined rock masses belonging to the Tambò and Suretta basement units, show a similar behaviour. Joint orientations and properties are quite similar, and the small variability in lithological characteristics does not significantly control the discrepancy in rock mass quality (Apuani et al., 2009). The rock masses of the meta-sedimentary cover, the Spluga Syncline, show a general greater state of deformation. However, for all the lithological and structural units, some common properties have been observed: the water is mostly absent, the discontinuities are slightly weathered, without infillings and with a medium persistency. The other parameters, i.e. JCS, JRC, aperture, spacing, J_v and consequently RQD, show a great variability, which seems not to be directly related to the lithology. Indeed, in spite of the lithological variability should obviously be responsible for variations in rock mass quality, it is worth to note that all RMR values are included in only two classes, irrespectively of the lithology: they range from 45 to 77, half of them belong to the “fair quality” class ($41 < \text{RMR} < 60$), while the other half belong to the “good quality” class ($61 < \text{RMR} < 80$); mostly of RMR values are included between 50 and 70.

It can be stated that in the study area the geomechanical quality of rock masses (expressed by the RMR) mainly depends on the geometrical features which show the greater variability, i.e. spacing and the correlated values of J_v and RQD (Priest & Hudson, 1976), JCS and conditions of discontinuities (with particular reference to aperture and roughness). These properties, which are related to tectonic actions, could be considered as regionalized variables, as the RMR. Actually, the fracturing degree of a rock mass, and consequently its RMR, depends on the geological and structural history of the rock mass, but it is worth to note that they describe the features and quality of the rock mass nowadays, resulting from all the involved geological events. The fracturing degree, as well as the RMR, can be seen as global property of the rock masses, depending on all its fractures, despite of their formation mechanism.

2.3 Geostatistical analyses

Geostatistical analyses have been performed in order to estimate rock mass mechanical properties far from sampling locations.

Since the fracturing degree of a rock mass is resulted to be the parameter that more influences the rock mass quality and therefore the mechanical and hydro-geological rock mass behaviour, the geostatistical analyses focus on these three parameters:

- the horizontal intercept, which is the mean distance among all fractures in a rock mass, independently from their orientation, measured along an horizontal scanline;

- the Rock Mass Rating, which is a quality index of the rock mass, computed as the sum of the following parameters: the uniaxial compressive strength of rock matrix, the Rock Quality Designation –RQD–, the spacing of discontinuities, their conditions, and ground water conditions;
- the Volumetric Joint Count (J_v), which has been derived from the average spacing of each discontinuity set.

The statistical population is represented from all the investigated rock masses outcropping in San Giacomo Valley and the homogeneity of the data samples has been guaranteed, because the same support (a scanline 20 metres long) has been used in all the geomechanical surveys, with a surveyed height of about 2 metres.

The geostatistical analyses have been performed using as regionalized variables the horizontal intercept, the J_v and the RMR, and have been developed following these phases:

1. exploratory spatial data analyses;
2. semivariogram analysis;
3. estimation;
4. validation.

2.3.1 Horizontal intercept

The horizontal intercept is the mean distance among all fractures in a rock mass, measured along a horizontal scanline two metres long, independently from the orientation of the fractures.

First of all, the Exploratory Spatial Data Analyses –ESDA–, has been carried out with the aim to evaluate the frequency distribution of the collected data; actually a lot of geostatistical techniques can be applied only if the Regionalized Variable –RV– has a Gaussian distribution. The first step in the ESDA consists of the computation of the main statistical parameters (**Table 5**), which include central tendency, dispersion and shape parameters.

| <i>Statistical parameter</i> | <i>Intercept [cm]</i> | <i>J_v [n°/m^3]</i> | <i>RMR</i> |
|------------------------------|-----------------------|--|------------|
| Number of observations | 61 | 97 | 55 |
| Minimum | 5.2 | 6.67 | 45 |
| Maximum | 41.2 | 66.58 | 77 |
| Mean | 19.16 | 25.273 | 59.7 |
| Median | 16.90 | 21.429 | 59 |
| Skewness | 0.70 | 0.646 | 0.3 |
| Kurtosis | -0.40 | -0.443 | 0.3 |

Table 5 - Main statistical parameters of horizontal intercept, J_v and RMR

The horizontal intercepts has been measured only in 61 locations. Sampling values range from 5.2 to 41.2 centimetres, the resulting mean value is equal to 19.16 cm for intercept, with a standard deviation of 10.02. The median is equal to 16.9 cm.

The frequency distribution is clearly unimodal (**Figure 14**), and since the mean is greater than the median value, there is a positive (also called right) non-parametric skew: the polygon distribution is characterized by a long right tail; actually the skewness of 0.70 indicates the tendency to concentrate the values towards the right extreme: the tail on the right side is longer than the left side.

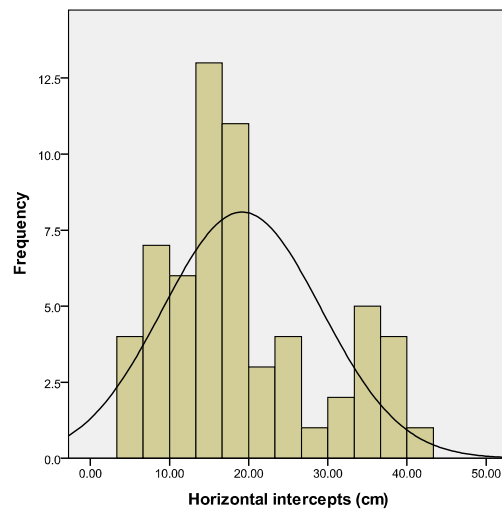


Figure 14 - Frequency distribution of horizontal intercept, the continuous line represents the best-fitted normal distribution function

Since many geostatistical techniques are more reliable if the variable of interest have a Gaussian distribution, it is necessary to verify if the variable has a normal distribution and if it is not the transformation of data in to a Gaussian one is essential.

The occurrence of Gaussian distribution can be verified through some graphical and statistical tests, but the main problem is that the most common statistical tests are designed on the assumption that the observations are independent and identically distributed. In geostatistical applications on rock mechanics, however, this is not usually the case, because data locations, being constrained by the positions of outcrops and their accessibility, are often clustered rather than being located on a regular grid. However, random selection of sampling locations may produce spatial clusters of data but will not introduce any significant bias (Pardo-Igúzquiza & Dowd, 2004). When preferential sampling occurs, observations that are close together (clustered) provide partially redundant information that must be taken into account. The solution to preferential sampling is preparation of a compensated sample to eliminate the clustering, only then the classic normality tests can be applied. In this case study, the analysis of the spatial disposition of the 61 sampling locations of horizontal intercept, have been performed through the nearest neighbour index, which uses the distance between each point and its closest neighbouring point to determine if the point pattern is random, regular or

clustered. The nearest neighbour index is expressed by the average distance between each point and its nearest neighbours, divided by the expected distance (i.e. the average distance between neighbours in a hypothetical random distribution). If the index is smaller than 1, the pattern exhibits clustering; if the index is bigger than 1, the trend is toward dispersion or competition. In this study case it tends to 1, with a small standard deviation, showing that the pattern of the sampling locations is neither clustered nor dispersed. Therefore the data de-clustering is not necessary and the frequency distribution has been verified using directly the data.

Intercept values approximate a log-normal distribution, so the values have been transformed using their natural logarithm, and the normality of transformed data has been verified using various graphical and statistical tests, such as Shapiro-Wilk test and Kolmogorov-Smirnov test with Lilliefors correction.

The Shapiro-Wilk test (Shapiro and Wilk, 1965) is considered one of the most powerful tests for checking the normality of distribution, especially for small samples (i.e. with less than 100 data values), so is suitable to investigate the Valchiavenna case study. It is based on the assumption that, if the dataset has a normal distribution, the sorted values are highly correlated with the corresponding quantiles taken from the normal distribution. Using the raw horizontal intercept values the assumption of normality is rejected, because the obtained W-value is lower than that provided by the critical table. Considering the logarithm of horizontal intercept it is possible to accept the null hypothesis (i.e. the normality of the distribution of the observed values), because the W-value is greater than the critical value and the observed significance level is greater than the effective one (equal to 5%).

The Kolmogorov-Smirnov test is a non-parametric test, which is particularly effective when at least 40 values of the sample under study are known. This test compares the observed cumulative distribution function for a variable with a specified theoretical distribution. The maximum absolute difference (between the observed cdf and the theoretical one) is called KS parameter, lower it is, greater the proximity between the experimental and the theoretical distribution is. Here the Kolmogorov-Smirnov test with correction Lilliefors (Lilliefors, 1967) has been used, because it is particularly reliable with small samples (as in this case study). With the horizontal intercept data, the null hypothesis is rejected, because the value of the KS parameter is higher than the critical one provided by the appropriate table, then the observed distribution deviates significantly from the theoretical Gaussian distribution. Instead, with the natural logarithms of horizontal intercept the null hypothesis is accepted, in fact the observed significance is greater than the actual one, and the maximum absolute deviation from the theoretical curve is below the critical value for obtaining a Gaussian distribution.

The Gaussian distribution of the log-transformed horizontal intercept has been verified. Since the standard Gaussian distribution, with mean and variance equal respectively to 0 and 1, is required, the Gaussian anamorphosis process has been performed, with the aim to transform the Gaussian distribution of transformed horizontal intercept into a standard Gaussian distribution (**Figure 15**).

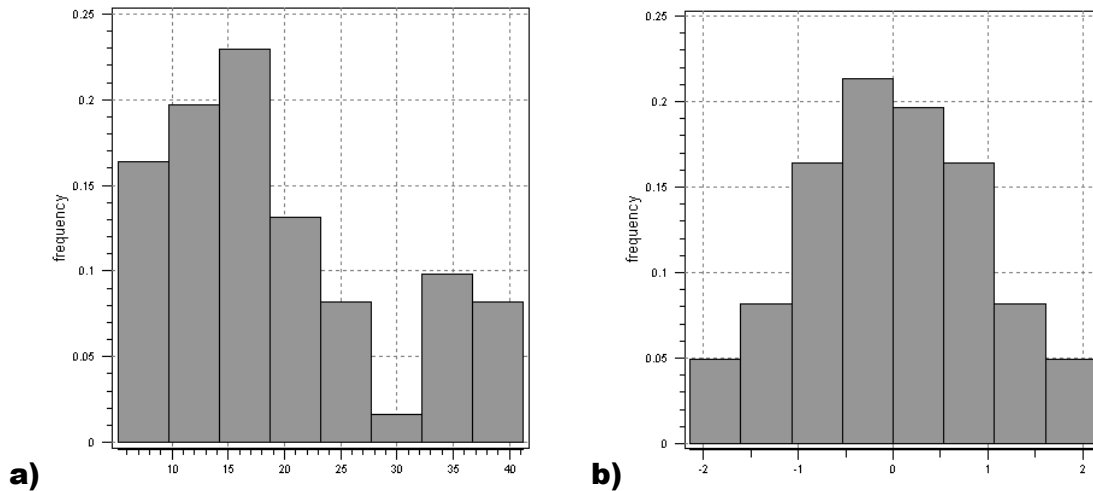


Figure 15 - Frequency distribution histograms of: raw horizontal intercept data (a), and transformed horizontal intercept data, after the Gaussian anamorphosis process (b)

Since many of the models used in geostatistics are based on the assumption of spatial stationarity, the validity of stationarity property (i.e. the absence of regular trends in space) needs to be verified. The occurrence of this property can be checked either analysing the variogram or observing the arrangement of the measured values in space. Actually if the variogram does not reach a sill any trend in the data set occurs. The absence of trend can be also verified representing the intensity of the variable (i.e. the horizontal intercept) in respect of the spatial coordinates, in terms of latitude and longitude (Figure 16).

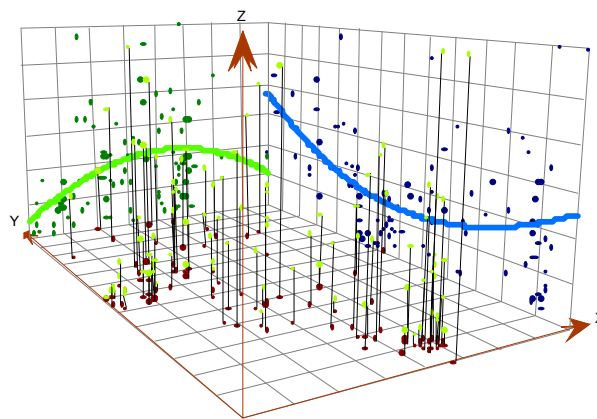


Figure 16 - Study of the presence of trend, carried out plotting the logarithm of horizontal intercept (on z-axis) in function of latitude (on y-axis) and longitude (on x-axis), and calculating the regression lines (i.e. solid lines) in x and y directions

The parameter under study does not present any systematic trend in space, because the values cannot be interpolate by a monotone ascending or descending function in the studied domain, then it is possible to accept the assumption of stationarity of the variable. The absence of trend allows applying the kriging without trend, which accounts for local fluctuations of the mean limiting the domain of stationarity of the mean to the local neighbourhood centred on the location under estimation (Groovaerts, 1997).

The semivariogram analysis consists of the construction and analysis of semivariogram, a mathematical model that is able to capture the spatial correlation among data. The computation of the variogram is based on the Mean Ergodic Hypothesis (Papoulis, 1984), with ergodic fluctuations that are due to the limited, finite extent of the spatial domain being simulated. Simulations on an infinitely large domain result in statistics of a realization that exactly match the model statistics. As consequence, it is typically advised in traditional geostatistical practice, do not to use any lag distance greater than the half of size of the field, since the variograms constructed with too long lags are not reliable (not enough samples to provide a reliable variogram), and this statement has been observed in this work.

Variography has been here applied to recognize the spatial distribution of the horizontal intercept of the examined rock masses. An interpretation of variograms able to give a complete answer to the geological phenomena occurred in the studied area is truly difficult and complex, being San Giacomo Valley localized in an alpine dynamic context, which has not a simple geological history, with the superimposition of numerous short time events with major processes acting on geological time scales. However, it is easy to understand that geological characteristics that had been formed in a slow and steady geological environment are better correlated to each other than if they had been results of an often abruptly changing geological process (Marinoni, 2003), such as in the research area.

The variograms have been constructed using transformed data, with the support of the Stanford Geostatistical Modelling Software –SGems– (Remy et al., 2008) which has been used also in the estimation phase.

First of all, an omni-directional variogram (with angular tolerance of 90°) has been constructed using the transformed horizontal intercept data, in order to individuate if a correlation of the variable in the research area exists. Then the presence of any preferential correlation direction has been firstly sought graphically using a 2D variogram map (**Figure 17**), which is a plot of experimental variogram values in a coordinate system ($h_x ; h_y$) with the centre of the map corresponding to the variogram at lag 0.0 (Goovaerts, 1997). The variogram map shows that a main preferential correlation direction towards NE occurs. Afterwards, a more detailed research of major correlation direction has been conducted through the construction of several directional variograms, with angular tolerance of 22.5° . The lag tolerance has been always assumed equal to half of the lag distance. The directional variograms exhibit a main correlation direction towards ENE, which is irrespective of the scale. This direction, mathematically founded, needs a geological response before it could be applied. It recalls the direction of the structures formed during the Niemet-Beverin phase (D_3).

Actually, a well regionalized variable should show an invariance of scale (Ferrari et al., 2011), in other words the variograms should not show important changes varying the scale: the structure and the maximum correlation direction should remain approximately the same, although the small heterogeneities, which are neglected in the variograms with large lag, could be better highlighted in the variograms created using small lag. Therefore, the correlation structures of the horizontal intercept have been investigated at different

scales, taking into account the possible occurrence of anisotropies. Once determined the main correlation direction, three experimental variograms have been constructed at different scales, varying the lag distance from 250 meters to 1000 meters, and therefore increasing the maximum distance under study.

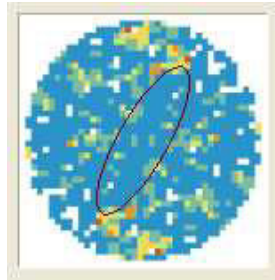


Figure 17 - 2D variogram maps of horizontal intercept transformed data

The variogram analysis has allowed assessing:

- the behaviour of variograms near to origin: all variograms not tend towards zero when h is zero. This discontinuity of the variogram at the origin, which corresponds to short scale variability, is called “nugget effect” and can be due to local heterogeneity of the geology structures, with correlation ranges shorter than the sampling resolution, or to measurements errors;
- the structure of variograms: variance values increases with the lag, indicating that the variability of horizontal intercept increases as the distance h among sampling points grows; the experimental variogram allows to identify the variogram model which best fits data; the horizontal intercept disposition go near to a nested model composed by a nugget effect model and a Gaussian one;
- the principal axes of anisotropy: the maximum correlation direction occurs where the range is major, while the minimum correlation direction was assumed perpendicular to maximum correlation direction; the maximum correlation of horizontal intercept has direction WSW-ENE;
- the sill: if the maximum sill value should be equal to the variance, and thus to one in transformed variables, is a debated topic, which has been considered by several authors (Journel & Huijbregts, 1978; Barnes, 1991; Goovaerts, 1997; Grigarten & Deutsch, 2001). One model with maximum sill equal to sample variance and a model having a sill value bigger than sample variance have been constructed, applied and validated; since the validation process shows that, in this case, the sill major than one provides the best results, in following phases models with sill bigger than sample variance has been considered. The sill decreases when lag distance increase;
- the range: the maximum correlation distance of horizontal intercept range decreases increasing the lag distance.

The variograms of horizontal intercept therefore show an invariance of scale, no significant changes occur varying the scale: the structure of the variogram is always best fitted by a nested Gaussian model, and the maximum correlation direction is always ENE-WSW (67.5° - 247.5°). The ergodic and stationarity hypothe-

ses, required for any geostatistical analysis, are respected: the experimental variograms have not a drift effect (i.e. they are not monotone ascending), but present a sill. A random function is mean-ergodic if the process has finite variance (i.e. a sill is reached within a finite distance). Experimental and theoretical variograms along the maximum correlation direction, obtained using different lag sizes, are shown in **Table 6** and a summary of the parameters used to create the variogram models has been reported in **Table 7**.

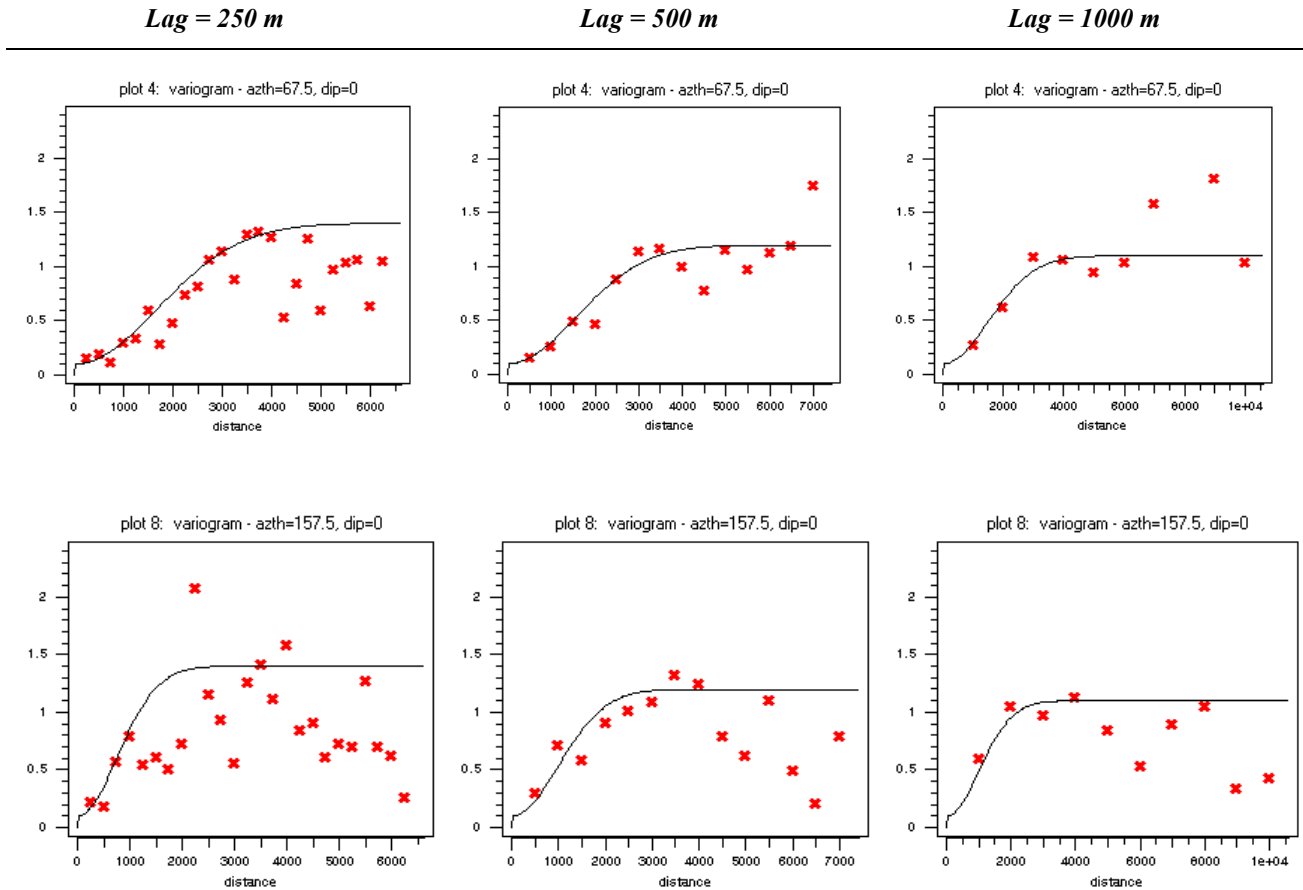


Table 6 – Experimental directional variograms (represented with red crosses) and variogram models (solid lines) of horizontal intercept transformed data, computed using different lags. The first row refers to the maximum correlation direction (ENE-WSW), the second row to the minimum correlation direction (SSE-NNW)

| Parameter | Lag = 250 m | Lag = 500 m | Lag = 1000 m |
|-------------------------------|--------------|--------------|--------------|
| Kind of model | Gaussian | Gaussian | Gaussian |
| Maximum correlation direction | 67.5°-247.5° | 67.5°-247.5° | 67.5°-247.5° |
| Nugget effect | 0.1 | 0.1 | 0.1 |
| Sill | 1.3 | 1.1 | 1 |
| Maximum range | 4125 | 3850 | 3700 |
| Minimum range | 1875 | 2450 | 2200 |
| Anisotropy ratio | 2.2 | 1.6 | 1.7 |

Table 7 - Parameters of theoretical variogram models

These variogram models have been employed for the prediction, which is the spatial interpolation of horizontal intercept values, among survey points. Initially, the ordinary kriging –OK– method has been performed, because it is the technique that provides the Best Linear Unbiased Estimator of unknown fields (Journel & Huijbregts, 1978; Kitanidis, 1997). OK is a local estimator that provides the interpolation and extrapolation of the originally sparsely sampled data in whole the domain, assuming that the values are reasonably characterized by the Intrinsic Statistical Model.

Since the variable under study shows a strong spatial anisotropy, the measurements inside a research elliptic region have been considered to perform the estimation process. The axes of the elliptic regions have been assumed parallel to the maximum and minimum correlation direction individuated by the variograms, the length of axes have been obtained doubling the ranges. A minimum of three and a maximum of twenty samples have been included in the calculation of every point, in order to take in account irregularity of data distribution and nugget effect. The grid used is defined by regular square cells, W-E and S-N oriented; with side of 100 meters. Results of OK are expressed with the map of expected values of horizontal intercept and related variance (Table 8). Since all the maps are quite comparable, in order to avoid excessive length, results with lag of 500 meters have not been reported.

The plausibility of the interpolation models has been investigated using the cross-validation procedure, which consists of sequentially estimation at each of n known locations using remaining $n-1$ sampled locations in the domain. This analysis, which compares estimates and actual known sampled values, shows that the estimation method adopted tends to overestimate low values and underestimate high ones, producing a marked smoothing effect (Figure 18); that leads to neglect the extreme values of sample distribution and therefore does not preserve the variability of the parameters under investigation.

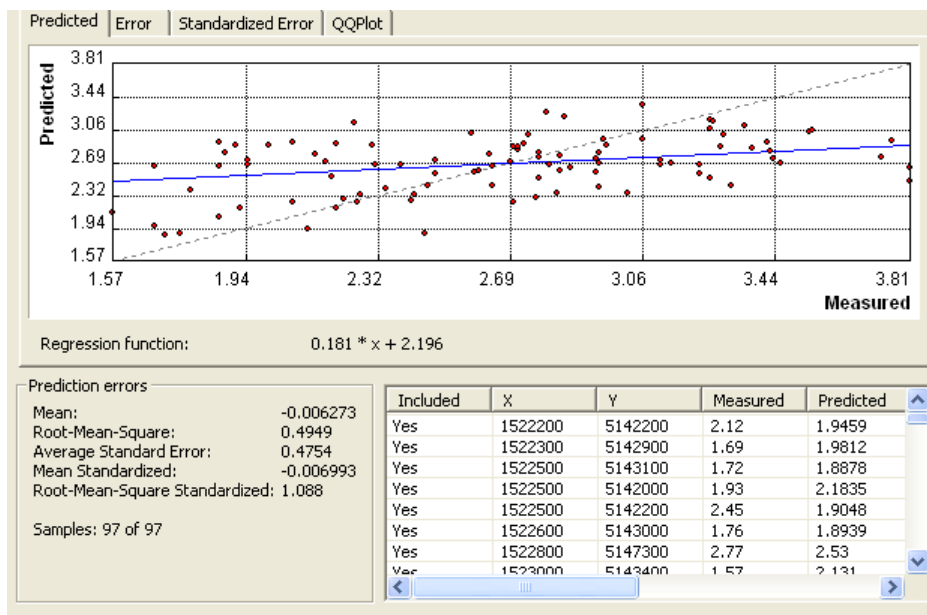


Figure 18 – Cross-validation of kriging model, which has been used to estimate the logarithm of horizontal intercept

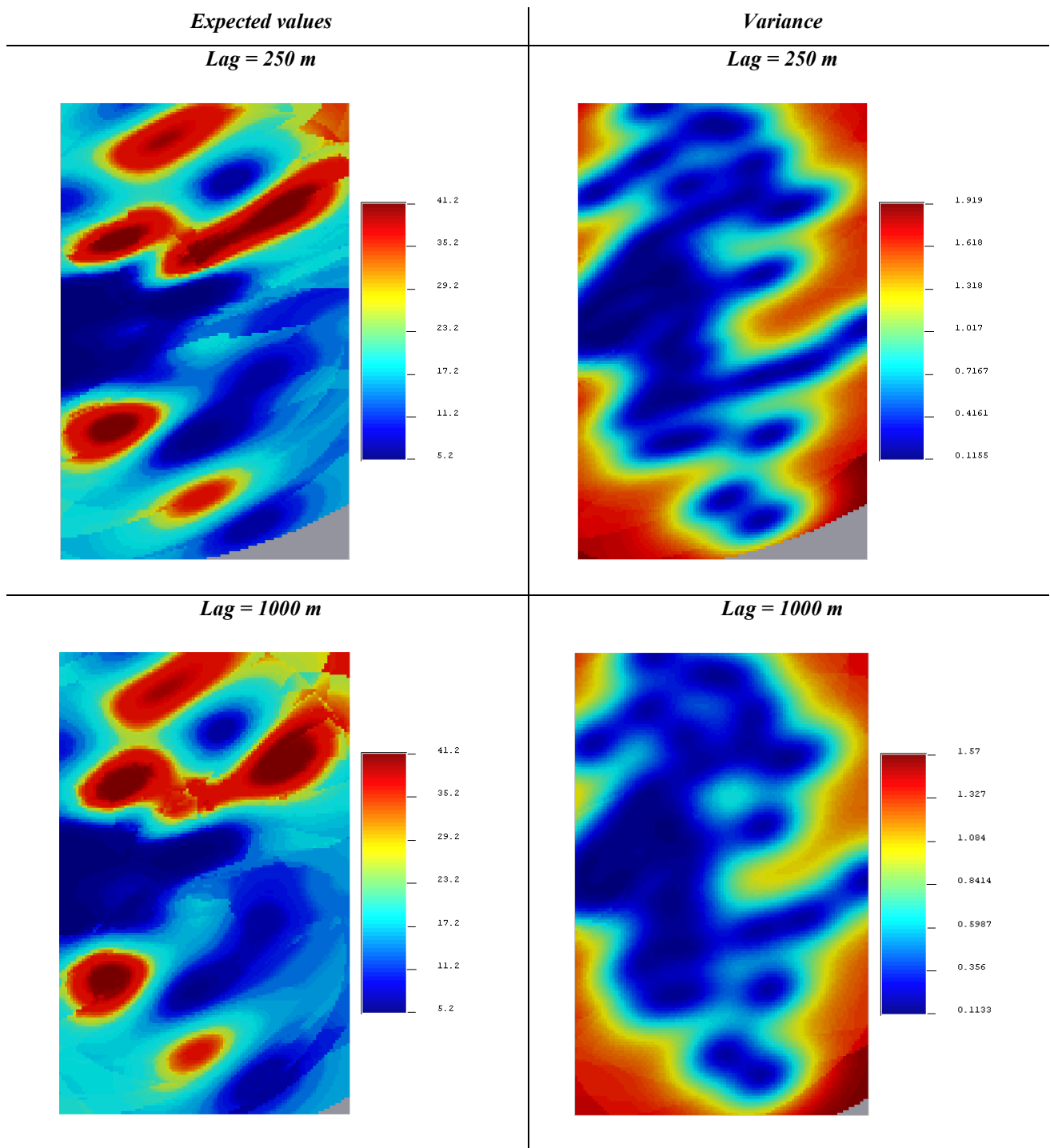


Table 8 - The expected values of horizontal intercept, estimated through Ordinary Kriging, are reported on the left side and with their associated variances on the right side. The lag distance increases from the top to the bottom of the table.

The smoothing effect, commonly found in the maps generated by this method, results in less variation in the estimated values, than in the observed values. This results in small values being overestimated, whereas large values are underestimated. The kriging estimations present only the simplistic spatial pattern and do not catch the detail. Such bias presents a serious shortcoming when the goal is to detect patterns of extreme values, such as areas with high fracturing degree in rock masses. Goovaerts (1997) emphasized that this smoothing effect is not uniform. It is dependent on the local data configuration: the smoothing effect is

minimal when the location of the observed data is nearby and increases as the distance from the location to the observed data increases. In addition, kriging is based on the spatial variations of observed data at sample locations. The kriged value at each unsampled location, therefore, includes an estimation variance (Juang et al., 2004). The model impacts of the smoothing effect are not very strong when the modelled parameter shows a low variability, but more variable the geology is, stronger the impact of smoothing effect is (Marinoni, 2003). In Alpine areas, such as San Giacomo valley, the smoothing effect is remarkable; therefore, a method, which avoids this effect, is preferable.

Geostatistical simulation techniques generate models without smoothing effect, taking into account the spatial variability of regionalized variable. This method does not provide the best linear unbiased estimate, but it creates realizations with the same variability as that observed in the field (Long & Billaux, 1987). Actually, we are not particularly interested in finding the best estimate of actual horizontal intercept in a given location, but rather, we could be interested in the spatial variability of this parameter, paying attention to the extreme values, which often represent critical points (i.e. area intensively fractured).

Among the various methods of simulation, considering the experiences presented in literature concerning the simulation of rock mass fracturing degree (Chilès, 1988; Billaux et al., 1989; Gringarten, 1996; Escuder Viruete et al., 2003; Koike & Ichikawa, 2006; Stavropoulou et al., 2007; Ellefmo & Eidsvik, 2009; Esfahani & Asghari, 2012), the sequential Gaussian simulation –SGS– has been chosen. It is a conditional technique, forced to take the measured values of the variable in the sampling points. Geostatistical simulations (or stochastic representations) can be seen as possible realizations of a spatially correlated random field, they all honour the spatial moments (mean, variogram) of the field.

SGS has been performed using the parameters of spatial continuity models previously defined through variogram analysis and the same grid and research ellipse of those used in the OK. Each simulation delivers a different realization, therefore simulations do not provide good local estimators, but they are good describer of spatial uncertainty. The various realizations might initially seem to be quite different, nevertheless, the variability and distribution of estimated values are very similar to those of the original data, and the smoothing effect, which has been observed, using OK, does not occur. Even if each simulation maintains the variability and distribution of samples, it provides a different map, hence in order to get a final map, it is necessary to calculate, in each location of the grid, a single estimated value of least squared error-type: the conditional expectation.

Final results of SGS have been expressed both in term of expected values and related variance (**Table 9**).

The optimal number of simulations has been chosen comparing the results of 10, 100 and 1000 simulations, through a validation process (**Figure 19**), carried out using an independent dataset of new training points.

In the present study the optimal number of simulations is 100, because it provides better results than those obtained using only 10 realizations and only little worse than those obtained from 1000 simulations which, however, require a gigantic times to run with only a small improvement of results.

HORIZONTAL INTERCEPT [cm]

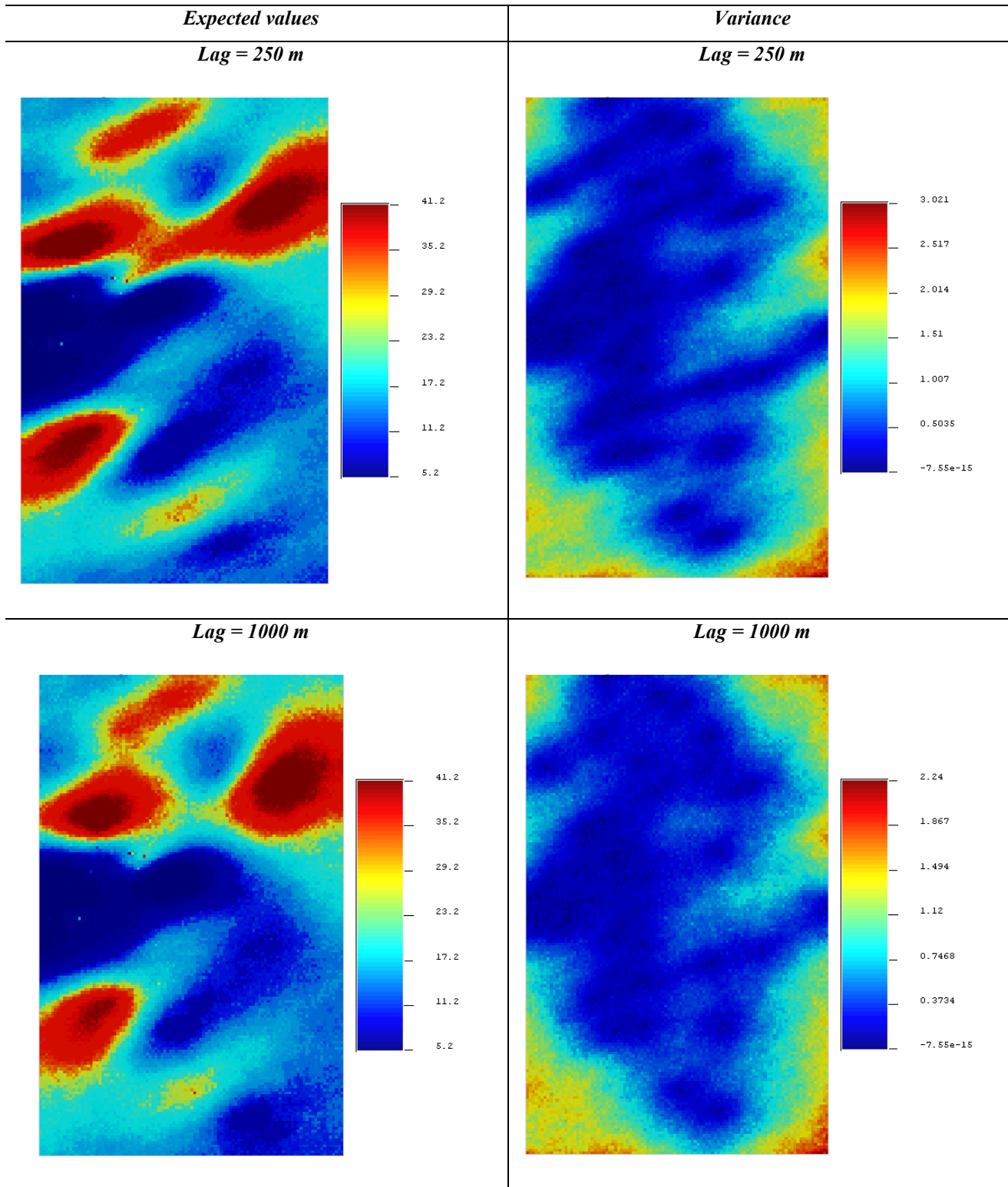


Table 9 - The expected values of horizontal intercept, estimated through 100 Sequential Gaussian Simulation, are reported on the left side and with their associated variances on the right side. The lag distance increases from the top to the bottom of the table

The two methods (Ordinary Kriging and Sequential Gaussian Simulation) provide quite similar outcomes for the central values of variable frequency distribution, while remarkable differences occur for the extreme values of data, indeed these are neglected in kriging results, while are maintained in those coming from

simulation. This is easily observable showing the results with the same colour bar (Table 10): in the map of OK results, all the dark blue areas, which correspond to fractured rock masses, lack.

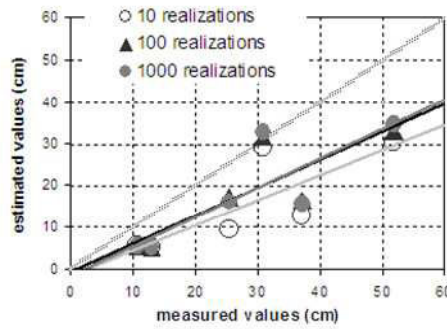


Figure 19 – Relationship between measured and estimated values of horizontal intercept

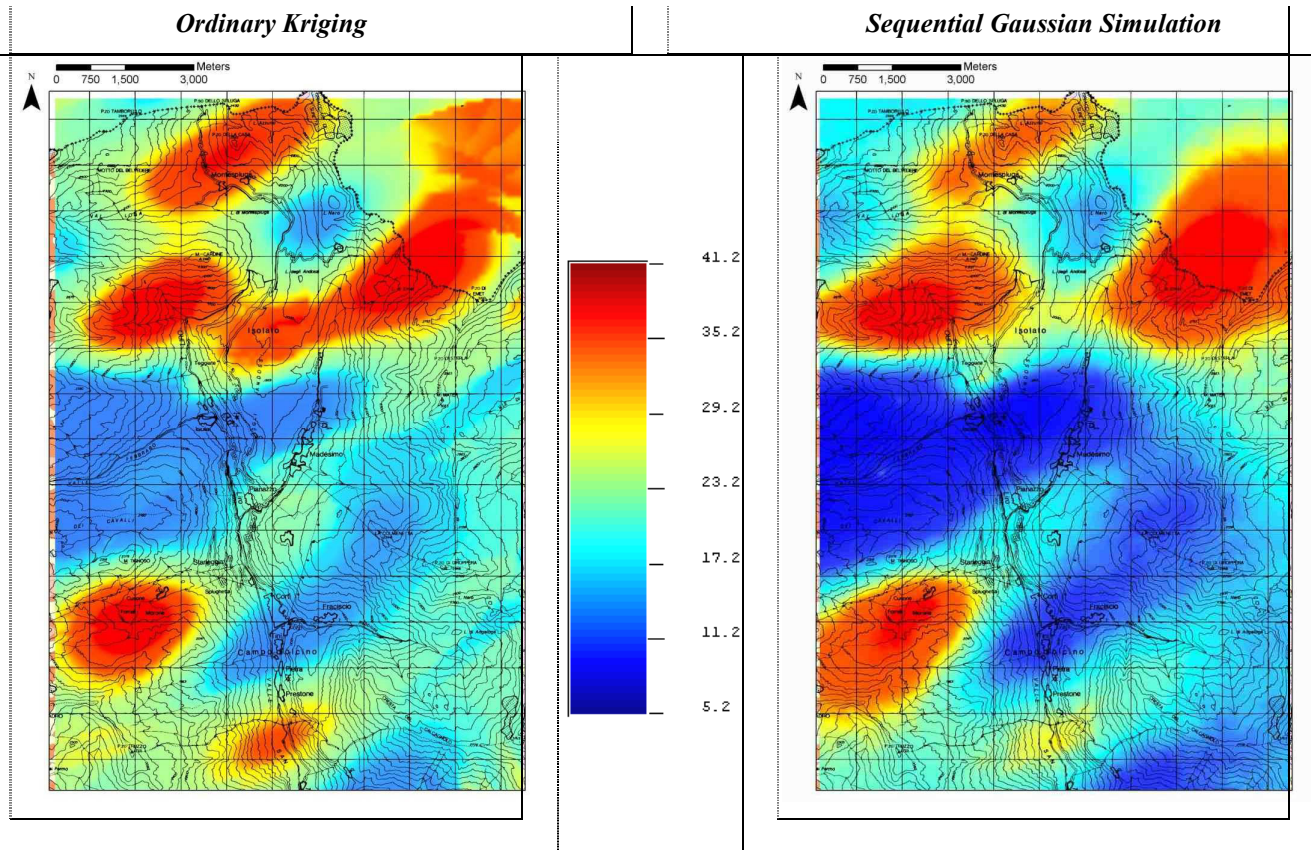


Table 10 - Estimated values of horizontal intercept, by means of Ordinary Kriging (on the left) and 100 Sequential Gaussian Simulation (on the right). Both maps have been represented using the same colour bar

The variance of estimation, and so the uncertainty, is obviously smaller using the OK methods, being the final SGS map derived from many different realizations. However, the variance is always very small near the data samples, and it increases going farther.

With the aim of comparing results obtained from the two different geostatistical techniques, a validation process has been performed, using an independent data set. About 10 new geomechanical surveys have been carried out in the research area to form this training point data set. The validation process has been

performed comparing measures of new sampling points with estimated values in their locations. The difference between actual and estimated values has allowed computing the following parameters (for each applied technique): mean error and its related root-mean-square, average standard error, mean standardized error and root-mean-square standardized error.

The minimum mean error has been obtained performing ordinary kriging with small lag distance, while minimum standard deviation of errors coming from sequential Gaussian simulation technique based on medium lag distance. A brief visual summary of the results is depicted in **Figure 20** the graph relates measured and estimated values of new sampling point dataset; the bisector is the place of points where the estimated values are equal to the measurements, the line closer to the bisector, is the regression line obtained from ordinary kriging with small lag. Nevertheless it is important to observe that training point data set does not contain extremely low values, which should have lower correspondence with kriging method. Generally the validation reveals a quite good accordance between estimated and measured data.

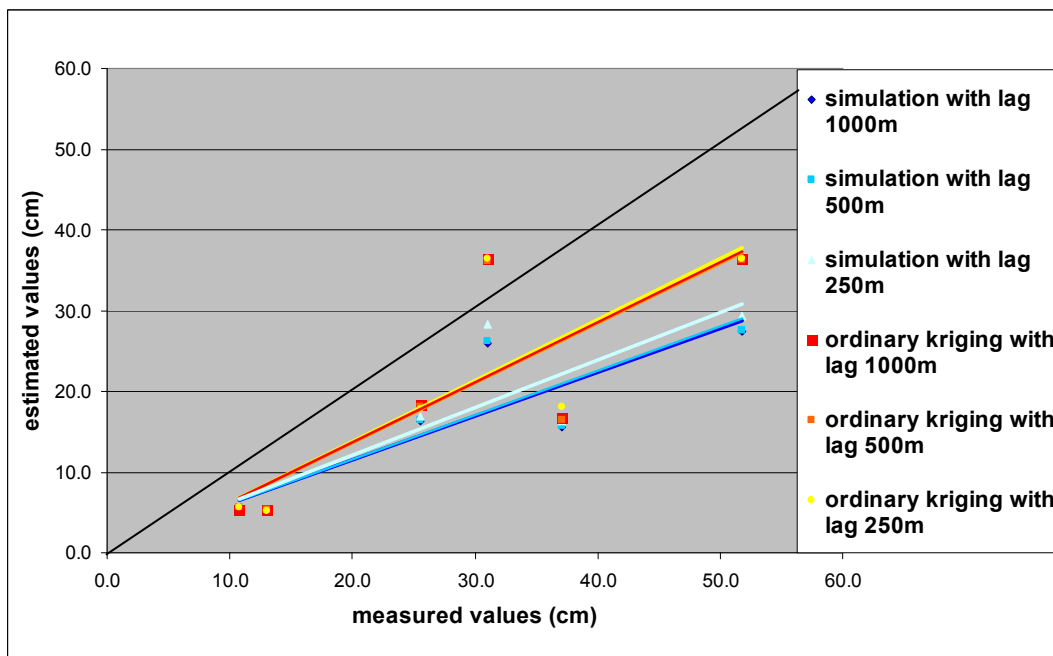


Figure 20 - Validation of horizontal intercept, this graph relates the measured with estimated values of an independent dataset

Although the validation process shows a quite good agreement between estimated and measured RMR values, the resulting maps (**Tables 8, 9 and 10**) seem too simplistic, actually they show a elemental behaviour, with gradual transitions among low and high values, which are localized in few zone. This kind of map are expected dealing for instance with water, soil contamination, etc., but not with rock mechanics properties. Actually a map with more scattered low and high values better depict the features of rock masses, where zones with low and high intercept values often occur, also within small distances, being rock masses heterogeneous.

Moreover, the resulting maps better describe a flat territory, but appear not reliable for Alpine valleys, such as San Giacomo valley. Actually in Alpine contexts, as well as in any mountainous region, also the topog-

raphy should play a key role in geostatistics. The contribution of elevation should be represented in the resulting map of rock mass properties. Actually the topography greatly affect the geometric relationships with the geological and structural setting, determining which rock masses are exposed.

It follows that also the elevation gradients should be considered when dealing with geostatistics in mountain territory. It is therefore necessary to have the altitude of each survey point, which should be considered during the variogram computation. It should affect the maximum correlation direction. Then, the estimation should be made not considering a plane, but using the DEM of the analysed territory. An attempt with this new approach has been taken into account in RMR and J_v estimation.

2.3.2 Rock Mass Rating

The Rock Mass Rating –RMR– is a quality index of rock masses, defines the geomechanical quality of a rock mass as the sum of five rates referred to the following rock and rock mass parameters (**Table 4**): the uniaxial compression strength of rock matrix, the Rock Quality Designation (RQD), the discontinuity spacing, the condition of discontinuities and the water presence. The resulting RMR value, which can ranges from 0 to 100, increases as the rock mass quality gets better, indeed the values have been classified in five classes of quality: poor (if RMR values are between 0 and 20), scarce ($21 < \text{RMR} < 40$), fair ($41 < \text{RMR} < 60$), good ($61 < \text{RMR} < 80$) and very good quality ($\text{RMR} > 81$).

This chapter aims to estimate the RMR, in a whole area, the San Giacomo Valley; the resulting map can be a useful tool to forecast the quality of outcropping rock masses as well as to derive their geomechanical behaviour. Actually the knowledge of rock mass quality indexes in an extended area is an important prerequisite in design of civil engineering and mining activities; the RMR is a widely used index to evaluate geomechanical features and stability conditions in areas interested by the planning and construction of large-scale engineering works, or affected by rock slope stability problems. The RMR classification has found wide applications in various types of engineering projects (such as tunnels, foundations and mines), as well as in geological risk management. The accuracy degree in predicting, evaluating and interpreting the quality of rock masses, along for instance a tunnel alignment, is a key for the successful execution of the project. Actually, the RMR is one of the rock mass classification systems which, as well as the Q-system (Barton, 1974), can be used as a guideline for the selection of the appropriate excavation technique, the kind of rock reinforcements and permanent support in tunnels, for the prevision of stand-up time, and for deriving the deformability parameters of the rock mass. At the same time, the RMR can be also used to evaluate the landslide susceptibility of rock slopes, allowing to individuate the more critical portions of rock masses which could be prone to failure. For instance, rockfalls analysis needs an accurate study of the cliff and the localization of the source areas of blocks. Additionally, the rock mass quality affects the choice of the conceptual model used in numerical modelling and analysis: a highly fractured rock mass, with respect to the geological and engineering problem, can be modelled as an equivalent continuum media, while a massive rock mass, with few discontinuities, must be approached with a discrete model.

In preliminary studies, it is common practice to execute direct geomechanical surveys in few representative areas, where the logistic difficulties can be over-passed, reducing time and costs. In both applications (civil works and slope stability), the common measurement techniques of rock mass properties provide punctual values, referred to a specific sampling location. Therefore the reproduction of the spatial variability of geomechanical quality in a whole area can be a very useful tool, especially during the pre-feasibility and feasibility planning phases, particularly to individuate critical points. The availability of a continuous map of RMR values can therefore be used in land use planning, prevention, mitigation and management of risks, but also in the prevision of the behaviour of rock masses.

The occurrence of any spatial correlation structure of RMR, and so the possibility to consider the RMR as a Regionalized Variable, has been already investigated from Barla et al. (1974), even if it has been estimated using geostatistical techniques only since 2004 (Oh et al., 2004; You & Lee, 2006; Stavropoulou et al., 2007; Choi & Lee, 2007; Exadaktylos & Stavropoulou, 2008; Exadaktylos et al., 2008; Choi et al., 2009; Kaewkongkaew et al., 2011; Yi et al., 2013), especially for tunnel projects. In these works the kriging method has usually been applied to borehole data, sometimes integrated by geophysical surveys, with a secondary and only qualitative role. RMR values have always been considered as a single regionalized variable and not as the sum of more variables. Actually, the use of the RMR index as a unique regionalized variable can constitute a conceptual mistake, because the RMR considers parameters with different origin, assigning to them different weights, and so each parameter is not considered in an independent way. It is worth to note that, considering only the final RMR value and not the individual parameters, geostatistical analysis becomes easier and faster; this approach could be reasonable to assess the rock mass quality in a wide area and especially to individuate the critical sites without understanding why low RMR values occur, i.e. what is the parameter that renders the RMR so low.

However, for the sake of clarity, before describing the RMR resulting values, some details on the distribution of each parameter involved in the RMR calculation have been outlined.

The parameters considered in the RMR computation are:

1. *Uniaxial compressive strength of the rock matrix*: the first RMR parameter have been defined, where possible, considering the joint compressive strength (JCS), as indicated in the ISRM suggested method (ISRM, 1978). The JCS have been measured on abraded discontinuities, with Joint Roughness Coefficient (JRC) smaller than 9, using the Schmidt hammer, and correcting the rebound values on the basis of the hammer orientation. The calculation of JCS has been performed using the **Equation 40**.

The results (**Figure 21**) show a high variability of the JCS values, which are very scattered and range from 35 to 216 MPa, although the outcropping rocks are almost all paragneisses. It follows that in the studied area the lithology seems not to play a significant control on the JCS values, excepting the amphibolite lenses which always give high JCS values, which however are aligned and not higher than the maximum paragneiss value. As consequence, in this area, the estimation of the JCS values, in each

point of the domain, constrained by the outcropping lithology, should lead to meaningless results, due also to the lack of a significant number of sampling points for the lithologies, such as amphibolite and quartzite, which outcrop only sporadically, in small lenses or in veins and so in very localized zones.

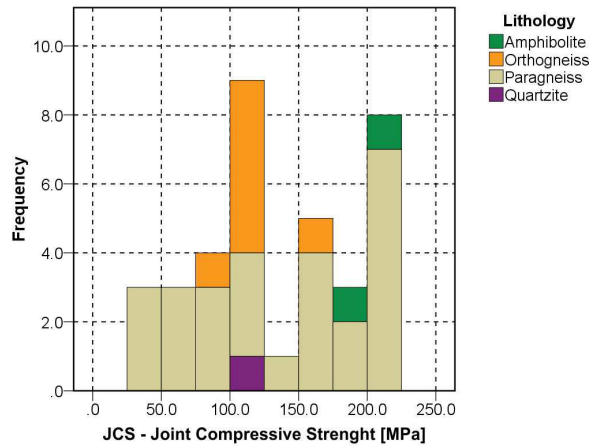


Figure 21 - Frequency distribution histogram of Joint Compressive Strength data, different colours represent different lithologies

2. *Rock Quality Designation (RQD)*: the second parameter used to calculate RMR has been indirectly derived, due to the lack of cores referred to the survey location. Palmstrom (1982) has suggested that, when cores are unavailable, the RQD may be estimated from the number of joints per unit of volume (J_v), in which the number of discontinuities per metre for each joint is added. According to Palmstrom (1974), the conversion formula for clay-free rock masses (Figure 22) is:

$$RQD = 115 - 3.3J_v \tag{43}$$

where J_v is the Volumetric Joint Count, which can be computed as:

$$J_v = \sum \frac{1}{S_{Kn}} \tag{44}$$

where S is the joint spacing (expressed in metres) for the each joint set K .

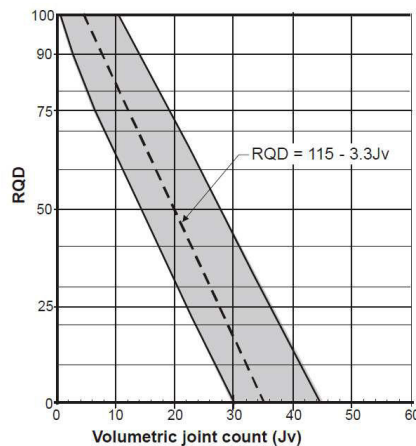


Figure 22 - Correlation between J_v and RQD with the variation range (from Palmstrom, 1974)

In the study area, the J_v values range from 6.7 to 66.6 fractures/m³, with a mean value of 25.3 fractures/m³, and a standard deviation of 13.3; the frequency distribution is clearly unimodal (**Figure 23a**), with a positive asymmetry. Also for the J_v is possible to note that the lithology does not play a key role on the fracturing density, being the values very scattered independently of the lithology, with the exception of orthogneiss, which always shows a low fracturing degree.

The J_v has been estimated also as an independent variable, in the whole studied area (Chapter 2.2.3).

3. *Spacing of discontinuities*: the spacing values have been directly measured for each discontinuity set, during the geomechanical surveys. The mean values, which have been calculated for each geomechanical station, have been reported in **Figure 23b** and range from 9.9 to 78.7 centimetres. Also in this case the values of mean spacings are very scattered, and are irrespective of the outcropping lithology.

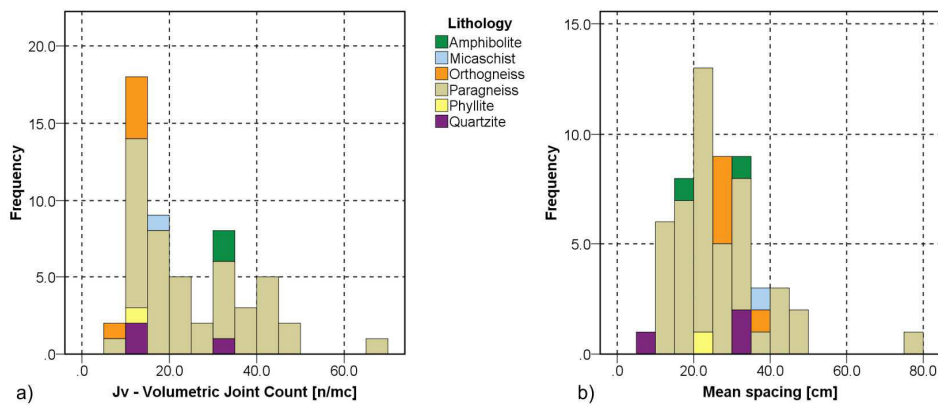


Figure 23 - Frequency distribution histogram of the Volumetric Joint Count (a) and the mean spacing (b); different colours represent several lithologies

4. *Conditions of discontinuities*: this parameter includes the following properties, which have been determined for each set:
 - persistence: it describes the discontinuity length; almost all the examined rock masses (the 86%) are characterized by a medium lateral persistence, that is between 50 and 90% (i.e. between 3 and 10 metres) of the outcropping rock mass;
 - aperture: it has been measured or estimated using the ISRM classes (ISRM, 1978). When the aperture class has been only estimated, in order to pass from a qualitative to a quantitative description of apertures, the maximum value of each class has been considered. This assumption has led to a poly-modal, discrete distribution (**Figure 24a**), in which it is however recognisable the highest peak, and so the maximum frequency, which is related to the smallest class value of the histogram. The mean aperture values range from 0.4 to 105 millimetres, and obviously no correlation exists with the lithology;
 - roughness of surfaces: the Joint Roughness Coefficient (JRC) is probably the most commonly used measure of roughness of rock joint surfaces. The JRC has been evaluated by visual comparison of

measured profiles against a set of standard JRC profiles produced by Barton and Choubey (1977). The mean JRC values for each investigated rock masses are between 4 and 14 (**Figure 24b**);

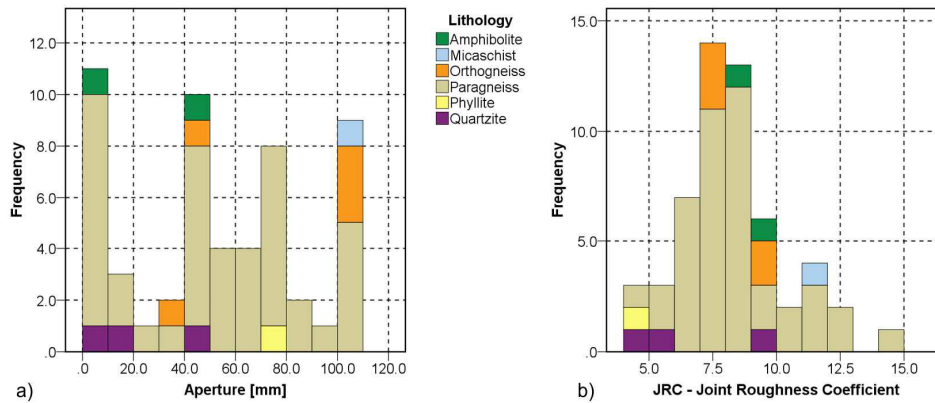


Figure 24 - frequency distribution histogram of the mean aperture (a) and the mean JRC (b); different colours represent different lithologies

- presence and kind of infilling: the infilling is absent in almost the 90% of the investigated sets;
- weathering condition: the rock masses show a low alteration degree, in particular it is frequent to observe slightly weathered discontinuities, which are bleached only on the surface.

5. *Groundwater conditions*: the fifth parameter of the RMR classification takes into account the occurrence of water along the discontinuities; different values have been assigned on the basis of general moisture conditions of the rock mass, which can be: completely dry (observed in the 64% of surveyed sites), damp (24%), wet (11%), dripping (never) or flowing (1%).

The sum of these five parameters leads to the Rock Mass Rating value, which describes the global quality index of the rock mass. All RMR values are contained in only two classes, irrespectively of the lithology (**Figure 25**): they range from 45 to 77, half of them belong to the “fair quality” class ($41 < \text{RMR} < 60$), while the other half belong to the “good quality” class ($61 < \text{RMR} < 80$); mostly of RMR values are included between 50 and 70.

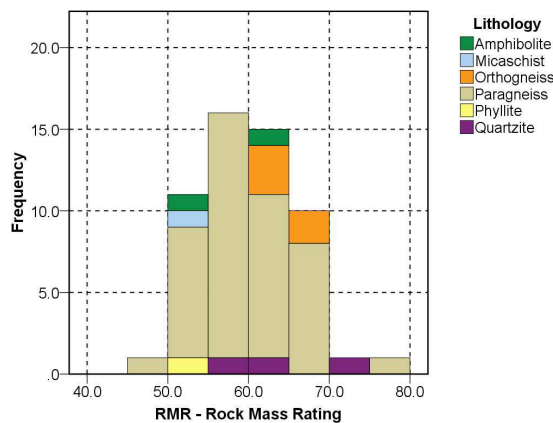


Figure 25 - Frequency distribution histogram of the Rock Mass Rating values; different colours represent different lithologies

Initially, the Exploratory Spatial Data Analysis consists of the computation of the main statistical parameters of RMR (**Table 5**), with the aim to determinate the frequency distribution.

The RMR index has been evaluated in 55 different locations, along the San Giacomo Valley. RMR values range from 45 to 77, the mean values is 60.6, with a standard deviation of 6. The median is equal to 59. The frequency distribution seems to be a Gaussian, indeed it is clearly a unimodal distribution, without a significant asymmetry (**Figure 26a**), being skewness and kurtosis, being both equal to 0.3, close to zero.

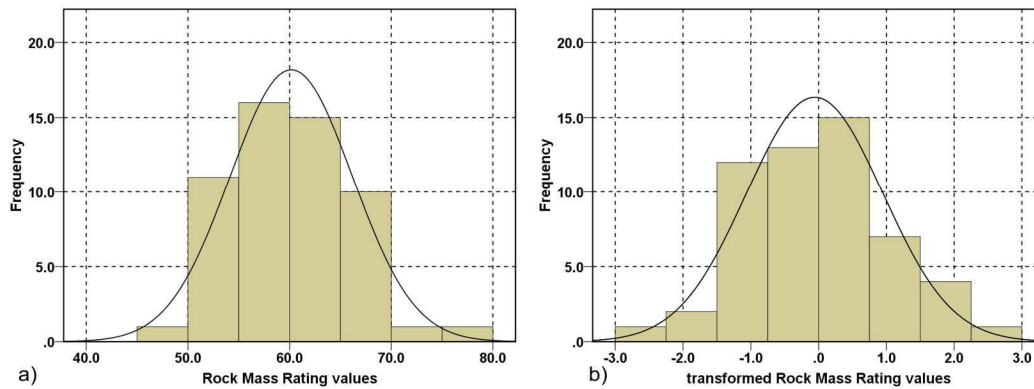


Figure 26 - Frequency distribution histograms of raw (a) and transformed RMR (b), with superimposed the Gaussian distribution

Since many geostatistical techniques are more reliable if the variable of interest has a standard Gaussian distribution, it is necessary to verify if the variable has a normal distribution.

The preferential sampling does not introduce significant spatial clusters, being the nearest neighbour index equal to 1 (with a standard deviation of 0.03); hence, the most common statistical tests can be used to verify if the univariate distribution of the data is Gaussian.

Actually, the normality of RMR distribution has been verified using various graphical and statistical tests, such as Shapiro-Wilk test and Kolmogorov-Smirnov test with Lilliefors correction; hence the Gaussian distribution of RMR has been confirmed with a significance level of 1%. Since the standard Gaussian distribution, with mean and variance equal respectively to 0 and 1, is required, the Gaussian distribution of RMR has been transformed in a standard one (**Figure 26b**), through a process called Gaussian anamorphosis.

As many geostatistical methods are based on the spatial stationarity property, the absence of systematic trends has been verified, representing the magnitude of variable along different directions in the space. The stationarity hypothesis of RMR in the studied domain has been confirmed.

The variography, based on the modelling of semivariogram, has been here applied to recognize the RMR spatial distribution of the examined rock masses.

The correlation structures of RMR have been investigated at different scale and the possible occurrence of anisotropies has been taken into account. First of all an omni-directional variogram, which relates the distance among pairs of sampling points with their variance, has been constructed (with angular tolerance of

90°) in order to individuate if a correlation of the variable in the research area exists. The presence of any preferential correlation direction has been firstly sought graphically using the 2D variogram map.

A more detailed research of maximum correlation direction has been conducted through the construction of several directional variograms, with a variation direction of 45° and an angular tolerance of 22.5°. Three experimental variograms have been constructed at different scales, varying the lag distance from 250 to 1000 metres, and therefore increasing the maximum distance under study. The lag tolerance has been assumed equal to the half of lag distance.

According to the horizontal intercept results and insights, experimental variograms have been determined using both a classical 2D approach and an almost 3D one: in the former the distance among pairs of samples depends only on latitude and longitude, in the latter, altitude also contributes to the distance and it should play an important role where elevation gradients are worthy of note, such as in the study area.

When the approach changes, the maximum correlation direction becomes lightly different: in the 2D approach it is towards NNE (22.5°-202.5°), whilst in the almost 3D one it has a dip direction toward NE (45°) with a dip angle of about 20°, this orientation is in accordance with the discontinuity set developed parallel to the regional foliation, which dips towards East with a low dip angle, and therefore has a remarkable geological significance. Nevertheless, there are some analogies between the two different approaches, being the variable under study the same. First of all, almost all the experimental variograms are better fitted by a spherical theoretical model, therefore the variance values increases with the lag, until a sill, this indicates that the variability of RMR increases as the distance h among sampling points grows, and so that RMR is a regionalized variable. The presence of a finite sill in all the experimental variograms indicated that the stationarity and ergodic hypotheses are respected.

Experimental and derived theoretical variograms, along the maximum correlation direction, obtained using different lag sizes, are shown in **Table 11**, while **Tables 12 and 13** reports the parameters used to create the variogram models, with the 2D and almost 3D approach, respectively.

The invariance of scale has been respected also for the RMR, even if the dip angle of the experimental variogram with short lag (equal to 250 metres) obtained with the almost 3D approach is smaller of 10° than the variograms with medium and long lags.

The variogram models do not tend to zero when h is zero, this discontinuity of variogram at the origin, which corresponds to the short scale variability, is called nugget effect and can be due to local heterogeneities of the geology structures, with correlation ranges shorter than the sampling resolution, or to measurements errors; it is worth to note that the nugget effect of all variograms is close to zero and it is bigger in the 2D approach, this could be related to the fact that altitude of sampling point is neglected in the 2D approach. Actually a so small nugget effect is also because the support of the measure (equal to 20 metres) is significantly smaller than the range.

The experimental variograms show that generally the sill decreases when lag distance increases, because the small heterogeneities are neglected and consequently the variance reduces.

Finally, it is possible to note that maximum ranges increase with lag distance, because the considered distance is longer, while minimum ranges decrease. Hence, the anisotropy ratio increases with the distance.

Lag = 250 m

Lag = 500 m

Lag = 1000 m

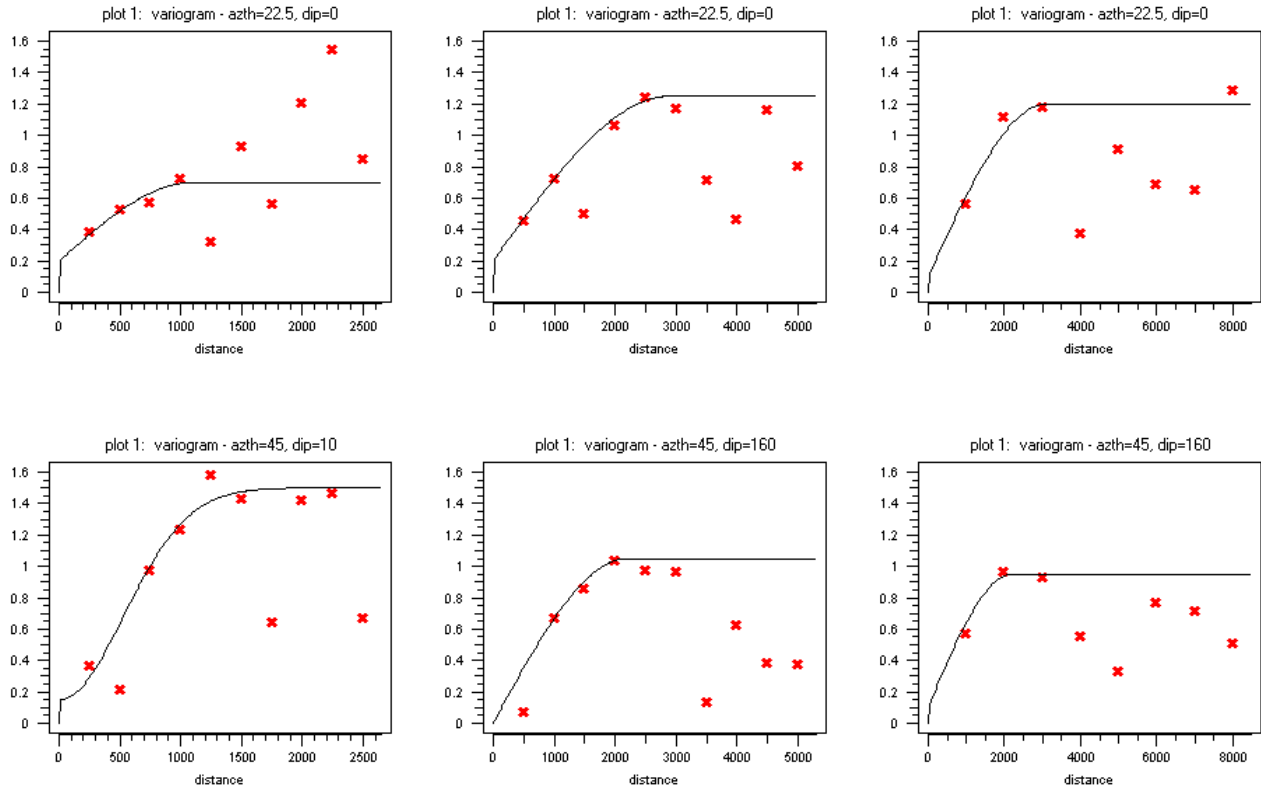


Table 11 – experimental directional variograms (represented with red crosses) and variogram models (solid lines) of RMR transformed data, computed using different lags and different approaches: the first row refers to the classical bi-dimensional approach, while the second one to the almost three-dimensional one

| 2D APPROACH | | | |
|-------------------------------|--------------------|--------------------|---------------------|
| <i>Parameter</i> | <i>Lag = 250 m</i> | <i>Lag = 500 m</i> | <i>Lag = 1000 m</i> |
| Kind of model | Spherical | Spherical | Spherical |
| Maximum correlation direction | 22.5°-202.5° | 22.5°-202.5° | 22.5°-202.5° |
| Nugget effect | 0.2 | 0.2 | 0.1 |
| Sill | 0.7 | 1.25 | 1.2 |
| Maximum range | 1100 | 2900 | 3100 |
| Minimum range | 400 | 300 | 200 |
| Anisotropy ratio | 2.8 | 9.7 | 15.5 |

Table 12 - Parameters of theoretical variogram models

| <i>ALMOST 3D APPROACH</i> | | | |
|--------------------------------------|--------------------|--------------------|---------------------|
| <i>Parameter</i> | <i>Lag = 250 m</i> | <i>Lag = 500 m</i> | <i>Lag = 1000 m</i> |
| Kind of model | Gaussian | Spherical | Spherical |
| Dip direction of maximum correlation | 45° | 45° | 45° |
| Dip angle of maximum correlation | 10° | 20° | 20° |
| Nugget effect | 0.15 | 0 | 0.1 |
| Sill | 1.5 | 1.05 | 0.95 |
| Maximum range | 1300 | 2200 | 2200 |
| Minimum range | 700 | 700 | 200 |
| Anisotropy ratio | 1.9 | 3.1 | 11 |

Table 13 - Parameters of theoretical variogram models

The prediction has allowed estimating RMR values in the whole domain. In the 2D approach the prediction has been carried out using a grid which represents the study area in term of longitude and latitude, while in the almost 3D model also altitude has been considered. Since borehole data are not available, the RMR index has been estimated only on the topographic surface and not in depth. The used grid is defined by regular square or cubic cells, of 100 metres for each side.

The parameters of the described theoretical variograms have been employed for the spatial interpolation of RMR values, initially by means of kriging technique. Among the different kriging methods, several authors (You & Lee, 2006; Choi & Lee, 2007; Choi et al., 2009; Yi et al., 2013) have used Indicator Kriging –IK– to estimate RMR classes, but since in the study area RMR values fall within only two classes, instead of the categorical approach of IK, the numerical one of Ordinary Kriging –OK– has been chosen. Furthermore the IK needs an indicator transformation, which always implies a loss of information: the extra information about significant high or low values which fall within the same class is lost, actually it does not play a role whether a value is only a little bigger or very bigger than the chosen threshold. The OK, which has been already used two times in the RMR estimation (Stavropoulou et al., 2007; Kaewkongkaew et al., 2011), has been chosen with the aim to take in account the entire data set.

Since RMR shows a strong spatial anisotropy, the measurements inside an elliptic research region, with axes parallel to maximum and minimum correlation directions (individuated by the directional variograms), have been considered to perform the estimation process. In order to take into account the irregularity of data distribution, the axes of ellipse have been computed as the double of ranges. Inside each ellipse a minimum of five and a maximum of twenty data were considered; if in one research region there were less than five data the estimation has not been performed, because the associated variance would be too high.

The plausibility of the interpolation models has been investigated using a cross-validation procedure, which shows that the estimation method adopted tends to overestimate low values and underestimate high ones,

producing a marked smoothing effect, which leads to neglect the extreme values of sample distribution and therefore does not preserve the variability of the parameters under investigation. The cross-validation also shows that the smoothing effect occurs, and it is bigger in almost 3D models than in the 2D ones. Actually, the smoothing effect is not constant and more variable the geology is, stronger the impacts of smoothing effect are (Marinoni, 2003). With the aim to avoid this smoothing effect, Sequential Geostatistical Simulation –SGS– technique has been applied. SGS has been performed using the parameters previously defined through variogram analysis and the same grids and research ellipses of those used for OK.

The optimal number of simulations has been chosen comparing the results of 10, 100 and 1000 simulations, through a validation process. The best compromise between the accuracy of results and the computation time resulted from 100 simulations.

The **Figures 27 and 28** compares the estimated RMR values obtained by OK (**Figure 27**, on the left side, and **Figure 28a**) and SGS (**Figure 27**, on the right side, and **Figure 28b**), using the 2D the almost 3D approach, both with lag equal to 500 metres. Un-estimated areas (white regions in **Figures 27 and 28a**) are due to elliptical research region with less than five samples.

The resulting maps are quite different, even if both OK and SGS techniques provide quite similar outcomes for the central values of variable frequency distribution, while remarkable differences occur for the extreme values of data, indeed these values are neglected in the OK results, while they are maintained in those coming from SGS technique.

Considering the 2D domain, the resulting maps of RMR show the same problems of the horizontal intercept resulting maps: they are too continues, while it is very likelihood that rock mass have more heterogeneous properties. The 3D kriging map appears much more continuous than the 2D maps, because the variograms with the almost 3D approach is characterized by a lower anisotropy ratio than the variogram computed with the classical 2D approach. Actually in the 2D maps the effect of the anisotropy ratio is too strong.

The 3D simulation map, which allows also abrupt local variation of RMR values, seems to better count for the geological settings and topography than the 3D kriging and 2D maps, even if it is still quite far from the expected map.

With the aim of comparing results obtained from these two different techniques and approaches, a validation process has been performed, using an independent data set. About 10 new geomechanical surveys have been carried out in the research area to form the training point data set.

The validation process has been performed comparing measures of new sampling points with estimated values in their locations. The difference between actual and estimated values has allowed computing the following parameters (for each applied technique): mean error and its related root-mean-square, average standard error, mean standardized error and root-mean-square standardized error.

Ordinary Kriging

Sequential Gaussian Simulation

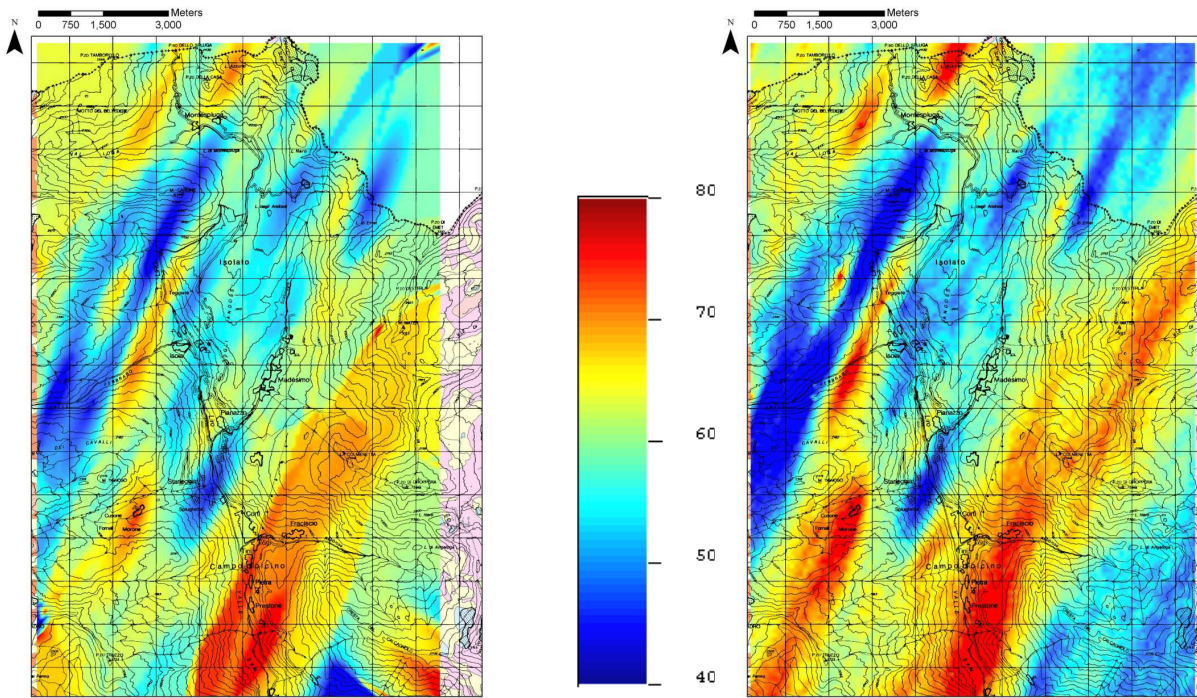


Figure 27 - Maps of RMR expected values estimated by OK (on the left) and SGS (on the right), with 2D approach and medium lag

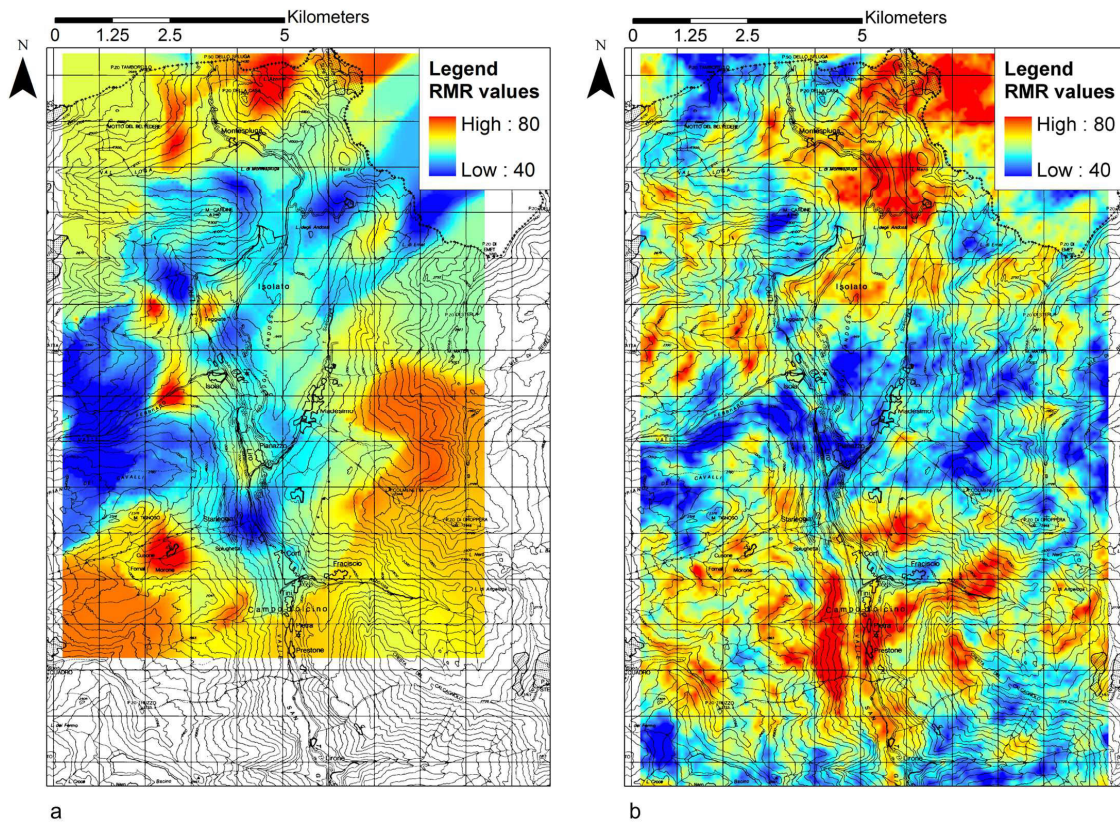


Figure 28 - Maps of the expected Rock Mass Rating values estimated using Ordinary Kriging (a) and Sequential Gaussian Simulation (b), with the almost three-dimensional approach and medium lag (500 metres)

In the 2D models the minimum mean error has been obtained performing OK with the longest lag distance (equal to 1000 metres), while the minimum standard deviation of errors comes from SGS technique based also on long lag distance (1000 metres). Generally the validation reveals a quite good agreement between measured and estimated data in new sampling locations; the results of SGS are lightly better than those obtained from OK. Nevertheless kriging results obtained from a 2D grid are better than those from an almost 3D one. Overall the best results come from SGS, implemented on a 3D grid, with a medium lag distance (equal to 500 metres), which represents the best compromise between small and big heterogeneities considered by the variogram. Actually, the almost 3D approach shows a notable difference between OK and SGS results, being the smoothing effect of kriging very high, indeed only the central values are exactly estimated with kriging method.

A brief visual summary of the results is depicted in **Figure 29**, the graph relates measured and estimated values of new sampling point dataset; the bisector is the place of points where the estimated values are equal to the measurements, the line closer to the bisector, is the regression line obtained from the SGS with medium lag and 3D grid.

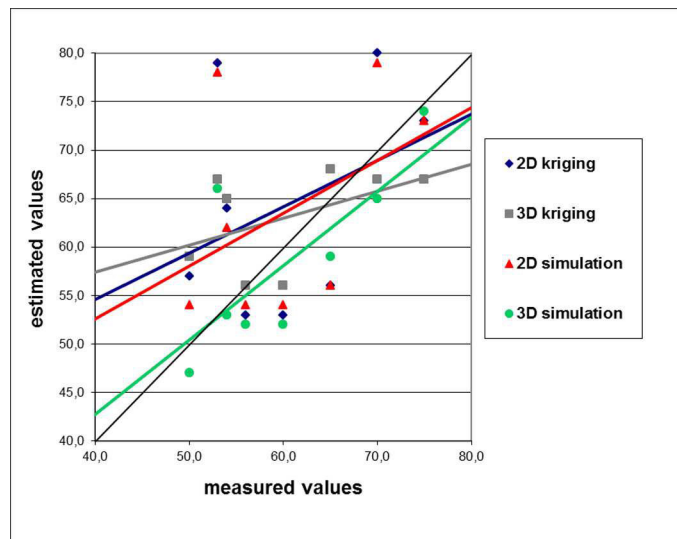


Figure 29 - The graph associates measured values with the estimated ones, comparing two different technique and approaches

Although the validation process shows a quite good agreement between estimated and measured RMR values, the resulting maps (**Figures 27 and 28**) seem not to properly count for the geometric relation between geological and structural setting and topography. Although the almost 3D approach shows a good improvement, the topography seems to affect only lightly the map, actually in some zones the RMR values are irrespective of isohypses, although the variograms have gentle dip angles. The model might be affected by such a parameter of the RMR sum, not adequately described and poor correlated.

All the RMR parameters imply geometric features, with the exception of the groundwater condition. It is worth to note that, although the RMR classification was born especially in reference to the underground rock masses involved in tunnelling, and so to the groundwater circulation, during the geomechanical sur-

veys the external moisture conditions of rock mass are revealed; these conditions are affected by the local climatic situations of the days before the survey, especially in Alpine areas where the weather can be very changeable. Furthermore, in the research area the presence of water has been surveyed with very different conditions from site to site: the surveys have been carried out during different seasons and hence with several climatic and weather situations; in particular in San Giacomo valley, as well in all Alpine valleys characterized by heavy snows in winter, the presence of water differs enormously from week to week, according to the global snow-melt regime. Consequently this parameter has not been surveyed in standard conditions and therefore could be not representative and properly introduced in the geostatistical analysis.

With the aim to uniform the weight related to the presence of water, considering that the 64% of the investigated rock masses were completely dry during the surveys and only the 1% showed flowing condition, all RMR values have been computed again with the assumption that all rock masses were dry during the survey campaigns and so attributing 15 points to the last RMR parameter. The “dry RMR” values obviously are higher than the previous RMR values, although they fall again in the “fair” and “good” quality classes (**Figure 30**): the mean and median values are slightly higher than those computed considering also the water, whilst the extremes values, referred to dry rock masses, do not change. The dry RMR has been computed in 54 locations, it ranges from 45 to 77. The mean and median values are both equal to 62. There is a unique mode in 66. The skewness and the kurtosis are both close to zero (respectively equal to -0.267 to -0.177). The distribution shows a slight negative (or left) skewness, so the Gaussian anamorphosis has been performed once again in order to apply geostatistical techniques.

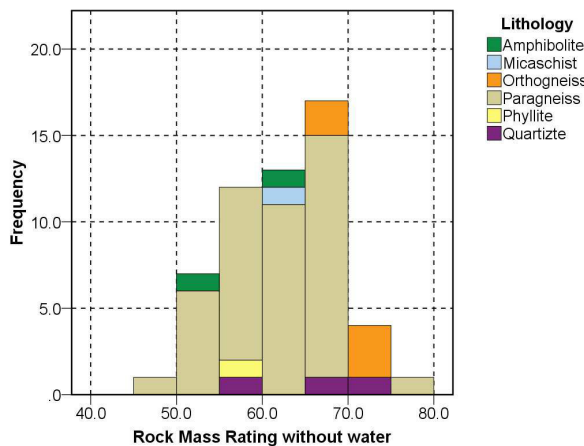


Figure 30 - Frequency distribution histogram of the RMR without water; different colours represent diverse lithologies.

The transformed data have been used to compute directional variograms, applying the almost 3D approach, which had already proven to be the most effective. The maximum correlation direction is slightly rotated towards East and now exactly coincides with the mean discontinuity set developed parallel to the regional foliation, whit dip angle is equal to 10°. Using an almost 3D approach, beyond the maximum and the minimum correlation directions, there is also the medium one. In this case the maximum correlation direction, in term of dip direction and dip angle, is 67.5°/10°, the medium correlation direction is 157.5°/0° (SSW-

NNW), and the minimum correlation direction is 157.5°/80°. Obviously, lacking depth data, significant variograms along the minimum correlation direction do not occur, and the range of the minimum correlation direction has been always posed equal to 200 metres (a bit shorter than the smallest lag, because the first point of the variogram is not correlated). As consequence, the anisotropy ratio (computed as the ratio between the maximum and the minimum range) is meaningless.

Lag = 250 m

Lag = 500 m

Lag = 1000 m

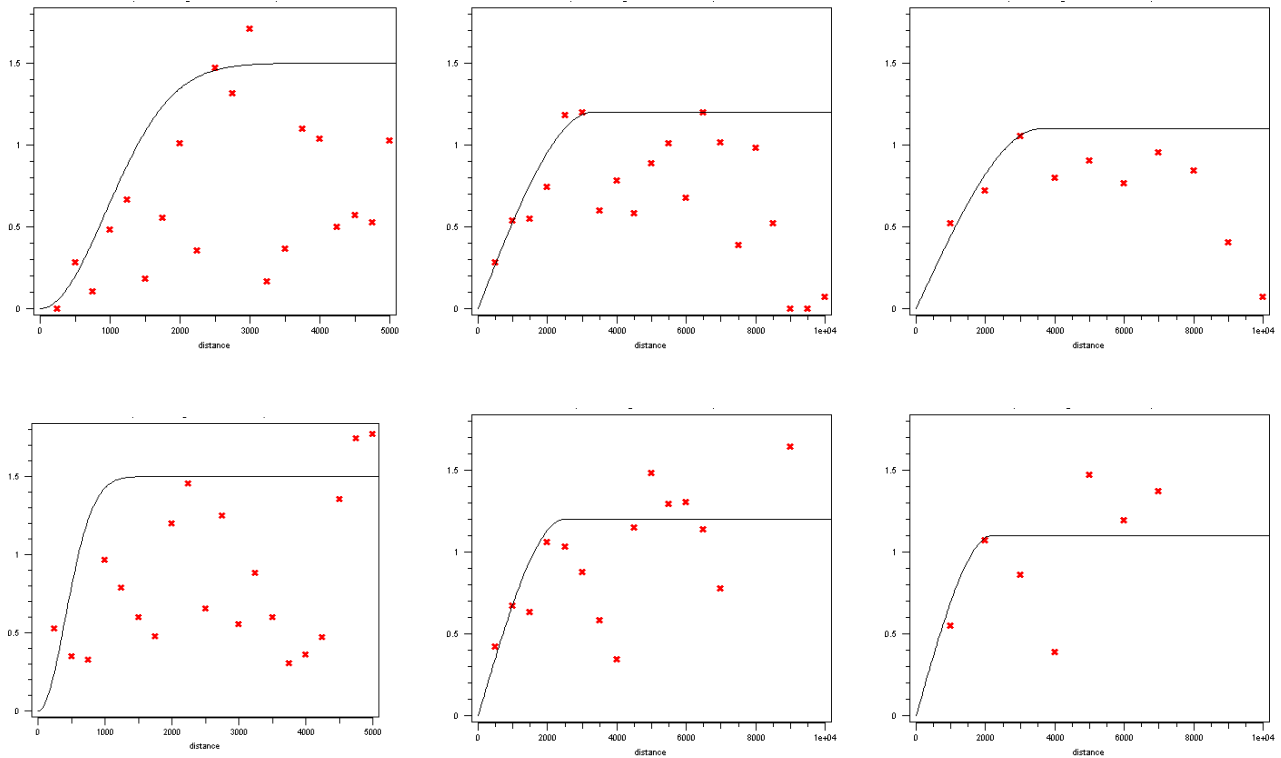


Table 14 – Experimental and theoretical variograms of dry RMR transformed data, computed using different lag distances. The first row is along the maximum correlation direction, while the second row is along the medium correlation direction

| ALMOST 3D APPROACH | | | |
|--------------------------------------|--------------------|--------------------|---------------------|
| <i>Parameter</i> | <i>Lag = 250 m</i> | <i>Lag = 500 m</i> | <i>Lag = 1000 m</i> |
| Kind of model | Gaussian | Spherical | Spherical |
| Dip direction of maximum correlation | 67.5° | 67.5° | 67.5° |
| Dip angle of maximum correlation | 10° | 10° | 10° |
| Nugget effect | 0 | 0 | 0 |
| Sill | 1.5 | 1.2 | 1.1 |
| Maximum range | 2300 | 3300 | 3600 |
| Medium range | 800 | 2100 | 2000 |
| Minimum range | 200 | 200 | 200 |

Table 15 - Summary of values obtained by modelling experimental variograms of dry RMR values

The invariance of scale has been also observed using the “dry RMR” data. The theoretical models, which better fit the experimental variograms, are again spherical models for the variograms with bigger lags and a Gaussian model for the variogram with the shortest lag, which therefore shows a greater continuity than the others. The features of the chosen variogram models are reported in **Tables 14 and 15**.

All models confirm that when the lag increases the sill decreases, because increasing the distance the small heterogeneities are neglected, consequently the variance reduces; on the contrary the maximum range increases with lag distance, because the distance considered is longer. It is important to note that the nugget effect is equal to zero in all the variograms calculated without water and it can be considered a good clue, because typically the nugget effect is related to measurement errors or to short scale variability, with correlation range shorter than the sampling resolution, hence to the use of a not correct sampling grid. Considering the rock masses dry, the nugget effect is removed and so the estimation results should be improved.

The prediction has been carried out as for the “wet RMR”, here only the results of the estimation performed by SGS, carrying out 100 realizations, on a 3D grid are presented (**Figure 31**).

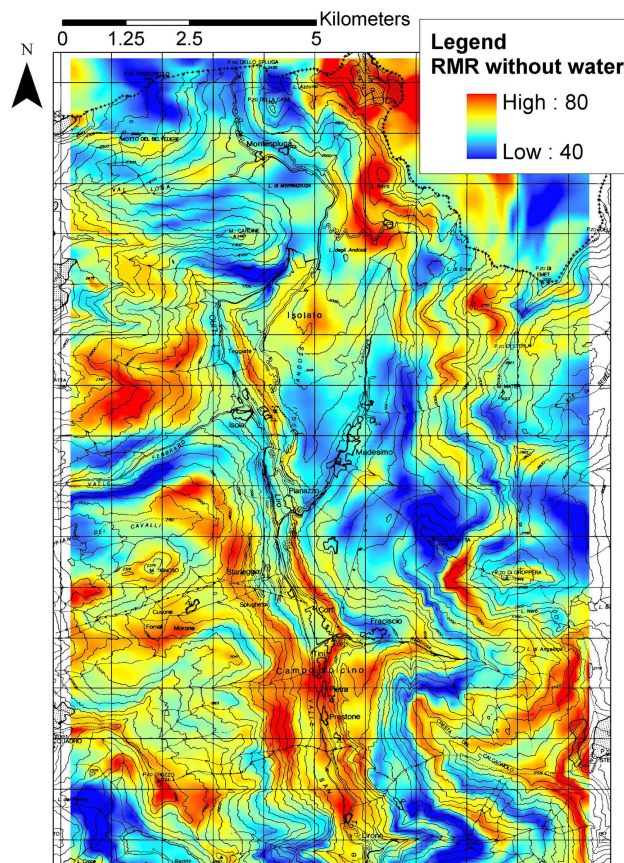


Figure 31 - Map of expected dry RMR values, estimated by SGS with almost three-dimensional approach

The expected RMR values map now meets some important geological evidences: for instance the low quality of the rock masses, which outcrop on the South-East of the map with an arched shape, corresponds to the big niche of the historical Cimiganda landslide; the dam of Montespluga lake is on rock with low qual-

ity, actually it leans on carbonatic rocks, with many karst conducts, which leads to big problems related to the high permeability and the low capacity of the reservoir. However, near the border of the simulation domain the uncertainty is bigger, for instance on the SW corner, the Truzzo metagranite outcrops and RMR values slightly higher than the predicted values are expected. Also on the NE corner there is something wrong: the rock masses on Surettahorn, one of the highest mountains in Chiavenna Valley, result to have high quality, while at these high altitudes a lower RMR index is expected, due also to the numerous freezing-thawing cycles that contribute to fracture the rock masses in their shallower portions.

The validation (**Figure 32**), performed as for the wet RMR, shows that the best results come from the dry RMR dataset, especially using the short lag, which is able to capture also the small variability and heterogeneities.

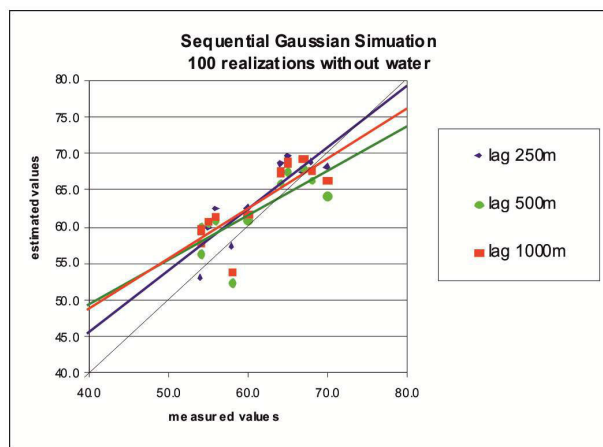


Figure 32 - Validation of the dry RMR simulation results'

The comparison between results of 100 SGS, using the almost 3D approach, of the predicted dry and wet RMR (**Figure 33**) shows that the former are better than the latter: in this context, the use of dry RMR data improves appreciably the results.

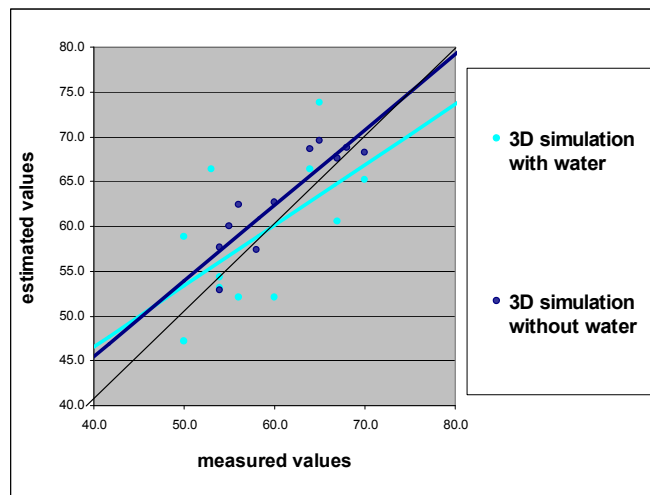


Figure 33 – Comparison between dry and wet RMR results, obtained by 100 SGS, using the almost 3D approach

However, the contribution of the almost 3D approach revealed to be essential when geostatistics needs to be applied in mountain areas.

It is worth to note that this work investigates outcropping rock masses and the estimation regards rock masses at shallow depth. No depth data are available in the region, except for few geomechanical surveys carried out in an underground hydraulic power plant, having a depth of 155 metres below the surface, which lead to RMR values between 54 and 59, in the range of the RMR values of outcropping masses. Therefore not considerable increases in rock mass quality are observable at these depths, but this fact could be related to the adopted excavation method. Therefore the results are confined on the outcropping rock units that are affected by environmental erosion and weathering (action of water and air, freezing-thawing, roots of plants, temperature fluctuations and thermal fatigue, etc.). It does not consider the quality of the same rock units at some depth below the skin of the surface. Hence, it is suitable only for shallow application, such as the analysis of surface excavations.

2.3.1 Volumetric Joint Count

The same procedure has been applied also using as Regionalized Variable the Volumetric Joint Count (Jv). It is a measure of the number of joints within a unit volume of rock mass, and describes the fracturation degree of a rock mass, in three dimensions. It can be computed applying the Equation 44.

The Exploratory Spatial Data Analyses, which is the first step in any geostatistical analysis, implies the computation of main statistical parameters. The descriptive statistical parameters of Jv (**Table 5**) can be summarized as follow. The Jv has been calculated in each sampling location, therefore there are 97 Jv values, ranging from 6.7 to 66.6 fractures/m³. The resulting average value is equal to 25.27 fractures/m³, with a standard deviation of 13.27. The median is of 21.43 fractures/m³.

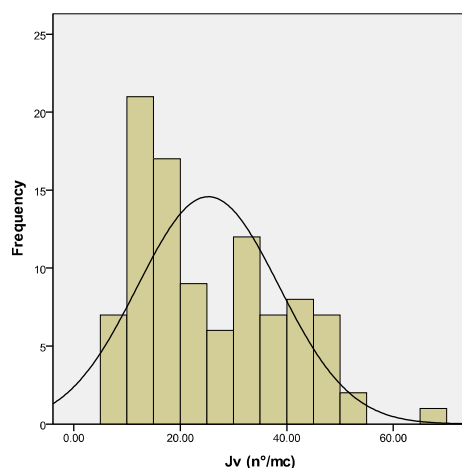


Figure 34 - Frequency distribution histogram of raw Jv data; the continuous line is the best-fitted normal distribution function

Being the distribution unimodal (**Figure 34**), since the median is smaller than the mean, there is a positive (right) non-parametric skew, with a long right tail. Actually, the skewness of 0.65 indicates the tendency to

concentrate the values towards the right extreme: the tail on the right side is longer than the left side. The kurtosis is equal to -0.44.

Obviously this distribution is not the standard Gaussian distribution required in geostatistics, but recalls a log-normal distribution. As it has been demonstrated by the nearest neighbour index, which tends to 1, the disposition of sampling locations is neither clustered nor dispersed. Therefore, the data de-clustering is not necessary and the frequency distribution can be verified using the standard statistical tests. Since the frequency distribution of J_v values approximates a log-normal distribution, so the values have been transformed using their natural logarithm. Afterwards, the normality of transformed data has been verified using various graphical and statistical tests, such as the Shapiro-Wilk test (Shapiro and Wilk, 1965) and the Kolmogorov-Smirnov test with Lilliefors correction (Lilliefors, 1967). Since the standard Gaussian distribution, with mean and variance equal respectively to 0 and 1, is required, the Gaussian anamorphosis process has been performed (**Figure 35**).

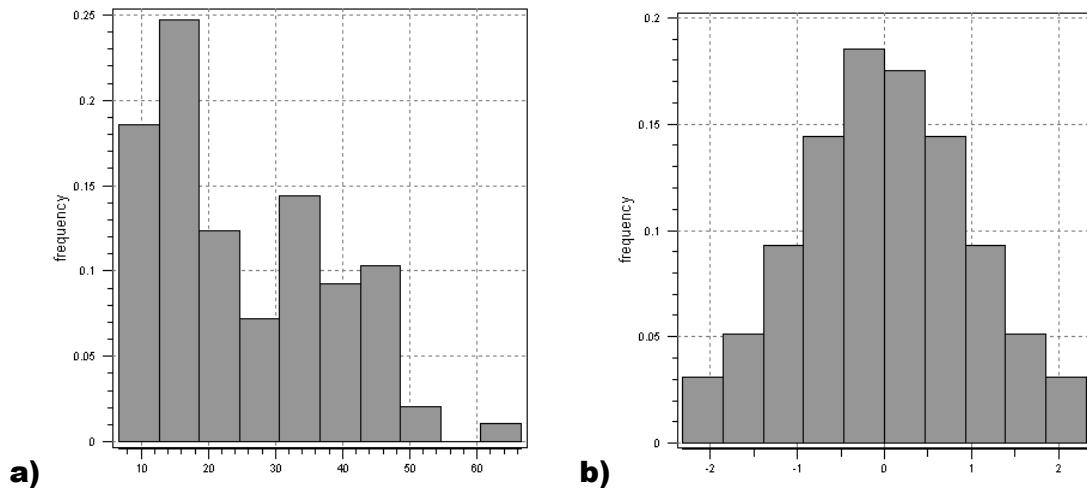


Figure 35 - Frequency distribution histograms of raw J_v data (a), and transformed J_v data, after the Gaussian anamorphosis (b)

The absence of trends has been verified and has allowed confirming the stationarity property of the considered variables over the studied domain.

First of all, an omni-directional variogram has been constructed with the aim to individuate if a correlation of the variable in the research area exists. The presence of any preferential correlation direction has been firstly sought graphically using the 2D variogram map (**Figure 36**).

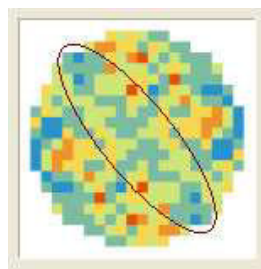


Figure 36 - 2D variogram maps of J_v transformed data

The maximum correlation direction of J_v is towards SE, approximately perpendicular of the maximum correlation direction of the horizontal intercept. This is a good result because, although these two parameters are independent, both describe the fracturation degree of a rock mass, but in different (opposite) ways: increasing the intercept the fracturation degree decreases, while rising the J_v the fracturation degree increases.

A more detailed research of major correlation direction has been conducted through the construction of several directional variograms, having an angular tolerance of 22.5° . Three experimental variograms have been constructed at different scales, varying the lag distance from 250 meters to 1000 meters, both using the 2D and almost 3D approach. The lag tolerance was assumed equal to the half of the lag distance.

Lag = 250 m

Lag = 500 m

Lag = 1000 m

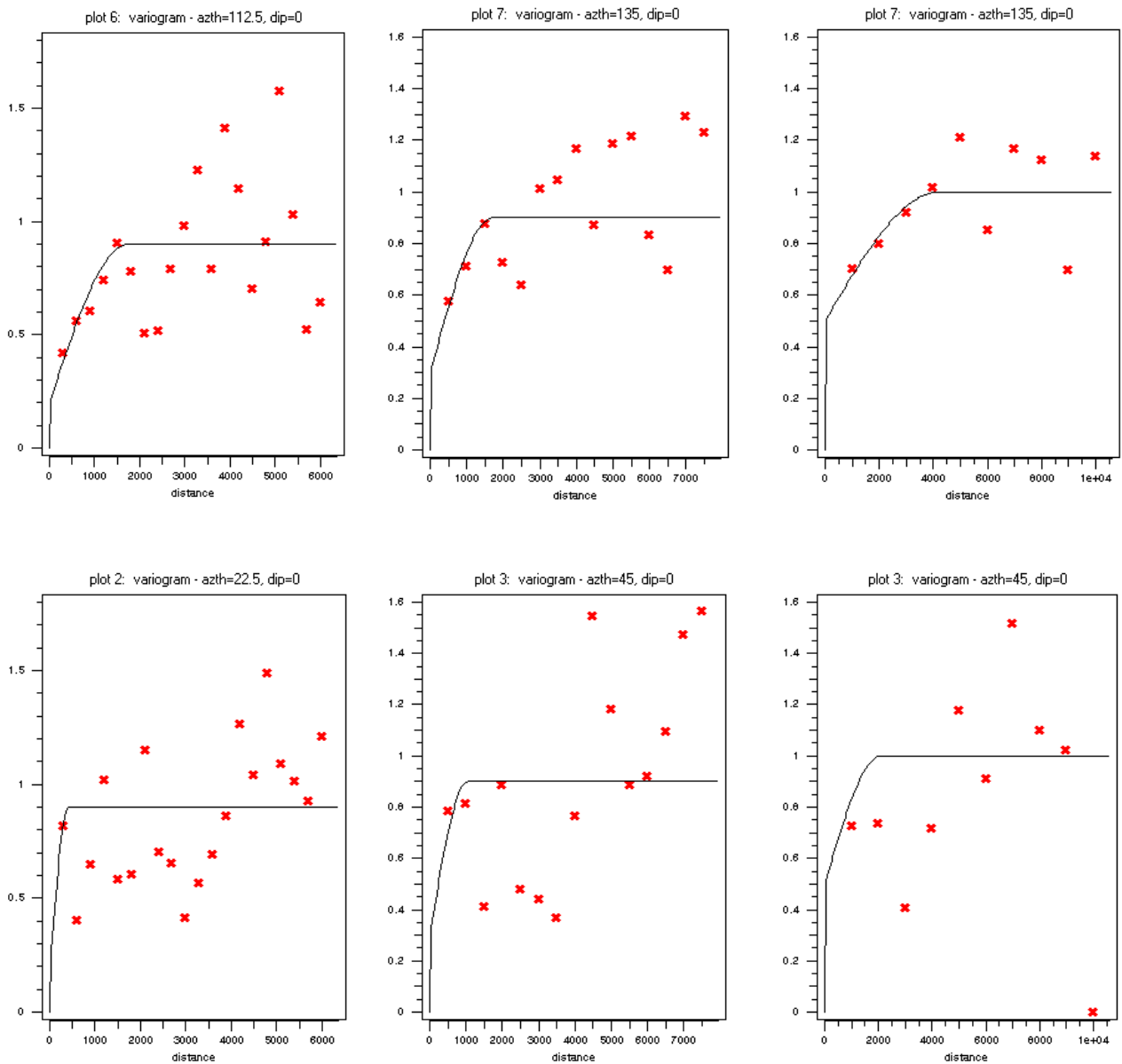


Table 16 – Experimental and theoretical variograms of J_v transformed data, computed using different lag distances and the 2D approach. The first row refers to the maximum correlation direction and the second row to the minimum correlation direction

The invariance of scale is respected also in this case: all the variograms show a preferential correlation direction SE-NW (with a tolerance of $\pm 22.5^\circ$), and can be modelled using a spherical model (**Table 15**). The minimum correlation directions (always perpendicular to the main correlation direction) show very weak correlations. The parameters of the theoretical models that best fit the experimental variograms are reported in **Table 17**.

| <i>Parameter</i> | <i>Lag = 250 m</i> | <i>Lag = 500 m</i> | <i>Lag = 1000 m</i> |
|-------------------------------|--------------------|--------------------|---------------------|
| Kind of model | Spherical | Spherical | Spherical |
| Maximum correlation direction | 112.5°-292.5° | 135°-315° | 135°-315° |
| Nugget effect | 0.3 | 0.35 | 0.5 |
| Sill | 0.9 | 0.9 | 1 |
| Maximum range | 1300 | 1500 | 4000 |
| Minimum range | 300 | 1000 | 1800 |
| Anisotropy ratio | 4.3 | 1.5 | 2.2 |

Table 17 - Parameters of theoretical variogram models, using the 2D approach

The sills are always around the unit, being the data transformed; the maximum and minimum ranges increase with the lag. The nugget effect of J_v is bigger than the nugget effect of the horizontal intercept, this could be related to the fact that while intercept derived from direct measurements, the J_v is calculated from the mean of many measurements carried out on many different sets. Actually, the nugget effect of the variograms is very high and this could be a problem, because the variograms are reliable, only if the nugget effect is below 1/3 of the total sill, and this is not the case. The nugget effect and so the random component is too high, and the variograms are not able to capture and to model the regionalized variable. Using these models in the estimation procedure the results are meaningless, and the validation procedure reveals the lack of agreement between measured and estimated data in the new sampling location (**Figure 37**): high J_v values are estimated as low J_v values, and viceversa.

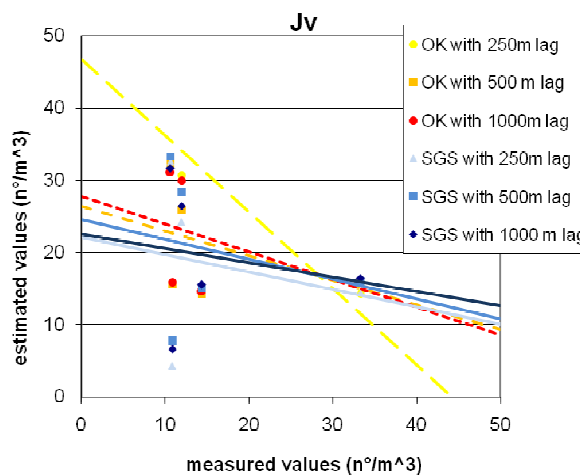


Figure 37 – Validation of the J_v values estimated using the 2D variograms models

Actually, a small improvement can be done by raising the sill of the variogram with the longest lag distance up to 1.2, with a maximum range of 5900 metres (**Figure 38**).

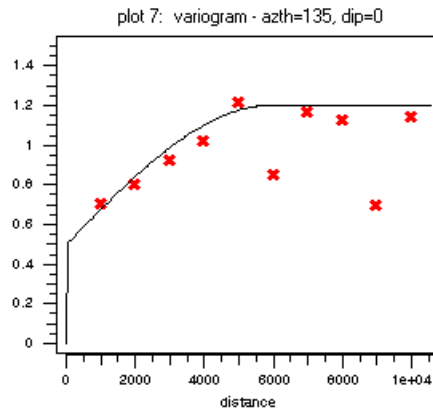
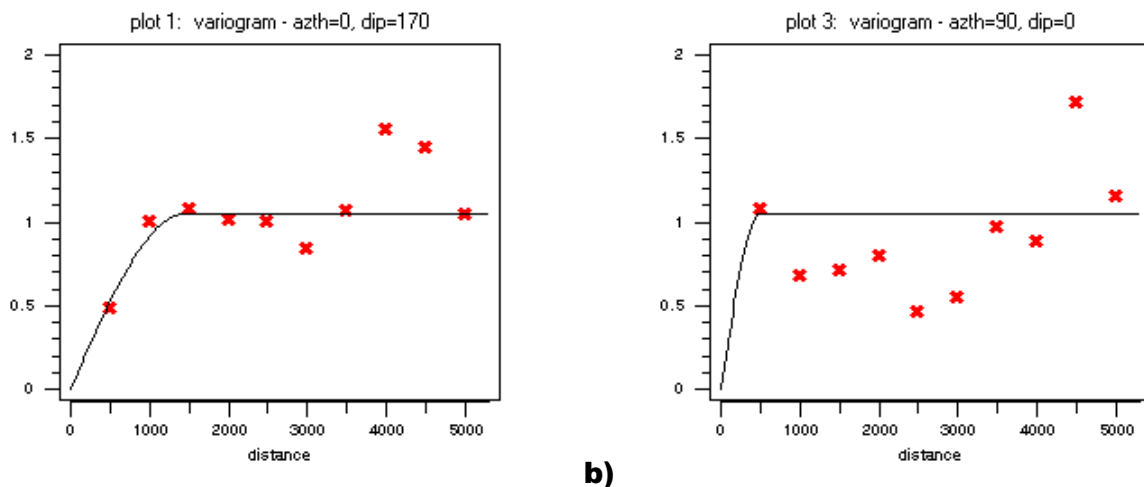


Figure 38 – Experimental and theoretical variogram of Jv transformed data, computed with 1000 metres lag and 2D approach

Considering the almost 3D approach, and the main correlation direction considerably changes: it is now N-S, with a gentle dip angle (equal to 10°), having dip direction towards S (**Figure 39a**). This direction is parallel to the main axis of the Chiavenna valley. Actually, it is well known that the fractures, especially those one at shallow depth, formed following the paleo-topography, in response to changes in palae-stresses, related to the glacial phases. It is therefore reasonable to find this direction for a fracturation index, from a 3D point of view. Actually the main correlation direction found with the 2D approach (SW-NE) does not find an immediate geological response. Maybe also for this reason the resulting nugget effects are so high. In effect the nugget effect of the almost 3D variogram is zero, with a sill of 1.05, a maximum range of 1450 metres, a medium range (in the direction E-W) of 500 metres (**Figure 39b**), although with a weak correlation, and a not determinable minimum range, due to the lack of depth data. However the minimum range has been assumed equal to 100 metres, being the dimension of the grid side.



a)

b)

Figure 39 – Experimental and theoretical variograms of Jv transformed data, computed with medium lag (500 metres lag), using the almost 3D approach, along the maximum correlation direction (a) and the medium correlation direction (b)

The variogram models described above have been employed for the prediction of J_v values, in the areas located among the survey points. Using the parameters of variogram models both the Ordinary Kriging – OK– method and the Sequential Gaussian Simulation –SGS– have been performed. Since the directional variograms of J_v show a strong spatial anisotropy, the measurements inside a research elliptic region (for the 2D approach) or ellipsoidal volume (for the almost 3D approach), with axes parallel to maximum, medium and minimum correlation direction individuated by the variograms, have been considered to perform the estimation process. The lengths of the axes have been obtained doubling the ranges. In the calculation of every point, a minimum of 3 and a maximum of 20 samples have been considered, in order to take in account irregularity of data distribution and nugget effect. The used grid is defined by regular square or cubic cells, for the 2D approach and the almost 3D one, respectively. The grids are west-east and south-north oriented, with each cell having side of 100 meters.

The optimal number of simulations has been chosen comparing the results of 10, 100 and 1000 simulations, through a validation process. The optimal number of simulations resulted again equal to 100 (Figure 40), because it is the best compromise between accuracy of results and computation time.

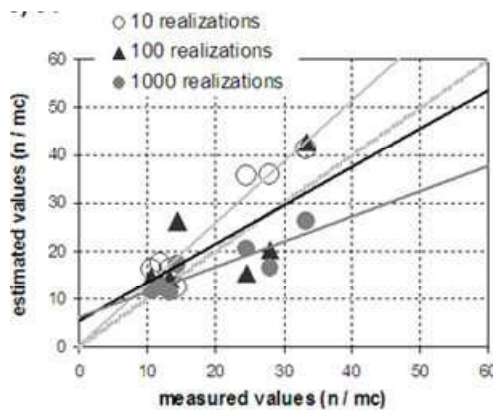


Figure 40 - Relationship between measured and estimated values of J_v , useful to individuate the best simulation number

Final results of OK and SGS (in term of conditional expectation obtained from 100 simulations), obtained applying the 2D approach and using the data of the variogram with lag 1000 meters and sill equal to 1.2 (Figure 38), have been reported (Table 18), in term of expected values and related variance. These maps report all the problems typical of the 2D approach, which have been already described for intercept and RMR, that render these maps not credible. The same considerations, which have been previously done, are still valid. The two methods (OK and SGS) provide quite similar outcomes, even if the smoothing effect occurs only in the OK map. The variance maps show again that the uncertainty is very small near the data samples, and it increases going farther. The variance is always smaller when the OK method is adopted, being the final SGS map derived from many different realizations. However, these maps show meaningless results, as demonstrated in the validation (Figure 37): with a so high nugget effect, although rising up the sill to 1.2, the variograms are not able to correctly capture and reproduce the spatial variability of the J_v : the estimation procedure give values that not match with the values of the new training point dataset.

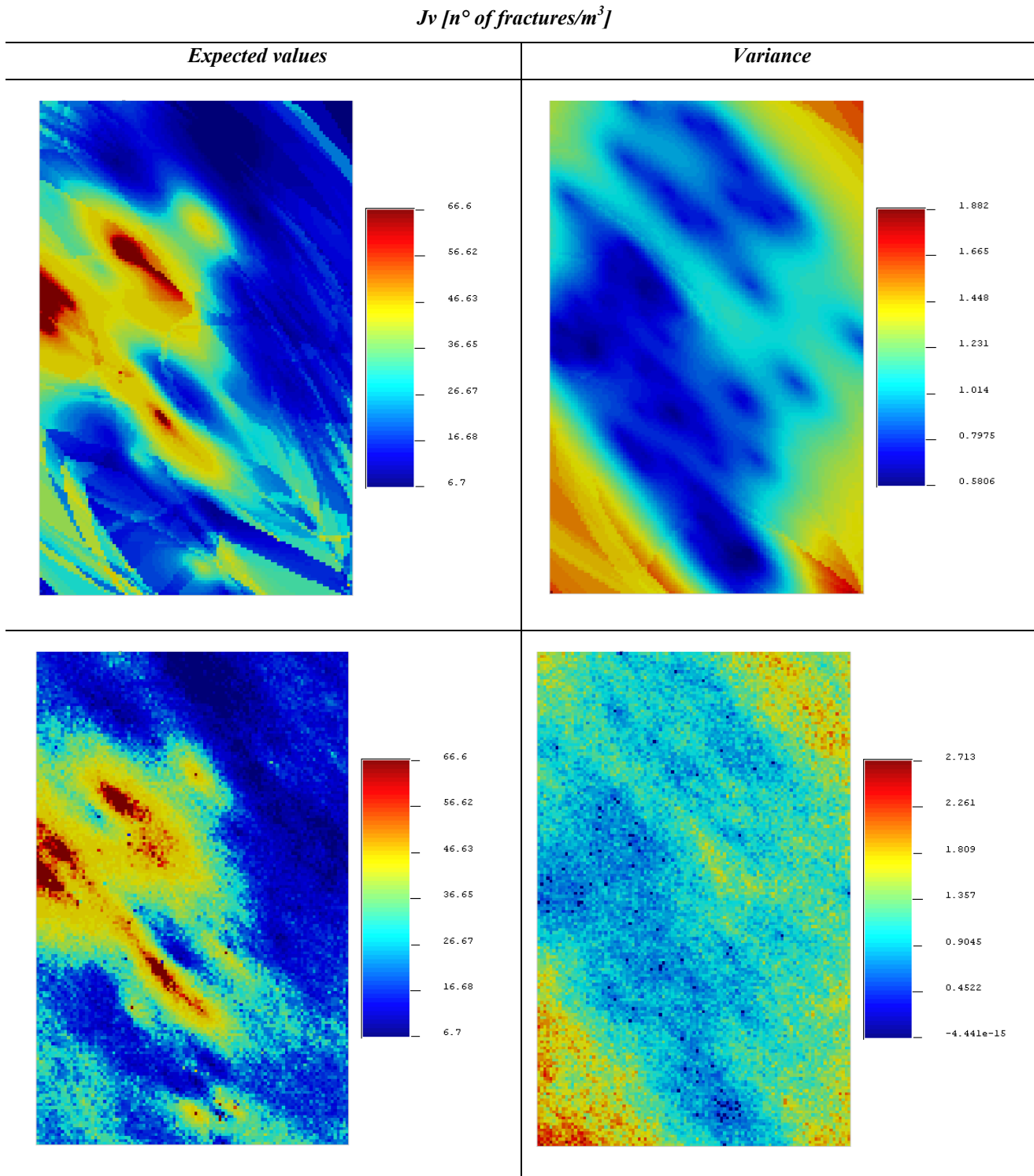


Table 18 - The expected values of J_v , with related variances, estimated using the variogram with 1000 m lag and 2D approach. The first row depicts the result obtained from Ordinary Kriging and the second from 100 Sequential Gaussian Simulations

The problems related to the 2D domain and to so high nugget effect values, are avoided using the almost 3D approach, in which the estimation is performed within a cube and then the values lying on the Digital Elevation Model are extracted (**Figure 41**).

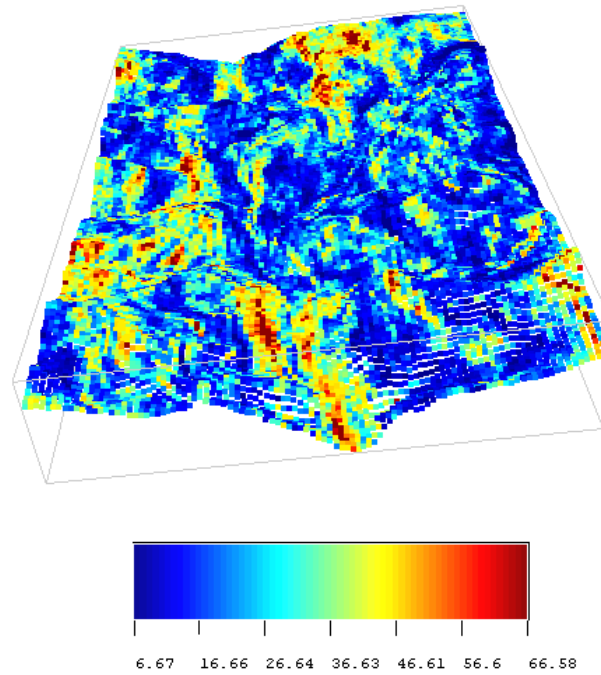


Figure 41 - Determination of the expected values J_v , extracting from the cube of simulation those on the Digital Elevation Model

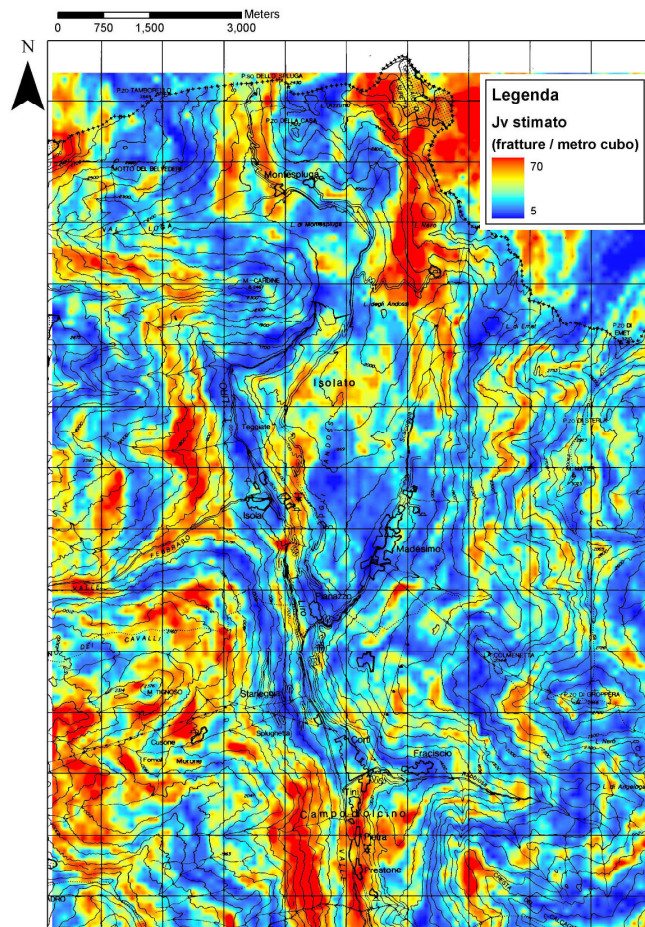


Figure 42 - Map of expected J_v values, obtained by SGS (100 simulations), with the almost 3D approach and 250m lag

The map of expected J_v values (**Figure 42**), obtained by SGS, through 100 simulations, using the almost 3D approach, better represents the geological features of the study area and their relations with the topography. Areas with high elevation, as the Surettahorn (located in the NE corner of the map) where the thermal cycles are frequent, exhibit high J_v values, and therefore are intensively fractured. On the left hydrographical side of the Febbraro valley (located in the middle of the map, towards West), the enlarged zone of rock with high J_v values represents a Deep Seated Gravitational Deformation zone.

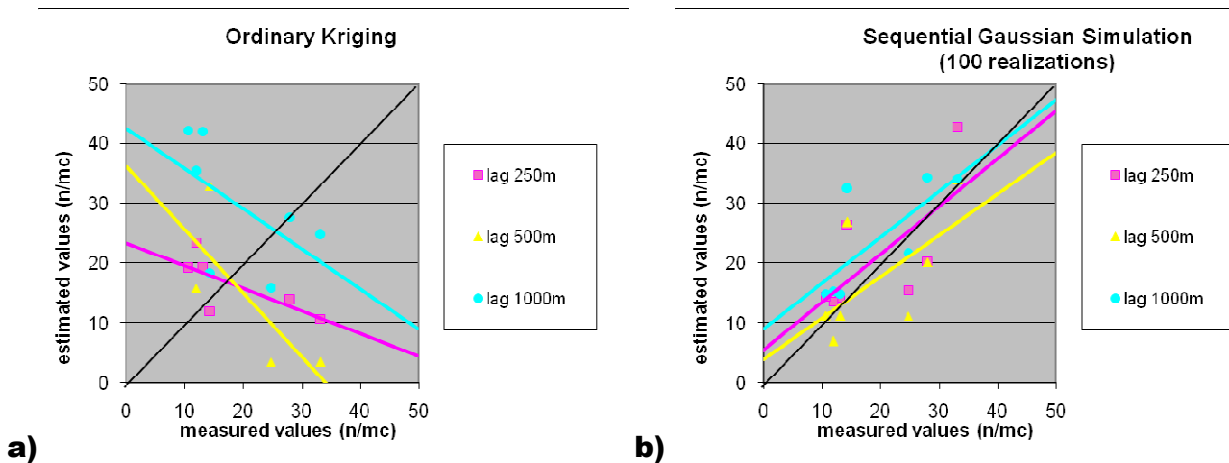


Figure 43 – Comparison between measured J_v values in new sampling locations and estimated J_v values, varying the lag distance and the technique, i.e. Ordinary Kriging (a) and the Sequential Gaussian Simulation (b)

The validation shows that, even if the almost 3D approach is used, the OK technique is not able to predict the values of the Regionalized Variable in a correct way, especially for long lag distances (**Figure 43a**). Significant improvements occur when the SGS technique is performed (**Figure 43b**), with the almost 3D approach. The best results come from the model based on the variogram computed with the shortest lag distance (i.e. 250 metres).

2.4 Conclusions

Procedures and results about the estimation of geomechanical properties in an Italian Alpine valley have been here presented.

Geomechanical characterization has been carried out by surveying rock discontinuities in 97 different sites and by classifying, according to RMR system, the examined rock masses, which exhibit both good qualities and quite similar geometrical and mechanical parameters in each surveyed sites.

Some geostatistical analyses have been carried out to examine the spatial variability of the rock mass quality index called RMR, and the rock mass fracture density, which have been described using two different and independent parameters: the horizontal intercept and the Volumetric Joint Count (J_v), derived from spacing measurements.

The analysis of each individual parameter, which composes the RMR index, suggests that the values are scattered independently from the lithology, this can be due to the fact that all the rock masses are poly-metamorphic and, although having different protoliths, they were subjected to similar geo-structural events. Therefore the rock mass quality is mostly controlled by large-scale brittle strain events; hence in the study area the regional geological structural history seems to have repercussions more important than the individual lithological changes. This peculiarity renders appropriate to consider the analysed properties (horizontal intercept, RMR and Jv) without diving them per lithology. Actually, all these properties depend on the geological and structural history of the rock mass, but they describe the geomechanical features of the rock mass nowadays, resulting from all the involved geological events. They are global properties of the rock masses, depending on all their fractures, despite of their formation mechanism.

Geostatistical implementations have been carried out to examine the spatial variability of horizontal intercept, RMR index and Jv; their spatial structures have been investigated by means of the semivariogram analysis. Some correlations in the space have been determined at different scales, although the general correlation structure remains constant at all scales, considering separately both 2D and almost 3D approaches, which revealed to be fundamental in mountain region. The maximum correlation directions, determined with the almost 3D approach are towards ENE, with a dip angle of 20° for the RMR, and towards South with a dip angle of 10° for the Jv. The maximum correlation directions have a remarkable geological significance: which one of RMR coincides to the orientation of the discontinuity set developed almost parallel to the regional foliation, which is characterized by low spacing values and very high persistence, thus it is reasonable that this set affects the RMR index more than other sets. The maximum correlation direction of the Jv is parallel to the axis of the main valley and so the exfoliation joints, with formed following the paleo-topography.

The modelling of experimental variograms allowed estimating the variables out from survey points, using two different techniques: Ordinary Kriging and Sequential Gaussian Simulation. The validation process, carried out on an independent dataset, reveals a quite good accordance between estimated and measured data, especially performing the SGS on an almost 3D model (which takes into account also the vertical distance between survey locations): in a Alpine valleys the remarkable elevation gradient cannot be neglected during both the variogram modelling and the prediction stage.

With the OK the extreme values are always smoothed, and this could lead to serious drawback especially when zones with minimum or maximum rock quality have to be individuated. Both OK and SGS supplied the best result using short lag distance, which permits to consider also small heterogeneities. The simulation technique seems to be more influenced by differences in lags than the kriging.

In summary, geostatistical methods allow to forecast the distribution of horizontal intercept, RMR and Jv values far away from the points of survey, in a very extent area. In Alpine region the best geostatistical technique seems to be the Sequential Gaussian Simulation founded on an almost 3D variogram whose ani-

sotropy has to find correspondence with the geological features. Simulations should be performed on the 3D domain and always validated with an independent data set. The resultant predictive map should reveal a relation with the regional geological and geomorphological features of the area.

3. GRIMSELPASS CASE STUDY

This new study case has been studied with the help and support of the Professor Simon Loew and the Ph.D. student Martin Ziegler, of the engineering geology group of the Eidgenoessische Technische Hochschule – ETH – of Zürich, where I spend some months during my Ph.D.

The geostatistical approach described in Chapter 2, has been applied also to another Alpine area, located in Switzerland (near to Grimselpass), with the aim to understand if the methodology, which works quite well in Chiavenna Valley, is exportable and applicable in other Alpine contexts. It is necessary to understand if rock mass properties can be estimated far from sampling locations also in other areas.

The applied methodology is based on four main steps:

1. Exploratory Spatial Data Analysis;
2. Semivariogram Analysis: the construction of semivariogram is essential to find the spatial correlation structures required in the prediction step;
3. Prediction: through Ordinary Kriging or Sequential Gaussian Simulation, on a 3D grid;
4. Validation: comparison between measured and estimated values, in new sampling locations.

There are some differences between the two study cases; the main differences are related to the modality of acquisition of data. In Valchiavenna, data have been recorded in situ, directly on outcropping rock masses, through geomechanical surveys carried out investigating approximately the same area of rock mass for each survey (20 metres in length and 2 m in height). In the Grimsel case study, data from the outcrops located on the northern side of Grimselpass have been collected, using indirect techniques, i.e. photogrammetric models of the rock walls, which allow considering also inaccessible and very big outcrops, with variable areas of investigation. In addition, these data have been then integrated with in field data, collected by Martin Ziegler, through classical geological and qualitative superficial surveys. It follows that the data regarding the Grimsel area are quite different from those collected in Valchiavenna, these differences allowed to deep the study, and some new questions arise:

- Can the photogrammetric analysis of inaccessible outcrops be used to predict better rock mass properties?
- Which information can be deduced and which properties can be treated with the photogrammetric approach?
- Which are the advantages and the limits of applying the geostatistical analysis to these data?
- Which are the consequences in the expected scale effect on the distribution map of rock mass properties?

Obviously, by image analysis techniques, only data regarding the geometric properties of rock masses can be collected, while it is not possible to infer any information concerning the conditions of discontinuity, such as roughness, aperture, weathering conditions, infilling, Joint Compressive wall Strength index, and so on. Actually, these properties are essential for the determination of the main quality indices of rock masses according to the main classification systems. Only the detailed direct surveys, carried out in accordance with the ISRM (1978) suggested methods, permit to calculate, for example, the Rock Mass Rating values, as it has been done in the Valchiavenna case study. As consequence, in this second case study the attention has been focused on the information more easily deducible from the image analysis, i.e. on the geometric features of the discontinuity, such as orientation, joint trace length and spacing. Obviously these data are referred to a specific set, and therefore they have approached in a different way from the first case study: in Valchiavenna, the geostatistical approach has been applied considering the geomechanical quality as a result of all the geological events undergone by the rock mass. In the Grimselpass case study, with the aim to take in account also the geological events occurred in the study area, the geostatistical analysis has been carried out considering different kind of joints, with different age and mechanisms of formation and development, separately. Initially, the attention was focused especially on the youngest brittle deformation, i.e. the exfoliation joints, also known as sheeting joints. They are a set of joints developed almost parallel to the surface of the ground, especially in plutonic igneous intrusions such as granite; probably because of the unloading of the rock mass when the cover is eroded away (Palmström, 1995). Afterwards, also the tectonic joints, which are discontinuities formed from the tensile stresses accompanying uplift or lateral stretching, or from the effects of regional tectonic compression (ISRM, 1975), have been considered and analysed.

3.1 Geographical and geological settings

The area of research is located in Switzerland (Uri canton), in the Central Alps, along the upper Hasli valley between Guttannen and Grimsel Pass, which, with the elevation of 2165 m.a.s.l., is a Swiss mountain pass, connecting the valley of the Rhone river in the canton of Valais and the upper valley of the Aar in the canton of Bern. Due to the high altitude of this area, and its continental location, the climate is cold, with a fair amount of precipitation (especially snow). Snow usually falls from late September until late June, and, during this period, the pass is often closed, due to deep snow cover. Also for this logistic reason, data have been collected from photogrammetric models.

Regarding the geological context, the Grimsel region is located in the central part of the Aar Massif (**Figure 44**), which is one of the external crystalline massifs of the Alpine chain (the largest one in Switzerland). The Aar Massif belongs to the Infrahelvetic complex and forms the basement of Helvetic nappes (Choukroune & Gapais, 1983).

The Aar Massif is composed mainly of two large plutons, the Grimsel granodiorite and the Aar granite both of Late Variscan age, which have been intruded into Palaeozoic migmatites and amphibolites (Albrecht, 1994; Schaltegger, 1994). These plutons have been deformed in the Alpine orogeny under greenschist facies metamorphic conditions (Voll, 1976), during NW vergent thrusting developed due to Alpine continent–continent collision (Pfiffner et al., 1990). All deformation structures recognizable in the granite are of Alpine age, indeed, the only regional penetrative foliation, which affects the granite, passes into the overlying Helvetic units. Alpine deformation within the Massif is heterogeneous, producing anastomosing shear zones (usually with mylonitic fabric developed toward their centre) that are irregularly distributed within the less deformed host granitoid (Choukroune and Gapais, 1983).



Figure 44 – Tectonic sketch map of Switzerland, the star depicts the location of Grimsel Pass

Along the Aar Valley, large volumes of granite with no fabric (isotropic) or a weak grain-shape foliated fabric are preserved. The foliation strikes consistently ENE-WSW and dips steeply towards the south. The degree of development of the foliation varies strongly and the granite appears locally rather isotropic and undeformed. Typically, not foliated to weakly foliated zones appear as three-dimensional lens-shaped pods surrounded by foliated material (Figure 45). These lenses are oriented parallel to the regional foliation. Ductile shear zones within the granite are revealed by the occurrence of granite mylonites and ultramylonites, and are marked by local variations of foliation trajectories. Such zones of large strain occur on different scales. They are often found along margins of weakly deformed lenses but also away from lenses,

within the regionally foliated material. The direction and sense of shear depends upon the orientation of the shear zones with respect to the regional foliation (Choukroune & Gapais, 1983).

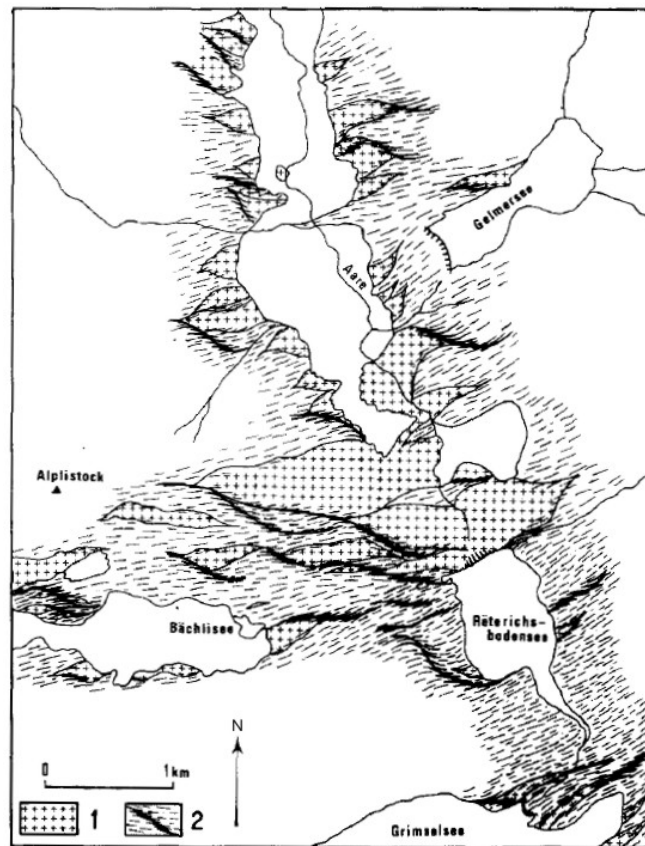


Figure 45 – Map of aspect of foliation trajectories: 1 is an isotropic foliated granite, 2 is the trace of regional foliation and major deformation zones within foliated granite (from Choukroune & Gapais, 1983)

Three major sets of shear zones (**Figure 46**) are developed (Rolland et al., 2009) in the study area.

The first one (Stage 1 shear zones- ShZ_1), the most pervasively developed, is characterized by the foliation associated with the Alpine metamorphic event. It is almost vertical and shows considerable variation in strike, trending most commonly towards ENE. Strain is concentrated mainly in the cores of shear zones, where mylonitic fabrics are developed. The mineral stretching lineation in the mylonites is steeply plunging and the sense of shear alternates between top-to-north and top-to-south. The mineralogy of this stage is biotite – phengite – epidote, which developed at the expense of Hercynian feldspars and biotite.

Shear zones related to the stage 2 (ShZ_2) are more localised and mainly controlled by phengite alignments. They also dip subvertically (80°) and are subparallel, anastomosing structures striking towards 70° , and concentrated in a “belt” a few hundred metres wide, with individual zones corresponding to topographic depressions. The mineral stretching lineation (commonly outlined by elongate phengite grains) is generally sub-horizontal in the central part of the Stage 2 shear zone network, whereas it becomes subvertical toward its southern rim. The shear sense in the dip-slip zones is generally top-to-north. The strike-slip structures have a dextral sense. In the proximity of individual Stage 2 shear zones, and particularly toward the south-

ern part of the belt of Stage 2 shear zones, the Stage 1 foliation and mylonitic shear zones are bent into the 70° strike direction and are rather pervasively phyllonitized. The northern rim of the Stage 2 shear zone network, and locally its southern side near the NE corner of Totesee, is marked by a zone of cataclasis which includes fault breccias (of variable thickness, from 1 to 10 m) with a biotite-rich matrix. This brittle fault zone predates Stage 2 ductile shearing, as is seen from localisation of small-scale ductile shear zones on biotite-rich brittle precursor fractures and breccia matrix on this northern rim, where the overall amount of Stage 2 brittle shearing is relatively small.

The Stage 3 shear zone network (ShZ3) consists of more discrete brittle fracture zones. Both sinistral and dextral brittle faults occur. Dextral brittle faults strike close to that of the Stage 2 mylonitic foliation (70°), with visible offsets, whereas sinistral faults are slightly oblique (120° – 130°), without visible offsets.

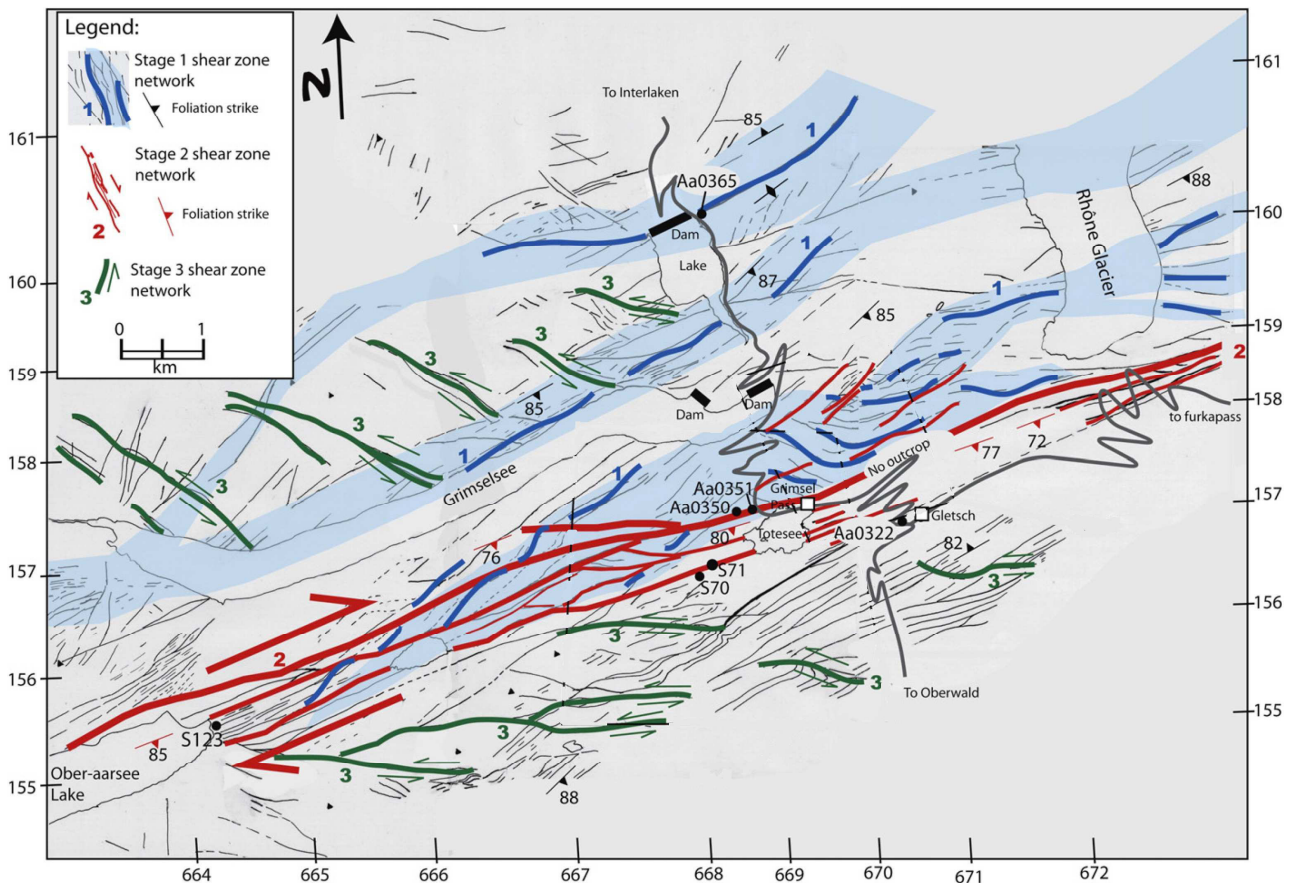


Figure 46 - Shear zone network mapped in the Grimsel pass area. Shear zones have been distinguished in three age groups (Stages 1–3). The thin grey lines are highly foliated shear zones recognised from photo interpretation, many of them belong to Stage 1 (from Rolland et al., 2009, modified).

Regarding the lithology, the northern side of the Grimsel pass is composed of late Variscan intrusive rocks of the Aar massif, characterized mainly by different lithologies (Figure 47), which from the north to the south are:

- the Mittagfluh Granite,

- the Central Aar Granite,
- the Grimsel Granodiorite,
- the Gneiss Schiefer Zwischen-zone (an intermediate zone of schists),
- the southern Aar Granite, also known as the southern stripe of the Central Aar Granite.

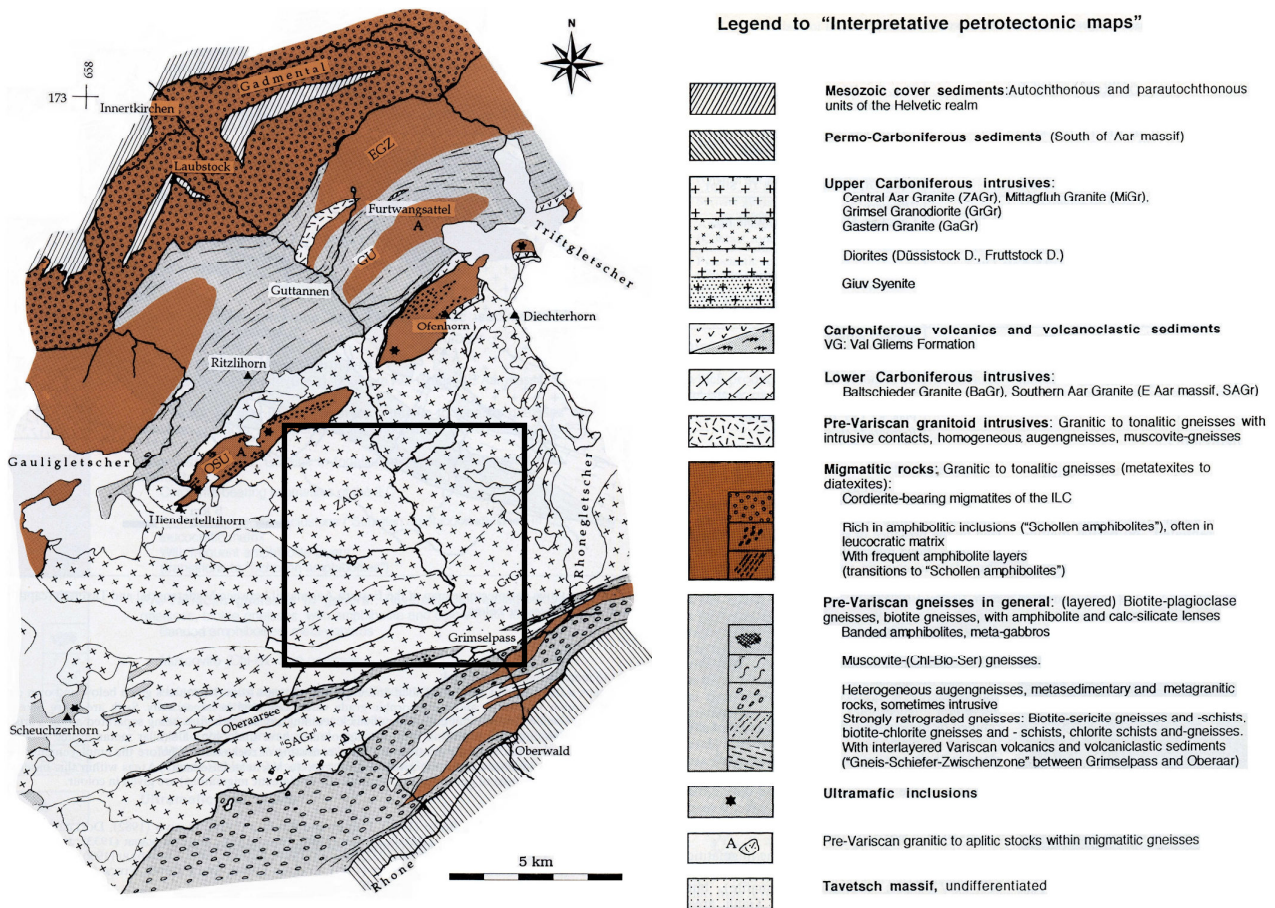


Figure 47 – Geologic map of Grimsel pass zone (from Albrecht, 1994), the rectangle represents the study area

In the study area the main outcropping lithologies are the Grimsel granodiorite (in the south) and Central Aar granite (in the north); the boundary between them is diffuse and often described as a rhythmic 'stratification' without magmatic transition, whereas to its south the Grimsel Granodiorite borders on the metamorphic country rock with a sharp contact.

The Central Aar Granite is a medium-grained, slightly porphyritic, hypidiomorphic and rather homogeneous granite. Its main components are feldspars (white alkali feldspar and green plagioclase), quartz and biotite (around the 5% in volume). The age of the Central Aar Granite is Variscan (297 ± 2 Ma). The Central Aar Granite can present a massive or foliated structure, having a main foliation dip direction towards SE, with an high dip angle (typically around 70°).

The Grimsel Granodiorite, which actually varies in composition from granodioritic to granitic as well as quartz-monzodioritic, is darker than Central Aar Granite, having greater amount of dark mica (about the 10-15% in volume). It also contains larger alkali feldspar augen (often up to 2-3 cm long), greater amount of titanite (of honey yellow color) and smaller amount of quartz than the Central Aar Granite. The Grimsel granodiorite is also richer than the Central Aar granite in aplitic dykes, leucogranitic stocks and lamprophyric dykes (most of them kersantites), which intruded during a late phase of Variscan magmatic activity. The age of the Grimsel granodiorite is 299 ± 2 Ma.

The shear zone networks are developed especially within the Grimsel granodiorite. The Stage 1 shear zones are typically enriched in biotite, without signs of late alteration or tectonic reactivation. The Stage 2 shear zones are mostly rich in phengite aggregates, which develop at the expense of biotite and feldspars. On the microscopic scale, progressive deformation is accompanied by increasing alteration of feldspar porphyroclasts into phengite. Micro-scale observations indicate progressive deformation within a single deformation phase. Neocrystallised phengite is not deformed and no clasts of previously crystallised phengite were found transposed into the main foliation. Secondary chloritisation is common. The Stage 3 shear zones and faults are brittle-ductile. In thin section, the typical observed assemblage is chlorite β -quartz, and no phengite is present (Rolland et al., 2009).

The rock masses are interested by several discontinuities, faults (identified with S) and joints (K), some of them appear in the whole study area (**Figure 48**).

The brittle faults can be classified in six groups, although only two of them are the main systems of brittle faults, recognizable at regional scale. They dip very steeply and striking at about 70° for dextral strike-slip (S0), and 130° for sinistral strike-slip (Rolland et al., 2009), S1. The brittle faults S1 ($138^\circ/75^\circ$), corresponding to the shear zone 3 (ShZ₃), and S3 ($175^\circ/75^\circ$) form the side gullies in the main valley, while S4 ($244^\circ/71^\circ$) is mainly encountered in higher regions, the other two fault orientations S2 ($163^\circ/73^\circ$) and S5 ($220^\circ/74^\circ$) are of less importance within the study site (Sutter, 2008).

In the study area, beyond the exfoliation joints (whose orientations follow the topography), there are three systematic joint sets and some minor joint sets that occur only locally. The two dominant, most widespread and diffuse joint sets are: K1 and K2, having respectively dip direction and dip of $139^\circ/71^\circ$ and $244^\circ/76^\circ$ (Sutter, 2008). The majority of joint sets, in contrast to the exfoliation joints, show a relative constant orientation, quite smooth surfaces, and hydrothermal mineralization; also Alpine extensional veins can be encountered in the study area (Ziegler et al., 2013).

S2 and S3 are the oldest discontinuities and started to form approximately at 20 Ma during ductile deformation with later brittle overprint. During a later phase of brittle deformation (less than 10 Ma) K1 and K2 formed, as well as the fault S1 and S5 (Sutter, 2008). Obviously, the youngest discontinuities are the exfoliation joints.

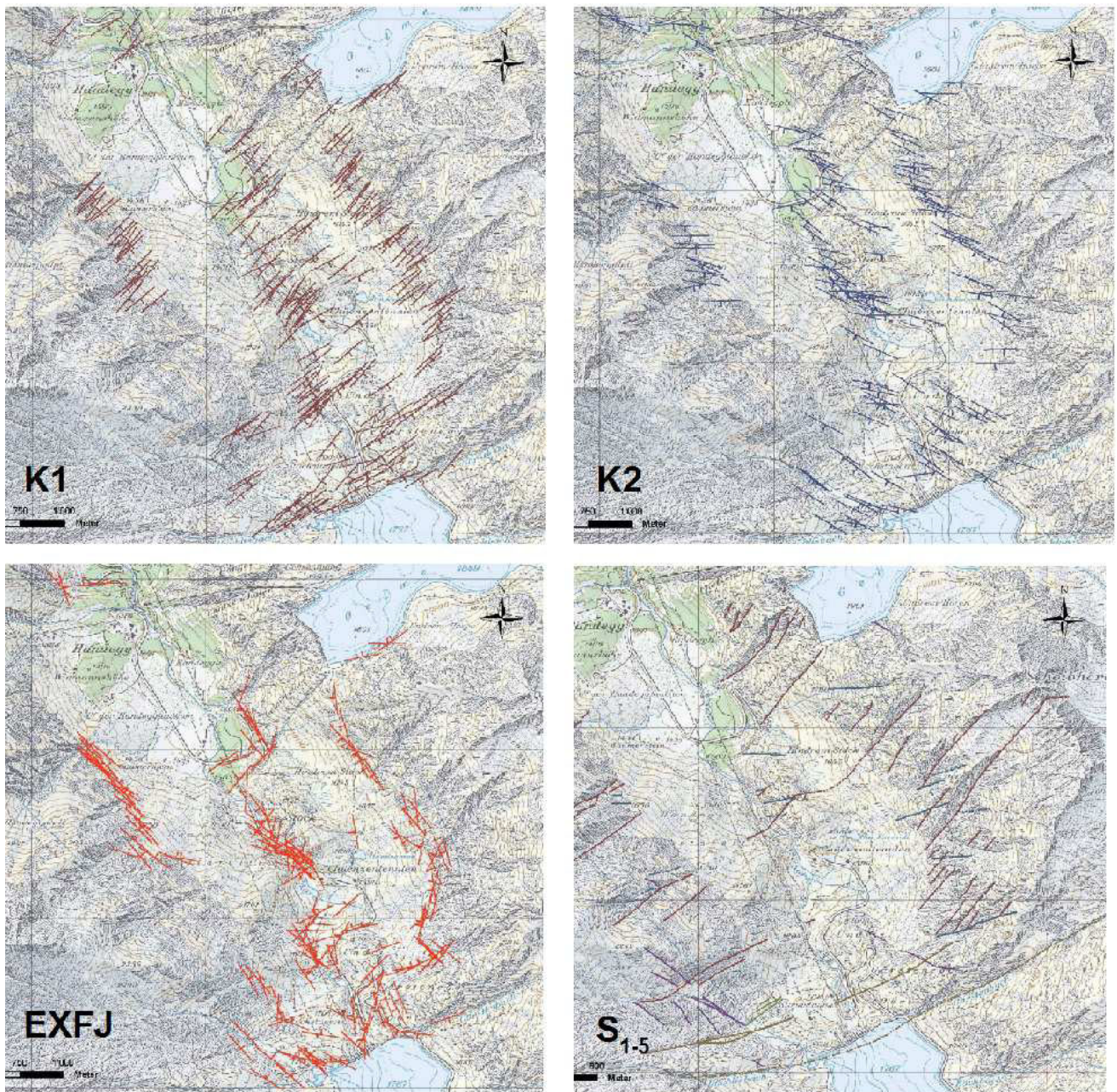


Figure 48 – Main joint sets (K1, K2), exfoliation joints (EXFJ) and faults (S1-S5) of the Grimselpass area (from Sutter, 2008). The orientations of exfoliation joints change according to the topography

3.2 Exfoliation joints

The exfoliation joints, also known as sheeting joints, stress-release joints, post-uplift joints or Talklüfte, have orientations sub-parallel to the actual or a former ground surface, and are typically restricted to shallow subsurface, without affecting the rock mass in depth, but weakening significantly the rock mass near the surface.

Beyond the orientation, which follows the slope of the surface of the time they formed (Dale, 1923), the exfoliation joints have a lot of peculiar features allowing to distinguish them from the other kinds of joints.

Since the exfoliation joints are among the youngest discontinuities developed in the bedrock, they do not depend on primary rock structures in the rock mass and can crosscut any discontinuities zone, such as pre-uplift joints, (older) faults, mafic dykes, aplites or pegmatites, bedding planes, foliation, or magmatic flow layers, at various angles (Brunner & Scheidegger, 1973). Being so young, the surfaces of exfoliation joints are generally free of secondary hydrothermal minerals (Holzhausen, 1989).

The exfoliation joints surfaces can be flat to curved (Johnson, 1970), which decreasing curvatures with depth, and frequently show fractographic features such as plumose structures (Bahat et al., 1999).

The exfoliation joints are restricted to the shallow subsurface with a maximum depth of around 100-200 metres. Increasing the depth the exfoliation joint dip decreases (Jahns, 1943), while the spacing increases (from a few centimetres to metres).

The exfoliation joints exhibit a high lateral persistence, also longer than 100 metres (Carlsson, 1979), and subdivide the rock mass into slabs, with a strong anisotropy. Most commonly, exfoliation joints occur in hard rocks, especially in granitic and other plutonic and volcanic rocks, but they are not only limited to magmatic rocks, actually exfoliation joints have been observed also in massive sandstones (Bradley, 1963), as well as in marbles, limestones and conglomerates. The occurrence of this kind of joints is not restricted to certain latitudes, and they can be found in some different climatic zones, in both glaciated and non-glaciated zones.

Although some literature is available on the exfoliation joints, their precise formation process are not yet completely understood; their formation seems to occur especially with the opening mode (mode I), when the maximum compressive stress (σ_1), oriented sub-parallel to the ground surface, is considerably higher than the least surface-normal principal stress (σ_3), estimable from the overburden thickness (Hast, 1969). These so high stresses near the surface can originate from the elastic rock mass response to erosional or ice unloading, active regional tectonics, and/or topographic changes in areas with high relief.

Regarding the age of formation of exfoliation joints, the differences in orientation between this kind joints and the actual topography, together with variations in the degree of superficial weathering, suggest that exfoliation joints may have formed episodically in many areas eroded by glaciers during the Quaternary (Dale, 1923; Kieslinger, 1958; Glasser, 1997). A change in topography and subsequent stress reorientation may therefore lead to different exfoliation joint generations (Bucher & Loew, 2009).

3.2.1 Features and generations of exfoliation joints near Grimselpass

The study area, having a so high elevation, is not strongly affected by vegetation, and, also for the action of glaciers, it is possible to observe big polish rock surfaces. It follows that outcrops and discontinuities are easily and almost continuously observable in this area.

The accurate field mapping of the exfoliation joints at Grimselpass has been done by Martin Ziegler, who investigated the superficial outcropping features of the exfoliation joints, and tried to recognize them also in depth, inside subsurface tunnels and reconnaissance boreholes.

Martin Ziegler characterized the exfoliation joints, through in situ observations, computer-based mapping (with a laser rangefinder, high-resolution orthophotos and LiDAR-based digital terrain models), in an area of approximately 70 km² (excluding glaciers and lakes). Categorical information on orientations, visible length, spacing, surface weathering, and roughness of exfoliation joints have been integrated into a GIS database (Ziegler et al., 2013).

The exfoliation joints were firstly classified with a geometrical approach, on the basis of the difference between their orientation and that one of the today ground surface, in parallel, nearly parallel or not parallel (i.e. with a difference of more than 10°). This geometric classification does not necessarily reflect different generations of joint sets, because not all landforms have the same age. With the aim to distinguish the relative ages and so the different generations of exfoliation joints, their spatial distribution and characteristics have been analyzed in combination with the corresponding landscape features, assuming that:

- new exfoliation joint sets form within relatively short periods compared to the time required for morphology changes (Bahat et al., 1999);
- at the time of their formation, exfoliation joints were roughly parallel to the overlying landscape surface;
- without subsequent erosion, exfoliation joint spacing increases with depth;
- deep exfoliation joint sets may contain sections of relatively constant joint spacing;
- new crosscutting exfoliation joint sets only form if reactivation of pre-existing faults and joints is not mechanically feasible: after significant rotation of local principal stress orientations and changes in local slope morphology (Sibson, 1985);
- the maximum depth of exfoliation joint formation of a particular set is related to the amount of erosion associated with this set, so the elastic rock mass response to erosional unloading originates the high near-surface differential stress required for the formation of exfoliation joints (Voight, 1966).

Using these assumptions and some observations related to differences in dip angle between slope and exfoliation joint dip, spacing and conditions, Ziegler et al. (2013) have subdivided the exfoliation joints of Grimselpass area in four distinct exfoliation joint generations, each one of them is related to a corresponding paleo-landscape morphology (**Figure 49**) and present distinct features (**Figure 50**).

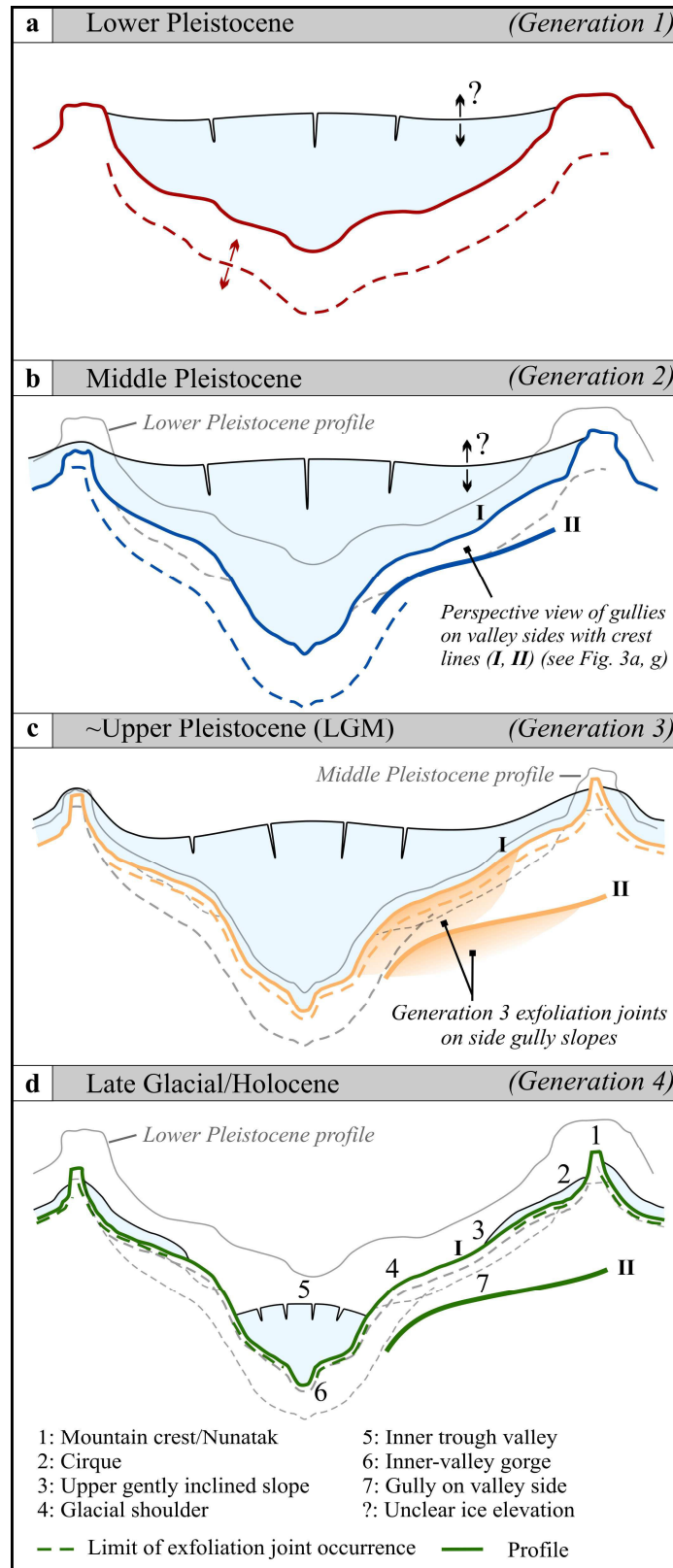


Figure 49 – Evolution of cross-sections from the lower Pleistocene to the Late Glacial/Holocene, together with associated, mapped exfoliation joint generations (from Ziegler et al., 2013)

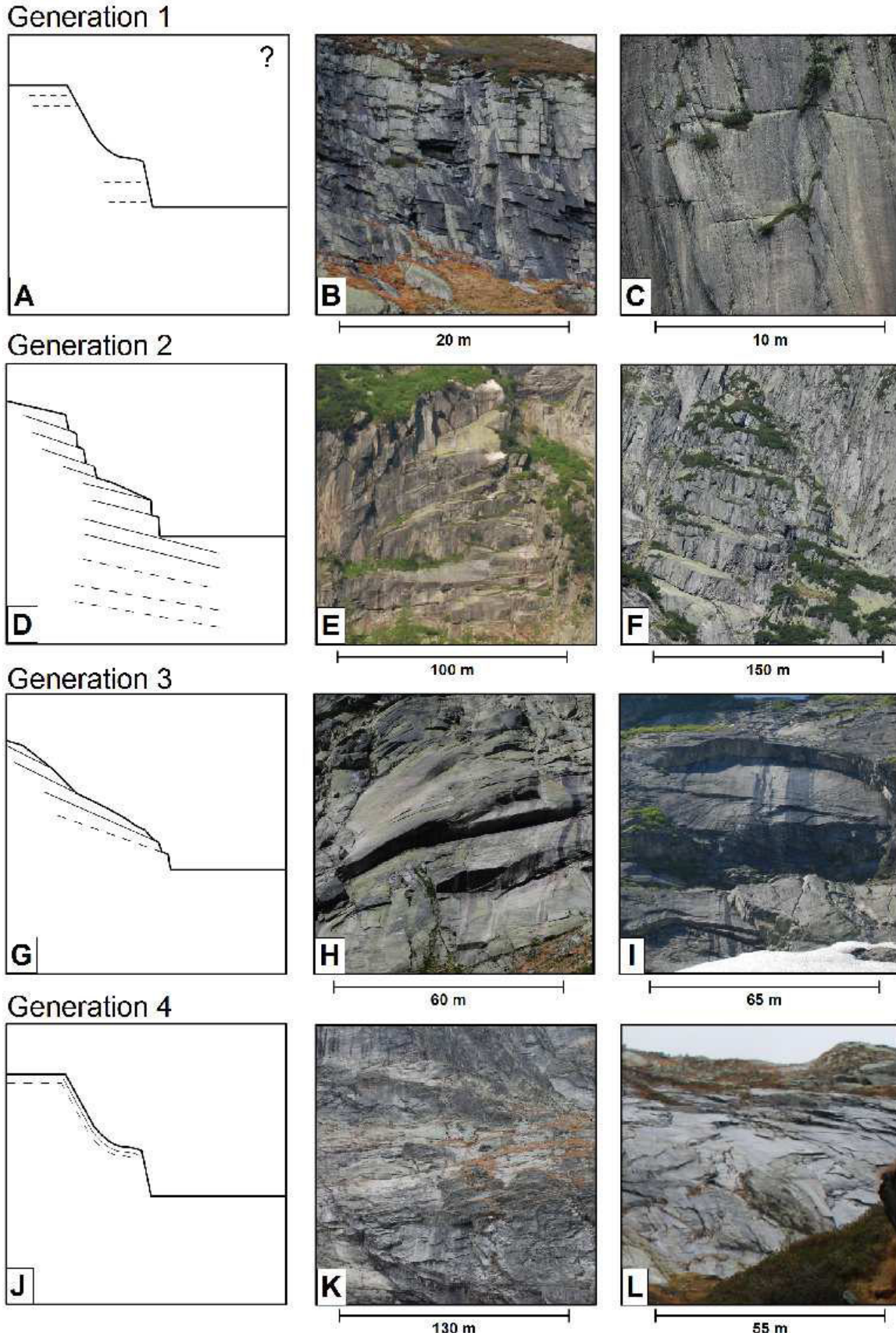


Figure 50 – Sketch of exfoliation joint generations individuated in the Grimsel area (from Bolay, 2013). The flat joints of generation 1 (A-C) are observed on steep slopes. The generation 2 shows a clear difference between the set dip and the slope and together with cross joints forms steps in the slope (D-F). Generation 3 (G-I) follows closer the slope, with higher joint dip. The generation 4 is almost perfectly parallel to today's topography and shows high curvature and small spacings (J-L)

The generation 1 is the oldest and least common generation of exfoliation joints encountered in the study area. Its age has been estimated to go back at the Lower Pleistocene (during early stage of trough valley erosion and prior). These exfoliation joints, occurring within the main and hanging trough valleys, are visible only on few nearly vertical rock walls. These exfoliation joints are significantly less inclined than the valley slope: they exhibit a remarkable difference (bigger than 30°) between the dip angle of the slope and that one of the exfoliation joints, hence only little influence of topography on the exfoliation joint orientation is observed. Due to the low exposure of the joint set it cannot be assured that these joints are exfoliation joints or if they belong to a flat joint set that is not caused by exfoliation. However, the joint traces of this generation are thin, with very small aperture. The surfaces are moderately weathered, widely spaced (with spacings of decametric orders), and nearly planar with small curvature. The exfoliation joints of this generation are frequently accompanied by other joints with one set perpendicular to the exfoliation joints, occasionally crosscutting the exfoliation joints. The joints of this generation have been encountered until a maximum depth between 50 and 100 metres.

The estimated age of this generation 1 depends on the assumed average erosion rate (0.1 mm/y), and the hypothetical maximum thickness of the Pliocene exfoliated rock mass of about 250 m. The formation of this generation was related to the change in valley morphology associated with intense glacial erosion.

The generation 2 is younger than the generation 1 and older than the generation 3. The formation of the second generation goes back to the U-shaped through valley formation, happened during the Middle Pleistocene. The generation 2 is the most prominent in the study area and is concentrated along the main valley flanks: the exfoliation joints of this generation are very abundant in the U-shaped main valley and can sometimes be found at gently inclined higher slopes. Structural data from subsurface galleries, boreholes, and the ground surface within the inner trough valley shows that exfoliation joints of this generation curve continuously from one valley side to the other, i.e., they dip steeply on slopes and are sub-horizontal at the valley bottom (Ziegler et al., 2013). However, the exfoliation joints of this generation can be followed not only in valley troughs, but also in places from the troughs onto linear, gently inclined upper slopes. The exfoliation joints of generation 2 show a difference in dip angle with the slope of about 20° , and are often very persistent, coinciding with the local orientation of valley; they have a very wide joint spacing (from metric to decametric order), greater than the other generations. The exfoliation joints of generation 2 are slightly weatehered, being mostly free from secondary minerals. The surfaces of this generation show only little curvature and fractographic features. The exfoliation joints of generation 2 can reach great depth (up to 260 m). They formed because of the erosion of the inner trough valley, happened considerably earlier than the last glacial period: the exfoliation joints of generation 2 at Grimsel Pass cut across roche moutonnées of the Last Glacial Maximum –LGM–, not following the more recent erosional surface. Therefore, this generation of exfoliation joints should be older than the LGM.

The generation 3 of exfoliation joints at Grimselpass goes back to the Upper Pleistocene (LGM). The exfoliation joints of this generation have orientations, which mimics younger new morphological features such as fluvial gullies and inner-valley gorges, formed after the incision of the trough valley. These features have a smaller scale than the inner trough valleys and can lead to greater joint set curvature. The angular difference between the dip angle of the slope and that one of the exfoliation joints of this generation is smaller than 5° . The exfoliation joints of generation 3 are characterized by less weathered joint surfaces (fresh to slightly weathered) and are more closely spaced (up to a few metres) at the ground surface, in comparison with exfoliation joints of generation 2 joints. From this generation is not possible to deduct clear information about the maximum depth of propagation of this generation. In areas that have not been significantly altered by erosion, where topographic curvature has not changed decisively, joints of generation 3 and 2 can have similar orientations, rendering difficult to distinguish them: at locations where joint set spacing and weathering of generation 2 and 3 are similar, it is difficult to differentiate them. About the age, it is likely that the trimlines below many mountain crests at Grimsel formed during the Last Glacial cycle (Würmian) and roche moutonnées are of LGM age, as well as the generation 3 (Ziegler et al., 2013).

The generation 4 is the youngest generation encountered in the Grimselpass area, which presumably formed after the LGM, during the Late Glacial or Holocene period. Generation 4 has been found only at very high elevations, close to mountain ridges, and so in few locations, almost exclusively located within the extent of Late Glacial ice. The exfoliation joints of this generation are characterized by a distinct parallelism to the present-day topography, they follow the local slope geometry very closely. The exfoliation joints belonging generation 4 show really close spacing (always below 1 metre) and macroscopically unweathered (fresh) joint surfaces, which are curved even on small scale. This generation of joints affects the rock masses only until very shallow depths, actually this set has been observed only near the surface and never in depths greater than a few metres. Due to these peculiar characteristics, it seems probable that the formation of this generation is not controlled by erosion-induced stress changes, but by the action of chemical or physical forces, such as differential expansion and contracting during heating and cooling over the daily temperature range, related at these altitudes to freeze-thaw cycles.

Summarizing, the topography changes during the geological periods and therefore a difference between the slope angle and the dip angle of an exfoliation joint set can develop. In general, younger an exfoliation joint set is, higher the conformity to the recent topography will be. Besides other criteria, such as degree of joint surface weathering (if a joint shows significantly more weathering it is likely to be older) the difference in dip angles is a good indicator of relative exfoliation joint generation age: a greater dip angle difference indicates an older exfoliation joint generation (Ziegler et al., 2013).

3.3 Photogrammetric models of outcropping rock masses at Grimsel

A photogrammetric model (**Figure 51**) is a three dimensional images of the rock mass which allows to measure its geometric properties. Along the upper Hasli valley 42 photogrammetric models have been re-

alized by the Master student of ETH Stephan Bolay (Bolay, 2013), assembling some photos and adding reference points.



Figure 51 –Example of photogrammetric model

The creation of each model requires two images taken from slightly different positions of the same scene; these photos can be used to construct a 3D image and digital terrain model. While in the normal visual perception two images are recorded by the left and the right eye, in photogrammetry two parallel pictures are taken with the same calibrated camera (in this case the Nikon D89 with 18-70 mm zoom lens was used). The differences in the stereo pair of images allow reconstructing a 3D image of the overlapping area. The photos have been taken on a baseline as parallel as possible, i.e. at the same distance and angle to the target slope, using several focal lengths in order to allow for detailed models of the rock slope. The distance along the baseline between the pictures has varied from 1/8 to 1/5 of the distance to the image target.

Since the rock masses are inaccessible, it has not been possible to place any target point on the rock walls (and so on the photos) to georeference them. Therefore, the georeferencing process has been done using reference control points (i.e. points with known coordinates) derived from a Laser range finder (Vectronix Vector IV) connected to a GPS station (Leica Zeno 15). Ten non-collinear reference points were used per each model for the process of referencing, although only three are normally required. A so high number of reference points was used in order to account for potential wrong points and therefore to improve the accuracy of model. The georeferencing of the 3D model is a very important step, because enables to measure orientations and distances of geologic structures, such as fractures and exfoliation joints. The software 3GSM ShapeMetrix^{3D} (3G Software & Measurement, 2007) has been used to construct photogrammetric models and to measure the rock mass features.

In this way, 42 models of rock masses have been realized, allowing investigating not accessible, but visible, outcrops, to measure some geometrical properties of joint sets and to check if the hypothesis about the main features of different exfoliation joint generations is honoured also out from accessible locations.

Each model have been analysed, and those one with errors in georeferencing or scaling have been individuated and corrected. Using the photogrammetric approach, the geometric properties of the rock mass discontinuities have been measured; hence, for each model, using the software 3GSM ShapeMetrix^{3D}, the following data have been collected:

- orientations;
- trace lengths;
- kind of terminations;
- length of rock bridges;
- sinuosity index;
- spacing.

In order to include the geological history of the rock masses in the geostatistical approach, distinguishing the occurred deformative phases, in this case study, the exfoliation joints (i.e. the youngest phase), and tectonic joints have been considered separately. The collected data have been afterwards used in the geostatistical analysis, with the aim to furnish their regional distribution map, and understand if the method works well, not only using data of classical geomechanical survey (as it has been demonstrated for the Valchiavenna case study), but also using indirect survey techniques, such as the photo-analysis. Obviously the location of the 42 models are not placed according to a regular sampling grid, and their positions are strongly dependent on the location of outcrops (as for the Valchiavenna case study), but not on their accessibility. The photogrammetric models are unevenly scattered, but mainly located along the sides of an Alpine valley (**Figure 52**), with about aligned disposition, especially along the Eastern slope. This sampling schema could have great influence on the semivariogram results and complicate the detection of the real main correlation direction.

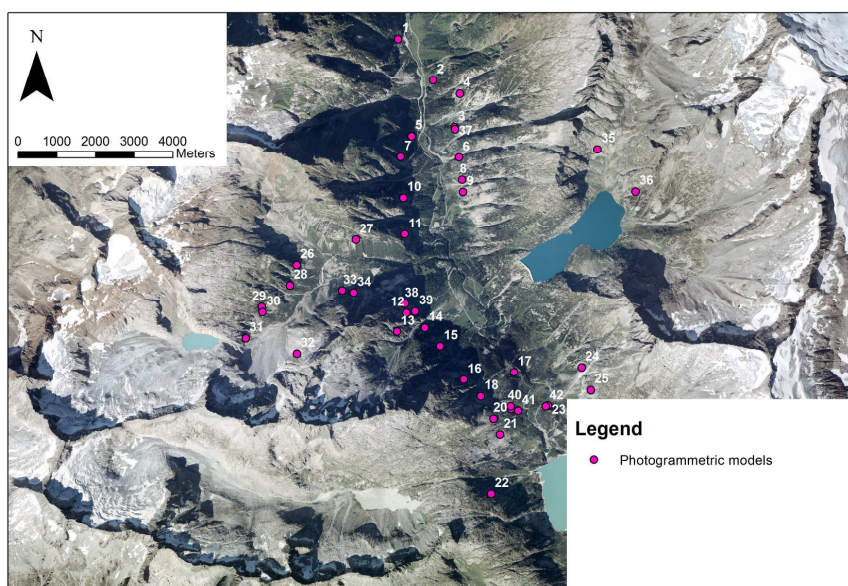


Figure 52 – Location of the photogrammetric models along the Hasli valley

3.4 Data collection of geometric features of exfoliation joints

Since the in-field observations show remarkable differences among generations of exfoliation joints, the dominant generation of joints has been attributed at each model (**Figure 53**). In case of models showing the presence of more than one generation of exfoliation joints, only the prevalent has been considered and measured. 5 models belong to the first (and oldest) generation of exfoliation joints (**Figure 54**), 24 to the second (**Figure 55**) and 13 to the third (**Figure 56**). The fourth generation of exfoliation joints (**Figure 57**), which is the youngest, has not been considered, because of its intrinsic features. Indeed this generation is characterized by a scale, but also a formation mechanism, completely different from the other generations. First, the spacing values are very small, and the resolution of the photogrammetric models is not good enough to measure accurately so small spacing values, in the best case, the errors have almost the same order of the measurements, implying a big uncertainty. Moreover, the discontinuities belonging to this set should affect the rock masses only very close to the ground surface, being mainly related to thermal variations; they are never encountered in depth and so they have very localized features, hardly treatable as regionalized variables. Furthermore the joints of this generation are strictly parallel to the today surface and so are often not observable, additionally their presence is almost exclusively located within the extent of Late Glacial ice (Ziegler et al., 2013), occurring typically at very high elevation. It follows that they are visible only on very scattered locations, so, with only few widespread sampling points, the geostatistics cannot give good results. For all these reasons, no models of the last generation of exfoliation joints have been analyzed.

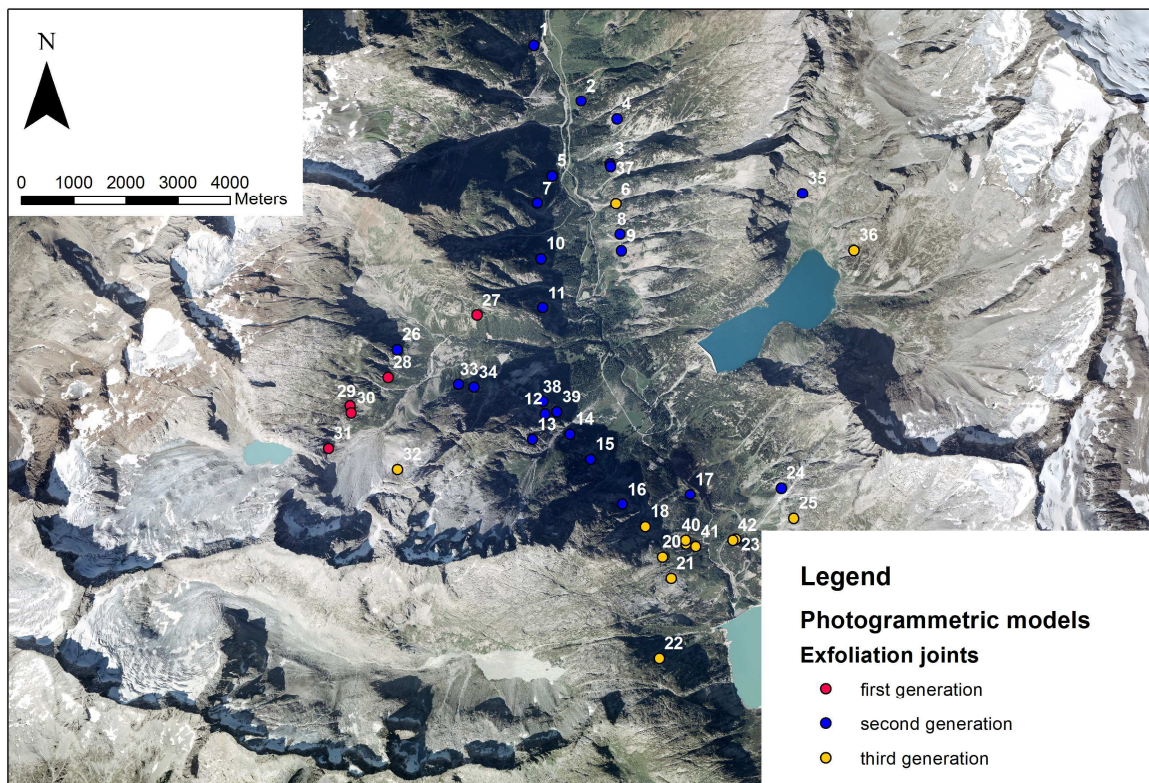


Figure 53 – Photogrammetric models subdivided according to the generation of exfoliation joints



Figure 54 – Example of photogrammetric model with exfoliation joints belonging to generation 1 (model n°28)



Figure 55 – Example of photogrammetric model with exfoliation joints of generation 2 (model n°9)

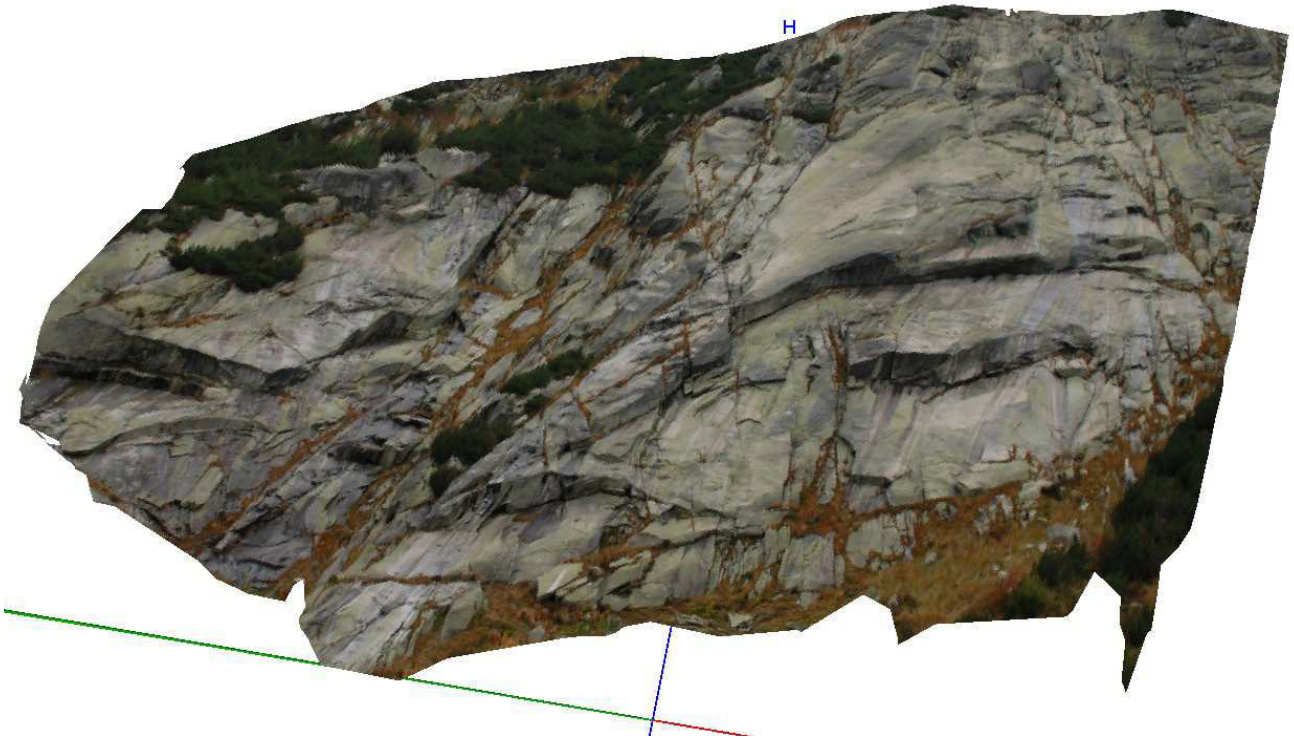


Figure 56 – Example of photogrammetric model with exfoliation joints belonging to the generation 3 (model n°18)



Figure 57 - Example of exfoliation joints of generation 4 (photo from Stephan Bolay)

The exfoliation joints data have been collected, when possible, both along strike and dip direction, separately (**Figures 58 and 59**). Generally, exfoliation joints are easier observable and measurable along the strike than the dip direction; indeed the trace of the exfoliation joints along the dip direction is clearly visible only in rock masses having incision or similar morphological features. Moreover, the traces of exfoliation joints along the dip direction are often superimposed to other tectonic joint sets, complicating their distinction. Furthermore, it has been easier to measure the geometric properties of rock masses affected by younger generations of exfoliation joints; the data collection has become more and more difficult increasing the ages of the joints (and so decreasing the generation). Actually, the oldest generation has an orientation that differs a lot from the actual topography, rendering the traces of the exfoliation joints not entirely visible, especially along their dip direction. In other words, the features of exfoliation joints belonging to the generation 3 (**Figure 60**), the youngest considered, are more clearly visible, recognizable and so measurable than the generations 2 (**Figure 61**) and 1 (**Figure 62**), respectively.

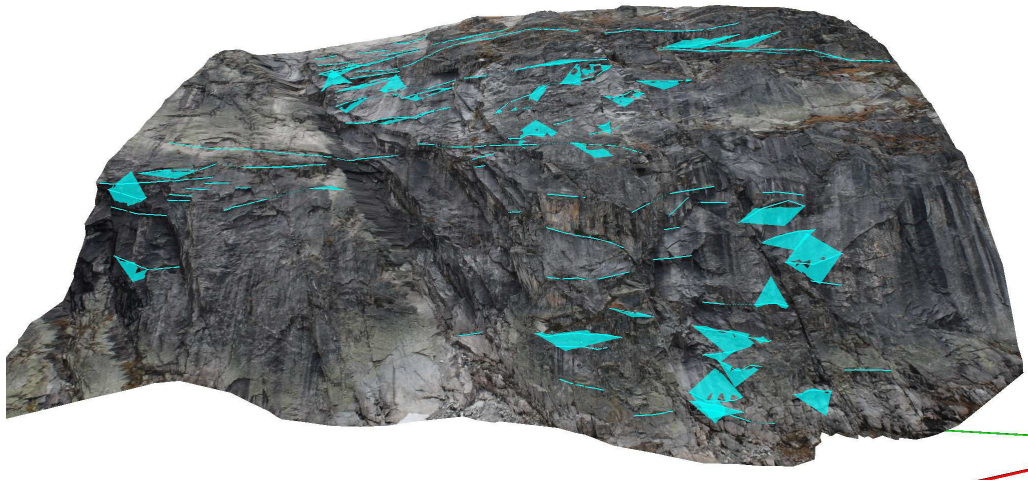


Figure 58 - Data collected along the strike of exfoliation joints of generation 3 (model n°32)

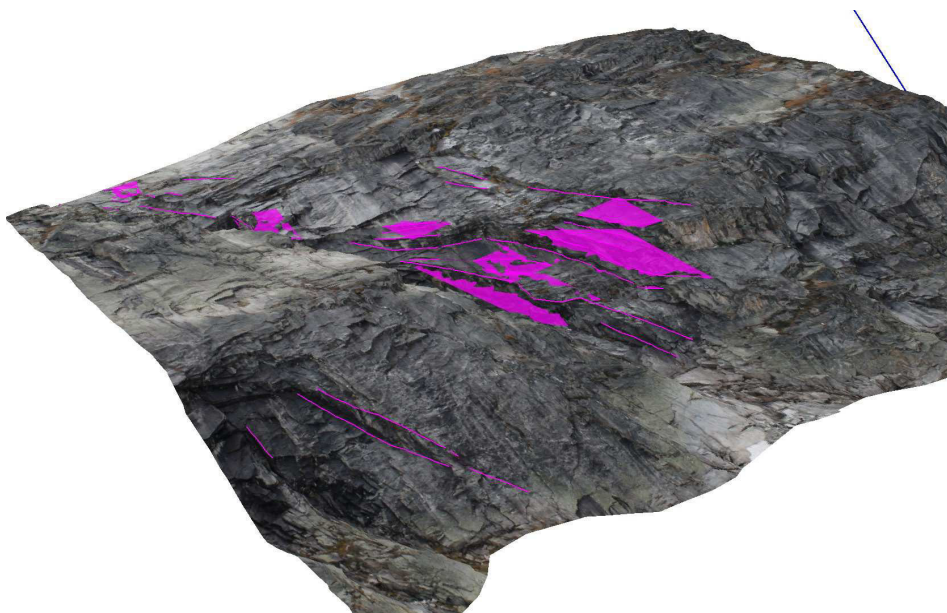


Figure 59 - Data collected along the dip direction of exfoliation joints of generation 3 (model n°32)

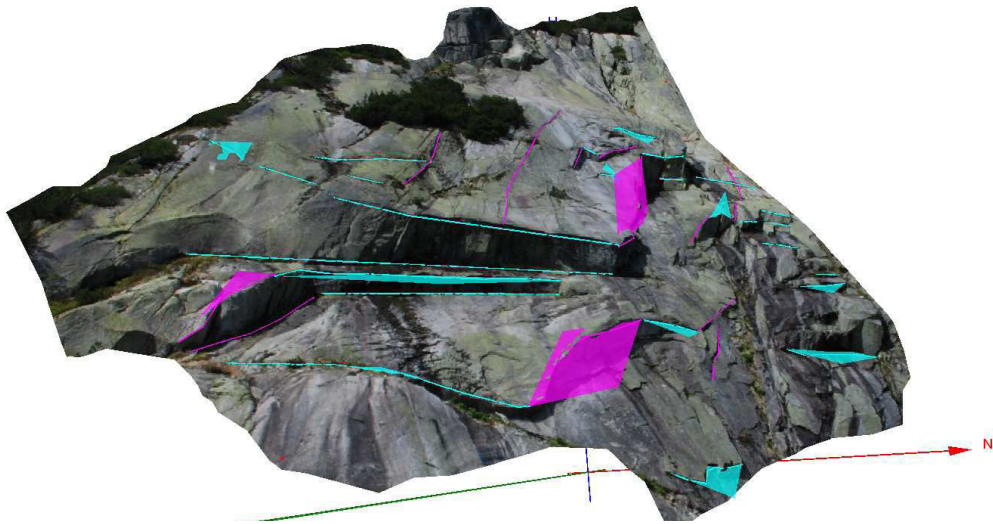


Figure 60 - Data collected along strike (in light blue) and dip direction (in pink) of exfoliation joints of generation 3 (model n°41)

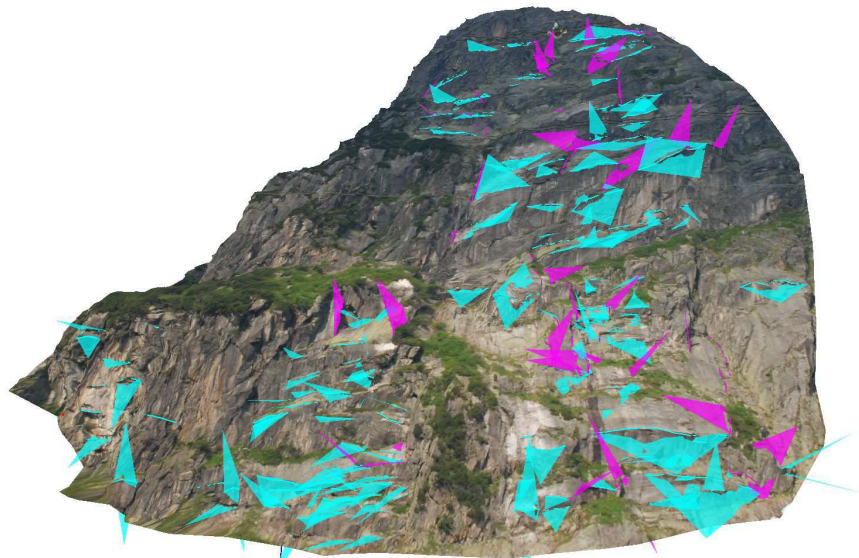


Figure 61 - Data collected along strike and dip direction of exfoliation joints belonging to the generation 2 (model n°12)

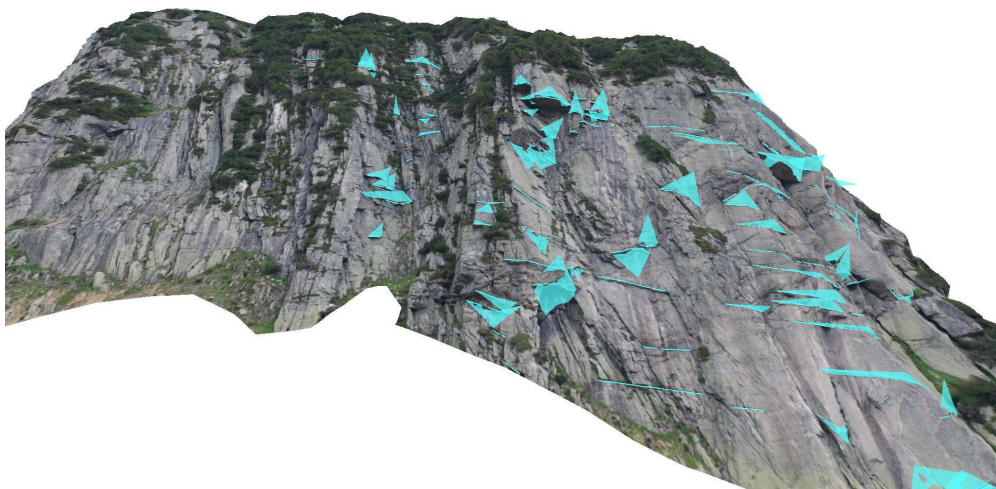


Figure 62 - Data collected along strike of exfoliation joints belonging to the generation 1, in this model (n°27) the trace of exfoliation joints along the dip direction is not clearly visible

3.4.1 Orientations

There are various ways to measure the orientation using the photogrammetric approach. Actually, the orientation of a plane can be inferred surrounding the plane itself (with areal approach) or starting from the traces of joints. The aerial approach is the most accurate, because the second one calculates orientation from lines and not from areas. Actually, the delimitation of a plane leads to more accurate measures of the orientation than a line with a fitted plane. Nevertheless, considering the huge number of discontinuities that will be considered in the present study, the second approach has been adopted. Of course the measurements of orientations have been performed only with trace length having a sufficient variation in depth (a sufficient exposure) to be fitted by a plane (using the least squares method), whose orientation (in term of dip direction and dip angle) has been measured. If the size of the plane gets significantly small, the orientation measurement can get uncertain. However, the results obtained using this approach has been compared with those ones collected by Stephan Bolay, a master student of the ETH, who used the areal approach. Actually the measures are comparable, because the error done using the joint trace approach is minimized by the considerable number of collected data, which lead the mean values inside the region obtained with the areal approach (some example are reported in **Table 19**).

All the orientations measured on each photogrammetric model, have been reported into a stereographic plot, using the Lambert projection, which is an equal area projection that allows extrapolating the mean values of orientations, and comparing the result of measurements along dip direction (reported in pink colour) with those along strike (in light blue colour).

Analysing the obtained stereographic plots, it is possible to note that a bigger dispersion occurs along the dip direction (whose orientations are reported in pink colour) than along the strike (in light blue colour), which shows a distribution of poles more concentrated. Actually, the traces of exfoliation joints along the dip direction are more difficult to find and follow, especially for the oldest generation. In addition, the joint traces along the dip direction often can be confused with those of other sets of joints (not related to exfoliation). The analysis of stereographic plots allows observing an increasing of the dispersion of poles with the age of the exfoliation joints, but it could be related to the fact that the older generations have a different orientation from to the today topography, leading to only thin joint traces and not planes visible.

The measures of orientations have been carried out especially to verify if the investigated trace lengths, along the strike and dip direction, belong to the same plane and so to the surfaces of exfoliation joints. Actually, event if it is very easy to recognize the exfoliation joints in younger generations, for older ones it can be difficult, especially along the dip direction, because old exfoliation joints often are not well visible, with limited exposures of their surfaces. Indeed, while in the in situ survey the kind of joint can be determined also considering small-scale features (such as the presence of secondary hydrothermal minerals, etc.), using the photogrammetry the determination of the parallelism between the joints and the topography is the easiest and most suitable approach to establish the kind of a joint. Regarding the subdivision into generations,

the dip angle difference is a good indicator of the generation, but it is not sufficient on its own, also other parameters, such as spacing and curvature, have to be considered.

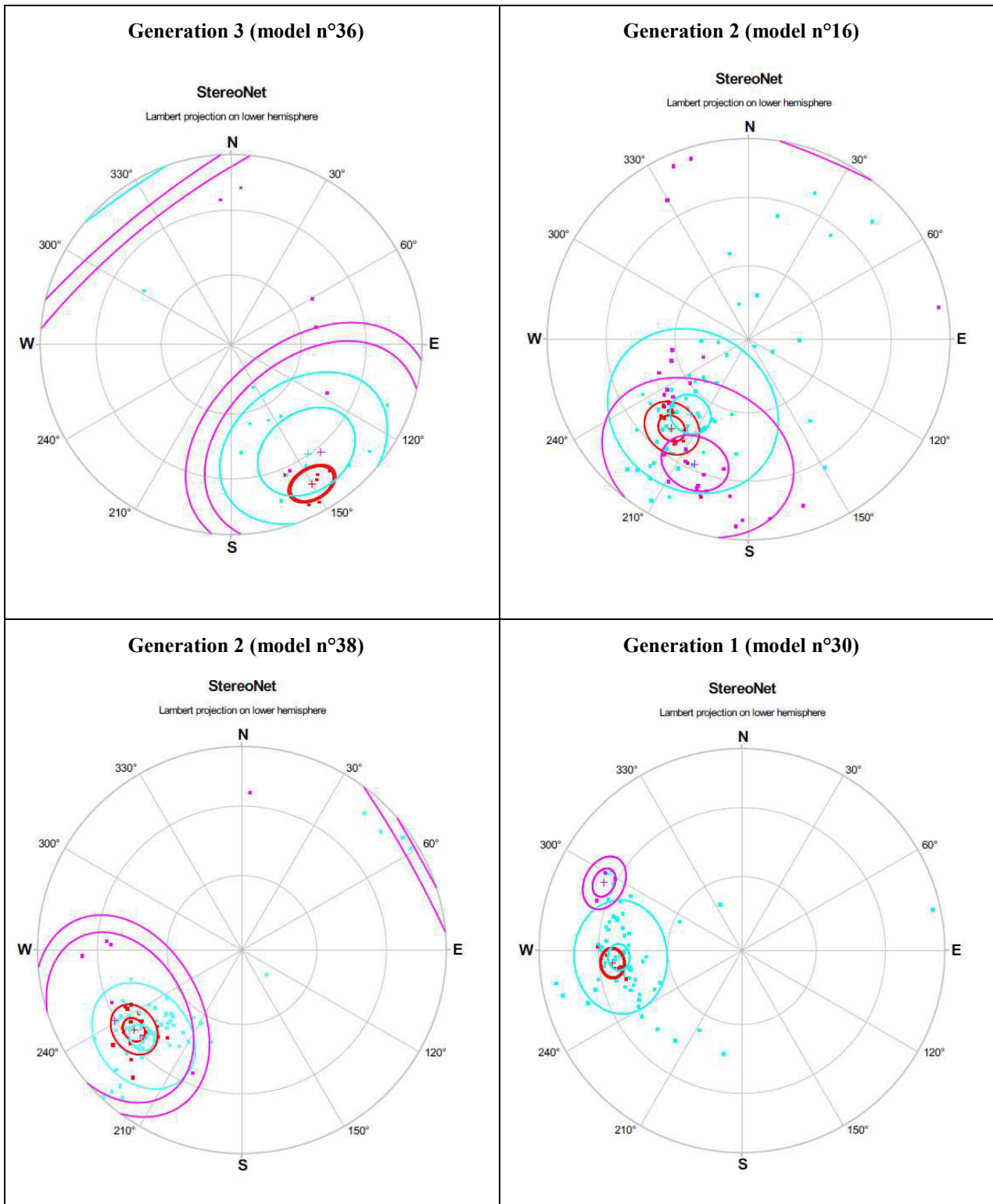


Table 19 - Poles of exfoliation joints on stereographic Lambert projection relative to some different models. Data have been collected collected along the strike (depicted in light blue) and dip direction (in pink), from the joint traces. The red poles have been measured by Stephan Bolay delimiting the exfoliation surfaces

3.4.2 Trace lengths and terminations

Trace length is typically measured as the linear distance between the end points of the intersection of a joint with an exposed surface. If both ends of a trace are not observable, the length recorded is a censored length (Baecher, 1983). The measure of joint trace lengths on the surface exposures is very important because it allows to crudely quantify the persistence (ISRM, 1978), which implies the size or areal extent within a joint plane. Frequently rock exposures are small compared to the area or length of persistent joints, and the real persistence can only be guessed. Persistence is an important rock mass parameter, but one of the most difficult to quantify in anything but crude terms. Joint continuity or persistence can be distinguished by the terms persistent, sub-persistent and non-persistent (ISRM, 1978), or more simply as continuous and discontinuous. Less frequently, it may be possible to record dip length and the strike length of exposed joints (**Figure 63**) and thereby estimate their persistence.

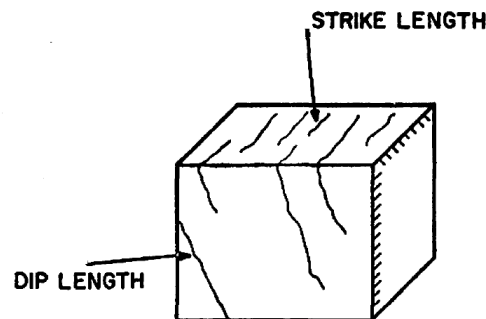


Figure 63 – Example of trace lengths measured along both strike and dip direction (from Baecher, 1983)

The use of photogrammetric models allows measuring the joint trace lengths more easily than in field, due both to the possibility to collect data also in the inaccessible portion of the outcrop, and to the advantages (especially in term of time, costs and independence on the weather) related to the use of image analysis techniques. Therefore, the trace lengths of exfoliation joints have been measured, tracing out the visible trace of each exfoliation joint, along its strike and, when possible, dip direction too. Joint trace lengths have been measured along the surface of exfoliation joints, following them and so considering also their roughness. Of course, the number of collected trace lengths, especially along the strike, has resulted to be influenced by the areas of photogrammetric models (**Figure 64**): the number of data tends to increase with the area of the photogrammetric model, in other words bigger models allow collecting more data.

Obviously, the number of sampled traces differs from model to model (**Figure 64**), ranging from 25 (for the models n°6 and n°25) to 224 (for the model n°1). The models have been numbered according to their locations, which can be seen in **Figures 52 and 53**.

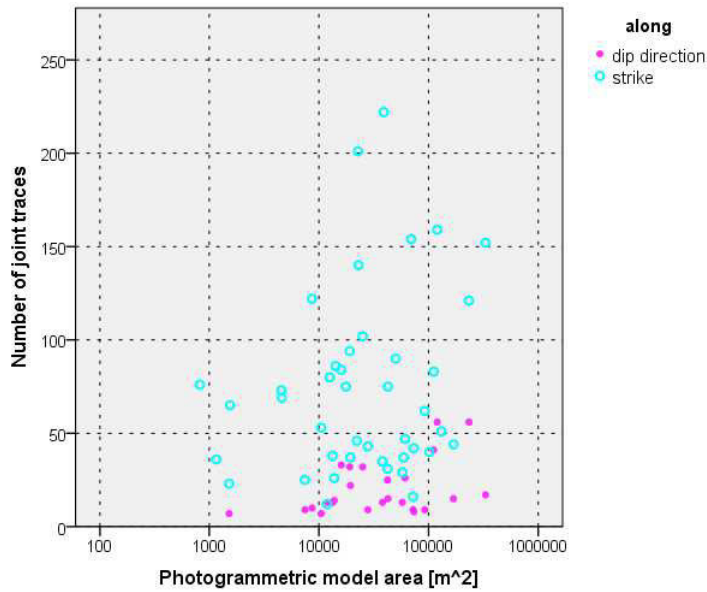


Figure 64 – Relation between the area of photogrammetric models and the number of collected data, along strike and dip direction

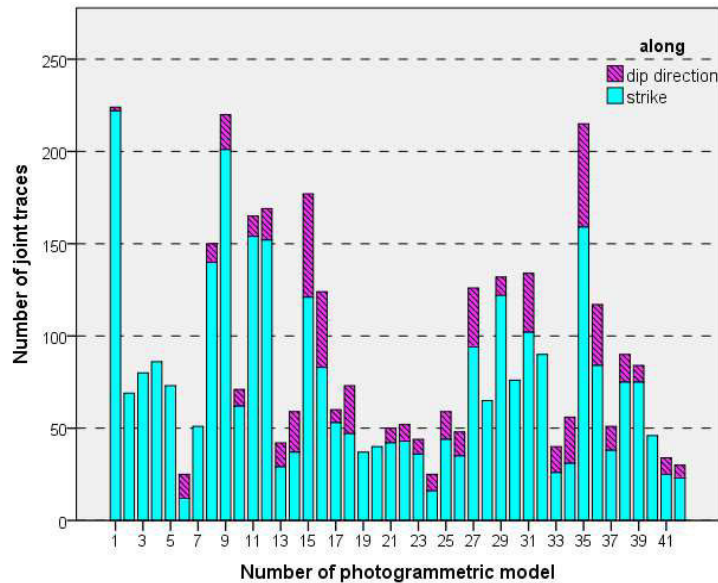


Figure 65 – Frequency histogram relative to the number of collected joint trace lengths for each photogrammetric model, subdivided according to the direction of measure (along strike or dip direction)

The data collected along the strike are more numerous than those ones collected along the dip direction, due to the intrinsic characteristics of the exfoliation joints, which being more or less parallel to the actual landscape surface render the visibility of these exfoliation joints along the dip direction quite low (especially for old generations). Actually, it has not been possible to collect any data along the dip direction in 11 models: 3 of them belong to the third generation, 6 to the second and 2 to the oldest generation. Since in total there are 13 models belonging to the third generation, 24 to the second and 5 to the first, the percentage of models without clear features along the dip direction (equal to 23% for the third generation, 25% for the second and 40% for the first) increases with the age of exfoliation joints.

No clear relationships have been individuated between the number of collected data and the generation of joints (**Figure 66**). The first generation of exfoliation joints has approximately a similar number of collected data for all the considered models, with a marked dependence on the area of the model. The second generation shows an enormous widespread of values, with always a weak trend with the model size. The third generation of joint, even if it is the most clearly visible on the outcrops, is characterized by a smaller number of data than older generations.

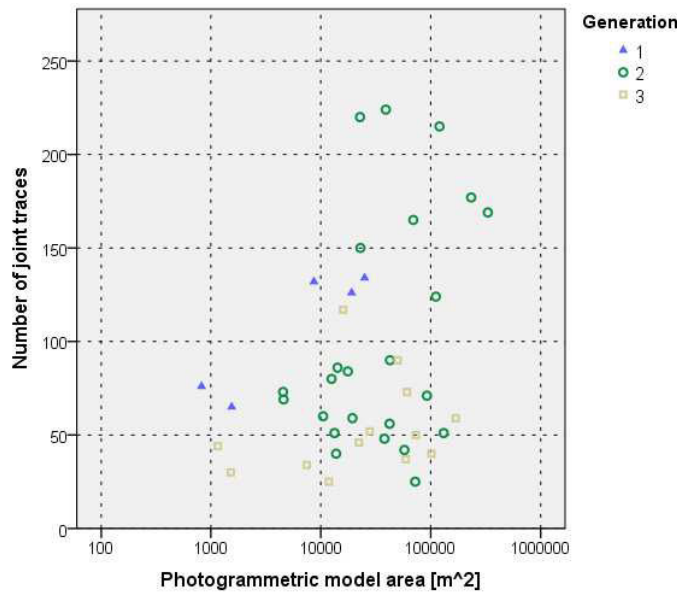


Figure 66 – Relation between the area of the photogrammetric model and the number of collected data, subdivided according to the generation of exfoliation joints

Despite of the number of data, among generations some differences in the trace length values are clearly observable. The minimum, mean and maximum trace lengths, measured per each model, have been reported, subdivided for generation of exfoliation joints, in box-plots (**Figure 67**), which show that the measured values are generally bigger along the dip direction than along the strike (**Table 20**). It could be due to the fact that the dip direction of exfoliation joints often follows other discontinuity sets, and when they have similar orientations to distinguish them is quite difficult. Between the minimum and the maximum values, there is a difference of about one order of magnitude. Generally, increasing the age of the exfoliation joints, and so decreasing the generation, the values of trace lengths become shorter and shorter, but this could be due mainly to the facts that old generations of exfoliation joints are not so clearly visible.

| <i>MEAN TRACE LENGTH [m]</i> | | | |
|---|----------------------------|---------------------|--------------------------|
| <i>Generation of exfoliation joints</i> | <i>Along dip direction</i> | <i>Along strike</i> | <i>All data together</i> |
| Generation 1 | 8.4 | 4.6 | 6.0 |
| Generation 2 | 15.2 | 11.7 | 13.3 |
| Generation 3 | 17.5 | 11.8 | 14.3 |

Table 20 - Values of mean trace lengths, subdivided for generation and direction of measure

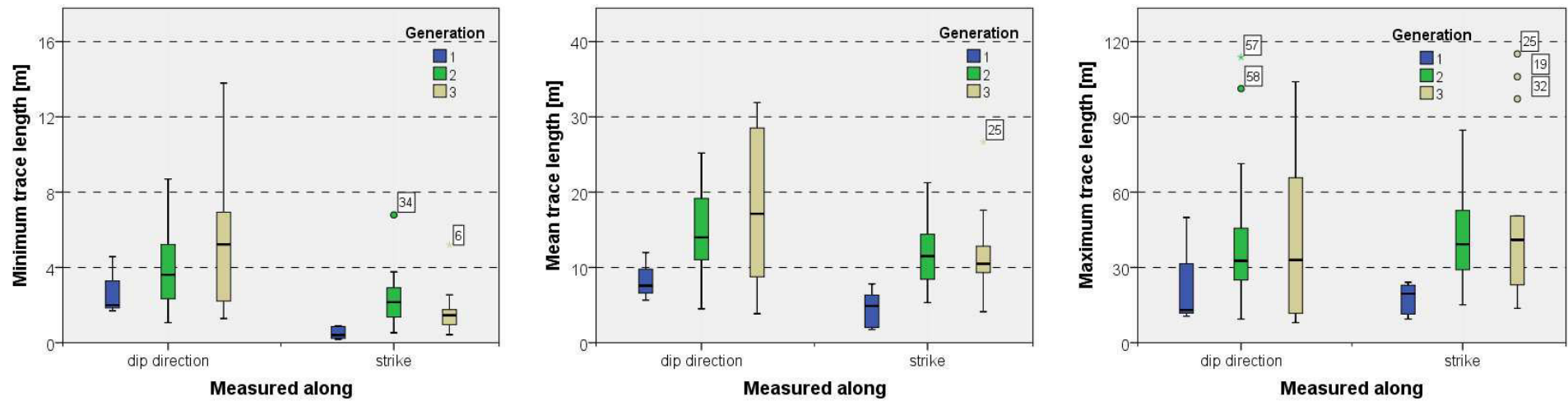


Figure 67 – Box-plots of the minimum, mean and maximum trace lengths (from left to right, respectively) collected from the photogrammetric models, along both strike and dip direction, classified for generation of exfoliation joints. The labels on the box-plots indicate the number of model having anomalous values, with the numeration of models which ranges from 1 to 42 for the strike (according to the Figures 50 and 51) and from 43 to 84 along the dip direction. In this way to find the real number of the model along the dip direction (according to the Figures 50 and 51) it is necessary to subtract 42, for example the model n° 57 actually is the model n° 15 ($57 - 42 = 15$)

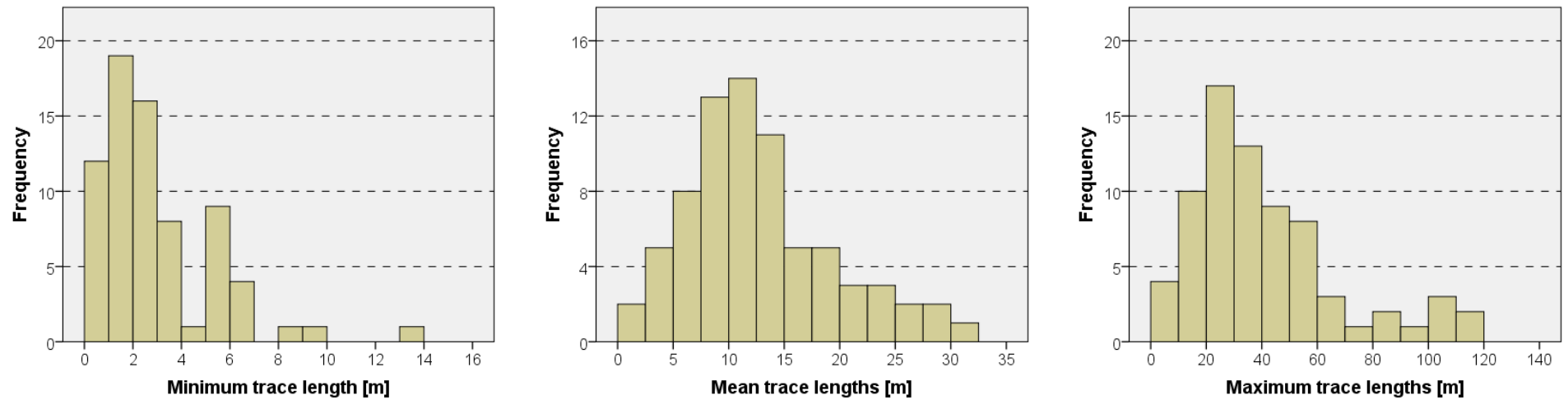


Figure 68 – Frequency distribution histograms of minimum, mean and maximum trace lengths collected from photogrammetric models

Considering all the data together, in spite of the generation and the direction of measure, it is possible to note that the frequency distribution of the trace length data tend to a lognormal distribution (**Figure 68**), as confirmed by the statistical test of Kolmogorov-Smirnov , with Lilliefors correction (Lilliefors, 1967), with a significance level of 5%. This property is respected considering the data of minimum, mean and maximum trace lengths. The lognormality of trace length data is consistent with a broad literature of statistical data analysis in geology (Agterberg, 1974). Actually, it is common and well understandable that short trace lengths, more frequently occur. The reported distributions of joint trace length are less consistent than those for spacing, perhaps caused in part by strong biases implicit in many common sampling plans and in part by the way data are grouped into histograms prior to analysis (Palmström, 1995). However, lognormal distributions are the most frequently reported (McMahon, 1974; Bridges, 1976; Baecher et al., 1977; Barton, 1977; Baecher & Lanney, 1978; Villaescusa & Brown., 1992; Kulatilake et al., 1993; Aler et al., 1996), even if some authors (Robertson, 1970; Steffen et al., 1975; Call et al. 1976; Baecher et al., 1977; Cruden, 1977; Priest and Hudson, 1981; Kulatilake et al., 1993; Aler et al., 1996) have used exponential distributions in analysis, primarily for computational convenience, but there is little empirical verification of this assumption. Lognormal distributions of geometric properties are common observations in geology, but may merely be an artefact of sampling biases; if this is true, then more refined statistical works or more creative data collection schemes will be required to characterize joint size distributions (Baecher, 1983). As consequence, before starting with the geostatistical analysis, it is necessary to check if some biases are occurring in the dataset. A bias is a difference among elements of the sampled population in their probability to be sampled, for example joint sup-parallel to an outcrop have less chances of being sampled than joint perpendicular to that outcrop, and this is a bias in sampling due to the orientation (Terzaghi, 1965). Also during the sampling of trace length and so of the joint size biases often occur (Cruden, 1977). The trace length biases have been subdivided in three common kinds (Beacher & Lanney, 1978):

- Size bias: the probability of a joint to be sampled is proportional to its length (large joints have higher probability to be sampled than small joints), it is due to the fact that larger joints have greater probability of intersecting an outcrop than the smaller ones;
- Truncation bias: short joint are systematically excluded from samples, a minimum joint length to measure (called “cutoff”) is often chosen and joints smaller than this length off are not recorded;
- Censoring bias: the full trace of the joint cannot be measured when the joint is not entirely visible; the trace lengths of joints without both ends observable provide only a lower bound of their length. It follow that the probability of a joint to be censored is proportional to its trace length.

If these biases are not considered, they can lead to misleading conclusions about the population of joints. In this study, the size bias has been searched, considering firstly the total area of each photogrammetric model (**Figure 69**). It results that length of joints is directly proportional to the outcrop size: increasing the outcrop

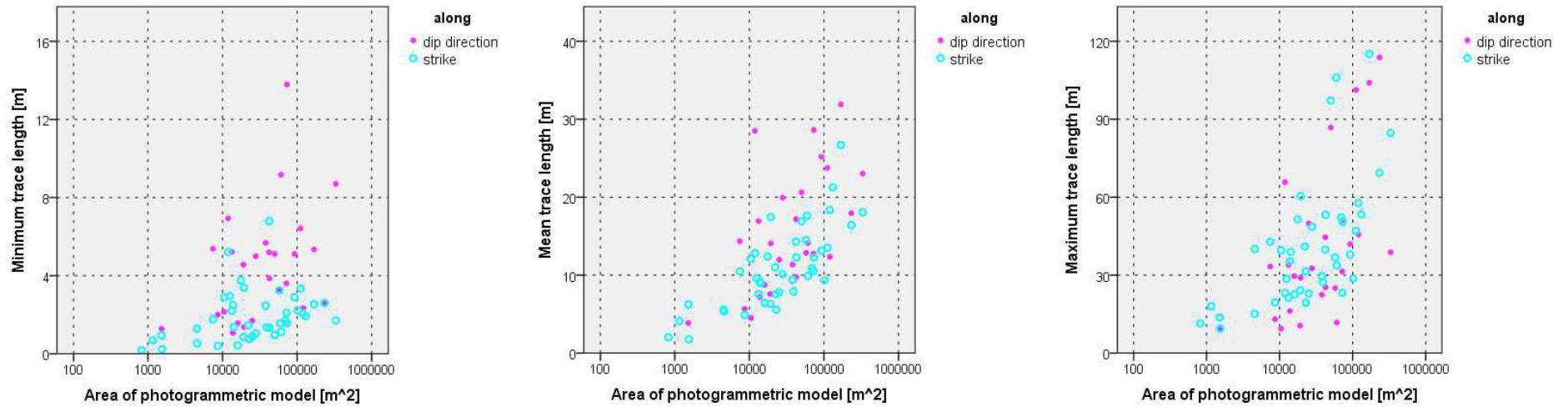


Figure 69 - Dependency of the trace length data on the photogrammetric model size

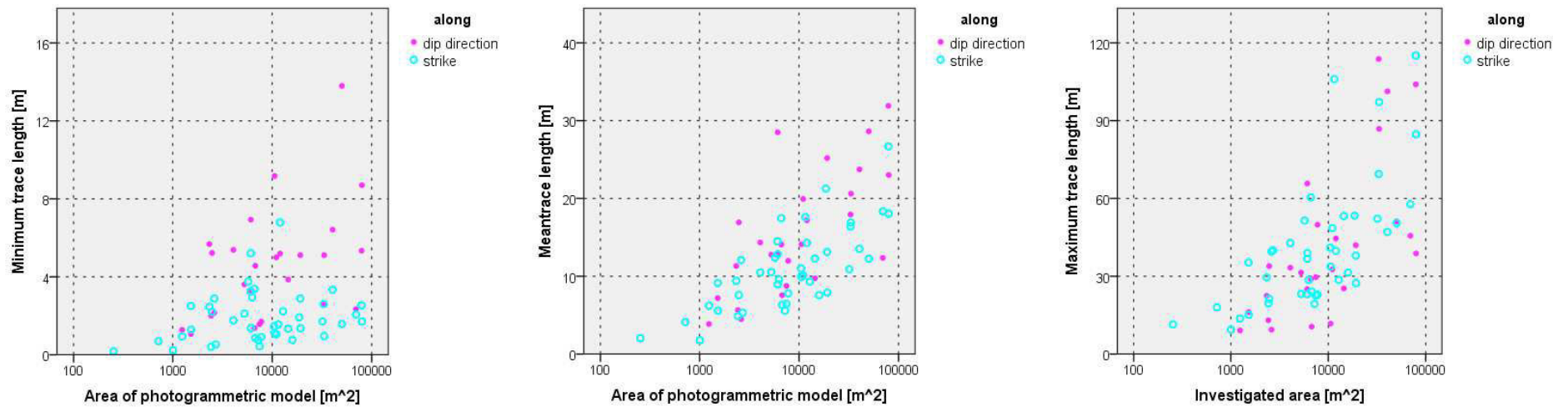


Figure 70 - Dependency of the trace length data on the real investigated portion of the photogrammetric model

size, the average joint trace length increases, both along strike and dip direction. This dependency is respected considering the minimum, the mean and the maximum trace length values, separately; the weakest tendency has been observed for the minimum trace length, while the clearest occurs for the mean trace length, although to find a reliable regression line is not an easy task, being the coefficient of determination - R^2 - always smaller than 0.6. The highest value of R^2 , equal to 0.57, has been found for the mean trace lengths, measured along the strike. Generally, R^2 values are higher along the strike than the dip direction, denoting a better correlation along the strike of exfoliation joints. Since in the photogrammetric model analysis not the whole area of the model has been measured (for example the zones near the fringe of photogrammetric model often have very low resolution), the real investigated area of each outcrop has been taken into account. It has been calculated subtracting from the total area of each model the areas of zones where it was not possible to carry out any measure, i.e. areas with vegetation cover (**Figure 71**), shadow zones and part with low resolution (**Figure 72**).

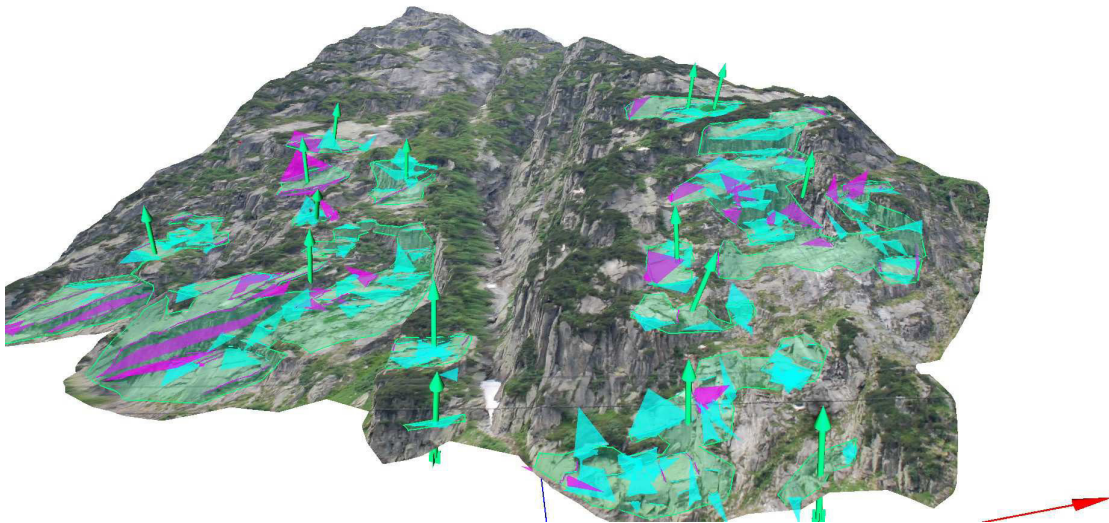


Figure 71 - Calculation of the investigated area (zones with vegetation have not been taken into account)

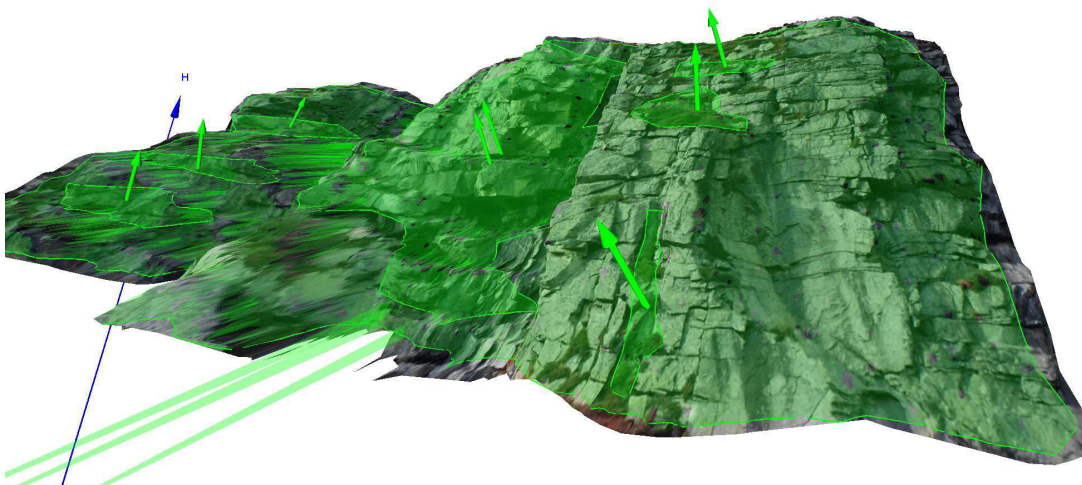


Figure 72 - Calculation of the investigated area (zones with low resolution have been excluded)

The percentage of the investigated area respect to the total outcrop size has been calculated (**Figure 73**) and it is worth to note that very often less than the 50% of the outcrop is measurable: the mean investigate area is of the 43% along the dip direction and the 47% along the strike.

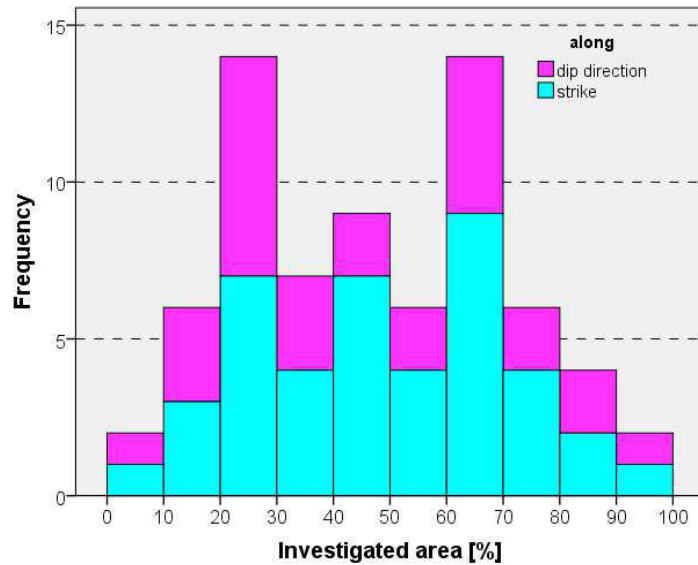


Figure 73 – Frequency distribution histogram of the investigated area of photogrammetric model

The percentage of the investigated area seems to be almost independent on the generation of exfoliation joints (**Figure 74**), even if the youngest generation (the third) is more easily investigable, due to its strong parallelism with the today topography.

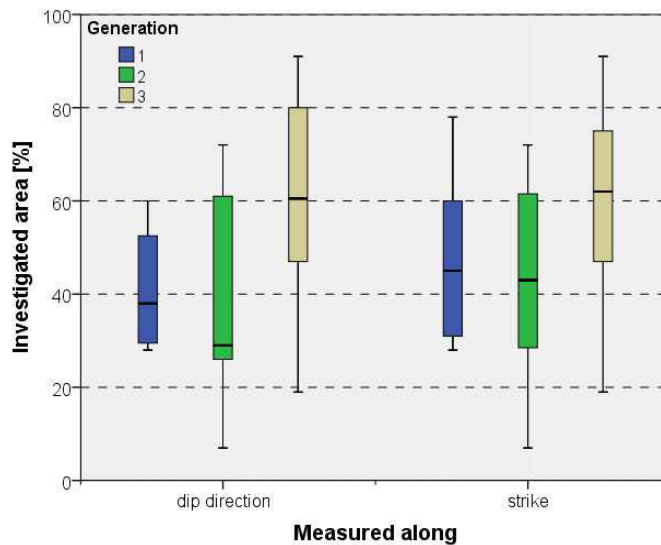


Figure 74 – Box plots of the investigated area, subdivided according to the direction of measure and the generation of exfoliation joints

The percentage of the investigated area is obviously strongly dependent on the area of the photogrammetric model (**Figure 75**): smaller models lead to smaller investigated areas, increasing the area of the photogrammetric model also the investigated area increases.

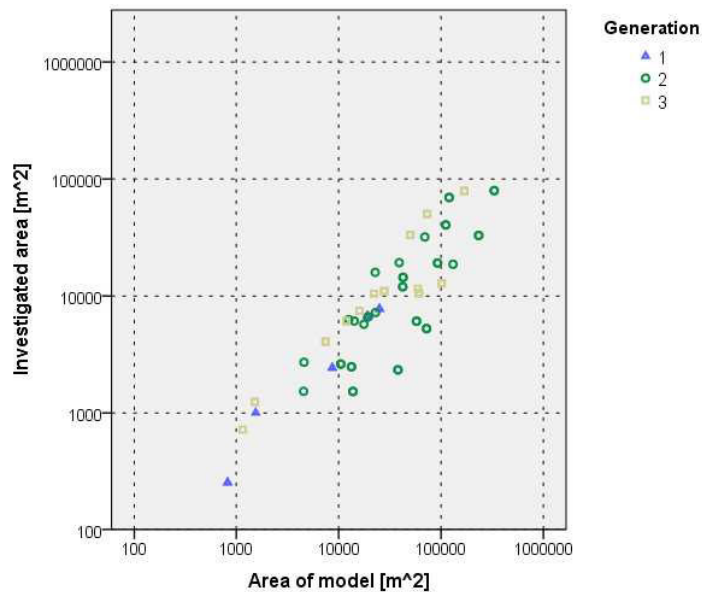


Figure 75 – Relationship between the area of the photogrammetric model and investigated area, subdivided for generation of exfoliation joint

Although considering the real investigated area instead the area of the photogrammetric model, the relationship with the trace lengths (**Figure 70**) does not change significantly. The values of minimum, and especially of mean and maximum trace lengths increase with the investigated area of the outcrop, but the coefficients of determination are still too small to find significant regression, indeed they are still below 0.6, although there a bit bigger along the dip direction than before.

Since the dependency of trace lengths on the area of photogrammetric model has been demonstrated, but a simple equation to avoid the size bias has not been found, the models have been subdivided in some portions, having the same area (**Figure 76**), with the aim to verify if this bias does not occur considering identical sampling area.

The trace length data have been recollected inside each area, but, in this way, a systematic error in the trace length measurements has been inserted. Actually, the central portions of the outcrop at the bottom of the model are characterized by a good resolution and so small fractures are measurable too. Going up and laterally in the model, the resolution becomes low and low, and only the main, long fractures are visible and measurable. Actually, the resolution of the model is related to the distance between the position of the calibrated camera and the outcrop, to the focal lenses used and finally to the outcrop size. Hence, using this approach, the trace lengths, as well as the spacing, the rock bridge lengths, grow with the elevation, but it is an effect of the resolution of the model. Moreover, the subdivision of the model in some small rectangular portions does not allow measuring the trace lengths longer than the diagonal of the rectangle, but only a lower boundary of the real trace lengths and the number of the terminations outside from the window sampling grows a lot.

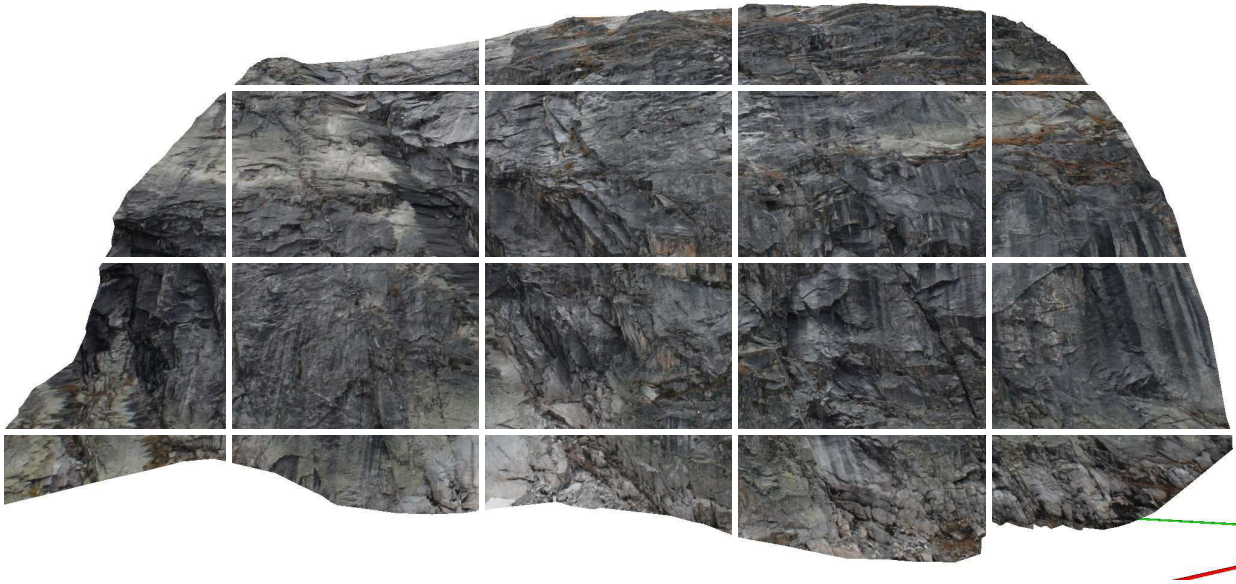


Figure 76 - Subdivision of a model in some portions having the same area

In this research a clear truncation bias lacks: the used cutoff changes from model to model (Figure 77), being strongly dependent on the resolution of the considered model. One a priori cutoff length has not been chosen, because the resolution varies considerably from model to model. The minimum measurable trace length of the worst model has not been chosen as a fixed cutoff length (model n°34 in Figure 77), because it should lead to neglect some measurable values in the models having better resolution. It follows that also the truncation bias cannot be treated in a simple way, but it can be individuate observing the histogram distribution of trace length; indeed if it was not lognormal but exponential, a truncation bias should occur. In the case study, being the trace lengths lognormally distributed, the truncation bias should not occur.

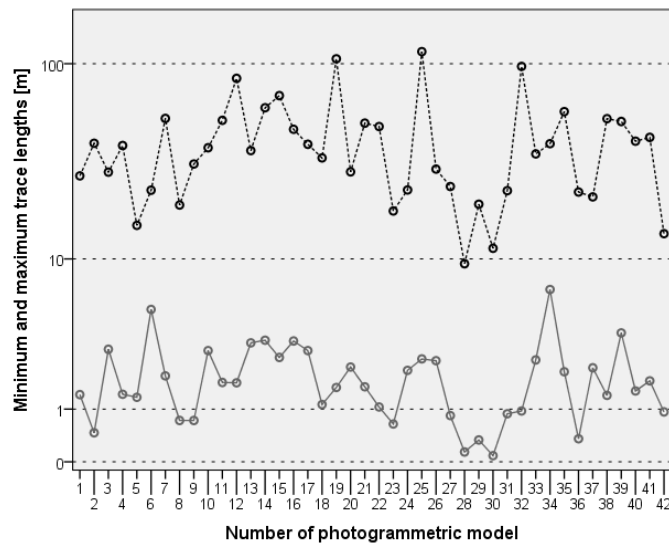


Figure 77 - Minimum (gray solid line) and maximum (black dashed line) trace lengths, measured along the strike

Finally, the censoring bias is related to the joints without both ends observable, and in these cases the real trace length of the joint cannot be measured, but only its lower boundary. Each traced joint is characterized by two tips (or terminations), and, during the data collection, each of them has been categorized in the following way:

- Tr: when the termination ends in rock;
- Td: when the termination ends against other discontinuities;
- Tx: when the real tip of joint is not clearly visible, ending out from the sampling window or also running off into soil cover, vegetations or shadow and low resolution zones (in the photogrammetric models).

The true trace length is therefore visible only for a subset of the joints, those one having one or both ends of Tx type cannot be entirely observed, thus for them only a lower band of trace length is observable. The number of occurrence of each kind of termination, encountered per each model, has been transformed into percentage, in order to render possible the comparison.

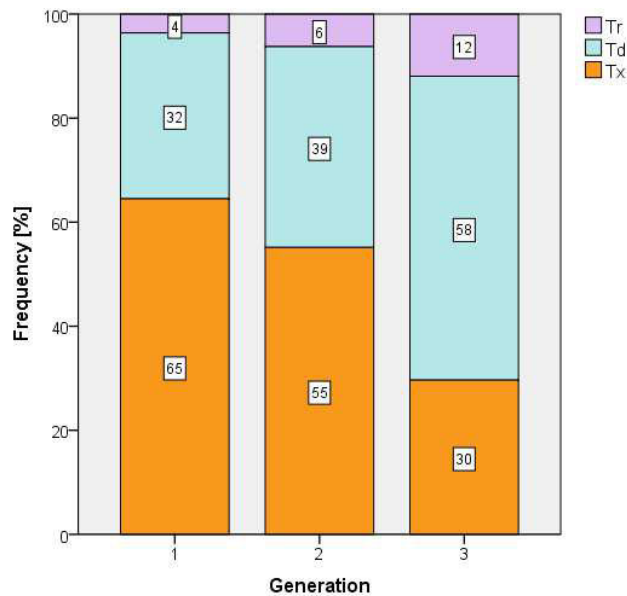


Figure 78 – Kind of terminations, subdivided according to the generation of exfoliation joints. Tr, Td and Tx indicate joints ending respectively in rock, against other discontinuities and with a not visible or unclear way

Subdividing the results according to the generation of exfoliation joints (**Figure 78**), it is possible to note that the not observable termination (Tx) occur especially in old generations of joints, actually decreasing the age, the number of joints with hidden or not clearly identifiable tips decreases considerably. This could be also related to the fact that exfoliation joints of first generation are visible mostly on small models (**Figure 66**), leading to cut longer trace lengths. On the contrary, the number of joints ending both in rock (Tr) and against other discontinuities (Td) increases with the generation, so the real tips of joints are more visible for younger generations. It follows that the older generations of exfoliation joints are not as well characterized as the younger, especially because of their orientation, which differs a lot from the today topogra-

phy, allowing seeing very often only a line and not a plane, with therefore has not clearly visible ends. This fact leads to shorter measurable trace lengths for the oldest and the middle generations of exfoliation joints, than the youngest (**Figure 67**).

To quantify the occurrence of the censoring bias kind of bias, the discontinuity terminations, which are two for each joint trace length, has been reclassified as:

- Terminated (Tr): if the considered discontinuity finishes in rock;
- Open (Td): if it stops against other discontinuities, which should be previously formed;
- Unknown (Tx): if it terminates outside of the outcrop, or if the tip is not clearly visible (i.e. when it is hidden by vegetation, or when it ends in a shadow or not clearly visible zones).

All the joints with one or both not visible ends (i.e. when at least one tip is of the Tx-type) have been removed, in order to consider only the “real trace lengths”, given by joints having both visible terminations (**Figure 79**).

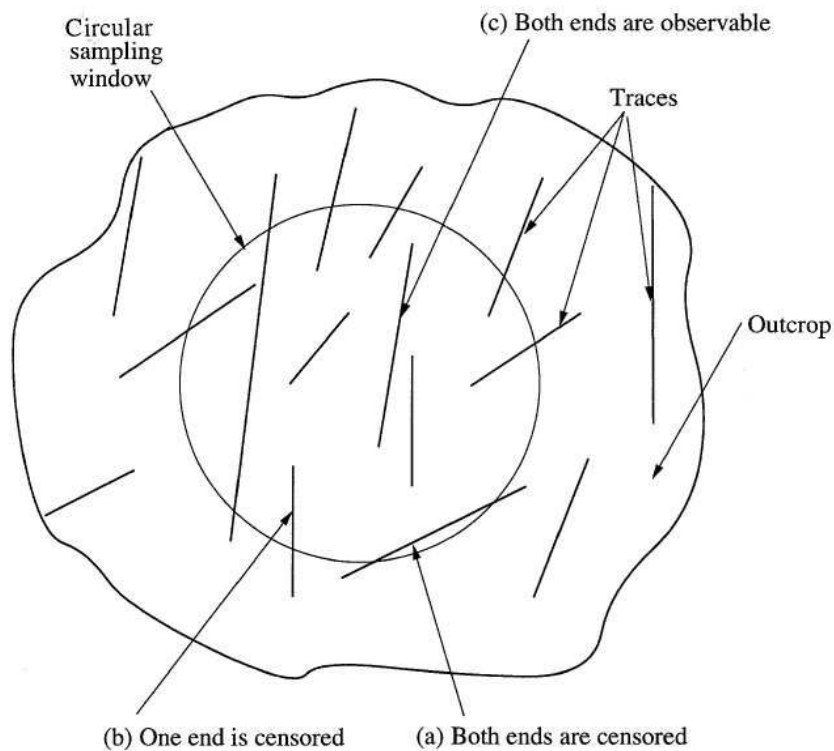


Figure 79 – Trace length can have none, one or both end observable. The real trace length can be measured only when both ends are visible (from Zhang & Einstein, 1998)

The number of visible terminations is very variable: there are some photogrammetric models having the majority of data with both visible ends (**Figure 80**), but also models with very few visible terminations (**Figure 81**), especially along the dip direction. Generally, especially high values of trace lengths are lost considering only the joints with both visible ends. Globally, the frequency distribution of trace lengths of joints with both visible ends often recalls again the lognormal distribution (especially along the strike).

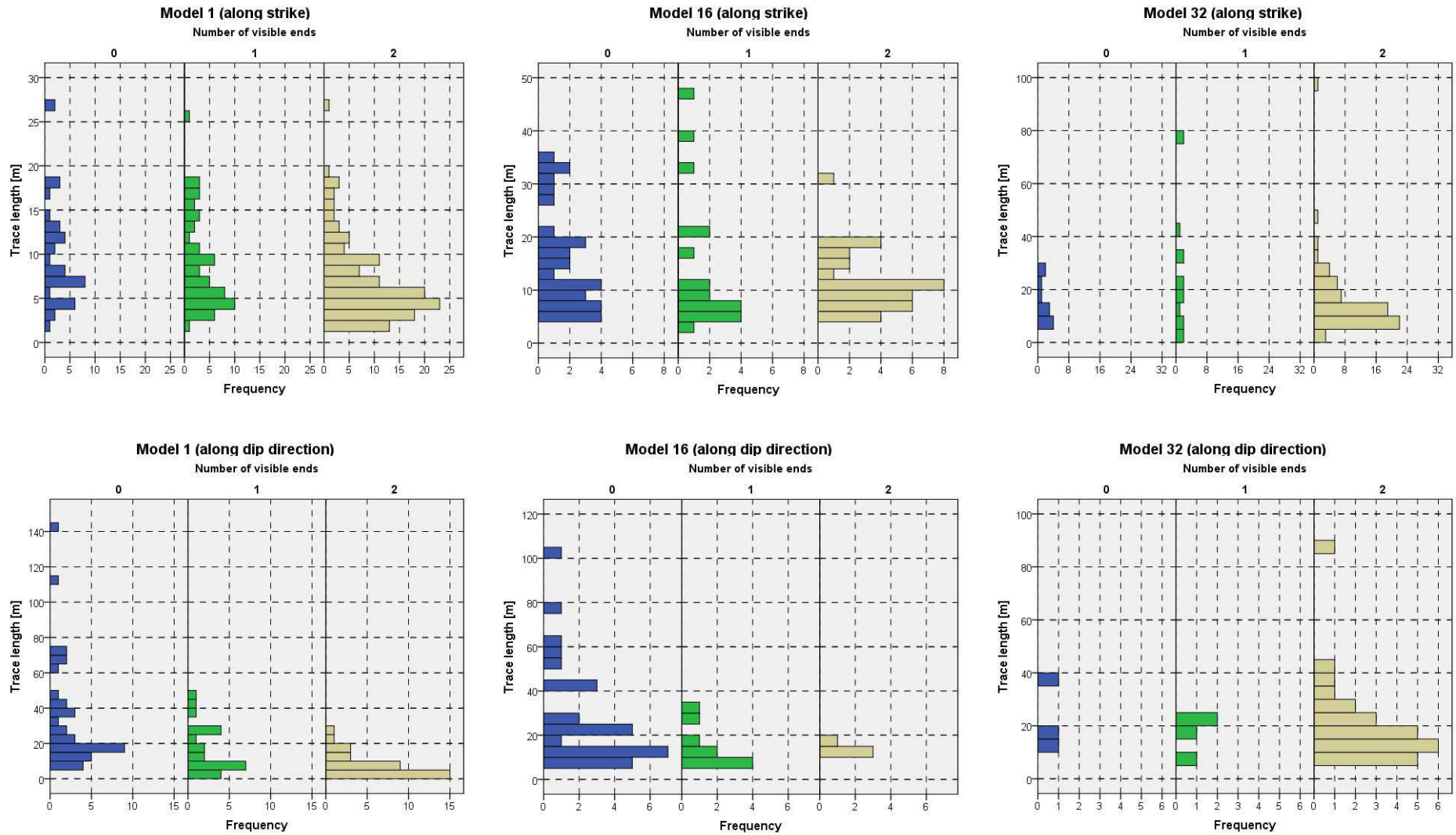


Figure 80 - Trace lengths subdivided according to the number of visible terminations per each joint (0= none, 1=one, 2= both)

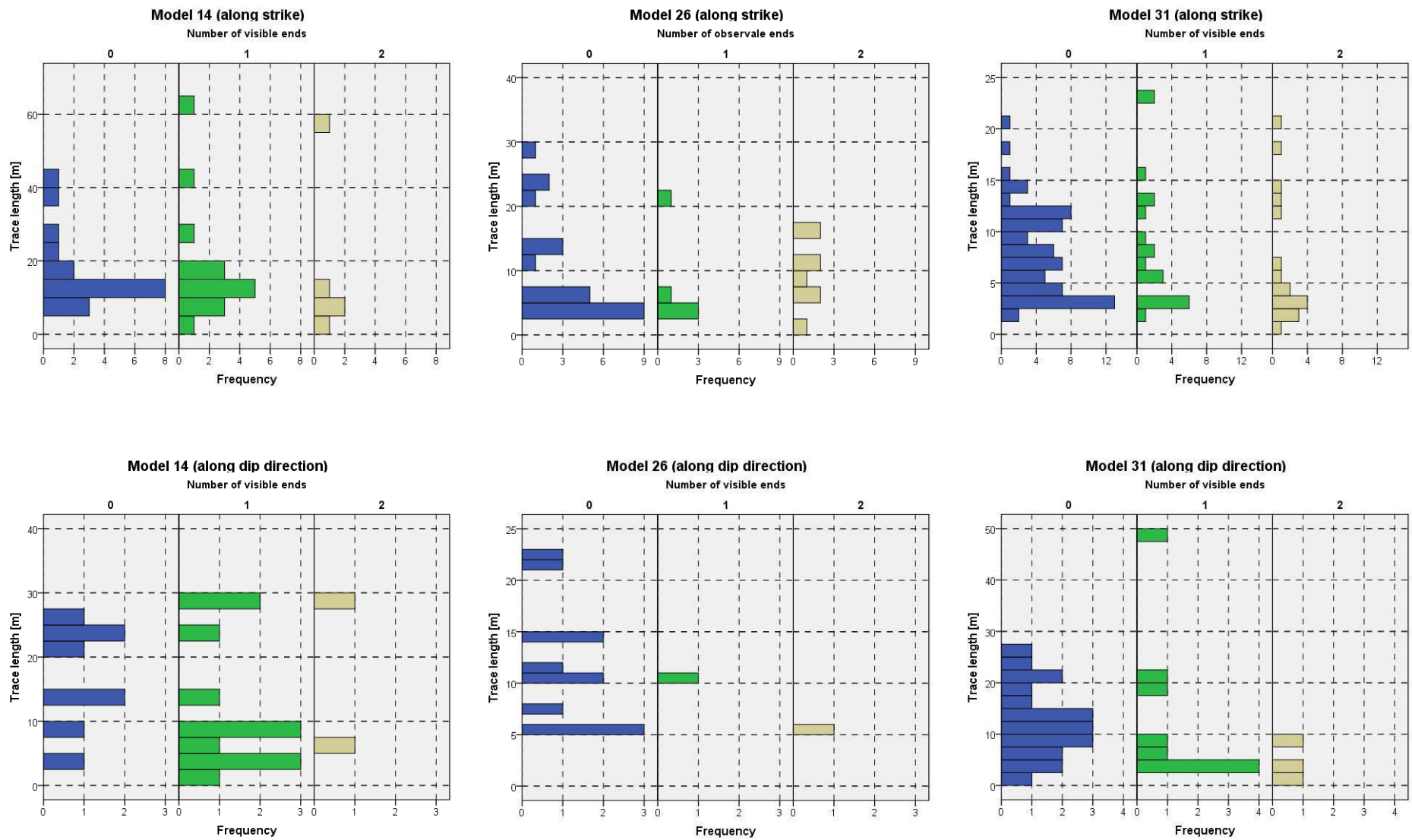


Figure 81 - Trace lengths subdivided according to the number of visible terminations per each joint (0= none, 1=one, 2= both)

The percentage of joints having both visible terminations (**Figure 82**) ranges from 0% (models number 17, 21, 29 and 39) to 86% (model n°42) along the dip direction, and from 9% (model n°17) to 83% (model n°40) along the strike. The not visible ends prevail along the dip direction: the average value of joints with both visible ends, and so real trace lengths measurable, is only of the 27% along this direction and it is of the 50% along the strike.

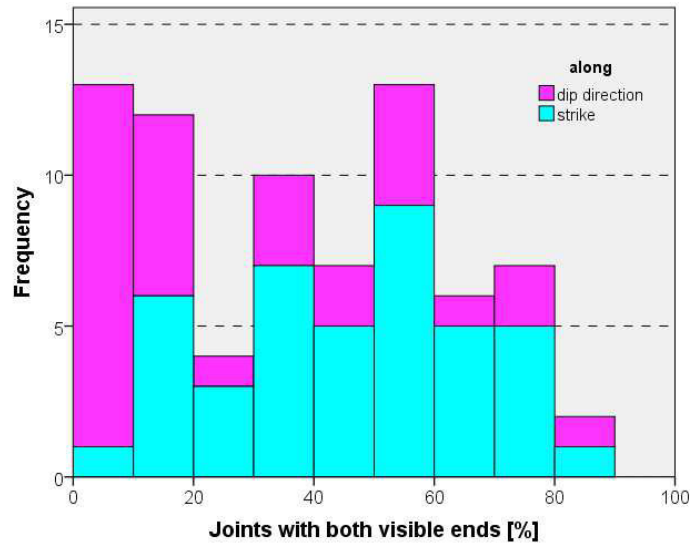


Figure 82 - Frequency histogram of the percentage of joints with both visible terminations

The percentage of joints having both visible terminations is, for each generation, bigger along the strike, than along the dip direction (**Figure 83**), and it increases with the generation: the youngest generation of exfoliation joints has the biggest percentage of joints with both visible tips. Considering only the data of trace lengths of exfoliation joints having both visible ends, a new dataset (in this text, with the aim to avoid excessive jargon, simply called “real trace length”) has been created and analysed.

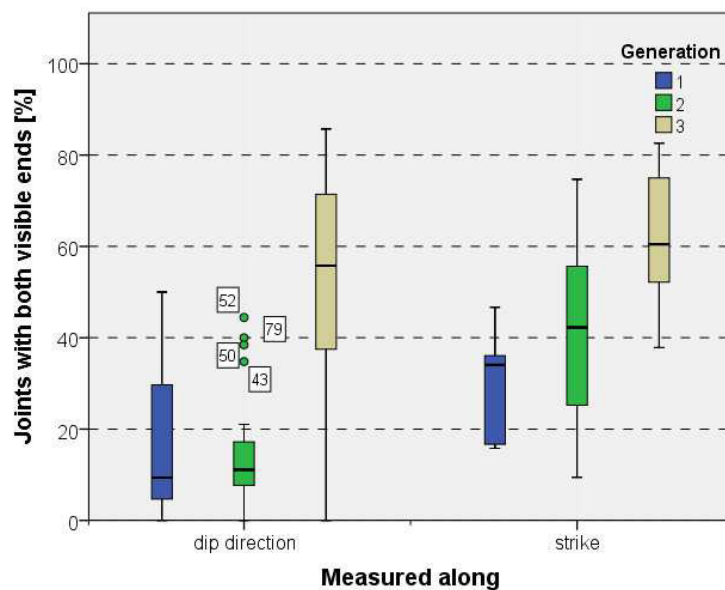


Figure 83 – Box plots of the percentage of joints with both visible terminations, subdivided for generation of exfoliation joints

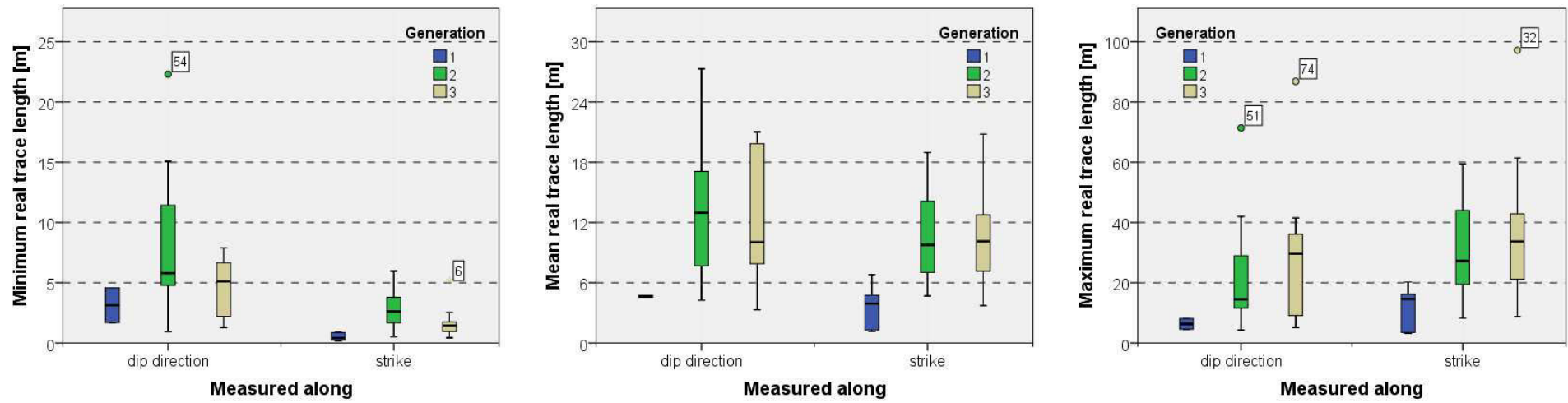


Figure 84– Box-plots of the minimum, mean and maximum real trace lengths, subdivided according to the direction of measure and the generation of exfoliation joints

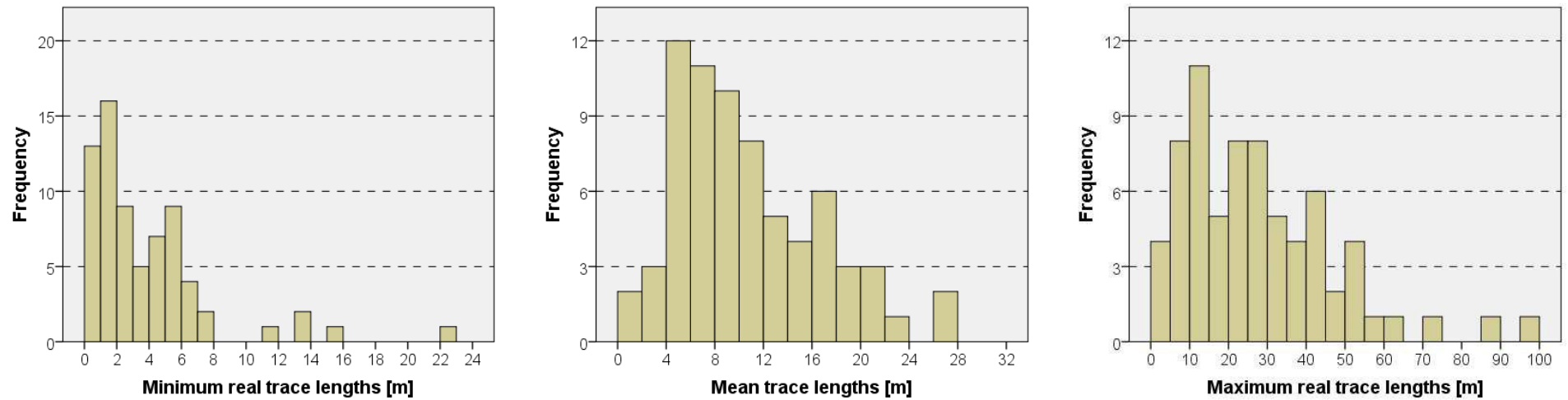


Figure 85 – Frequency distribution histograms of minimum, mean and maximum real trace lengths collected from photogrammetric models

The box plots of minimum, mean and maximum real trace lengths (**Figure 84**), measured per each model, show some similarity with those one previously described (**Figure 67**). In the new dataset the global trend, as well as the relationships with the direction of measure and the different generation of joints have been respected: the measured values are again generally bigger along the dip direction than along the strike (**Table 21**). Once again, the first generation of exfoliation joints is characterized by very short trace lengths, with a small range of values. The second and the third generation of exfoliation joints now are very similar, presenting close mean values (which are slightly higher for the second generation), with also comparable range. The number of outliers, which are values greater than the third quartile plus 1.5 the interquartile range (depicted in the box-plots with circles) is now reduced, as well as the number of extreme outliers, which are values greater than the third quartile plus 3the interquartile range (indicated in the box-plots with stars). Actually, considering only the joint traces having both visible ends, especially high values have been lost, because they, been so long, often finish outside from the sampling window. Indeed, the new dataset, compared with the previous one, excludes especially the big values of trace lengths: the values of mean real trace lengths (**Table 21**) are smaller than the values reported in **Table 20**, especially for the first generation of exfoliation joints, having the 65% of unknown terminations.

| <i>MEAN REAL TRACE LENGTH [m]</i> | | | |
|---|----------------------------|---------------------|--------------------------|
| <i>Generation of exfoliation joints</i> | <i>Along dip direction</i> | <i>Along strike</i> | <i>All data together</i> |
| Generation 1 | 4.7 | 3.6 | 3.9 |
| Generation 2 | 13.4 | 10.6 | 11.8 |
| Generation 3 | 12.4 | 10.2 | 11.1 |

Table 21 - Values of mean real trace lengths, subdivided for generation and direction of measure

Considering all the data together, in spite of the generation and the direction of measure, it is possible to note that the frequency distribution of the trace length data tend again to a lognormal distribution (**Figure 85**), this has been verified applying statistical Kolmogorov-Smirnov test, with the Lilliefors correction (Lilliefors, 1967), with a significance level of 5%. The lognormal distribution of trace lengths is honoured considering the data of minimum, mean and maximum trace lengths.

In conclusion, the research of possible biases occurring in the trace length data shows that:

- the trace lengths obviously increase with the investigated area of the outcrop, but without a regression line of remarkable statistic significance. This fact, combined with the great variability of the investigated areas (which range from few hundreds of m² to almost 80000 m²), allows neglecting the size bias;
- a systematic truncation bias does not occur in this research, because the used cutoff, being strongly dependent on the resolution of photogrammetric models, is very variable among models;

- the censoring bias has been removed from the initial dataset, considering only the entirely visible joints.

3.4.3 Rock bridge lengths

The rock bridges are reaches in rock, between interrupted traces of the same joint, delimited by two terminations in rocks (Tr).

In this study, only when the two interrupted joint traces are almost coplanar, the rock bridges have been measured: to have a rock bridge the reach in rock must be longer in the direction parallel to the discontinuities than in the direction normal to them. In other words, if there was an offset in the direction normal to the discontinuities bigger than the distance between the two tips in rock (measured parallel to them), this reach in rock had not been considered as a rock bridge, and not measured. The rock bridges have been measured along the surface, allowing in this way to consider also the roughness.

Because of the terminations in rocks have been observed especially along the strike, the rock bridges have been encountered almost only in this direction (**Figure 86**). The dispersion of values grows up with the generation, but this is mainly due to the number of data, which becomes bigger and bigger decreasing the age of the exfoliation joints, because of terminations in rock are more numerous for younger exfoliation joints. Moreover the models of generation 1 often have generally smaller areas than those of generation 2 and 3, leading to shorter measures.

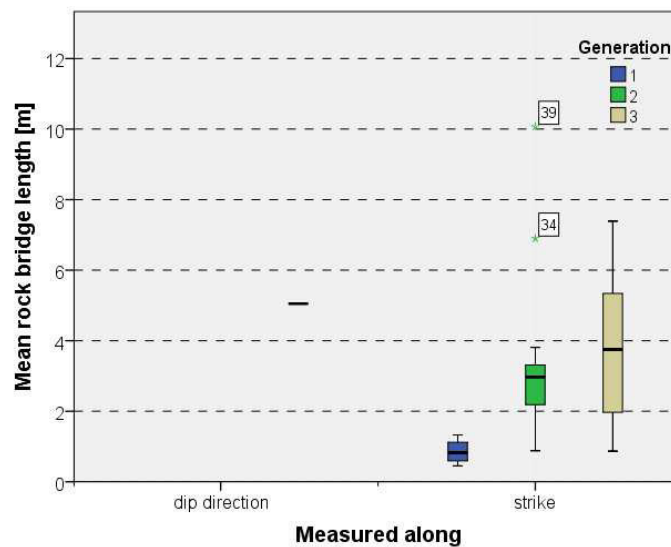


Figure 86 – Box plot of mean bridge lengths, subdivided according to the direction of measure and generation of exfoliation joints

The frequency distribution of mean rock bridge lengths (**Figure 87**) shows that especially short ones are frequent, even if those with a length between 3 and 4 metres prevail. This could be related to the fact that rock bridges shorter than 3 metres cannot be captured in models having low resolutions, and so the negative exponential distribution is not verified, due to the truncation of values smaller than the resolution of the photogrammetric model.

Above 4 metres of length, the number of rock bridges becomes smaller and smaller, increasing the lengths of the bridge. No rock bridges longer than 11 metres have been encountered.

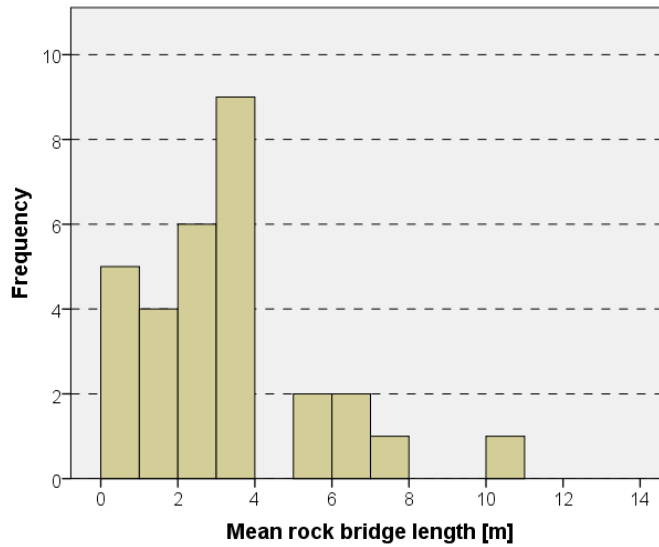


Figure 87 – Frequency histogram of the mean lengths of rock bridges

3.4.4 Sinuosity Index

From the trace lengths data, the Sinuosity Index –SI–, defined as the ratio between the real trace length and the Euclidean trace length (i.e. the minimum distance between the tips of the joint) has been computed for each measured exfoliation joint.

The SI gives a rough description about the roughness of the analyzed discontinuity: the SI is equal to one for straight lines, whilst it tends to infinite for close figures. It follows that SI tends to one for planar joints, while it becomes bigger and bigger increasing the undulation of the joint. The computed values of SI (Figure 88) indicate that the exfoliation joints are straighter along the dip direction than along the strike, and their sinuosity generally increases with the age.

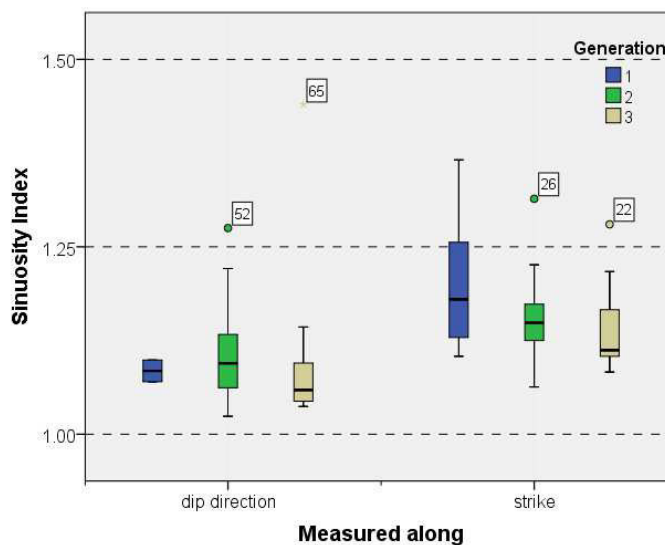


Figure 88 – Sinuosity Index values, subdivided for direction of measure and generation

3.4.5 Spacing

The spacing is the distance between two joints belonging to the same discontinuity set, measured perpendicular to them. Joint spacing can vary from some millimetres to many metres, and may often seem arbitrary. There are, however, sometimes certain trends in the density of joints caused by spacing. Commonly, spacing between joints varies from few centimetres in highly tectonized rocks (folded, faulted, and intruded) of all types to more than 10 metres in massive, horizontally layered rocks (Nieto, 1983). The regularity of joint spacing decreases with the amount of tectonic activity of the area. Rock masses that have undergone tectonic disturbance often present clusters of joints (called joint zones). The joint spacing often decreases near faults and shear zones. Spacing is also influenced by weathering, as there often is an increase in jointing density within the zone of weathering, especially where mechanical disintegration has taken place (Palmström, 1995). It is also well known that two joint sets in the same lithologic unit often have different spacing and spacing can change as a joint set evolves.

With particular reference to intrusive igneous rocks, such as those ones outcropping in the Grimsel area, Pollard & Aydin (1988) have observed that the spacing of joints in some sets is not uniform and distances between joints can range from less than 20 cm to more than 25 m, with clusters of joints outcropping sporadically.

In the Grimsel area, and in particular along the Hasli valley, the spacing among the traced exfoliation joints has been computed, using the photogrammetric approach, through the multiple scanline method, which considers the normal distance between joint traces, projecting them, with their orientation, onto a reference plane parallel to the mean orientation vector of the set. If a joint trace is so short or straight that it has not been possible to determinate its orientation with accuracy, the mean orientation of the set has been used for the projection. An example of the projected trace lengths, along the strike of the exfoliation joints, with the measures of spacing (perpendicular to them) has been reported in **Figure 89**, where each grey dashed line represents a measure of spacing.

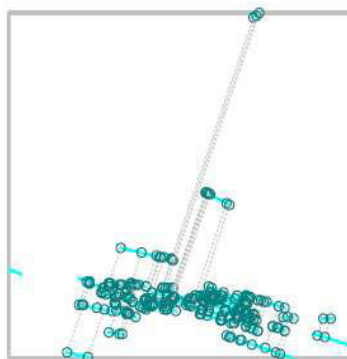


Figure 89 – Sketch of spacing calculation, along strike, with the multiple scanline method. The solid lines are the projected trace lengths of exfoliation joints along the strike and the dashed lines are the spacing

The spacings have been measured along both the strike and the dip direction of exfoliation joints, separately. Actually only the spacing values measured along the strike are representative of the real spacing of exfoliation joints, although the measured values along the strike and dip direction are quite similar (**Figure**

90). The spacing measured orthogonally to the dip direction is a sort of lateral spacing, which however contributes to determinate the fracturing degree of the rock mass.

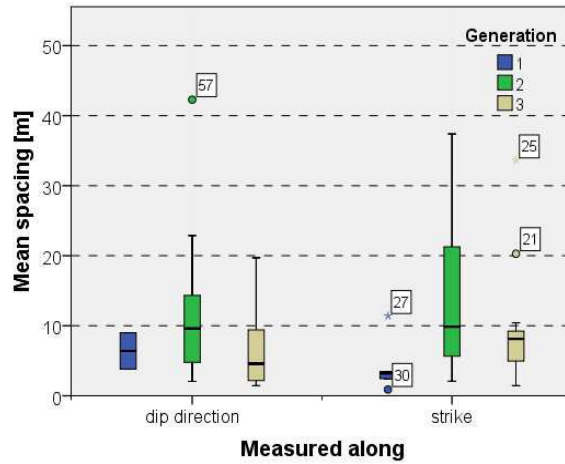


Figure 90 – Mean spacing data, collected from photogrammetric models, subdivided for direction of measure and generation

The spacing values have some peculiar features, in function of the considered generation (Table 22).

| <i>MEAN SPACING [m]</i> | | | | |
|---|----------------|----------------|-------------|---------------|
| <i>Generation of exfoliation joints</i> | <i>Minimum</i> | <i>Maximum</i> | <i>Mean</i> | <i>Median</i> |
| Generation 1 | 0.9 | 11.4 | 4.3 | 3.2 |
| Generation 2 | 2.1 | 37.4 | 13.1 | 9.9 |
| Generation 3 | 1.4 | 33.6 | 9.8 | 8.1 |

Table 22 – Spacing data, collected from photogrammetric models, along the strike of exfoliation joints

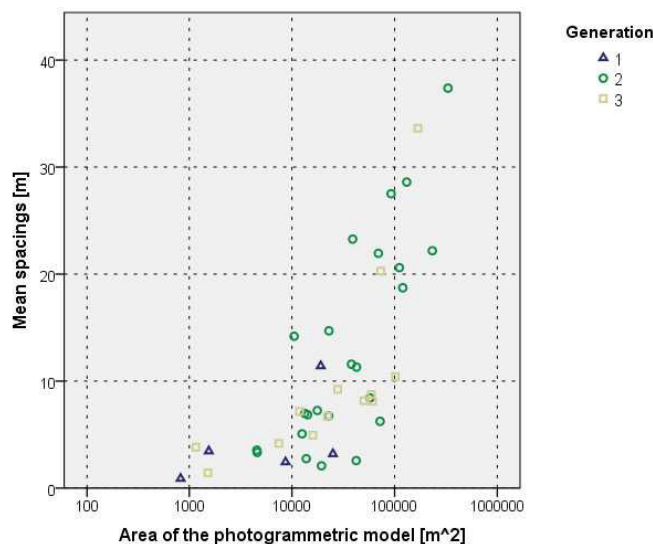


Figure 91 – Relationship between the area of the real investigated area and the mean spacing along strike

The oldest generation has the shortest mean spacing and the smallest range, which is also shorter than the in situ observations, which reports that joints of generation 1 are typically widely spaced (up to > 10 metres),

this difference could be due to the fact that the first generation is observable only on small photogrammetric models of outcrops (**Figure 91**).

The generation 2 shows the highest value of spacing, with also the wider range, while the spacing of the generation 3 has medium values and range. The observations for generations 2 and 3 are coherent with in situ surveys of Martin Ziegler, who observed that joints of generation 2 present very wide joint spacing (on the order of several metres to > 10 m), while joints of generation 3 are more closely spaced (up to a few metres) at the ground surface (Ziegler et al., 2013).

The measured mean spacing can seem too high values, but it is worth to note that measurements obtained from photogrammetric models are always bigger than those ones of in situ survey, due to the grater distance from the outcrop and so to a less accurate resolution of it. This fact allows observing only the main features of the rock mass (i.e. long trace of joint), but not the small ones observable in situ. However, the Central Aar Granite generally has a very good quality of the rock mass (Bieniawsky, 1989), being affected by few, wide spaced discontinuities, indeed in the Grimsel area there are some tunnels, such as the Grimsel Test Site, standing without supports. In this context, so high mean spacing values are therefore acceptable.

The median values of spacing are always smaller than the mean values of spacing, meaning that the distribution is asymmetric, indeed the mean spacing values, plotted independently from the generation and direction of measure, are lognormally distributed (**Figure 92**). This kind of distribution has been verified applying statistical Kolmogorov-Smirnov test, with the Lilliefors correction (Lilliefors, 1967), with a significance level of 5%.

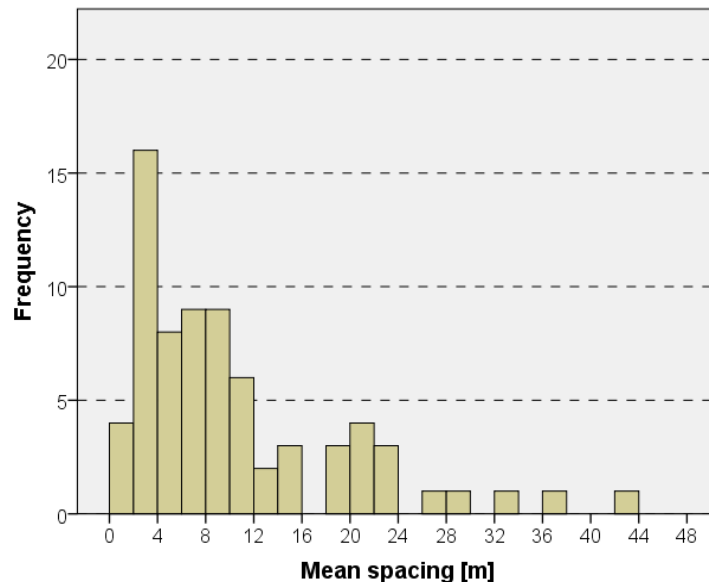


Figure 92 – Histogram distribution of mean spacing values

Joint spacing distribution laws remain a controversial subject in the literature, actually the relative frequency of joint spacing has been described by different distribution laws (Figure 50), which in order of frequency are: negative exponential distributions (Snow, 1969; Snow, 1970; Call et al., 1976; Priest & Hudson, 1976; Baecher et al., 1977; Priest & Hudson, 1977; La Pointe & Hudson, 1985; Baecher & Lanney,

1978; Villaescusa & Brown, 1990; Merrifi & Baecher, 1981) or log-normal distributions (Sen & Kazi, 1984; Rouleau & Gale, 1985; Bouroz, 1990; Narr & Suppe, 1991; Ruf et al., 1998), or also, more rarely, normal spacing distributions (Huang & Angelier; 1989). Why one distribution occurs in one case, and another in another case, remains unexplained (Dershowitz & Einstein, 1988). Rives et al. (1992) have described a change in the spacing distribution of a joint set, in response to the stage of evolution of the set. They observed that the fracture spacing distribution law evolves with increasing fracture set development (and increasing with deformation), from a negative exponential distribution (at a stage with only few fractures) to a log-normal distribution (at intermediate fracture density) and to a quasi-normal distribution (at high fracture density).

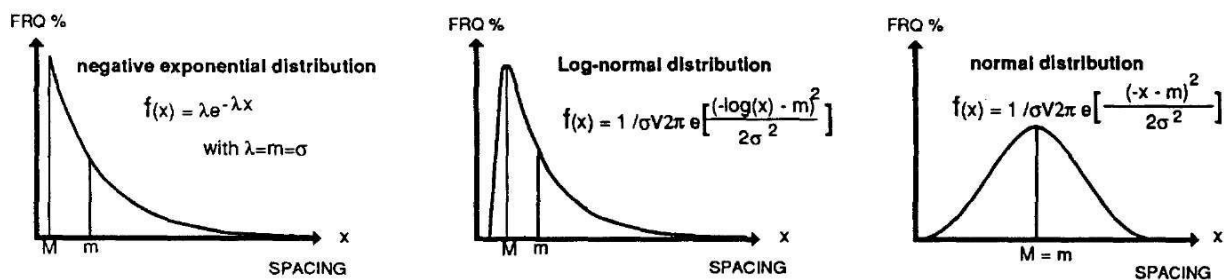


Figure 93 –The different types of distribution laws commonly used to describe spacing distributions; M is the mode, m the mean and σ the standard deviation (from Rives et al., 1992)

Sampling bias may go some way to explain the occurrence of different spacing distributions.

For example joint spacings, measured along sampling lines or in borings, generally show a negative exponential distribution. Actually during in field studies an important bias could arise if large spacings are ignored (Kulatilake & Wu, 1984) or, if all discontinuities (without separation of different types and different sets) are counted (for example in borehole cores), thus smaller spacing values are obtained. In these situations, small spacing values are represented more relative to large values, and the corresponding best fit is generally a negative exponential (Priest & Hudson, 1976; Barton & Zoback, 1990).

On the contrary, in analyses based on photo-interpretation, small spacings are generally ignored because of photographic resolution (Huang & Angelier 1989; Tsoutrelis et al. 1990). Frequency distributions of this type may apparently fit with a negative exponential distribution but the distribution is truncated at inferior values. It follows that the probability of small spacings plays a critical role in the choice of a distribution law.

In this study case, the frequency distribution is not exponentially distributed, due to the irregular truncation of small values: to have that kind of distribution some spacing values smaller than 2 metres are missing. This is certainly related to the fact that the mean spacings have been measured on photogrammetric models of very big outcrops, having a resolution that does not allow to recognise small features (i.e. short spacings) in the higher and more distant parts of these outcrops.

Moreover, also for the spacing, a constant minimum cutoff equal for all models has not been used, due to the big variations of resolutions among models, so the truncation bias occurs, due to the strong dependency on the image size and resolution, but it cannot be removed.

Regarding the size bias, the spacing values increase with the investigated area of model (**Figure 94**), and this fact is noticeable especially along the strike, although the coefficient of determination, calculated by a linear regression, is around 0.5, and so not satisfactory.

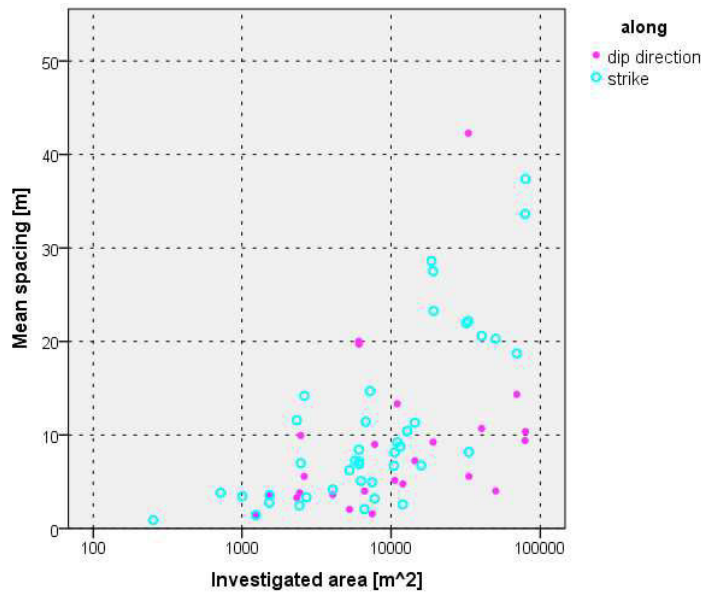


Figure 94 – Relationship between the area of the real investigated area and the mean spacing

Finally, the censoring bias does not occur for this kind of measure, indeed the spacing values are always bounded by two observable joints.

However, Dershowitz & Einstein (1988) indicate that the different distributions may be present in unbiased data. They suggest that independently created joints can lead to negative exponential distribution, whereas joints which interact can produce log-normal distributions. According to this statement, it is reasonable that exfoliation joints, which are the youngest joints, follow a log-normal distribution.

3.5 Geostatistical analysis of some properties of exfoliation joints

The geostatistical approach, followed for the Valchiavenna case study, has been applied also at the Grimsel site, considering the following properties of exfoliation joints: real trace lengths, spacing and difference in orientations between dip angles of exfoliation joints and dip angles of slopes.

Only the almost 3D approach has been applied to the Grimsel case study.

In a first stage of the analysis, the exfoliation joint properties have been treated independently of the joint generation, in order to understand if some regional trend, independent of the joint generation, occurs in the study area. Some difficulties are expected, due to the locations of measuring points, being the photogram-

metric models very scattered in the study area (**Figure 52**), as it frequently happens treating with geological means, where a non regular grid of sampling is common.

In a second step, the geostatistical analysis has been focused on single generations of exfoliation joints, treated one by one, with the aim to identify if also the geostatistical is able to capture the existing differences among generations of joints, which have been observed in situ. In this case, it is expected that the disposition and number of the photogrammetric models subdivided for generation (**Figure 53**) play a key role, affecting greatly the geostatistical procedures and results. The models belonging to the first generation of exfoliation joints are not enough numerous to carry out a significant geostatistical analysis, further more they are aligned, with direction SW–NE, so the anisotropy of the semivariogram would be strongly affected by this direction, rendering impossible the detection of the real main correlation direction. Furthermore, only short correlation should be found for the first generation, according to the distances among the models, which are shorter than those of other generations are. The models belonging to the second generation are more numerous and their disposition is more scattered, even if there is a preferential N–S direction, especially in the northern part, related to the main direction of the Hasli valley. Actually, it is quite common to find outcrops aligned along the axis of alpine valleys, but, for our purposes, it is necessary to understand how and how much this alignment affects the geostatistical analysis and therefore the results. For instance, with this sampling disposition, it is obvious to guess that the model number 35 should have a great influence on long distance correlations. Finally, the models belonging to the third generation of exfoliation joints are unevenly distributed in space and they do not follow any preferential direction. On the southern site, the models are located at short distances among themselves, while only three models (n° 6, 32 and 36) are located at far distances, but the models with medium distance lacks, this might cause a hole in semivariograms regarding medium distances.

3.5.1 Real trace lengths

The real trace lengths are the trace lengths cleaned from the censoring bias, and so only those of joints having both visible ends. This parameter has been used in the geostatistical analysis.

Before the construction of variograms, the data, having the lognormal distribution, have been transformed with the aim to obtain the normal distribution, through the Gaussian anamorphosis process. The so transformed real trace lengths of exfoliation joints have been investigated through the variogram analysis, according to the direction of measure. Since the farthest models are distant about 6 kilometres in the N–S direction (models number 1, on the north, and 22 on the south) and less than 5 kilometres in the E–W direction (model n° 31 on the western slope and 36 on the eastern slope), it is significant to look for correlations only shorter than 4 kilometres. Actually, the semivariograms are valid only below the distance computed as the semi-diagonal of the study area (Ciotoli & Finoia, 2005); the use of bigger distances leads to points in the variogram affected by too few pair of sampling positions.

The semivariograms have been constructed using two different lags, equal to 500 metres (**Table 23**) and 250 metres (**Table 24**), in order to verify if the invariance of scale found for the Valchiavenna case study is

still valid. The use of smaller lags is meaningless, due to the dimension of the investigated outcrops, which should not exceed the lag distance. The linear tolerance has been chosen equal to the half of lag, and the angular tolerance equal to 22.5°. For the variogram construction, the almost 3D domain, which considers the coordinates of latitude, longitude and elevation, has been analysed.

| TRACE LENGTH | Minimum | Mean | Maximum |
|--|--|--|--|
| Along strike | <p>112.5°/10°</p> <p>plot 14: variogram - azth=112.5, dip=10</p> | <p>112.5°-292.5°</p> <p>plot 13: variogram - azth=112.5, dip=0</p> | <p>135°/20°</p> <p>plot 20: variogram - azth=135, dip=20</p> |
| Along dip direction | <p>157.5°-337.5°</p> <p>plot 18: variogram - azth=157.5, dip=0</p> | <p>67.5°/20°</p> <p>plot 10: variogram - azth=67.5, dip=20</p> | <p>90°/20°</p> <p>plot 15: variogram - azth=90, dip=20</p> |
| Along both strike and dip direction | <p>225°/10°</p> <p>plot 7: variogram - azth=45, dip=170</p> | <p>22.5°/10°</p> <p>plot 4: variogram - azth=22.5, dip=10</p> | <p>45°/20°</p> <p>plot 10: variogram - azth=45, dip=20</p> |

Table 23 – Semivariograms of minimum, mean and maximum real trace lengths, calculated along strike, dip direction and considering all the data together, with lag equal to 500 metres

A clear, always constant, preferential correlation direction has not been individuated: semivariograms show different correlation directions, which vary with the considered parameter (minimum, mean or maximum trace lengths), direction of measure and lag, meaning that the disposition of sampling points does not affect too much the results. However, the correlation direction ESE–WNW (112.5°–292.5°), with a gentle dip, prevails (especially for short lag), although with some fluctuations (of 22.5° for azimuth and 10° dip angle), which are acceptable because close to the angular tolerance. The found direction recalls the previously described stage 3 of the shear zones, consisting of discrete brittle fracture and fault zones (Rolland et al., 2009).

The main correlation direction appears in all the variograms constructed along the strike, which show also the invariance of scale: changing the lag distance, the correlation direction and the structure of variogram are preserved, although with small fluctuations (of 22.5° for azimuth and 10° dip angle). The invariance of scale is globally honoured also in the other variograms, with the exceptions of mean trace lengths along dip, and minimum trace lengths considering strike and dip direction together. Along the dip direction, the main correlation towards ESE, with gentle dip, is respected only for mean and maximum trace lengths, with the shortest lag (equal to 250 metres); the minimum trace lengths have the main correlation towards NNW. With the longest lag (equal to 500 metres), the main correlation direction varies from ENE (67.5°) to SSE (157.5°), according to the considered parameter. This great variety of directions could depend on the fact that along the dip direction the sampling points and measurements are less numerous, leading to a bigger uncertainty with only few pairs of samples considered in the variograms. If all the data are considered together, a big variety of correlation direction arises. Decreasing the lag, the main correlation direction substantially changes, especially for minimum trace lengths. This could be because all data have been put together irrespectively of their direction of measure.

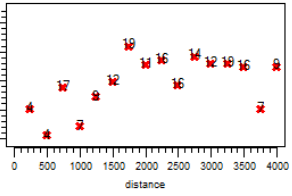
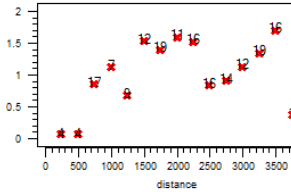
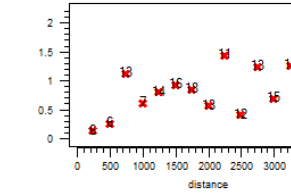
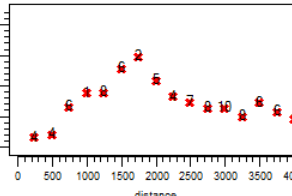
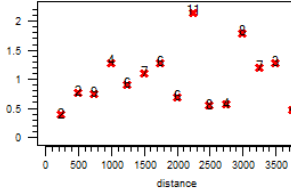
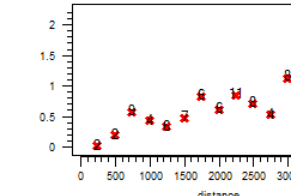
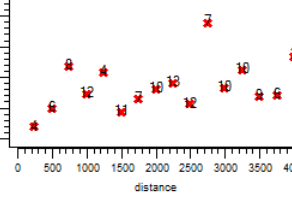
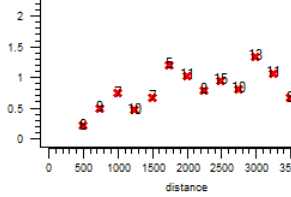
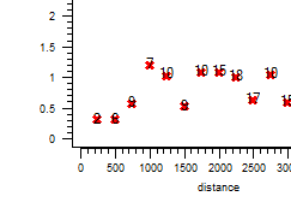
| TRACE LENGTH | Minimum | Mean | Maximum |
|--|---|---|--|
| Along strike | <p>112.5°/10°</p> <p>plot 14: variogram - azth=112.5, dip=10</p>  | <p>112.5°/10°</p> <p>plot 14: variogram - azth=112.5, dip=10</p>  | <p>135°/10°</p> <p>plot 19: variogram - azth=135, dip=10</p>  |
| Along dip direction | <p>337.5°/10°</p> <p>plot 17: variogram - azth=157.5, dip=170</p>  | <p>112.5°/10°</p> <p>plot 14: variogram - azth=112.5, dip=10</p>  | <p>112.5°/10°</p> <p>plot 14: variogram - azth=112.5, dip=10</p>  |
| Along both strike and dip direction | <p>45°/20°</p> <p>plot 10: variogram - azth=45, dip=20</p>  | <p>360°/10°</p> <p>plot 4: variogram - azth=0, dip=10</p>  | <p>22.5°/10°</p> <p>plot 4: variogram - azth=22.5, dip=10</p>  |

Table 24 – Semivariograms of minimum, mean and maximum real trace lengths, calculated along strike, dip direction and considering all the data together, with lag equal to 250 metres

Moreover, the dip angle assumes a strange behaviour: it very often dips towards E, but sometimes towards W. This inconstant rotation of the dip angle (and of the main correlation direction), changing the lag and the considered property, can indicate that a strong spatial relationship of real trace lengths lacks or that the variable has not been treated in the correct way.

Trying to explain this geostatistical behaviour, and reasoning on the exfoliation joints and their features, which are strongly related to the topography, it has been decided to subdivide the dataset according to the expositions of slopes, and so of exfoliation joints, into western and eastern slopes. On the western slope (i.e. the left hydrographical side of Hasli Valley) are located 28 photogrammetric models (**Figure 95**), having medium dip direction of slope and exfoliation joints towards East. The others 14 models pertain to the eastern slope (on the right hydrographical side of the valley), and have medium dip direction of slope and exfoliation joints toward West. Therefore, subdividing the dataset according to the direction of exposition of slopes, the variograms have been constructed, using only the shortest lag, due to the smaller investigated area.

| <i>TRACE LENGTH</i> | <i>Minimum</i> | <i>Mean</i> | <i>Maximum</i> |
|--|---|--|--|
| <i>Along strike</i> | <p>135°/10°</p> <p>plot 19: variogram - azth=135, dip=10</p> | <p>157.5°/10°</p> <p>plot 19: variogram - azth=157.5, dip=10</p> | <p>360°/20°</p> <p>plot 5: variogram - azth=0, dip=20</p> |
| <i>Along dip direction</i> | <p>337.5°/10°</p> <p>plot 17: variogram - azth=157.5, dip=170</p> | <p>135°/10°</p> <p>plot 19: variogram - azth=135, dip=10</p> | <p>315°/10°</p> <p>plot 17: variogram - azth=135, dip=170</p> |
| <i>Along both strike and dip direction</i> | <p>90°/10°</p> <p>plot 14: variogram - azth=90, dip=10</p> | <p>360°/10°</p> <p>plot 4: variogram - azth=0, dip=10</p> | <p>112.5°/20°</p> <p>plot 15: variogram - azth=112.5, dip=20</p> |

Table 25 – Semivariograms of real trace length data, calculated along strike, dip direction and considering all the data together, collected along the Western slope (with lag equal to 250m)

The variograms of western slope models are depicted in **Table 25**, while the 14 models of the eastern slope are too scattered and not enough numerous to find significant spatial correlations: the variograms have too many holes, becoming meaningless.

Considering only the data of the western slope, the variograms having the best structure are related to mean trace length values: the minimum trace length variograms have a remarkable nugget effect, and the maximum trace length variograms sometimes have high sill value (especially considering data along strike and dip direction together). Nevertheless, incoherent rotations of the main correlation direction again occur, however two main correlation directions result: NW–SE and N–S. The first direction mimics very well the mean orientation of the brittle faults, S1, of the shear zone 3. This main correlation direction has been identified only on the Western slope (especially along the strike), actually also the maps reported in **Figures 45, 46 and 48** show that in the study area these shear zones occur especially on the Western slope. The second direction N–S recalls the axis of the Hasli Valley, which has an N–S orientation. Although the meaning of changes in main correlation direction is hard to understand, it allows inferring that the disposition of sampling points (photogrammetric models) on the western slope does not influence the main correlation direction; otherwise, it will be always the same, despite of the considered parameter. The rotations of the main correlation direction of real trace lengths indicates that the parameter could not be treated as regionalized variable or that there is something misunderstood, maybe related to the not standard resolution of the photogrammetric models, leading to difference in measures.

Since in the data collection some differences have been founded among generations of exfoliation joints, the real trace length data have been subdivided and studied separately for each generation (**Table 26**).

The models of first generation are only 5, therefore not enough numerous to carry out a significant geostatistical analysis; moreover they are aligned with direction SW–NE (**Figure 53**), on the western slope, so variograms give results only towards NE, rendering impossible the detection of the real main correlation direction. Along the strike and considering all data together, the points seem to be correlated until 1 kilometre, but along the dip direction the spatial correlation is not visible. Actually, the distances among models do not allow finding complete variogram structures, although using the shortest lag (equal to 250 metres). Obviously, the constructed experimental variograms on generation 1 involve not enough pairs of sampling points and present too much holes between them to find the theoretical model that best fit them.

The second generation is the most diffuse in the study area, indeed 24 photogrammetric models are available. The models have a more scattered disposition than those of generation 1, even if their locations show some preferential alignments (N–S and NW–SE). The preferential N–S direction occurs especially in the northern part, and can be related to the orientation of Hasli valley. The variograms of mean trace length data, both along strike and along dip direction, show a preferential correlation direction having orientation N–S, even if without a very clean variogram structure. Considering all the data together, the variogram is clearer and has a main spatial correlation towards SE, with a gentle dip ($135^\circ/10^\circ$), with a sill close to one

and a range close 1000 metres. For this generation also minimum and maximum trace length values have been investigated through variographic analysis (**Table 27**).

| <i>MEAN TRACE LENGTH</i> | <i>1st generation</i> | <i>2nd generation</i> | <i>3rd generation</i> |
|---------------------------------------|---|--|--|
| <i>Along strike</i> | <p>45°/10°</p> <p>plot 9: variogram - azth=45, dip=10</p> | <p>180°-360°</p> <p>plot 3: variogram - azth=0, dip=0</p> | <p>112.5°/10°</p> <p>plot 14: variogram - azth=112.5, dip=10</p> |
| <i>Along dip direction</i> | <p>45°/10°</p> <p>plot 9: variogram - azth=45, dip=10</p> | <p>180°-360°</p> <p>plot 3: variogram - azth=0, dip=0</p> | <p>270°/20°</p> <p>plot 11: variogram - azth=90, dip=160</p> |
| <i>Along strike and dip direction</i> | <p>45°/10°</p> <p>plot 9: variogram - azth=45, dip=10</p> | <p>135°/10°</p> <p>plot 19: variogram - azth=135, dip=10</p> | <p>112.5°/10°</p> <p>plot 14: variogram - azth=112.5, dip=10</p> |

Table 26 – Semivariograms of mean real trace length data, calculated along strike, dip direction and considering all the data together, and subdivided for generation of exfoliation joints (with a lag of 250 metres)

The minimum trace lengths do not have a main preferential correlation direction: it results towards SSE along the strike, towards NW along the dip direction and towards ESE considering all the data irrespective of the direction of measurement. It follows that minimum trace lengths cannot be treated as regionalized variables, but this could be because the real shortest trace length value is often impossible to collect, moreover the smallest measurable value is strongly related to the resolution of photogrammetric models and to the distance from the outcrops, which change from model to model. Instead, the maximum trace lengths show more coherent and continuous variograms, having main spatial correlation towards ESE. Along the strike and considering all data together, sills are very high, denoting high variability in the dataset, and ranges (maximum correlation distances) are around 1 kilometre. Along the dip direction, both sill and range are remarkably smaller.

| <i>TRACE LENGTH</i> | <i>Minimum</i> | <i>Mean</i> | <i>Maximum</i> |
|--|--|--|--|
| <i>Along strike</i> | <p>157.5°/10°</p> <p>plot 19: variogram - azth=157.5, dip=10</p> | <p>180°-360°</p> <p>plot 3: variogram - azth=0, dip=0</p> | <p>112.5°/10°</p> <p>plot 14: variogram - azth=112.5, dip=10</p> |
| <i>Along dip direction</i> | <p>315°/10°</p> <p>plot 17: variogram - azth=135, dip=170</p> | <p>180°-360°</p> <p>plot 3: variogram - azth=0, dip=0</p> | <p>112.5°/10°</p> <p>plot 14: variogram - azth=112.5, dip=10</p> |
| <i>Along both strike and dip direction</i> | <p>112.5°/10°</p> <p>plot 14: variogram - azth=112.5, dip=10</p> | <p>135°/10°</p> <p>plot 19: variogram - azth=135, dip=10</p> | <p>112.5°/10°</p> <p>plot 14: variogram - azth=112.5, dip=10</p> |

Table 27 – Semivariograms of real trace length data, calculated along strike, dip direction and considering all the data together, and collected for the second generation of exfoliation joints (with lag equal to 250 metres)

Finally, there are 13 models belonging to generation 3, which are very unevenly distributed in space: they are very close on the southern part, while there are only three models (number 6, 32 and 36) disposed very far away; this disposition leads to incomplete variograms, lacking sampling points with an intermediate distance. Therefore the variograms of this generation have a clear structure for short distances (below 1500 metres), followed by a hole, and finally a few pair of points for long distances (above 2.5 kilometres). Detailed information on the structure of the variogram cannot be inferred from these graphs, but for sure the range is bigger than 1 kilometres. The main correlation direction is not clear, although the variograms towards ESE show a great continuity and correlation of points.

In conclusion, the variogram of real trace lengths, measured on exfoliation joints, does not show a main clear, always valid, preferential correlation direction. There are some incoherent rotations of main correlation directions, which have not been removed considering only one slope side or data subdivided according to the generation of exfoliation joints. However, the prevalent spatial direction towards ESE prevails, recalling the stage 3 of shear zones, consisting of discrete brittle fracture and fault zones, which are diffused

in the study area (**Figure 46**). In addition, the spatial direction towards N has been sometimes identified, especially for the second generation of joints, recalling the orientation of the main valley.

The variographic analysis of minimum real trace lengths illustrates a great variability in the main spatial direction, as well as in variogram structure. As consequence, this parameter can hardly be treated as regionalized variable in the study area, due to difficulties in collecting the minimum values and to the use of not constant cutoff value.

The mean and maximum trace length measured values are more continuous and show clearer spatial correlations, but without a main dominant constant direction, having a noteworthy geological significance, that allow best-fitting variogram models and performing estimation.

3.5.2 Mean spacing

The mean values of spacing are not normally distributed (**Figure 92**), therefore data have been transformed in order to obtain the Gaussian distribution required for the geostatistical analysis. Using the transformed values, variograms of mean spacing have been constructed, using different lags, respectively equal to 250 and 500 metres, with the aim to verify if the invariance of scale occurs also for this variable.

Considering all the data, divided according to the direction of measurement (along the strike and dip direction), the variograms (**Table 28**) have structures close to the classical theoretical models (especially along the strike), and are better than those obtained for the trace lengths.

| <i>MEAN SPACING</i> | <i>Lag = 250m</i> | <i>Lag = 500m</i> |
|----------------------------|--|--|
| <i>Along strike</i> | <p>90°-270°</p> <p>plot 13: variogram - azth=90, dip=0</p> | <p>112.5°/10°</p> <p>plot 14: variogram - azth=112.5, dip=10</p> |
| <i>Along dip direction</i> | <p>112.5°/10°</p> <p>plot 14: variogram - azth=112.5, dip=10</p> | <p>112.5°/10°</p> <p>plot 14: variogram - azth=112.5, dip=10</p> |

Table 28 – Semivariograms, along the maximum correlation direction, of spacing, subdivided for direction of measure

Globally the main spatial correlation direction is again towards ESE ($112.5^\circ/10^\circ$), and resembles the stage 3 of shear zones, which consist of discrete brittle fracture and fault zones.

The literature reports that the maximum variance in thickness (i.e. the minimum correlation direction of spacing) should be orthogonal to the main faults directions, therefore the maximum correlation should have the same direction of main faults, but this is true only in sedimentary rocks and considering synsedimentary faults, which influences the disposition and thickness of sediments. Variations in thickness are tightly linked to the action of synsedimentary tectonics that governs the creation of accommodation space available for the deposition of sediments (Franceschi et al., 2013).

In this case study, the faults and shear zones of stage 3 formed before the exfoliation joints, and it is unlike that they controlled the spacing variations of exfoliation joints. Therefore, it is reasonable that the occurrence of the main correlation direction towards ESE, with a gentle dip, does not find any geological response (in term of correspondence with the tectonic elements, etc.), thus it seems to be mainly related to the disposition of sampling points. Moreover, this main correlation direction is not always honoured: it occurs along the dip direction, for both short and long lag distances, and along the strike, but only with the longest lag. The short lag has main correlation direction towards E–W.

Along the strike, the ranges reach about 2 kilometres, with a sill near the unit, whilst, along the dip direction, the sill is higher than 1 and the variogram with short lag presents two pairs of points having high variance although they are located very near (250 metres). However, it is worth to note that spacing values along dip direction are only sort of lateral spacing, while the real classical spacing is that measured along the strike.

Since the variogram results seem quite promising, although a slight rotation of main correlation direction has been still observed, experimental variograms, obtained using $\frac{3}{4}$ of the available models, has been fitted with theoretical models. Not all the models have been considered, with the aim to leave some models for the validation of results. It has been observed that if only the half or $\frac{2}{3}$ of models are considered the resulting variogram is not enough representative, while the use of the $\frac{3}{4}$ of models to construct the variogram and the remaining $\frac{1}{4}$ to validate the results seems to be a good compromise. In this case, 32 models, randomly chosen, have been used to construct the variograms of mean spacing along the strike (**Table 29**) and 10 to validate the results. The variograms have been constructed with the short lag, in order to capture also the small heterogeneities, and show a main correlation direction again towards ENE.

The parameters best fitting the experimental variograms have been reported in **Table 30**. The chosen theoretical model is the Gaussian one, due to the features of the variogram near the origin, which show that the first two points of the variogram have almost the same variance. The nugget effect is quite low, the sill is slightly above one, while the maximum range overpasses 1 kilometre and the medium range is around 300 metres. The minimum range, being vertical and lacking the deep data, has been assumed the same order of magnitude of the grid used for the estimation process.

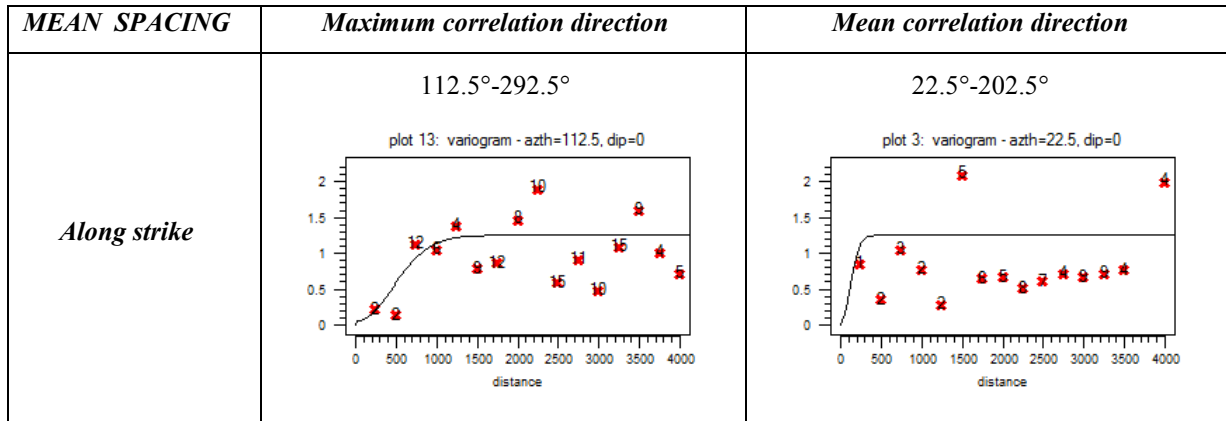


Table 29 – Models of variograms of mean spacing, along strike, with 250 metres lag, obtained considering 32 photogrammetric models, along the strike

| <i>MEAN SPACING</i> | | | |
|-----------------------------|----------------|---------------|----------------|
| <i>Models with 250m lag</i> | <i>Maximum</i> | <i>Medium</i> | <i>Minimum</i> |
| Correlation direction [°] | 112.5-292.5 | 22.5-202.5 | 112.5/90 |
| Range [m] | 1120 | 280 | 120 |
| Kind of model | Gaussian | | |
| Nugget effect | 0.05 | | |
| Sill | 1.30 | | |

Table 30 - Values of theoretical variogram models used to fit the experimental variograms

According to the methodology found for the Valchiavenna case study, the estimation has been performed using the sequential Gaussian simulation approach – SGS – with 100 realizations.

Since the parameters used to fit the experimental variograms reveal a strong spatial anisotropy, with an anisotropy ratio around four, the measurements inside an ellipsoidal research region (with axes parallel correlation directions) have been considered to perform the estimation process. In order to take into account the irregularity of data distribution and the nugget effect, the axes of ellipse have been computed doubling the ranges. Inside each ellipsoid, a minimum of three and a maximum of twelve data have been considered.

The results (reported in **Figure 95**) show a too systematic variation of spacing with gradual changes of spacing values, which does not occur in joint spacing on outcrops, where not uniform variations of joint spacing, with also sharp changes (**Figure 96**), are frequent. This is observable especially in the igneous rocks encountered in Hasli Valley. Actually the validation of results (**Figure 97**), carried out considering 10 photogrammetric models, show a very bad correspondence between measured and estimated spacing: small values of spacing have been overestimated, while medium and high ones underestimated. In conclusion, the variograms constructed using 32 models are not able to capture the spatial variation of spacing, which maybe does not occurred in the considered direction.

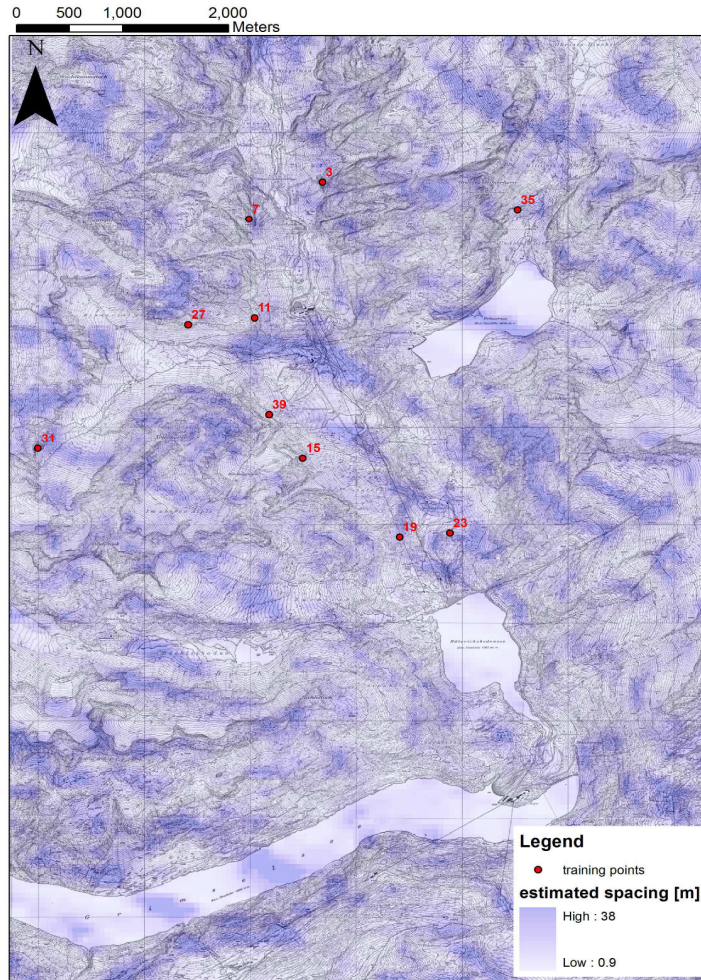


Figure 95 – Estimated mean spacing values (along the strike), through sequential Gaussian simulation considering data from 32 photogrammetric models. The red points are the 10 models used in the validation process



Figure 96 – Example of sharp variation in joint spacing, on the right hydrographical side of Raeterichsbodensee

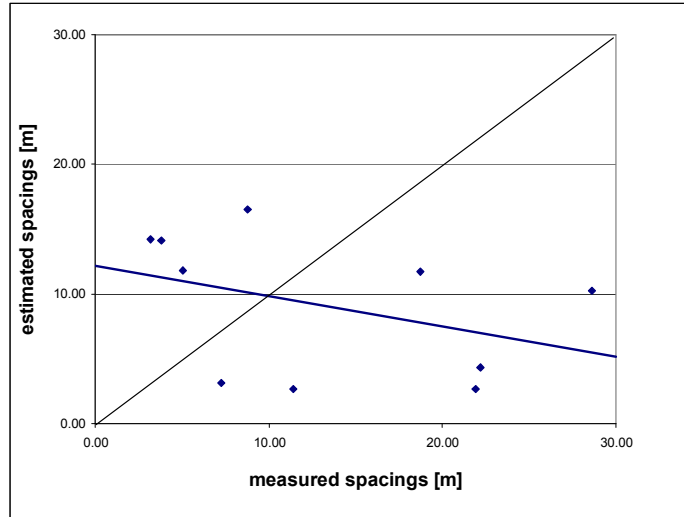


Figure 97 – Comparison between measured and estimated joint spacing of training point dataset

An additional effort has been done to investigate the possibility to define exfoliation joint spacing variability. Exfoliation joints are strictly related to the topography, and to take into account this fact, the dataset has been subdivided according to the dip direction of the slope.

On the Eastern slope (Table 31), correlations are identifiable only along the strike, indeed, there are few models, and so the pairs of data are not enough to find significant correlations, especially along the dip direction. The variograms have now a main correlation direction towards N, parallel to the axis of the main valley, and this is quite strange, because the considered dataset, belonging to the Eastern slope (i.e. to the left hydrographical side), has dip direction towards West.

| MEAN SPACING | Lag = 250m | Lag = 500m |
|--------------|---|---|
| Along strike | <p>360°/10°</p> <p>plot 4: variogram - azth=0, dip=10</p> | <p>360°/10°</p> <p>plot 4: variogram - azth=0, dip=10</p> |

Table 31 – Semivariograms, along the maximum correlation direction, of spacing, measured on the eastern slope

Considering only the data coming from the models located on the western slope (Table 32), a constant main correlation direction cannot be found, the best correlation direction changes with the lag and the direction of measures too. The prevalent correlation direction is towards NNE, with small dip angle. The previously found direction ESE–WNW is now honoured only for the variogram with short lag computed along the strike, therefore the mean spacing are not so strong correlated in this direction.

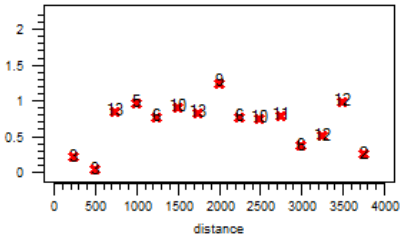
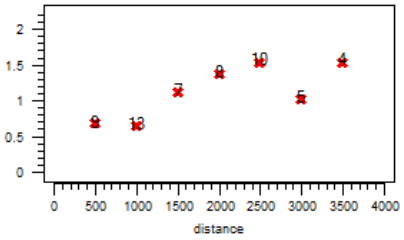
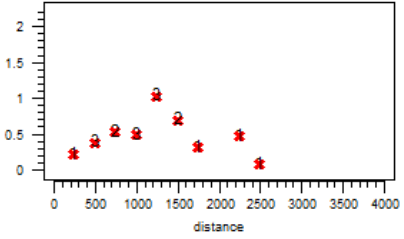
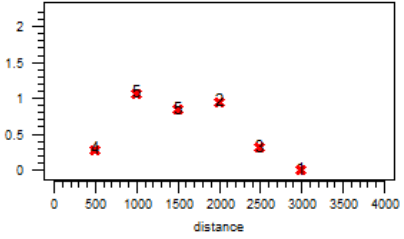
| <i>MEAN SPACING</i> | <i>Lag = 250m</i> | <i>Lag = 500m</i> |
|----------------------------|--|--|
| <i>Along strike</i> | <p style="text-align: center;">112.5°-292.5°</p> <p style="text-align: center;">plot 13: variogram - azth=112.5, dip=0</p>  | <p style="text-align: center;">22.5°/10°</p> <p style="text-align: center;">plot 4: variogram - azth=22.5, dip=10</p>  |
| <i>Along dip direction</i> | <p style="text-align: center;">22.5°/20°</p> <p style="text-align: center;">plot 5: variogram - azth=22.5, dip=20</p>  | <p style="text-align: center;">45°/20°</p> <p style="text-align: center;">plot 10: variogram - azth=45, dip=20</p>  |

Table 32 – Semivariograms, along the maximum correlation direction, of spacing, measured on the western slope

Since the subdivision for slope orientation give not good results, and considering the wide dissimilarity founding according to the exfoliation joint generations, the data have been subdivided for generation of exfoliation joints, even if the variograms of the generation 1 and 3 cannot be considered as significant.

Actually, the models of generation 1 are only five and are aligned in the direction SW–NE, hence the variograms can be performed only along this direction, and so are without a global spatial sense.

Regarding the generation 3, the disposition of models, although more numerous than those of generation 1, creates again incomplete variograms, with a big white hole in the middle, which does not allow to understand the real structure of the variogram.

The variograms obtained from the models of the second generation of exfoliation joints (**Table 33**) show two main correlation direction: towards N along the strike, and W–E along the dip direction. The variograms, along the strike, have sills close to one and ranges of about 1.5 kilometres, while variograms along the dip direction exhibit higher sill values than those along the strike, and ranges which vary on the considered lag (from less than 1 kilometre with the shortest lag distance, to 2.5 kilometres considering the longest one).

Since the real spacing is along the strike, it is reasonable that exfoliation joints exhibit a main correlation direction that is the same of the topography, and so of the main valley, $\frac{3}{4}$ of the models, belonging to generation 2, have been used to construct the experimental variograms (**Table 34**).

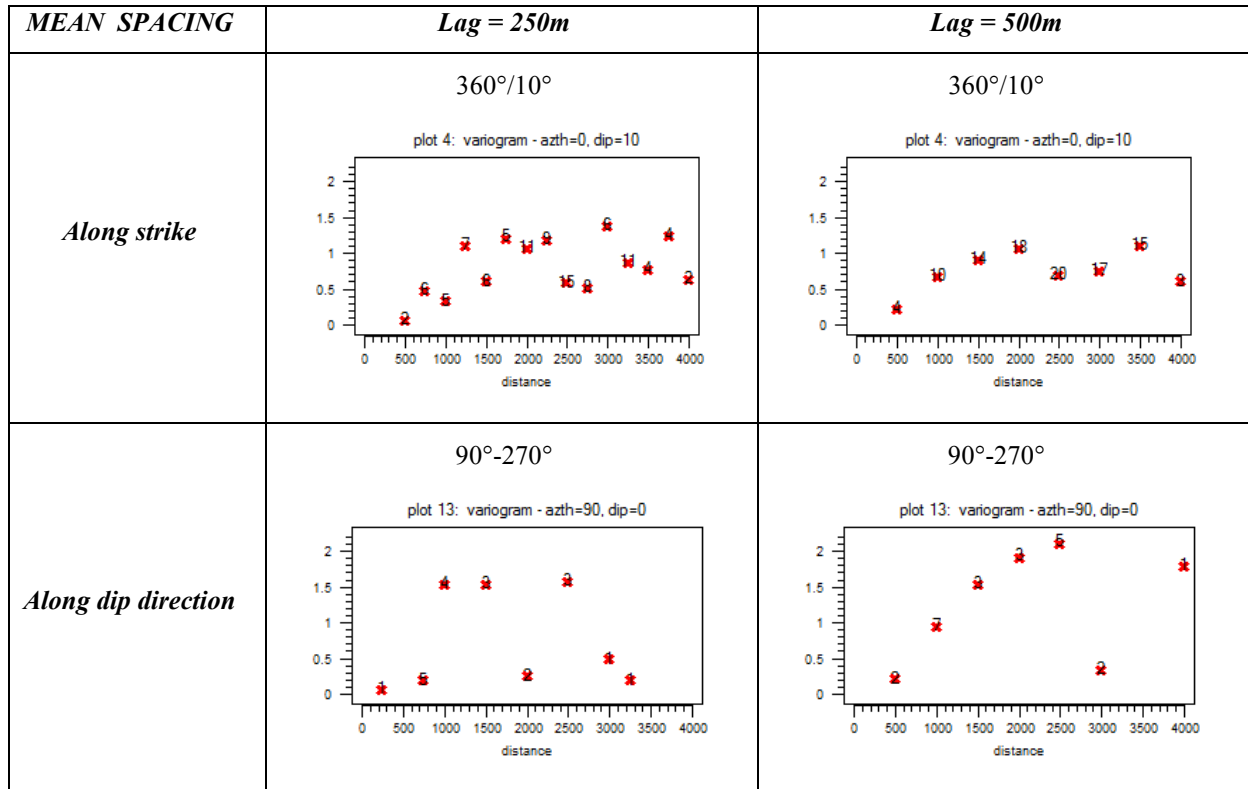


Table 33 – Semivariograms, along the maximum correlation direction, of spacing of joints belonging to generation 2

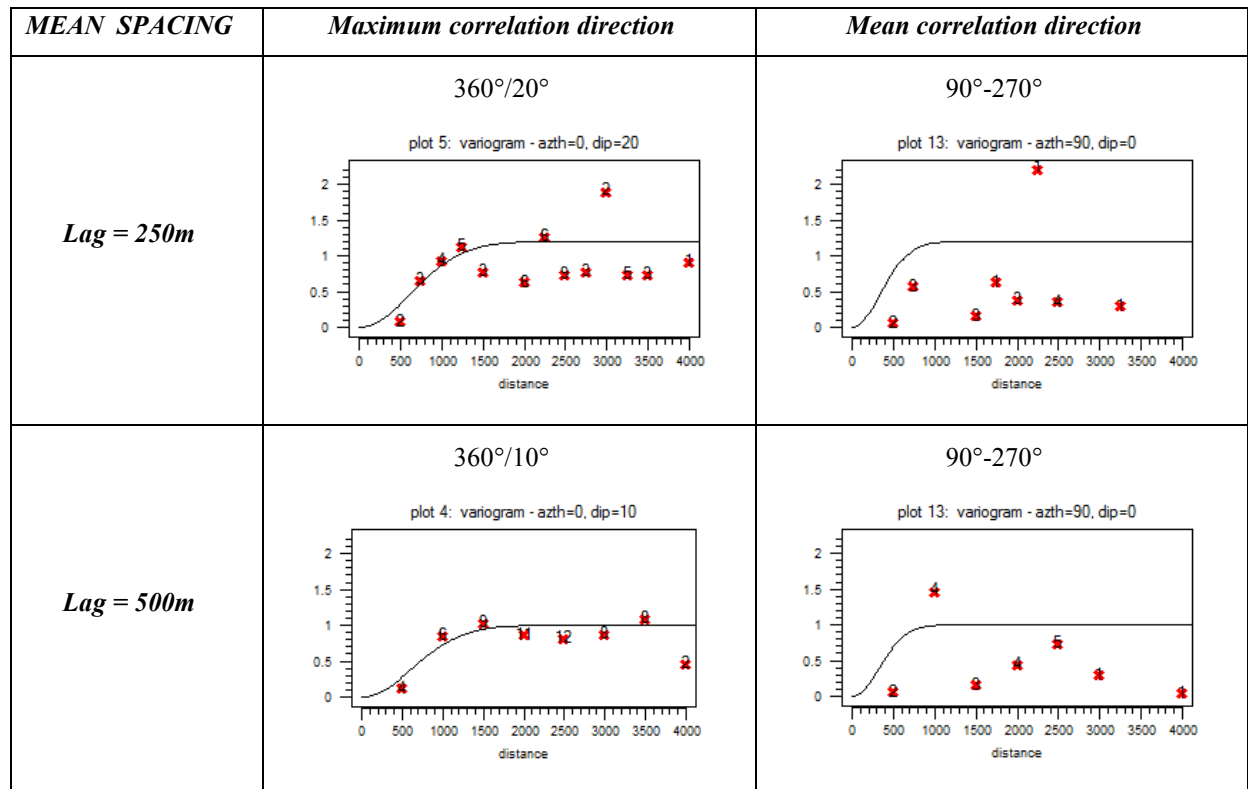


Table 34 – Theoretical models used to fit the experimental semivariograms of mean spacing, which have been measured on 18 photogrammetric models belonging to generation 2 of exfoliation joints

These variograms have been fitted by theoretical models (with parameters summarized in **Table 35**), which have been used to estimate spacing values (**Table 36**), using the SGS approach, with 100 simulations.

| <i>18 models of generation 2</i> | <i>250 metres lag</i> | <i>500 metres lag</i> |
|-----------------------------------|-----------------------|-----------------------|
| Kind of model | Gaussian | Gaussian |
| Nugget effect | 0 | 0 |
| Sill | 1.2 | 1 |
| Maximum correlation direction [°] | 360/20 | 360/10 |
| Maximum range [m] | 1530 | 1520 |
| Mean correlation direction [°] | 90-270 | 90-270 |
| Mean range [m] | 850 | 800 |
| Minimum correlation direction [°] | 180 / 70 | 180 / 80 |
| Minimum range [m] | 120 | 120 |

Table 35 - Values of theoretical variogram models used to fit the experimental variograms

The invariance of scale is now respected: the main features and parameters of variogram models remain almost the same, although considering different lag distances. With the shortest lag, the sill is bigger, and so the variability is higher, because also the small heterogeneities, which are neglected considering the longest lag, are taken into account. The decrease of sill with the increase lag has been already observed also in the Valchiavenna case study. The ranges remain more or less the same, despite the lag distance.

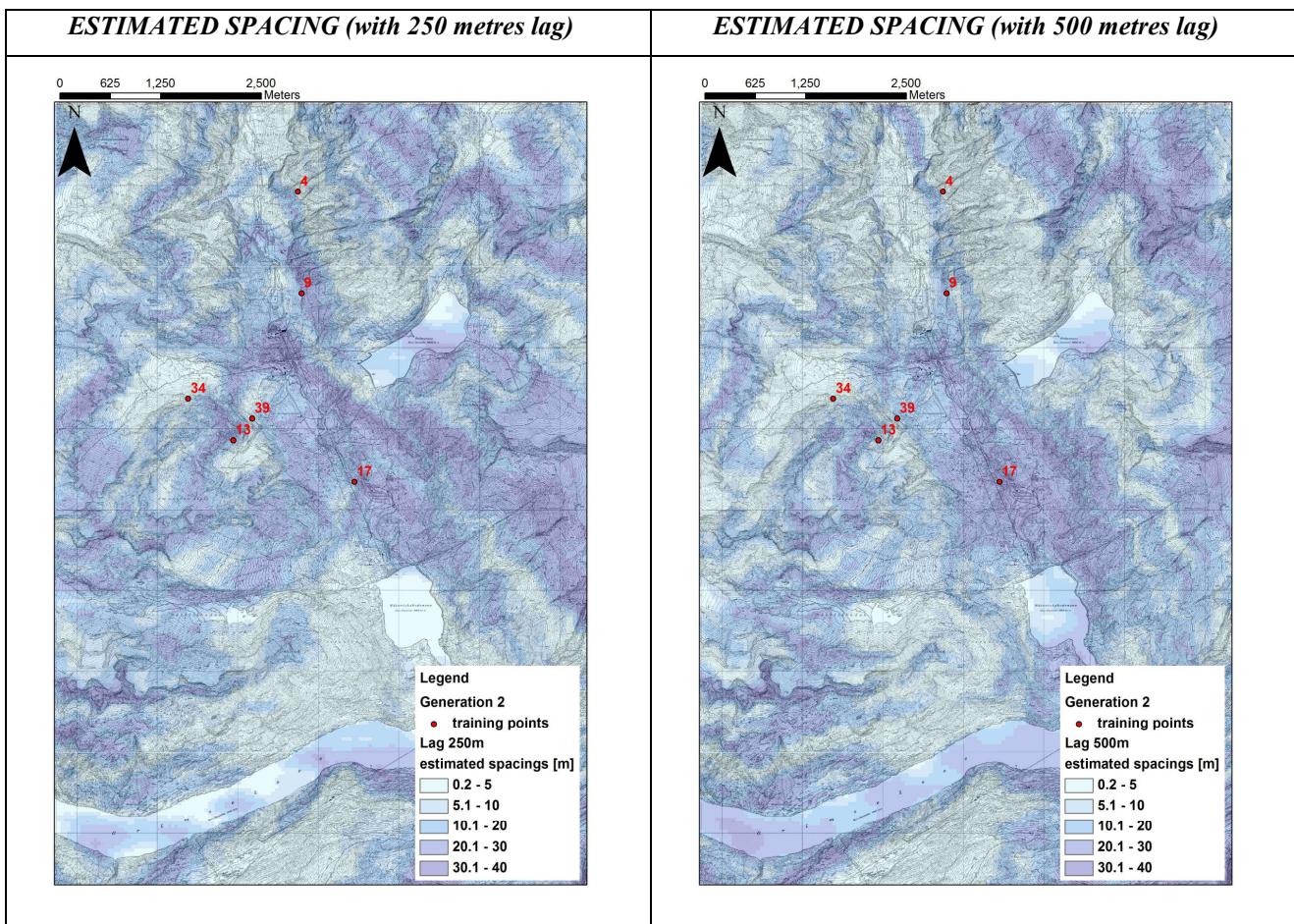


Table 36 – Estimated mean spacing values (along the strike), obtained from sequential Gaussian simulation, considering data from 18 models belonging to the second generation of exfoliation joints. The six red points are the models used in the validation process

The obtained maps are representative of the study area; actually, the pattern of spacing and the spatial distribution are similar to the spacing values observed in situ. At high elevations, where the freezing-thaw cycles are frequent and contribute to the fracturation of rock masses, low spacing values are obtained, even if no photogrammetric models are located at so high altitudes. Moreover, on the left hydrographical side of the lake Raeterichsbodensee, exfoliation joints are characterized by low spacing and this is respected in **Table 36** (especially considering the shortest lag distance). At the same way, bigger spacing values are observable along the valley, and this is respected in the map. The very strange fact is that spacing variations are mostly related to change in generation of exfoliation joints, while these maps, considering only data of the second generation of exfoliation joints, are able to describe all the variations of spacing.

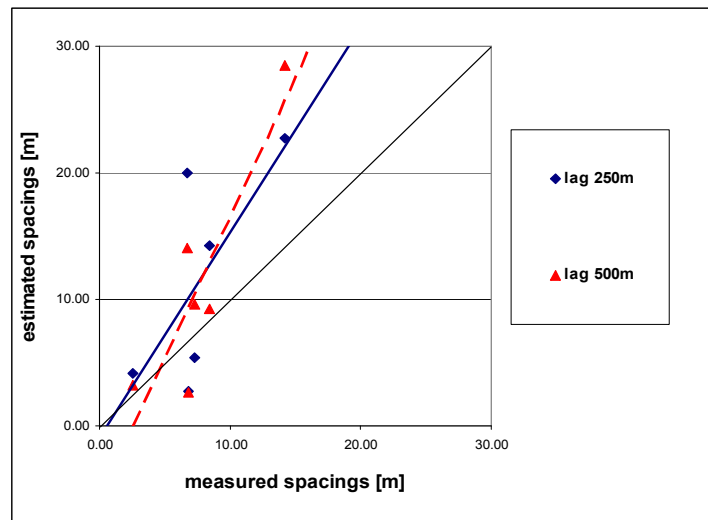


Figure 98 – Comparison between measured and estimated joint spacing of training point dataset. The rhombuses and solid line refer to the model with lag of 250 metres, while the triangles and dashed line refer to model with lag of 500 metres

The validation has been carried out considering six photogrammetric models, comparing the measured with the estimated spacing values (**Figure 98**); the agreement, considering only the second generation, is decisively better than that obtained considering all the data together, in spite of the generation of exfoliation joints. There is a tendency to overestimate the big values of spacing, especially using the longest lag.

3.5.2.1 Comparison with in situ surveys

Regarding the spacing, there is the possibility to consider also data coming from in situ surveys, collected from Martin Ziegler, who estimated the minimum and maximum spacing of the exfoliation joints occurring in 254 different locations (**Figure 99**).

Actually, the direct comparison between spacing values estimated from photogrammetric models, using geostatistical technique, and spacing values observed in situ, during the infield surveys, is not possible and reasonable, due to the different resolution in measurements, which commonly are more accurate using the direct observation (in situ survey), and also to the different approach.

From the photogrammetric models the spacing values have been directly measured, while during the in situ surveys they have been estimated, using classes of values.

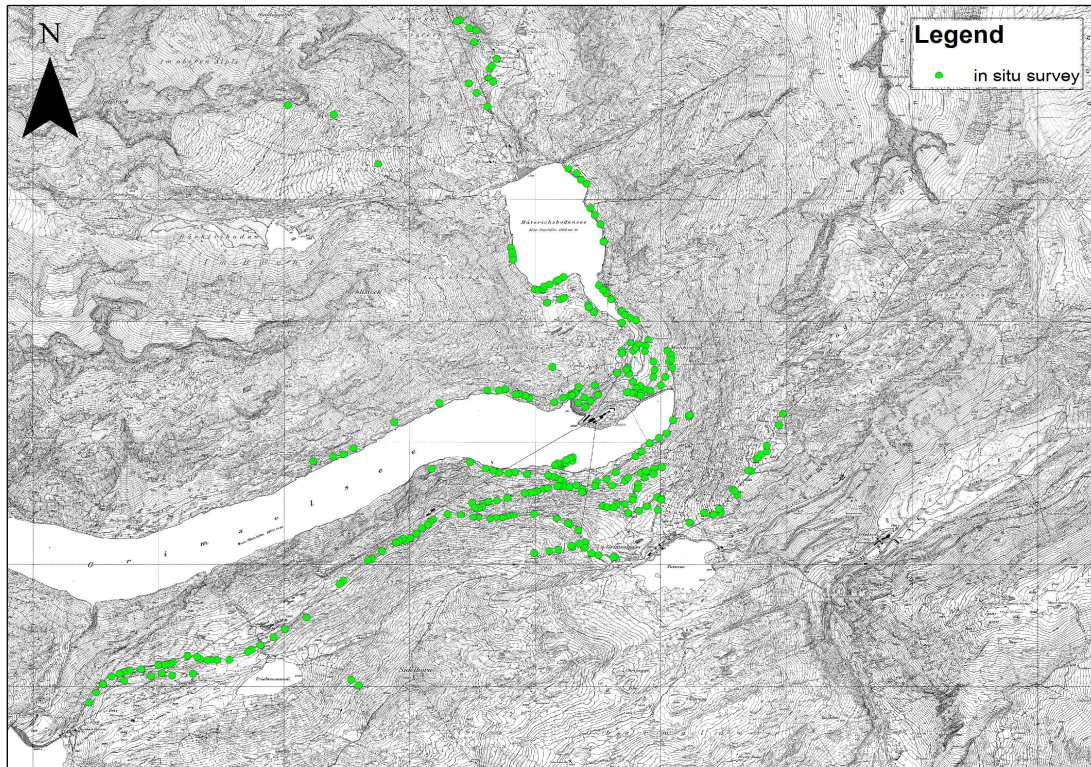


Figure 99 – Locations of in situ surveys (data collected from Martin Ziegler)

With the aim to verify if, also in this context, the spacing can really be treated as a regionalized variable, data of spacing coming from in situ survey have been considered, treating them as an independent dataset, with the aim to verify if the main correlation direction found for the photogrammetric models is still valid.

Obviously, moving from a continuous to a categorical variable (i.e. with classes of values) the geostatistical approach change: it is again based on the four main steps previously described (Exploratory Spatial Data Analysis, variography, prediction and validation), but the data need a transformation.

During the in situ surveys, the minimum spacing have been distinguished using the following values (expressed in centimetres): 0, 2, 6, 20, 60, 100, 150, 200, 300 and 400, while the maximum spacing have been estimated reporting the following values (expressed in centimetres): 6, 60, 100, 150, 200, > 200, 250, 300, > 300, 400 and 600. The mean spacing values have been computed averaging out the values of minimum and maximum spacing in each locations.

Since the infield estimations of maximum and minimum spacing have been done mostly in a qualitative way (**Figure 100**), without carrying out a statistical significant number of measures, all the values of spacing have been reclassified (**Figure 101**), with the aim to consider fixed thresholds between classes.

The spacing values have been subdivided in seven classes (**Table 37**), according to the thresholds reported in the ISRM guidelines for the quantitative description of discontinuities in rock masses (ISRM, 1978).

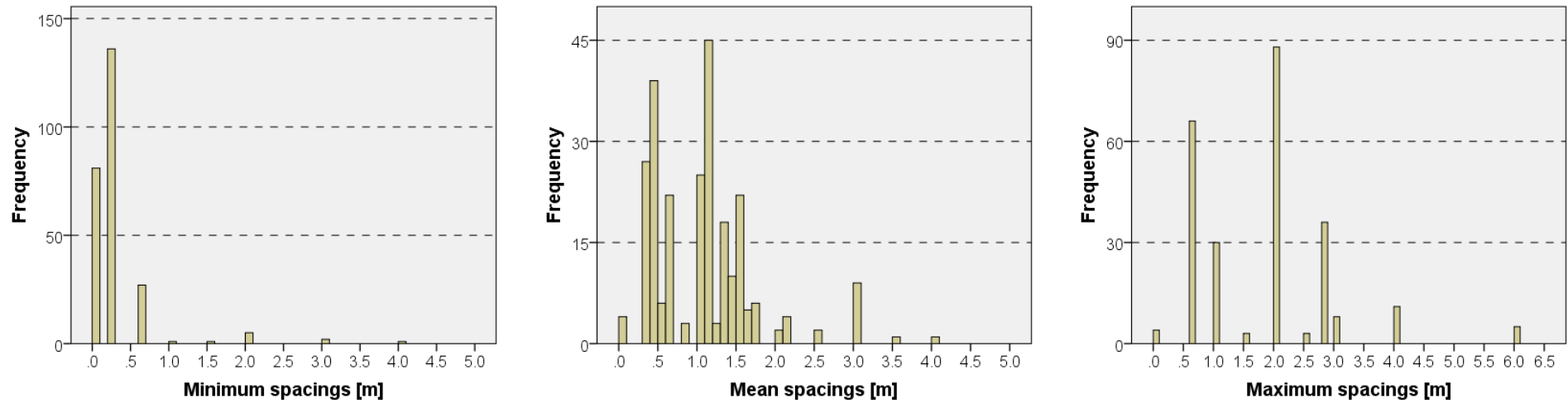


Figure 100 – Frequency histogram of spacing values of exfoliation joints observed during in situ surveys: it is clear that the values of minimum and maximum spacing, being discrete and not continuous values, have been estimated for classes. The mean spacing have been calculated, in each location, averaging out the minimum and maximum values

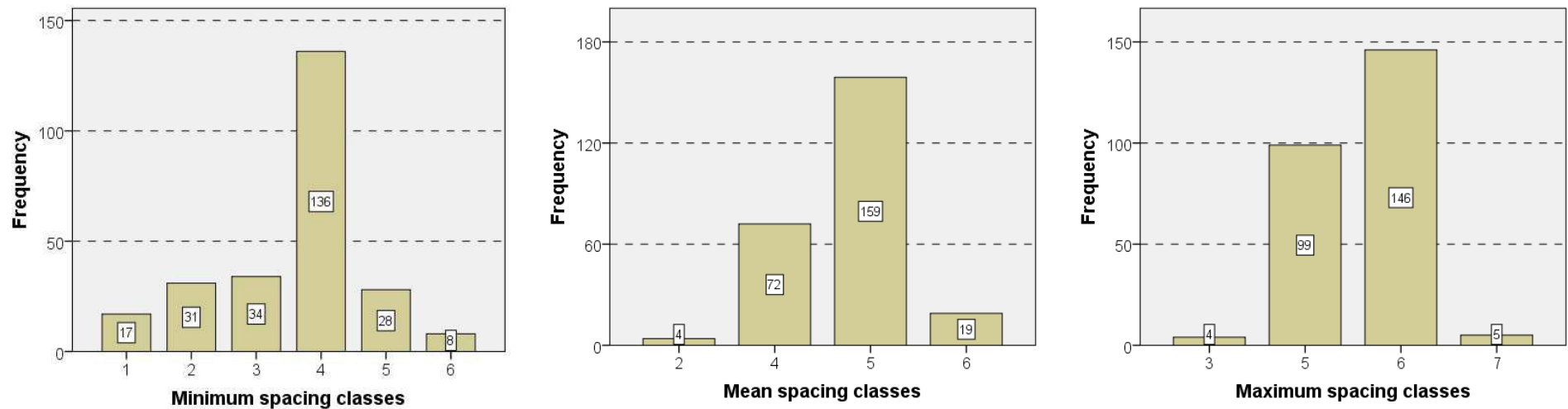


Figure 101 – Frequency histogram of spacing observed in field, reclassified according to the ISRM thresholds (ISRM, 1978), reported in Table 37

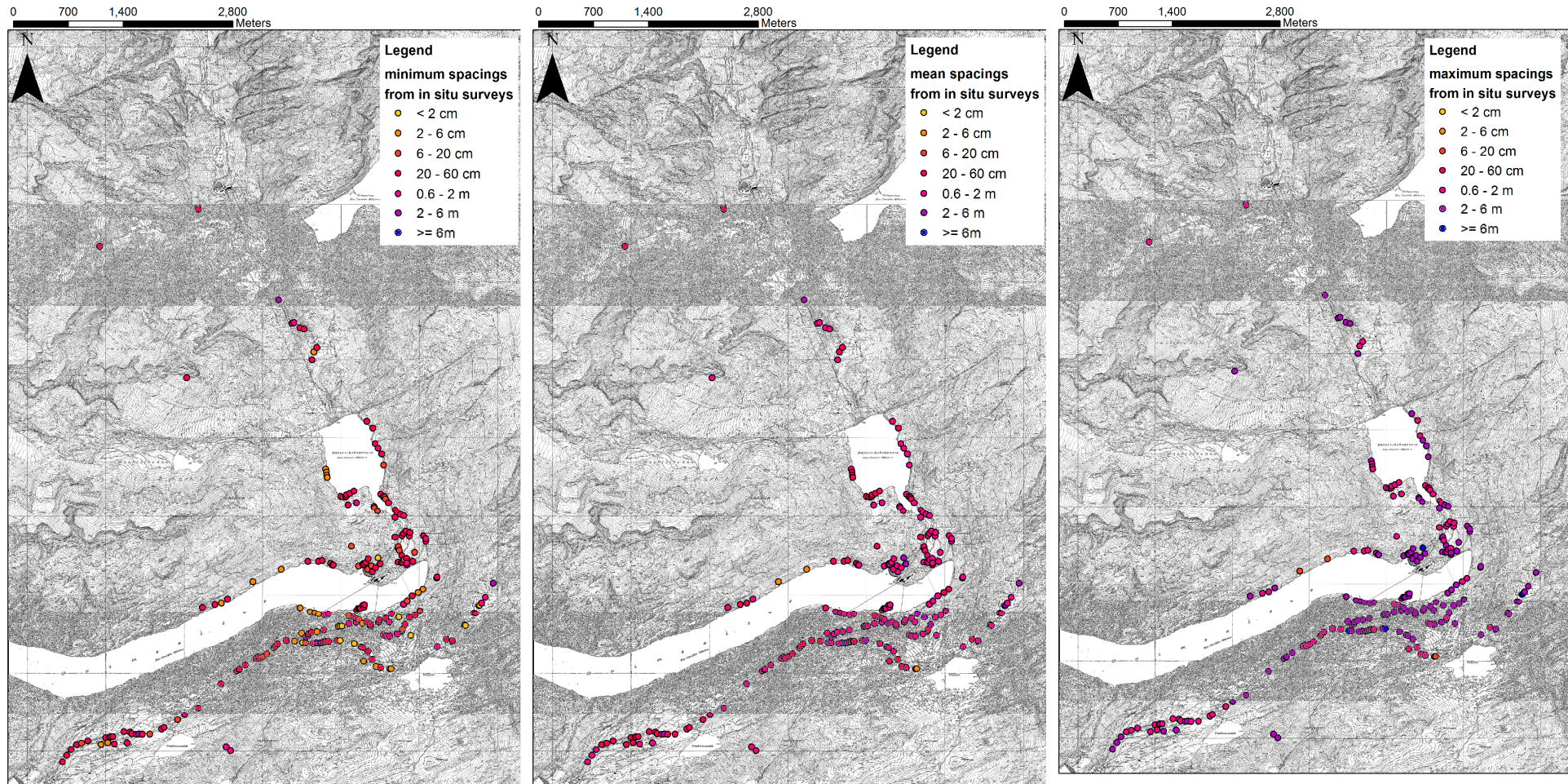


Figure 102 – Spatial distribution of in field spacing observations, about minimum, mean and maximum spacing values, reclassified according to the ISRM thresholds (ISRM, 1978)

| <i>Class n°</i> | <i>Values of spacing [cm]</i> | <i>Description</i> |
|-----------------|-------------------------------|--------------------|
| 1 | < 2 | extremely narrow |
| 2 | 2 ÷ 6 | very narrow |
| 3 | 6 ÷ 20 | narrow |
| 4 | 20 ÷ 60 | moderately large |
| 5 | 60 ÷ 200 | large |
| 6 | 200 ÷ 600 | very large |
| 7 | ≥ 600 | extremely large |

Table 37 – Classes of joint spacing, determined from in situ observations

The values of reclassified minimum, mean and maximum spacing have been reported in **Figure 102**, related to the location of measures.

The sampling points, very numerous, are disposed very near, and are mainly aligned along the roads. It will be therefore necessary to shorten the lag distance of variograms. Some preferential correlation direction might be found along the road alignments. With the aim to choose the main features necessary to construct the variogram the disposition of sampling points must be taken into account: the farthest models are distant about 6 kilometres in the E–W direction and almost 7 kilometres in the N–S direction, although clustered in the Southern part, 4 kilometres long. Thus, it is significant to look for correlations no longer than 3 kilometres, but considering the short distances among models in the Southern part and the plentiful number of observations, reflecting local characteristics, the lags have been chosen equal to 50 and 100 metres, with resulting maximum distances respectively of 1 and 2 kilometers.

A comparison between in situ surveys and estimation from photogrammetric models could be done only if also the results of photogrammetric models are reported according to the IRSM classes. Although using reclassified data for both measured in situ and estimated spacing, a direct comparison between the results of geostatistical estimation of spacing and in situ observations of rock masses cannot be performed, because of the different scales of observations: spacing values measured on photogrammetric models are always bigger than those taken directly on rock outcrops. It has been already reported that sampling bias in measurements from photos often lead to the omission of smaller spacing (Rives et al., 1992), while during in field studies large spacing are often ignored (Kulatilake & Wu, 1984), and thus from in situ approach the small spacing values are represented more relative to large values. Moreover, at the Grimsel site, in field data have been collected especially along roads, where the excavation method (i.e. blasting) greatly affects the spacing of the rock mass.

Reclassifying the spacing values of photogrammetric models, most of them fall inside the class n°7 (i.e. spacing bigger than 6 metres), which have been reported only five times (for maximum spacing) in observations in situ. Even comparing the mean estimated spacing values (by SGS), reclassified according to ISRM values, with the maximum spacing observed in situ, it is worthy to note that the former are always bigger than the latter (**Figure 103**).

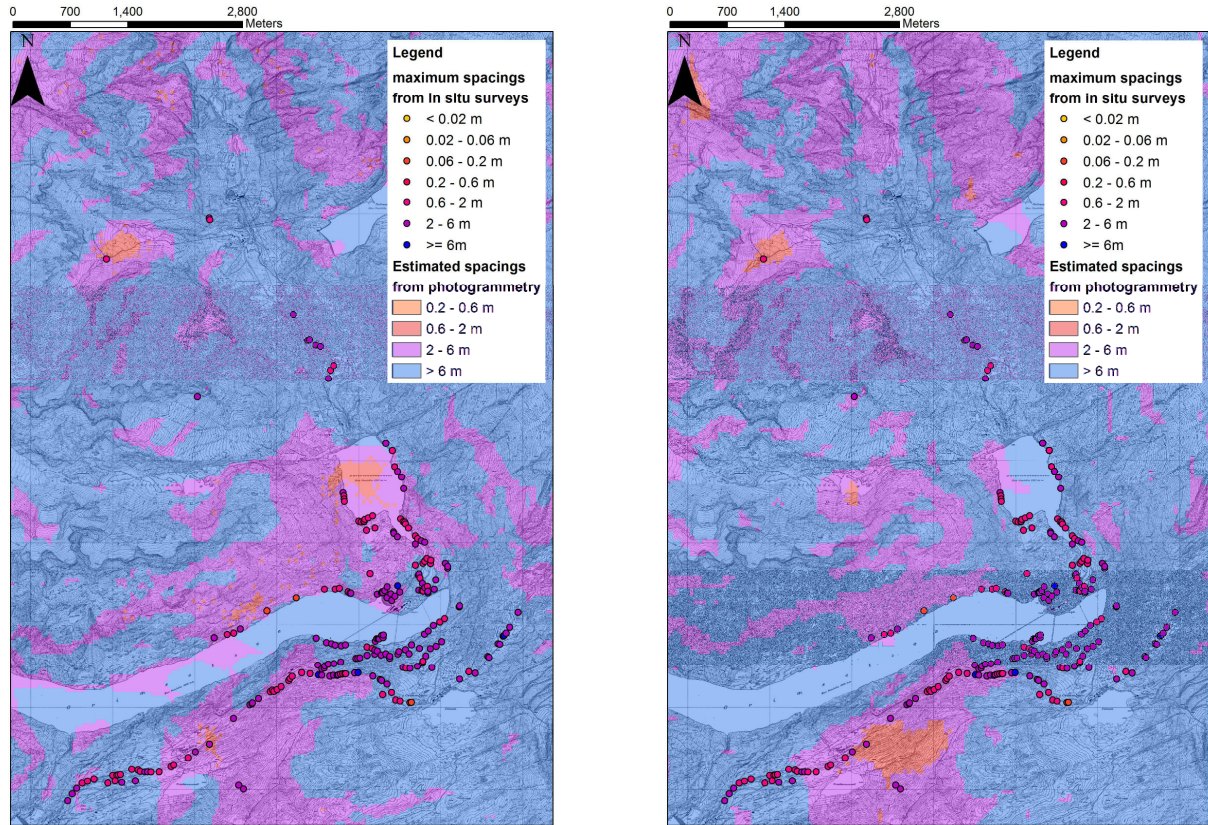


Figure 103 – Comparison between maximum spacing observed during in situ surveys and mean spacing estimated from photogrammetric models by sequential Gaussian simulations (with lag of 250 m on the left and 500 m on the right)

The spacing from in situ survey, being its values in classes, is a categorical variable (i.e. characterized by discrete values) and cannot be treated such as a numerical, continuous variable. The employment in geostatistics of variables described in classes, requires the indicator approach, which consists of the binary transformation of sample population. Defining indicators for categorical variables would lead to the following non-linear transformation of data value, into either a 1 or a 0:

$$i(\bar{u}_\alpha; z_k) = \begin{cases} 1, & \text{if } z(\bar{u}_\alpha) \leq z_k \\ 0, & \text{otherwise} \end{cases}$$

where $i(\bar{u}_\alpha; z)$ is the indicator transform at location \mathbf{u}_α depending on the presence of a specified z_k (in this case the specified class of spacing), and $z(\bar{u}_\alpha)$ is the observed categorical realization at location \mathbf{u}_α . In other words, using this method, each attribute to be modelled is described through a binary indicator variable that takes the value 1 if that attribute is encountered at a given location, and 0 if not.

The indicator approach is very often used, not only for categorical variables, because it is nonparametric: it does not need any assumption concerning the distribution of the modelled variable (i.e. the Gaussian distribution of data is not required). However, one has to be aware that the indicator transformation always implies a loss of information (Marinoni, 2003). Especially in the case of categorical variables, it does not play

a role whether, for instance, in our class 6 the spacing is 2 or 4 meters: in either case, an indicator of 1 would be assigned to and the extra information about significant small or big spacing value is lost.

Performing the estimation of binary-transformed indicator values requires the knowledge of the spatial correlation, which can be achieved through the indicator semivariogram, calculated on the binary-transformed indicator population. Multiple indicator variograms, one for each threshold value, are necessary and they cannot be modelled independently one from on other and must verify a few necessary order relations (Journel & Posa, 1990). The main advantage of the computation of indicator variograms, although it is very time-consuming, is the possibility to handle different anisotropies at different cutoffs. If the anisotropy changes too much between adjacent thresholds, the order relations violations become prohibitively large. Typically, experimental indicator semivariograms at extreme threshold values tend to be a bit erratic; indeed, for such extreme classes, the indicator variogram value depends on the spatial distribution of few data pairs. Actually, also in this case of study, the extreme classes of spacing tend to have decisively few or even no data values (**Figure 101**), which render the indicator variogram of these classes not comparable with those of the central classes, where a lot of data are present. Obviously if no or also all values fall inside a given class, the resulting indicator variogram will be a straight line (**Figure 104**), because, after the indicator transformation, all the data will be described by the same code (0 or 1), and so no variance among values will be identifiable in the dataset.

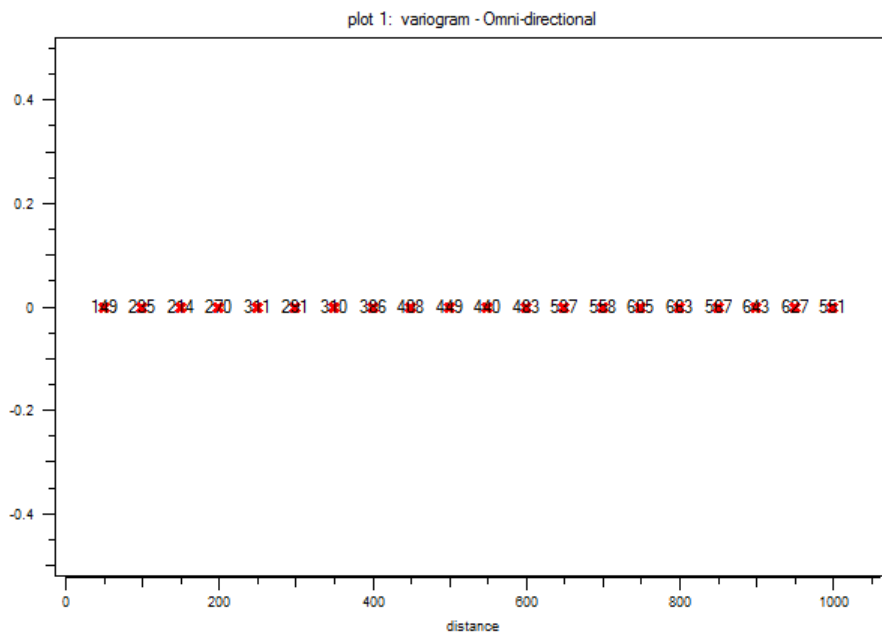


Figure 104 – Indicator semivariogram computed for the class n°3 of mean spacing, within no data values are present: all the pairs of points, being described by the code 0, have the same variance, resulting in a straight line of variogram. The variogram is the same in each direction, only the number of the involved pairs of sampling points changes with the direction

The minimum spacing values derived in field are included in the first six classes (n°1÷6) of spacing, no one value is within the biggest class (n°7). On the contrary, the maximum spacing values are obviously enclosed in the bigger classes and not in the smallest: the values fall inside the class n° 3, 5, 6 and 7, even if classes n°3 and n°5 contain very few values (respectively 4 and 5 data). The mean spacing show a better

The maximum correlation direction is again a bit erratic, but it is again mostly oriented WNW-ESE, although a geological reason about the occurrence of this main orientation eludes. The exception regards the class n°4 and 6: the former is towards ENE for the shortest lag but this could be related to the disposition of sampling points (**Figure 56**), and the latter is towards N for the shortest lag, recalling the direction previously founded from photogrammetric models, which effectively investigate the long spacing.

Changing the lag distances not enormous changes occur in the variogram: the main correlation direction remains approximately the same, although with small fluctuation of 22.5° , which are acceptable, because equal to the angular tolerance used to construct the semivariograms. The exception regards the class n°6, within there is a remarkable difference (67.5°) between the shortest and longest lag distance. Actually, the variograms computed for the extreme classes (which for the mean spacing are the classes n°2 and 6), have structures not as clear as central classes: the pairs of points in the variograms are more scattered.

The sill of the experimental indicator semivariogram varies from class to class, but it remains the same within the same class, in spite of the lag distance used. In fact the sill should be roughly equal to the indicator variance of the class, $F(z_k)[1-F(z_k)]$, where $F(z_k)$ is the mean of the indicator data $i(\mathbf{u}_\omega; z)$ (Goovaerts, 1997). Actually, when comparing indicator semivariograms at different threshold values, it is a good practise to standardize their sills to one dividing the semivariogram values by the indicator variance. Nevertheless, in this case, the sills have not been normalized, because, when a binary transformation (into 0 and 1) has been carried out, the variance is closely related to the number of verified data (1) inside the considered class. Thus leading the variance without the standardization, the semivariograms give immediately an idea of the number of values inside each class: the higher is the sill, the more numerous are the values within the considered class. For instance, considering the mean spacing, the indicator variograms (**Table 38**) have sills of 0.035 for class n°2 (only 4 values fall inside this class), 0.2 for class n°4 (with 72 values), 0.25 for class n°5 (with 159 data) and 0.08 for class n°6 (with only 19 values). Therefore, the sill of each class, being related to the number of values inside the class itself, does not change changing the lag. Consequently, considering the same sill within a class, the range of that class remains approximately the same despite the considered lag; obviously, it seems to increase a little considering the longest lag distance.

The use of the shortest lag seems to be more appropriate for spacing observed in situ, as demonstrated by: (i) the observed invariance of scale changing the lag; (ii) the detailed scale of in situ observations (with very short distances among sampling points), (iii) the results of Valchiavenna case study and spacing from photogrammetry at Grimsel site, showing that short lags, being able to capture also small heterogeneities, give better estimations.

Therefore, using the shortest lag distance, indicator variograms have been constructed for minimum and maximum spacing (**Table 39**). The indicator variograms exhibit too many different correlation directions: each variogram have its own main correlation direction, which differs from the other (especially for minimum spacing).

| SPACING | Minimum spacing (with lag 50 m) | Maximum spacing (with lag 50 m) |
|---------------------------|--|---|
| Class n°1 < 2cm | plot 5: variogram - azth=0, dip=20 | plot 1: variogram - Omni-directional |
| Class n°2 2 ≤ < 6 cm | plot 10: variogram - azth=67.5, dip=20 | plot 1: variogram - Omni-directional |
| Class n°3 6 ≤ < 20 cm | plot 12: variogram - azth=112.5, dip=170 | plot 14: variogram - azth=112.5, dip=10 |
| Class n°4 20 ≤ < 60 cm | plot 19: variogram - azth=157.5, dip=10 | plot 1: variogram - Omni-directional |
| Class n°5 0.6 ≤ < 2 m | plot 8: variogram - azth=67.5, dip=0 | plot 3: variogram - azth=22.5, dip=0 |
| Class n°6 2 ≤ < 6 m | plot 11: variogram - azth=112.5, dip=160 | plot 7: variogram - azth=45, dip=170 |
| Class n°7 ≥ 6 m | plot 1: variogram - Omni-directional | plot 12: variogram - azth=90, dip=170 |

Table 39 – Indicator semivariograms of minimum and maximum spacing subdivided for class, computed with lag equal to 250 m

Also in this case, experimental indicator semivariograms at extreme threshold values tend to be more erratic than those at the median threshold values. Therefore the application of the Multiple Indicator Kriging –

MIK –, consisting in the use of a variogram model for each class, appears to be not justifiable in this context, because the anisotropies at several cut-offs are too much different from each other. It is well known that when anisotropy changes too much between adjacent thresholds, the order relations violations become prohibitively large.

When the MIK is not applicable, the more common alternative is the Median Indicator Kriging, consists in inferring the median indicator variogram (i.e. the variogram for the median of input data), which can be used to detect pattern of spatial continuity whenever extreme-values data render the traditional variogram erratic (Goovaerts, 1997). The median indicator variogram is typically the most robust of all indicators, it tends to have the greatest range of continuity, and it is the easiest to define with some confidence from sparse data. The application of variograms from a single indicator to all thresholds reveals the main assumption associated with the median indicator method: the direction and range of continuity does not vary with changing thresholds.

The Median Indicator Kriging is a simplified form of MIK, which is frequently used when data sample is sparse and thus it is difficult or impossible to define grade continuity for a full range of indicators.

In order to apply this method the entire dataset of mean spacing, observed during the in situ surveys, has been splitted in two subsets: the first one (called the modelling dataset), including $\frac{3}{4}$ of the available data (i.e. 191 values), has been used to construct the indicator semivariogram of mean spacing at the median threshold (class $n^{\circ}4$). The second one, (the training point dataset), leading the remaining $\frac{1}{4}$ of data (equal to 63 values), have been used for the validation process. The dataset has been split according to the number of observation (ID), which depends on the location, putting three models in the modelling dataset and one in the training point dataset, so all the values having as ID number a multiple of 4 are in the training point dataset. In this way, the training points are scattered in the whole studied area.

The analysis of the number of values subdivided for class, allow understanding if the splitting is acceptable. The percentages of occurrence of values inside each class of spacing of both datasets (modelling and training point datasets) respect the frequencies of the entire dataset, which is the dataset before the splitting (Table 40), therefore this two datasets can be accepted and used.

| <i>SPACING</i> | <i>Entire dataset</i> | | <i>Modeling dataset</i> | | <i>Training point dataset</i> | |
|----------------|-----------------------|------------------|-------------------------|------------------|-------------------------------|------------------|
| | <i>N° of values</i> | <i>Frequency</i> | <i>N° of values</i> | <i>Frequency</i> | <i>N° of values</i> | <i>Frequency</i> |
| 1 | 0 | 0% | 0 | 0% | 0 | 0% |
| 2 | 4 | 2% | 4 | 2% | 0 | 0% |
| 3 | 0 | 0% | 0 | 0% | 0 | 0% |
| 4 | 72 | 28% | 54 | 28% | 18 | 29% |
| 5 | 159 | 63% | 117 | 62% | 42 | 67% |
| 6 | 19 | 7% | 16 | 8% | 3 | 5% |
| 7 | 0 | 0% | 0 | 0% | 0 | 0% |

Table 40 – Frequencies of data values in each dataset, subdivided por classes

Although the median class is the n°4, the maximum frequency of values, for each dataset, occurs in the class n°5. Therefore, the experimental indicator semivariograms of both classes (4 and 5) have been computed, using the 191 values of the modelling dataset (**Table 41**).

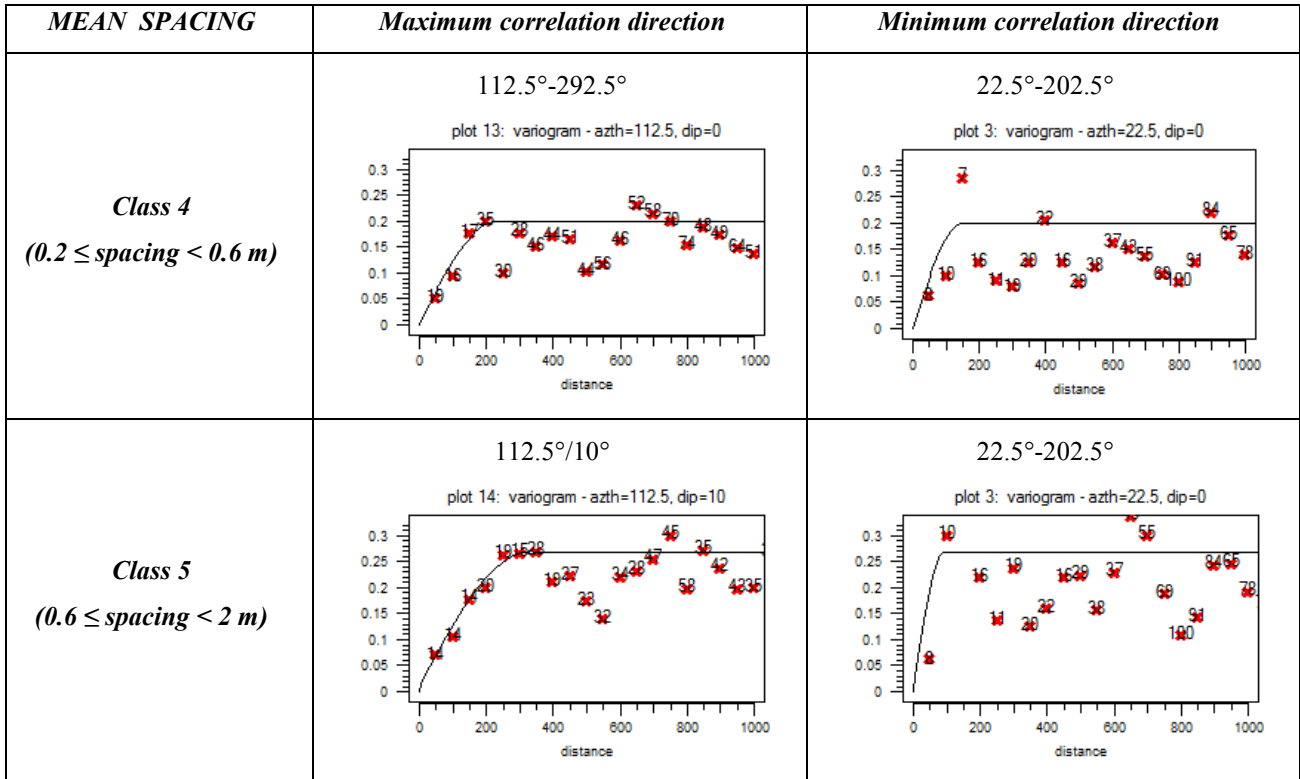


Table 41 – Theoretical models used to fit the experimental semivariograms of mean spacing, obtained from 191 in situ observations

Considering only 191 values, the main correlation direction is towards SSE for both classes, with a gentle dip angle for the class n°5, which has a higher sill, a longer range, but with a higher anisotropy ratio, than the class n°4. The parameters used to model the experimental variograms have been reported in **Table 42**.

| <i>MEAN SPACING</i> | <i>Class n°4</i> | <i>Class n°5</i> |
|-----------------------------------|------------------|------------------|
| Kind of model | Spherical | Spherical |
| Nugget effect | 0 | 0.01 |
| Sill | 0.2 | 0.27 |
| Maximum correlation direction [°] | 112.5-292.5 | 112.5/10 |
| Maximum range [m] | 230 | 325.5 |
| Mean correlation direction [°] | 22.5-202.5 | 22.5-202.5 |
| Mean range [m] | 160 | 94.5 |
| Minimum correlation direction [°] | 112.5/90 | 22.5/80 |
| Minimum range [m] | 60 | 31.5 |

Table 42 – Parameters of the theoretical models used to fit the experimental variograms of mean spacing, obtained from 191 in situ observations

Afterwards, the variogram models have been used to estimate the spacing values among sampling points. The popular pixel-based simulation method, called sequential indicator simulation –SIS–, has been used for

the estimation, being the data categorical (i.e. subdivided for classes) and non-parametric (that is without a Gaussian distribution). Following a random path through the three-dimensional grid, individual grid-nodes have been simulated, one after another, using constantly updated, thus increasing size, conditioning data-sets. The conditioning includes the original data (e.g., mean spacing of exfoliation joints) and all previously simulated values within a specified neighbourhood.

The SIS has been applied using the Median Indicator Kriging, which relies on the median indicator variogram. Initially, a set of 100 realizations has been carried out, using the median indicator variogram obtained for the spacing class n°4, which has been applied to all thresholds. Afterwards another set 100 simulations has been performed, using the median indicator variogram of the spacing class n°5.

The resulting maps (**Table 43**) show a very high scattering of the estimated values: both maps are quite alike, but no clear patterns of spacing can be found in the maps, although a main anisotropy direction towards ENE can be individuate in both maps.

The percentages of occurrence of classes of spacing (reported in **Table 40**) have been respected.

Also the maps of the variance are quite similar, although that one obtained using the median indicator variograms of class n°4 show smaller values and so smaller uncertainties.

The use of the previously used validation technique is not significant (**Figure 104**), due to the categorical feature of the variable: being the input values subdivided in classes, also the results are expressed in classes, and similar gaps (of 1 or 2 classes, in the case of study) result during the validation.

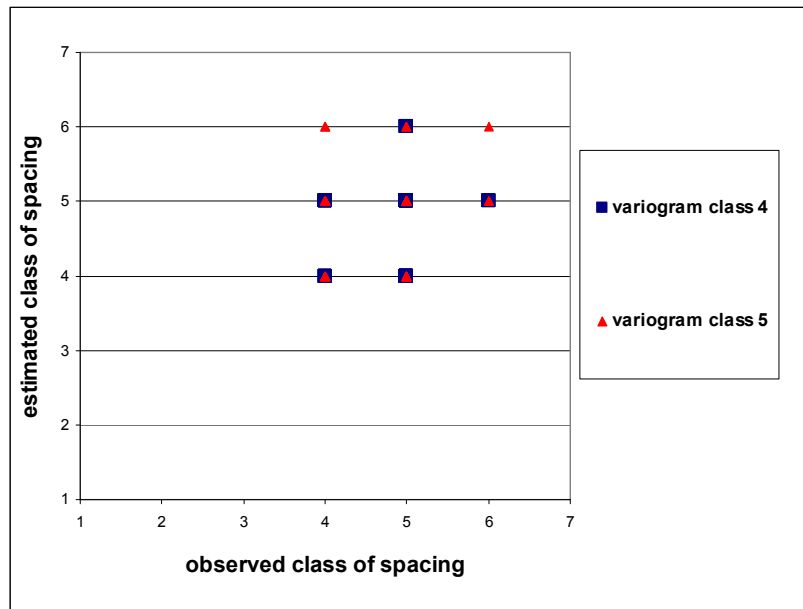


Figure 104 – Comparison between observed and estimated spacing classes, using the median indicator variograms of class 4 and 5

In order to compare the results of the two models, it is better to analyse how many estimated values match the observed spacing class and how many are far away. The results have been expressed in percentage (**Table 44**).

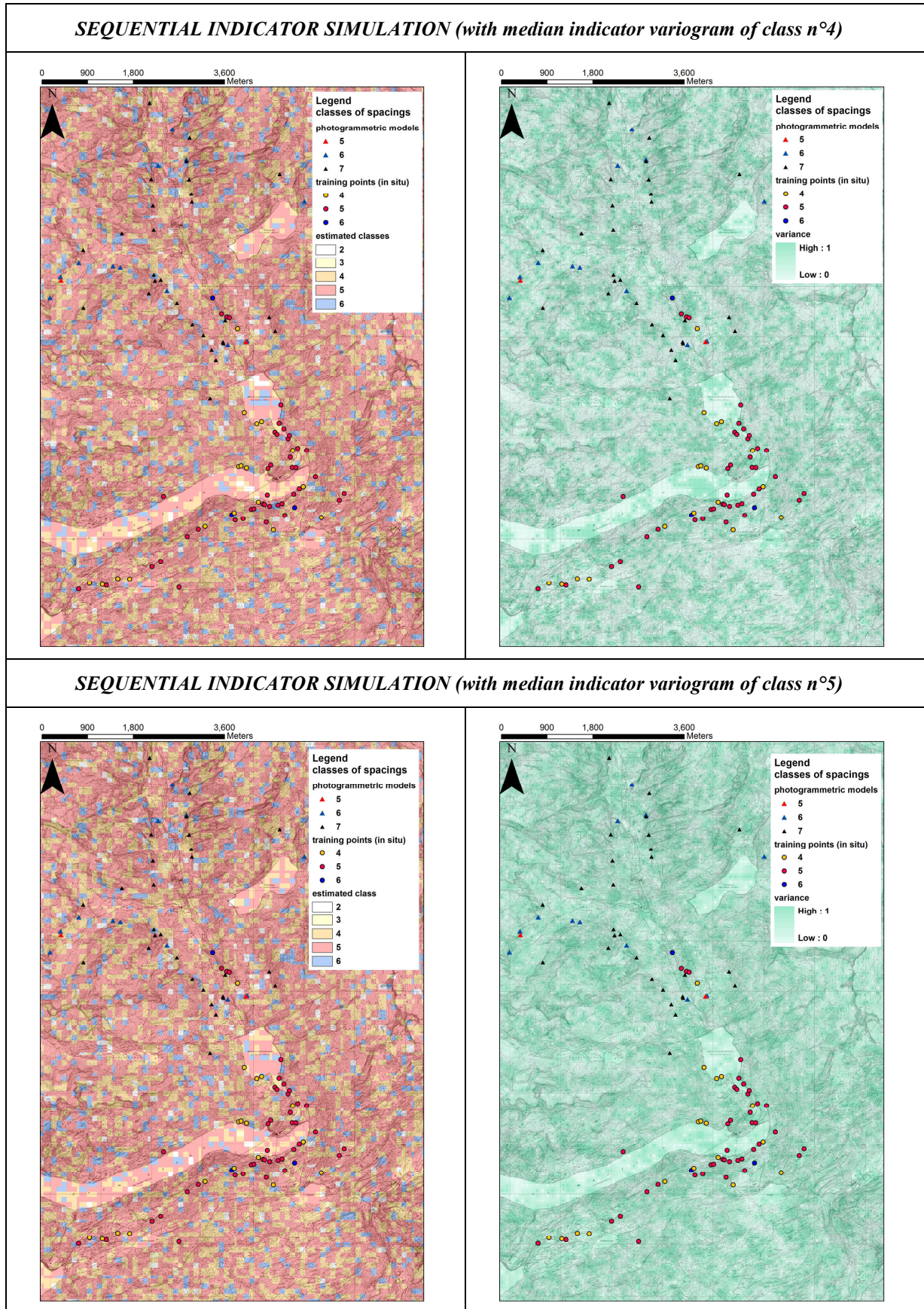


Table 43 – Maps of estimated classes of mean spacing (on the left), and associated variance (on the right), obtained considering in situ observations and performing the Sequential Indicator Simulation, through the median indicator kriging

The right class has been estimated in the 49% of the cases with the median indicator variogram of class n°4 and in the 57% of cases for class n°5. For the class n°4 the maximum difference is of 1 class, with a weak tendency to overestimate the class of spacing (i.e. to estimate a class which is bigger than the real observed one). For the class n°5, the differences between observed and estimated values include as maximum two classes of spacing; also for the class n°5 the overestimation prevails. Although the results of SIS, obtained using the Median Indicator Kriging of class n°5, show that the right class has been estimated more frequently than using the Median Indicator Kriging of class n°4, this last approach revealed better, because the resulting classes are closer to the observations than those derived from class n°5. Therefore, the uncertainty in the estimation is minor considering the indicator variogram of class n°4.

| <i>MEAN SPACING</i> | <i>Class n°4</i> | <i>Class n°5</i> |
|-------------------------------|------------------|------------------|
| Estimation of the right class | 49% | 57% |
| Overestimation of 1 class | 29% | 13% |
| Overestimation of 2 classes | 0% | 3% |
| Underestimation of 1 class | 22% | 12% |
| Underestimation of 2 classes | 0% | 0% |

Table 44– Comparison between the validation results of Sequential Indicator Simulation, obtained using the median indicator variograms of spacing classes n° 4 and 5

In conclusion, the spacing has been analysed considering data obtained from photogrammetric models and in situ surveys, separately.

The spacing from photogrammetric models, considering the exfoliation joints of the second generation, exhibit a main correlation direction towards N, with a gentle dip. This orientation reflects the main axis of Hasli Valley. The estimations, carried out through the Sequential Gaussian Simulation, have furnished results that have been positively validated using an independent dataset. These results cannot be compared to those obtained in situ, because a problem of up scaling occurs: the scales of observation are too different and therefore the spacing values measured by photogrammetry are systematic bigger than those measured in field are.

The spacing values observed in situ have been reported in classes, and therefore the indicator semivariograms, one for each class, have been constructed. These semivariograms are erratic: they show several directions of anisotropy, meaning that a strong, main correlation direction does not occur in the study area, considering the big scale of the in situ observations, which is in the order of magnitude of few metres. Therefore, only the median class of spacing has been considered and its spatial structure has been applied to all classes, using the Sequential Indicator Simulation, with median indicator kriging. The results show a great scattering of spacing classes, with also sharp changes, such as those observed in situ. However, the map cannot be considered reliable.

3.5.3 Orientations: difference between slope and exfoliation joint dip angle

The third considered property is not very common in rock mechanics. Actually, the difference between the slope angle of the outcrop and the dip angle of the exfoliation joint has been considered. This property contributes to distinguish among generation of exfoliation joints. Moreover, this angle affects the slope stability: for small values, proving that the dip direction is the same, sliding phenomena may occur.

The difference between slope angle (computed using an interpolated, smoothed surface obtained from the DTM, having a resolution of 100 metres) and the dip angle of the exfoliation joints has been calculated for each photogrammetric model and in situ survey. Actually, the dip difference can be computed in the same way for photogrammetric models and in situ surveys. The resulting positive values are 38 for the photogrammetric models, and 157 for the in situ surveys. The negative values, mainly related to a not precise interpolation of the DTM, are meaningless and so have been removed.

The mean dip difference is around 11° , for both photogrammetric models and in situ surveys.

Considering the data derived from the photogrammetric models, it is possible to note that the average dip angle differences increases with the age of the exfoliation joint generation and range up to almost 50° (**Figure 105**). The dip angle differences have a median value of 3° for the generation 3 of exfoliation joints, 11° for the generation 2 and 21° for the generation 3. The range increases, decreasing the generation: older joints exhibit bigger variations in dip difference than the younger. The last generation ($n^{\circ}4$), the youngest one, has not been considered, because it has been already observed that the method of dip angle difference can lead to errors for the youngest exfoliation generation. Actually, the generation 4 follows the slope very closely and can therefore show a large variation in joint dip angle and direction in case of complex slope geometry (Bolay, 2013).

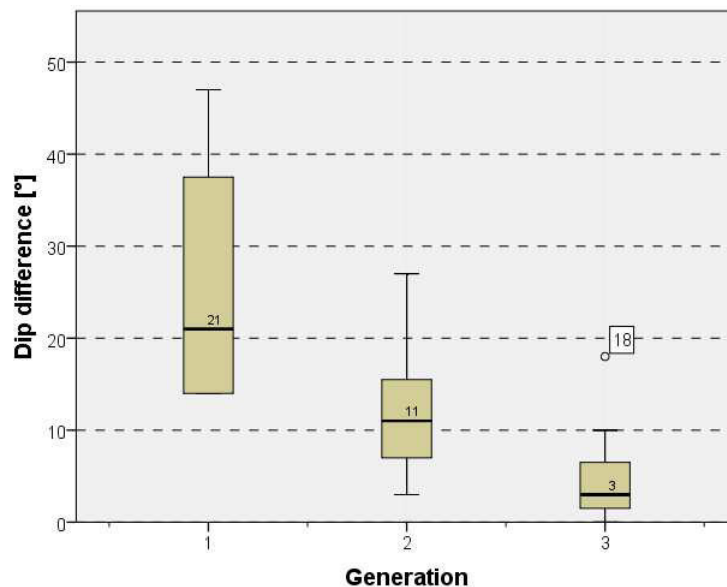


Figure 105 – Box plots of dip difference, measured from photogrammetric models, and subdivided for generation

The calculated dip differences from photogrammetric models follow a lognormal distribution, while those of in situ surveys exhibit a negative exponential distribution. With the photogrammetric approach, in the

models having low resolution, the slope angle values smaller than 3° are difficult to observe and measure. Considering the dip difference, no problem of up-scaling occurs, and the data of photogrammetric models and in situ observations can be put together, giving a negative exponential distribution, because the in situ measurements are more numerous.

The dip angle difference is a good indicator of the exfoliation joint generation, but it is not sufficient on its own. Other parameters such as exfoliation joint spacing and curvature need to be considered as well. If the dip angle differences are plotted against the mean number of joint intersections (expressed in joints per metre), the different generations will plot in specific areas (**Figure 106**) and provide a good method for the classification in conjunction with field observations. Actually, the dip difference can be a starting point to find the generation of exfoliation joints. During the in field observation, initially Martin Ziegler has classified exfoliation joints geometrically as being either parallel (type C), nearly parallel (type B), or not parallel (i.e. with more than 10° difference, type A) to the present-day ground surface (**Figure 107**). The orientation of the ground surface has been defined using an interpolated, smoothed surface such that steps or undulations of up to a few metres have been neglected.

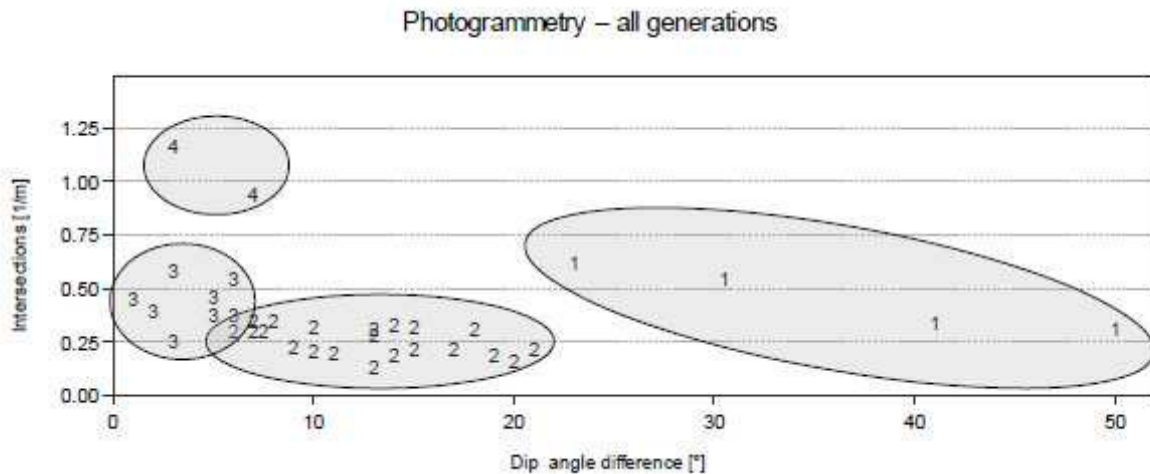


Figure 106 – The graph associates the dip difference with the mean number of joint intersection. It allows individuating different areas for each generation of exfoliation joints (from Bolay, 2013)

Erosion can lead to angular unconformities between exfoliation joints and the ground surface. Accordingly, the age of a landscape feature roughly assigns a maximum age to type C and type B exfoliation joints and a minimum age to type A exfoliation joints.

Besides geometrical classification, the three exfoliation joint types show characteristic differences in spacing at the ground surface, curvature, visible trace length, and weathering.

Because not all landforms are of identical age, the established exfoliation joint types (A, B and C) do not necessarily represent different joint sets (or generations). Therefore, the generation of exfoliation joints have been established considering also the spatial distribution and characteristics of exfoliation joint types in combination with corresponding landscape features. The spatial occurrence of mapped exfoliation joints, subdivided into Type A, B and C, has been reported in **Figure 108**.

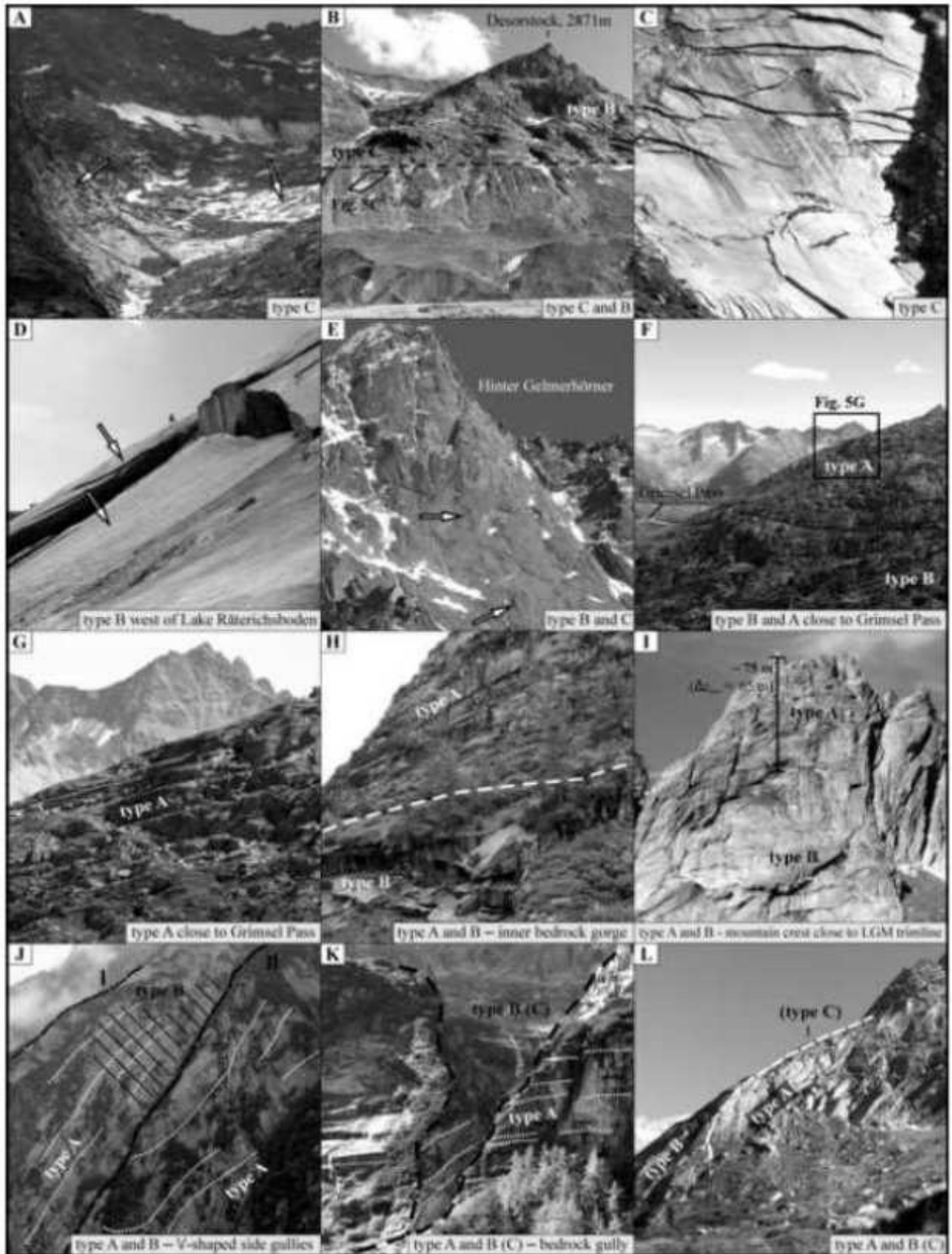


Figure 107 – Photographs of exfoliated rock masses in the Grimsel study area. The exfoliation joints of Type C (parallel to the ground surface) have been reported in figures A, B, C and E. The exfoliation joints of Type B (nearly parallel to the ground surface) are present in B, C, D, E, F, G, H, I and L. Finally the exfoliation joints of Type A (not parallel to the ground surface) occur in: F, G, H, I, J, K and L (from Ziegler et al., 2013)

The map (**Figure 108**) includes only exfoliation joints clearly visible at the ground surface. Thus, expected or assumed exfoliation joints beneath glaciers and sediment-covered areas, such as valley bottoms, talus slopes, and moraines, are not shown. The spatial distribution of exfoliation joints appears to be more variable within a single lithological unit, such as the Grimsel Granodiorite, Central Aar Granite, or Mittagfluh Granite, than among these various zones. Type B and C exfoliation joints do not occur (or are concealed) where (ductile-) brittle shear zones dominate the rock mass structure and/or are oriented subparallel to slopes. Similarly, type B and C exfoliation joints may be concealed on slopes where rock foliation and foliation-parallel joints are oriented subparallel to the slope. In contrast, less steeply inclined type A exfoliation joints can be well-developed at these locations. The mapped distribution of exfoliation joints in the Grimsel area suggests that the presence of tectonic joint sets, fault zones, and pronounced Alpine foliation have a significant effect on the formation of exfoliation joints (Ziegler et al., 2013).

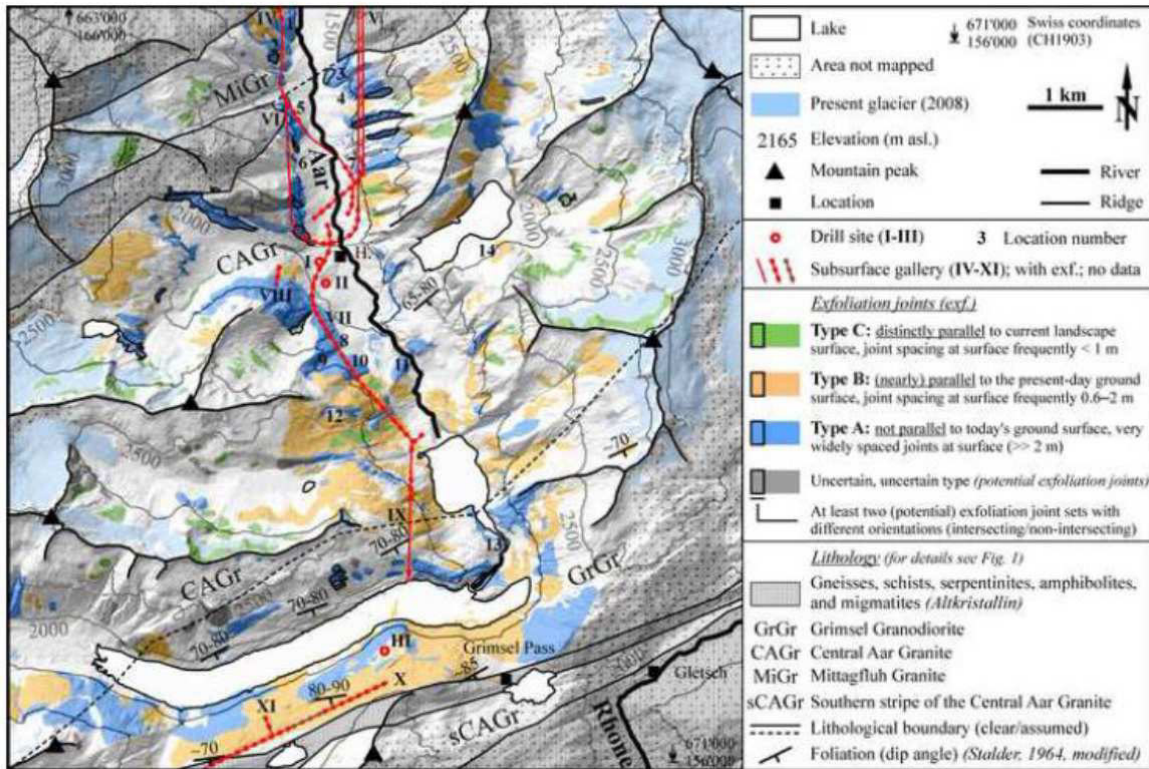


Figure 108 – Spatial distribution of exfoliation joints, subdivided in types according to unconformities with the slope angle, shown together with a simplified geological map (from Ziegler et al., 2013)

The dip difference values (**Figure 109**) have been subdivided into the following classes (**Figure 110**):

- Class 1 - Type C: exfoliation joints parallel to the present ground surface (dip difference $\leq 3^\circ$);
- Class 2 - Type B: exfoliation joints nearly parallel to the present ground surface ($3^\circ < \text{dip difference} \leq 10^\circ$);
- Class 3 - Type A: exfoliation joints not parallel to the present ground surface (dip difference $> 10^\circ$).

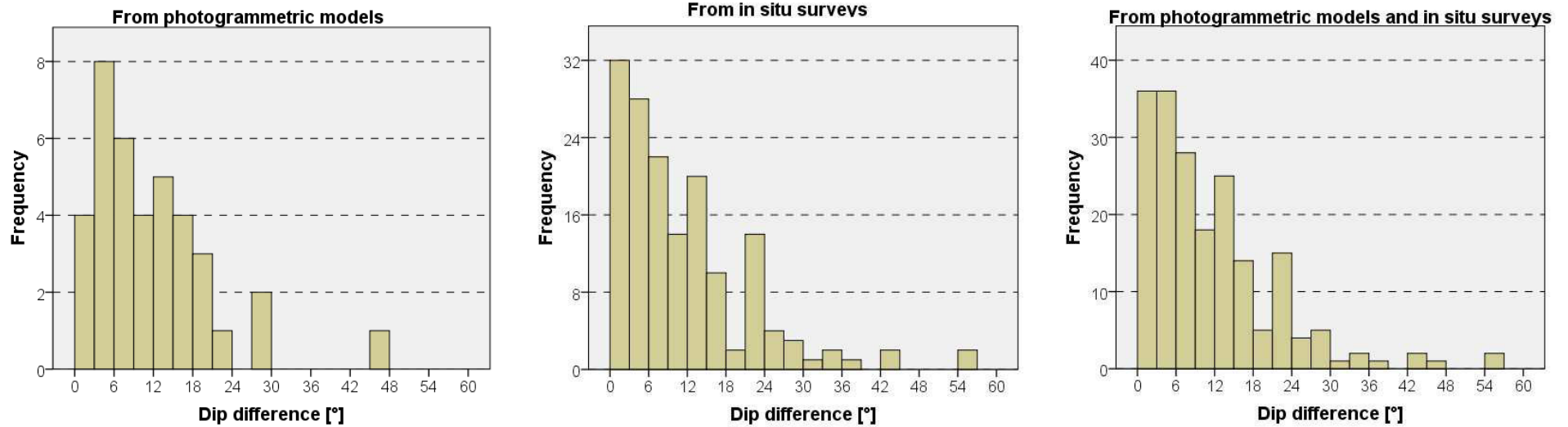


Figure 109 – Frequency histogram of dip difference values computed considering photogrammetric models, in situ surveys and both

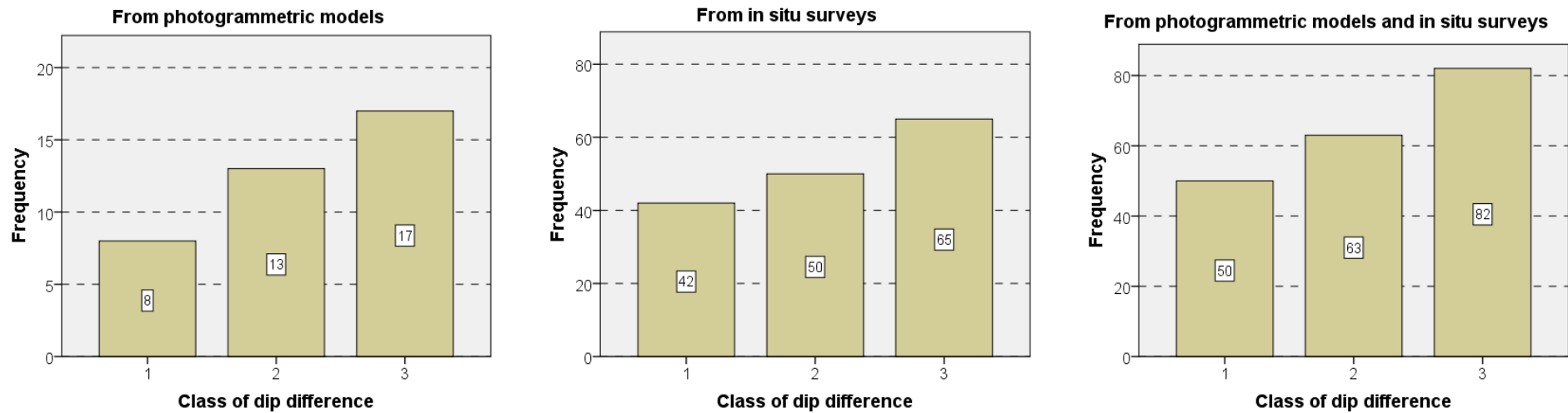


Figure 110 – Dip differences have been subdivided in classes according to the angular unconformities with the today ground surface: class 1 includes exfoliation joints of Type A (not parallel to the today ground surface), class 2 includes Type B exfoliation joints (nearly parallel to the today surface), and class 3 includes joint of Type C (which are parallel to the today ground surface)

The exfoliation joints of Type A prevail in the study area, followed respectively by Type B and C (Table 45). The indicator semivariogram have been constructed for each exfoliation joint type, divided according to the data source: photogrammetry, field surveys, and all together (Table 46).

| DIP DIFFERENCE | Photogrammetry | | In situ survey | | All | |
|----------------|----------------|-----------|----------------|-----------|--------------|-----------|
| | N° of values | Frequency | N° of values | Frequency | N° of values | Frequency |
| 1 (Type C) | 8 | 21 % | 42 | 27 % | 50 | 26 % |
| 2 (Type B) | 13 | 34 % | 50 | 32 % | 63 | 32 % |
| 3 (Type A) | 17 | 45 % | 65 | 41 % | 82 | 42 % |

Table 45 – Dip differences computed from photogrammetric models and in situ surveys, subdivided in classes, according to the parallelism with the today ground surface

| DIP DIFFER. | Photogrammetric models | In situ surveys | All data |
|---|------------------------|----------------------|----------------------|
| <p>Class 1 (dip difference $\leq 3^\circ$)</p> | <p>337.5°/20°</p> | <p>157.5°-337.5°</p> | <p>157.5°-337.5°</p> |
| <p>Class 2 (3° < dip difference $\leq 10^\circ$)</p> | <p>112.5°-292.5°</p> | <p>90°/20°</p> | <p>90°/20°</p> |
| <p>Class 3 (dip difference > 10°)</p> | <p>45°/10°</p> | <p>45°/10°</p> | <p>22.5°/20°</p> |

Table 46 – Indicator semivariograms of dip differences

Since the photogrammetric models are located distant among themselves, and investigate bigger portion of the outcrops than the in situ observations, whose sampling points are often very close, different lag distances has been used: 250 meters for data derived from photogrammetry, 50 meters for in situ observations and 100 metres considering all the data. The linear tolerance has been set equal to half lag and the angular

tolerance equal to 22.5°). The resulting indicator semivariograms show that, for a given class of dip difference, the main correlation direction is the same (with small difference in the order of the angular tolerance) in spite of the data source. The worst indicator semivariograms have been observed for the class 1, which is the least frequent. The variogram improves considering all the data together. The indicator variograms of other classes show structures that approximate more closely the theoretical models. The sills are dependent on the number of considered data, and so they vary from class to class, but also inside the same class, due to the different data source considered.

Since the variograms exhibit the same main correlation direction, all the data have been considered together in the modelling (Table 47). The main correlation direction is quite changeable from class to class: it generally dips towards N for classes 1 and 3 (having orientations respectively of NNW-SSE and NNE), but for class n°2 it dips towards E, with a dip angle of 20°.

| <i>DIP DIFFERENCE</i> | <i>Maximum correlation direction</i> | <i>Minimum correlation direction</i> |
|---|--|--|
| <p>Class 1 (dip difference $\leq 3^\circ$)</p> | <p>157.5°-337.5°</p> <p>plot 18: variogram - azth=157.5, dip=0</p> | <p>67.5°-247.5°</p> <p>plot 8: variogram - azth=67.5, dip=0</p> |
| <p>Class 2 ($3^\circ < \text{dip difference} \leq 10^\circ$)</p> | <p>90°/20°</p> <p>plot 15: variogram - azth=90, dip=20</p> | <p>180°-360°</p> <p>plot 3: variogram - azth=0, dip=0</p> |
| <p>Class 3 (dip difference $> 10^\circ$)</p> | <p>22.5°/20°</p> <p>plot 5: variogram - azth=22.5, dip=20</p> | <p>112.5°-292.5°</p> <p>plot 13: variogram - azth=112.5, dip=0</p> |

Table 47 – Theoretical models of experimental semivariogram, computed using data from both photogrammetry and in situ surveys

The indicator semivariograms of all classes can be modelled using the spherical model. Nugget effects, sills and ranges vary from class to class (**Table 48**). The nugget effect, sill and range are the smallest for the class number 2 (exfoliation joints nearly parallel to the today ground surface). The sill and range are maximum for class n°3 (exfoliation joints not parallel to the today ground surface), which also exhibit the highest anisotropy ratio.

| <i>DIP DIFFERENCE</i> | | | |
|-----------------------------------|----------------|----------------|----------------|
| <i>Parametre</i> | <i>Class 1</i> | <i>Class 2</i> | <i>Class 3</i> |
| Kind of model | Spherical | Spherical | Spherical |
| Nugget effect | 0.08 | 0 | 0.06 |
| Sill | 0.19 | 0.18 | 0.31 |
| Maximum correlation direction [°] | 157.5-337.5 | 90/20 | 22.5/20 |
| Maximum range [m] | 460 | 170 | 1280 |
| Mean correlation direction [°] | 67.5-247.5 | 180-360 | 112.5-292.5 |
| Mean range [m] | 160 | 90 | 60 |
| Minimum correlation direction [°] | 157.5/90 | 270/70 | 292.5/70 |
| Minimum range [m] | 60 | 60 | 60 |

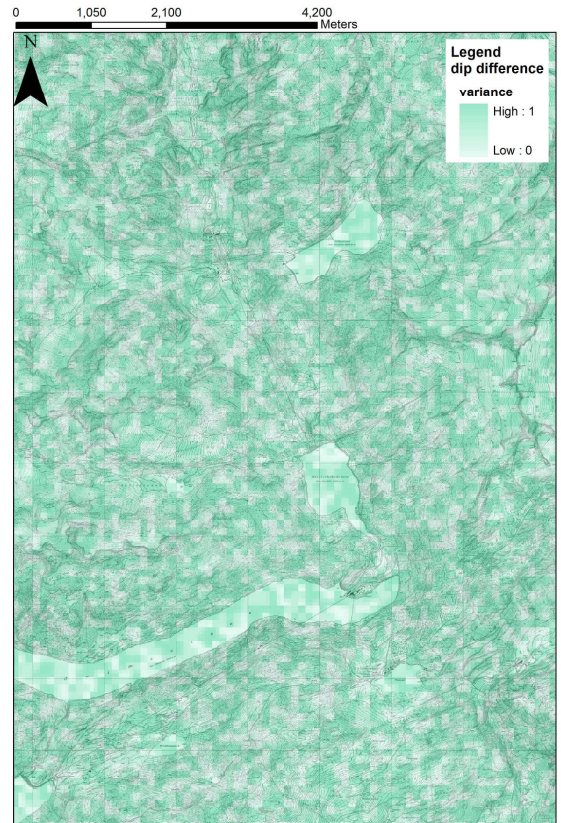
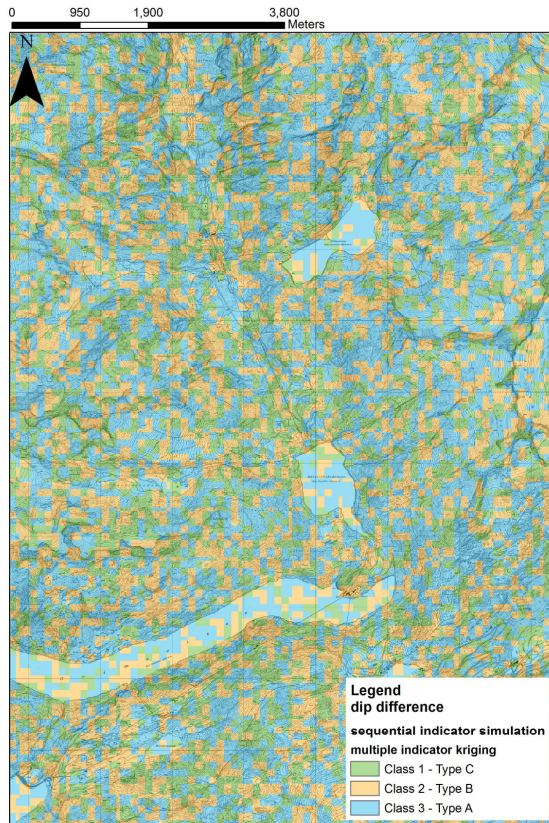
Table 48 – Parameters of the theoretical models used to fit the experimental semivariograms of dip difference

Since the data have been subdivided in classes, the Sequential Indicator Simulation technique, with 100 performed realizations, has been applied, through both Multiple Indicator Kriging (which use one variogram model for each class) and Median Indicator Kriging (which applies the variogram of the second class to all the classes).

The resulting maps (**Table 49**) exhibit a marked scattering of the values: the main correlation direction is not identifiable in the maps (especially using the SIS performed by MIK), and the class are not diffused over large areas such as the in situ observations. In my opinion, the SIS is not suitable for estimating rock mass properties. Actually, as shown for the estimated spacing values from in situ surveys (**Table 43**), the resulting maps are “homogeneously heterogeneous”, being characterized by the maximum entropy property, which does not match with the geological properties of the fractures.

Since data have been measured, it is better to consider their values than the classes, because the subdivision in classes, leads to a loss of information. Therefore, the variograms have been constructed using the computed values of dip difference. The lag distances have been assumed equal to 250 meters for data derived from photogrammetry, 50 meters for in situ observations and 100 metres considering all the data. The resulting variograms (**Table 50**) show that a unique maximum correlation direction does not occur in the study area; however, the variations are not so relevant, therefore this variable can be reasonably treated as a Regionalized Variable. The maximum correlation direction results towards NNE for data obtained from the photogrammetric models, towards NE for data obtained from in situ survey and with main direction N-S considering all the data together. The theoretical models that best fit the data have been reported in **Table 51** and their parameters in **Table 52**.

SEQUENTIAL INDICATOR SIMULATION (WITH MULTIPLE INDICATOR KRIGING)



SEQUENTIAL INDICATOR SIMULATION (WITH MEDIAN INDICATOR KRIGING)

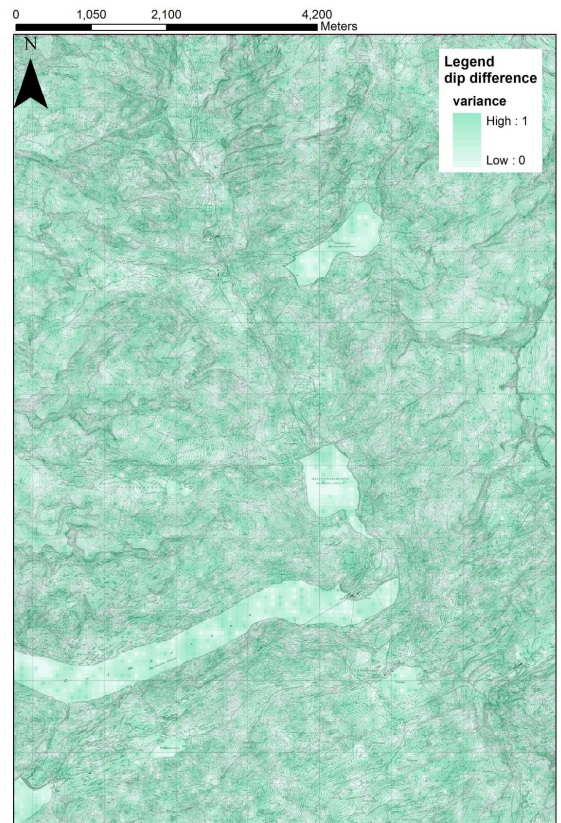
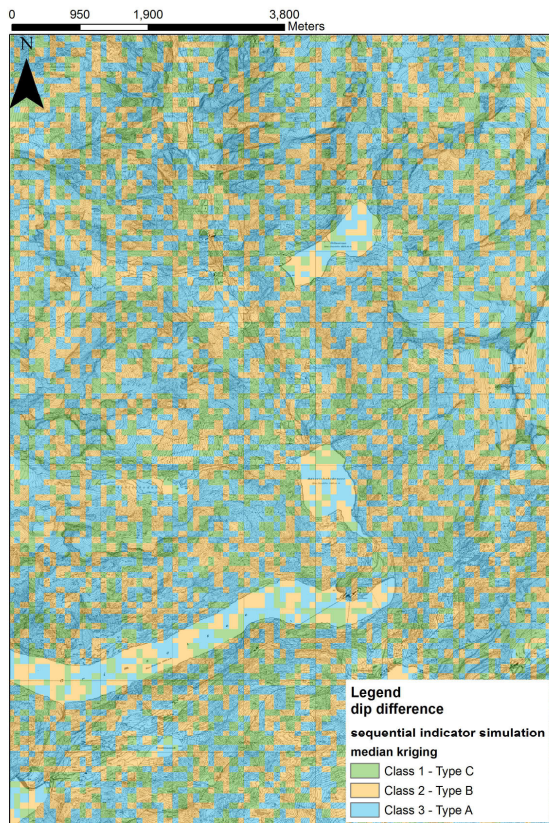


Table 49 – Parameters of the theoretical models used to fit the experimental semivariograms of dip difference

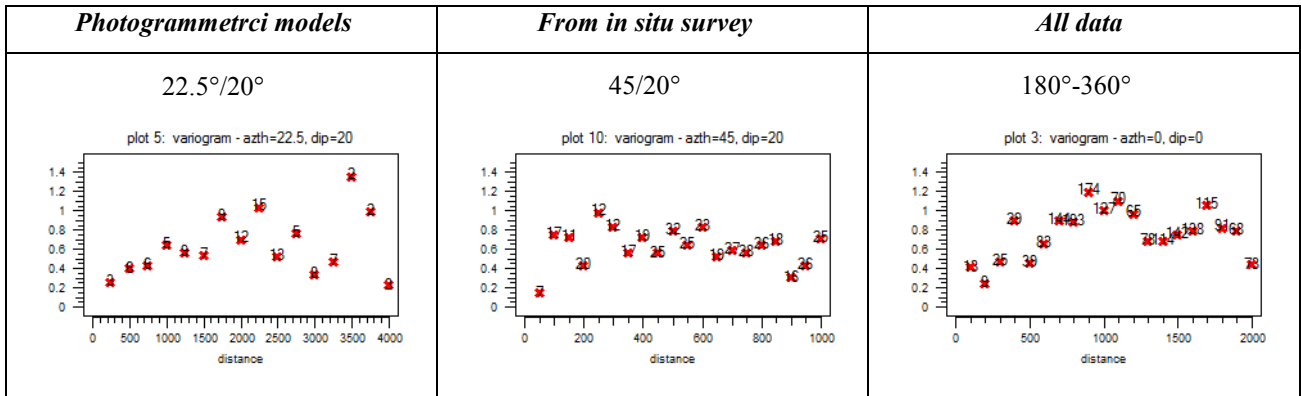


Table 50 – Experimental semivariograms of dip difference, along the maximum correlation direction, obtained using the measured values (not reclassified)

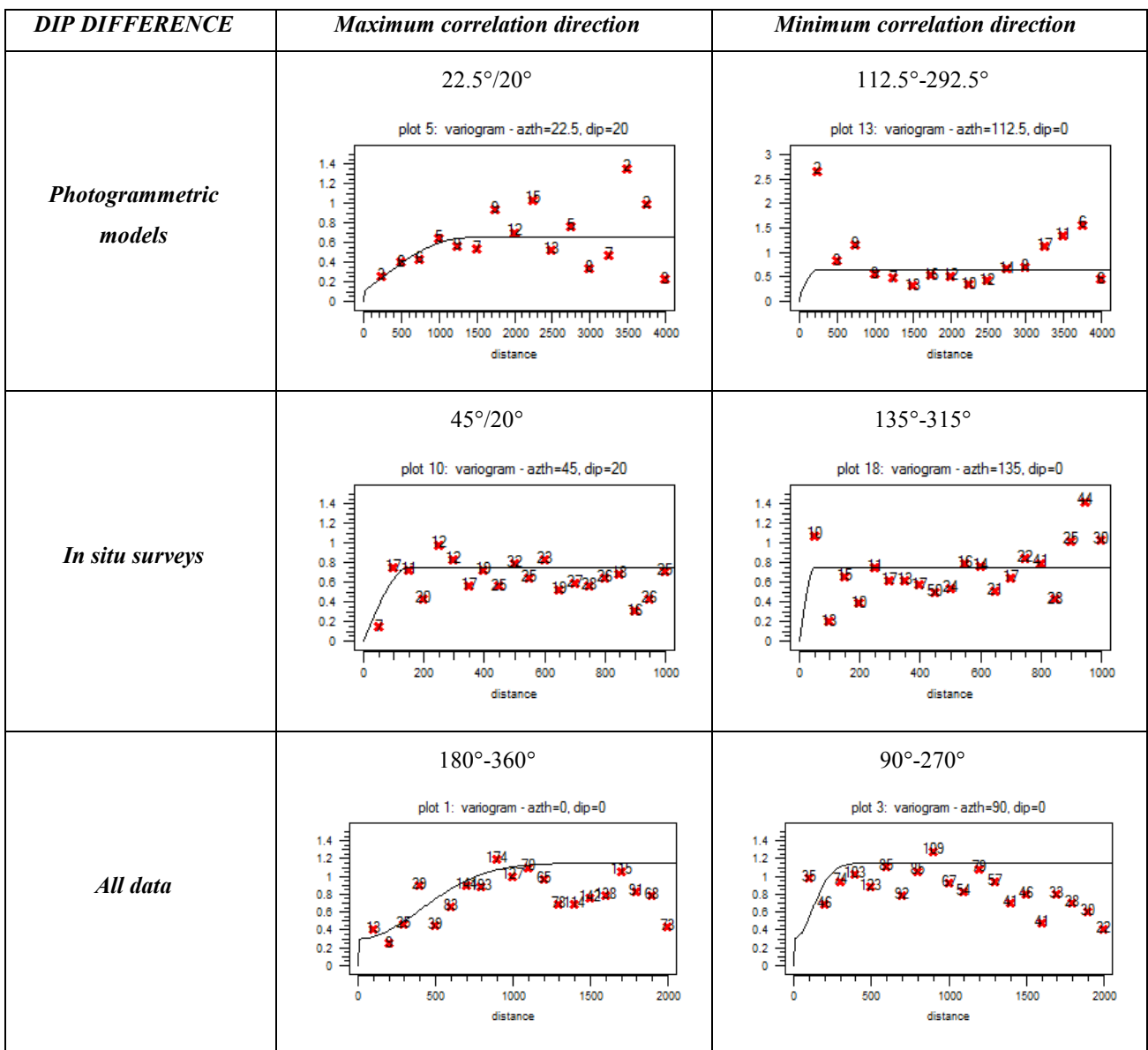


Table 51 –Theoretical models used to fit the experimental semivariograms of dip difference

Variograms of dip angles measured from photogrammetric models and in situ surveys can be fitted using a spherical model, while considering all the data together a Gaussian model is better. Data from in situ survey

are characterized by null nugget effect and very very short correlations. The nugget effect and ranges significantly increase, considering data from photogrammetric survey, but this is due to the dispositions of photogrammetric models and to the bigger distances among them, than the distances occurring among in situ survey locations. Considering all the data together, the nugget effect and sill are highest than the values measured only from photogrammetry or in situ survey indicating a bigger variability. The maximum range is a middle-way, while the medium range is longer than those of other models.

| <i>DIP DIFFERENCE</i> | | | |
|-----------------------------------|-----------------------|-----------------------|-----------------|
| <i>Parametre</i> | <i>Photogrammetry</i> | <i>In situ survey</i> | <i>All data</i> |
| Kind of model | Spherical | Spherical | Gaussian |
| Nugget effect | 0.1 | 0 | 0.3 |
| Sill | 0.65 | 0.75 | 1.15 |
| Maximum correlation direction [°] | 22.5/20 | 45/20 | 180-360 |
| Maximum range [m] | 1360 | 150 | 1000 |
| Mean correlation direction [°] | 112.5-202.5 | 135-315 | 90-270 |
| Mean range [m] | 240 | 50 | 300 |
| Minimum correlation direction [°] | 202.5/70 | 225/70 | 180/90 |
| Minimum range [m] | 120 | 50 | 40 |

Table 52 – Parameters of the theoretical models used to fit the experimental semivariograms of dip difference

Then, using the parameters of the modelled variograms, the SGS technique has been performed in order to estimate the dip difference values in the whole study area. The resulting values have been grouped in three classes, corresponding to the Types A, B and C, previously defined.

The resulting maps (**Table 53**), with the associate variances, show that the, although the small variation in the variogram models, the main pattern is constant in all the maps, even if it is captured with different scales. The photogrammetric approach, being characterized by the longest lag distance, conduct to a rough distinction among dip difference classes, while the map derived from in situ survey catch better the small details. The map derived using all the data is a middle way between the other two maps.

These three maps have been compared with the map of spatial distribution of exfoliation joint types (**Figure 108**), which was drawn up by Martin Ziegler, who reported that (Ziegler et al., 2013):

- type A exfoliation joints dominate in the northern part of the study area, being located within the inner U-shaped valley cross-section, on the valley shoulders and, more gently dipping, linear slopes above. Further, type A exfoliation joints occur on mountain crests and peaks, exhibiting the highest encountered (physical and chemical) degree of weathering, as demonstrated by change in rock color, ferrous staining, macroscopically visible porosity along joints, and rock disintegration. In the southern part of the study area type A and B exfoliation joints are interspersed and form an area that is for the most part exfoliated.

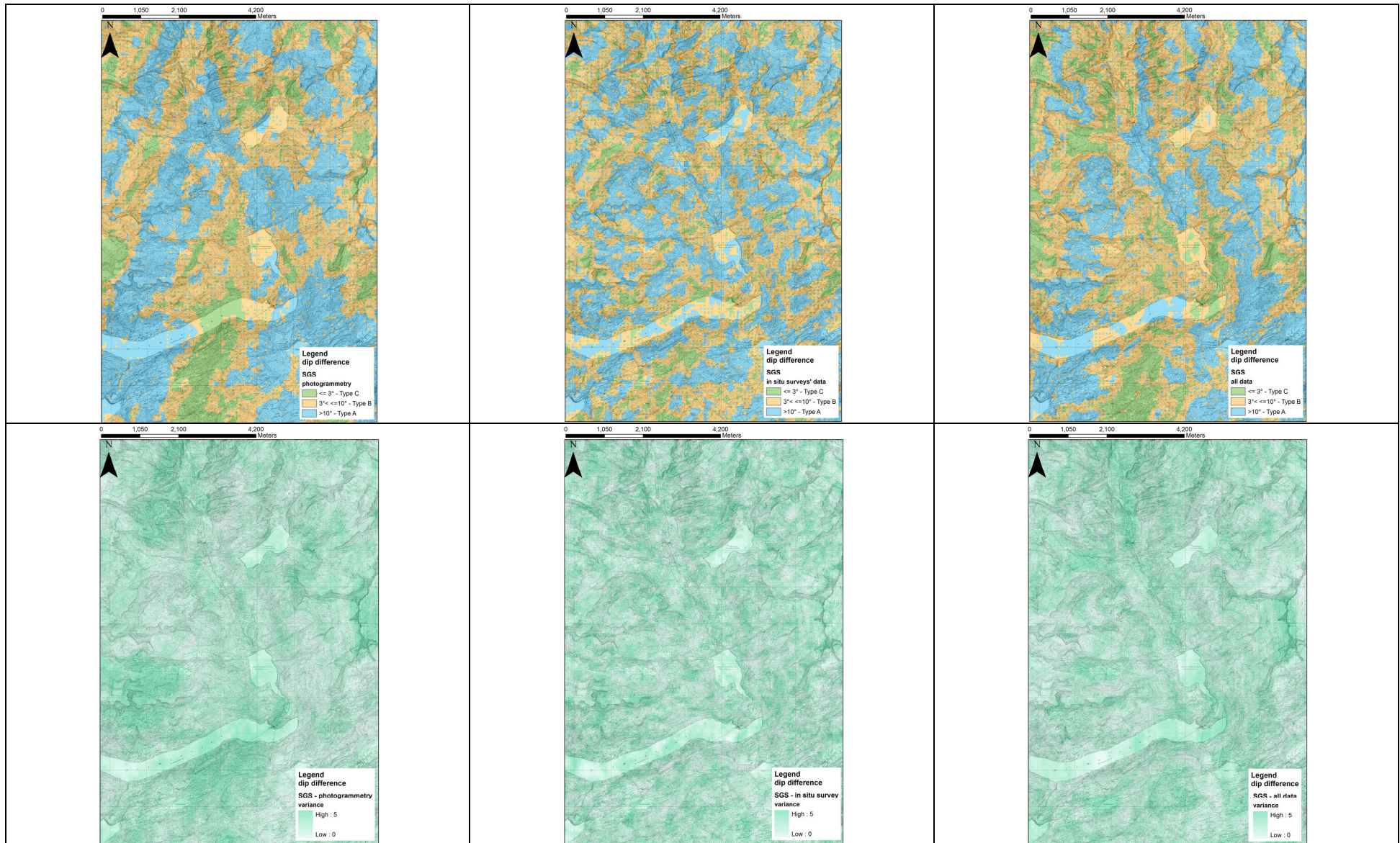


Table 53 – Parameters of the theoretical models used to fit the experimental semivariograms of dip difference

- type B exfoliation joints dominate in the southern part of the study area. They surround Lake Räterichsboden and occur in the eastern parts of the Bächli valley, near Lake Grimsel up to Grimsel Pass. In comparison with the southern side of Lake Grimsel, only a few type B exfoliation joints occur on the northern side of the lake. In the northern part of the study area, type B joints occur partly on steep slopes of V-shaped side gullies, where they in places contribute to slope instabilities, and at trough valley slopes northeast of Handegg. Furthermore, type B joints are found on slopes of the Ärlen and Gelmer hanging valleys and at the less inclined, upper slopes such as Garwydi, Uf Beesten, and Bächlisblatti above the shoulder inflexion points.
- Type C exfoliation joints mainly occur along high mountain crests and adjacent areas below, including cirque floors and headwalls. Where glaciers are receding today, type C exfoliation joints are frequently revealed. Few type C joints are located at lower elevations within the inner U-shaped main and hanging valleys. Type C joints are almost exclusively located within the extent of Late Glacial ice.

No one of the estimated map is as precise and reliable as the map drawn by in situ observation. However it is possible to observe that the map obtained from photogrammetric models is too simplistic, while that coming from in situ surveys is too much detailed and extrapolates values that do not exist in reality. The best compromise seems to be the map obtained using both techniques. It is able to well identify the glacial cirques, where especially type C exfoliation joints are present. However, also this map presents some limits (for instance, the B type exfoliation joints outcropping on the northern side of lake Grimsel are in part replaced with A type and C type exfoliation joints, and in this zone the uncertainty appears to be not as high as it is in reality).

The best solution, which allows individuating also the generation of exfoliation joints, should be to combine both dip difference and spacing values in geostatistical modelling.

3.6 Statistical analyses of tectonic joint sets

In the study area, beyond the exfoliation joints (whose orientations follow the topography), the rock masses are intersected by several older discontinuities, especially joints and faults.

The majority of tectonic joint sets, in contrast to the exfoliation joints, show a relative constant regional orientation and exhibit planar, smooth to slightly rough joint surfaces, with slickensides (indicating fault slip), and prominent hydrothermal mineralization. It follows that the exfoliation joints, due to their peculiar features, can be easily distinguished from the other joint sets (**Figure 111**).

Three main systematic, steeply dipping joint sets (K1, K2, and K3) are widespread in the study area, and two minor joint sets (K4 and K5) occur only in certain locations. The most diffused set is K1, which developed sub-parallel to the rock foliation. The structural orientations of these joint sets, reported from previous

studies, have been summarized, in term of dip direction and dip angle, in **Table 54**. Minor tectonic joint sets have been also reported, with the following orientations: 215-230/steep (Minder, 1932), 016/23 and 023/40 (Ziegler et al., 2013).

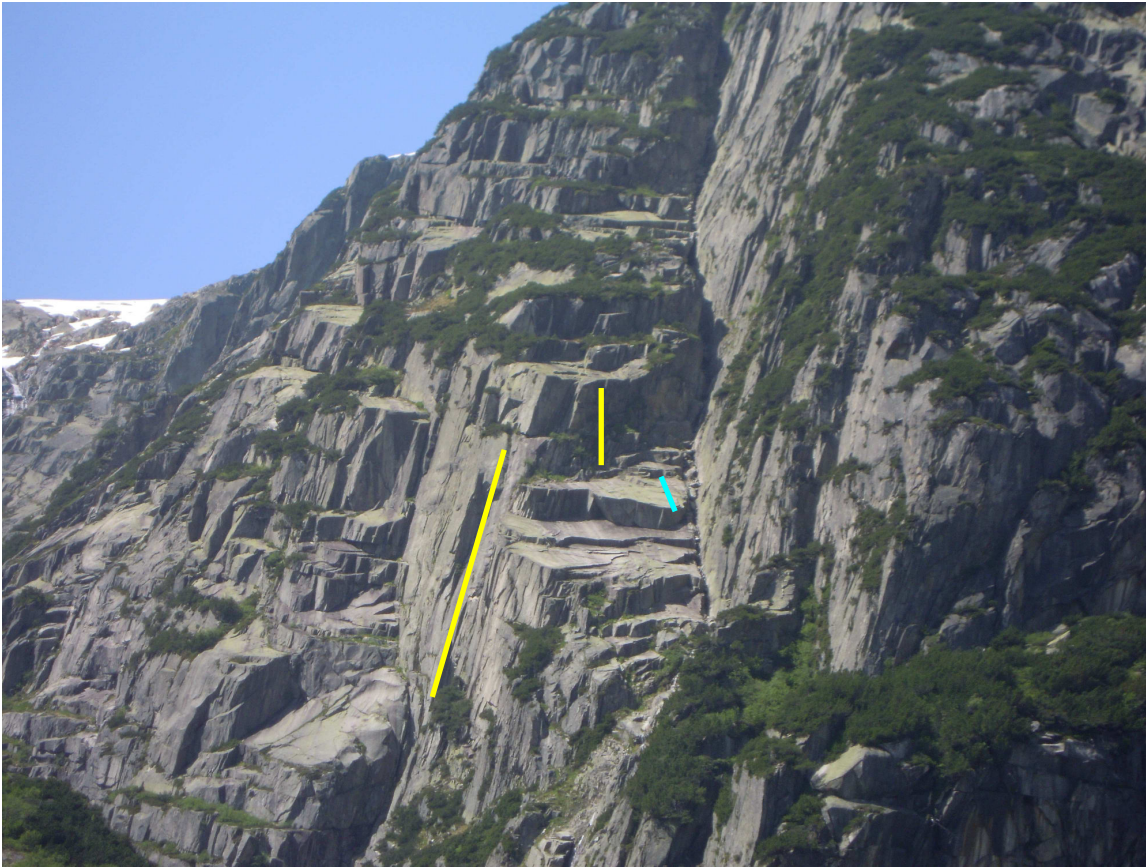


Figure 111 – Rock mass located in front of Lake Gelmer, on the left hydrographical side of Hasli valley. The dip direction exfoliation joints (indicated in light blue) form some sub-horizontal steps and are easily distinguishable from the other main joint sets (some examples of their dip direction have been depicted in yellow)

| REFERENCES | ROCK TYPES | K1 | K2 | K3 | K4 | K5 |
|----------------------|-------------|--------|----------------|-----------|--------|-----------|
| | | [°] | [°] | [°] | [°] | [°] |
| This study | CAGr | 137/69 | 242/90 | 188/67 | 329/55 | 157/71 |
| Ziegler et al., 2013 | CAGr, GrGr | 146/72 | 247/79 | 187/70 | 329/55 | - |
| Sutter, 2008 | CAGr | 139/71 | 244/76 | 198/72 | 330/64 | - |
| Keusen et al., 1989 | CAGr, GrGr | 142/77 | 233/80; 264/84 | 199/70 | 336/42 | 157/75 |
| Stalder, 1964 | GrGr | 146/78 | 252/82 | - | - | 160/76 |
| Bär, 1957 | GrGr | 153/80 | 242/85 | ~193/73 | - | ~164/84 |
| Minder, 1932 | sCAGr, GrGr | 138/73 | 250/68 | 190/steep | - | 158/steep |

Table 53 - Mean structural orientations (dip direction/dip angle) of major tectonic joint sets (K1– K5), reported in previous studies carried out along the upper Hasli valley and at Lake Grimsel (from Ziegler et al., 2013, modified). The investigated rock types are: Grimsel Granodiorite (GrGr), Central Aar Granite (CAGr) and Southern stripe of the Central Aar Granite (sCAGr)

Sub-horizontal to slightly inclined Alpine extensional veins (K6), rich in quartz and chlorite, occur frequently in the study area, with a mean dip direction and dip angle at the Grimsel site of respectively 009/22 (Ziegler et al., 2013). These extensional veins have been distinguished from similarly inclined exfoliation joints, from Martin Ziegler, according to their hydrothermal mineralization, orientation independent of topography, and non-uniform aperture. Alpine extensional veins also occur at various depths in bedrock. They formed during the lower and middle Miocene at depths of around 13 to 17 kilometres (Mullis, 1996). In this research, data of the main joint sets, affecting the investigated rock masses, has been collected, through the photogrammetric models.

The investigated rock masses generally show one or sometimes two main sets of tectonic joints for each model, being the minor ones not clearly observable using the photogrammetric approach. Actually it is well known that tectonic joints are discontinuities formed from the tensile stresses accompanying uplift or lateral stretching, or from the effects of regional tectonic compression (ISRM, 1975); they commonly occur as planar, rough-surfaced sets of intersecting joints, with one or two of the sets usually dominating in persistence (Palmström, 2001).

The most persistent joint set has been individuated in each photogrammetric model, and its geometric properties have been measured, using the software 3GSM ShapeMetrix^{3D} (3G Software & Measurement, 2007). When two main joints sets are present, both have been investigated; two joints sets have been measured in 7 of the 42 photogrammetric models. Similarly to the exfoliation joints, also for the tectonic joints the following data has been collected:

- orientations;
- trace lengths;
- kind of terminations;
- length of rock bridges;
- sinuosity index;
- spacing.

3.6.1 Orientations

The measures of orientation are very important, because they allow distinguishing among sets of joint. Actually, while in situ the kind of joint can be determined through the observations of the small features of rock masses (such as the presence of secondary hydrothermal minerals, etc.), using the photogrammetrical approach these observations cannot be performed, and the orientation play a key role in the discrimination among joint set. Being the orientation a critical factor in determining the joint set, the orientations have been measured, not only with the trace length approach (as previously described in the paragraph 3.4.1), but also surrounding the joint surfaces with areas having a sufficient exposure to be fitted by a plane (using the least squares method), whose orientation (in term of dip direction and dip angle) has been measured.

For each model, the measured orientation values have been reported into a stereographic plot, using the Lambert projection, which is an equal area projection that allows extrapolating the mean values of orientations. The discontinuity sets developed parallel to the considered rock wall are not prevalent in photogrammetric models, with few discontinuities, which are often very difficult to measure: therefore these sets have not been considered.

Initially, according to the previous studies, the joints have been subdivided into 5 joints sets (**Figure 112**), whose mean orientations have been reported in **Table 53**.

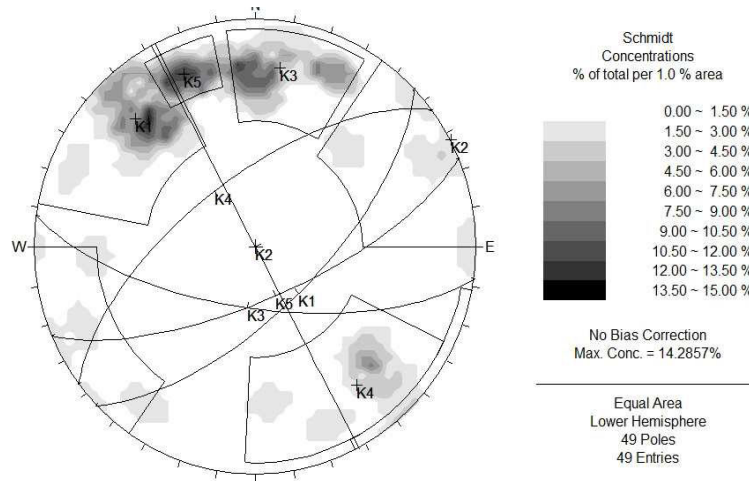


Figure 112 – Counter plot and mean orientations of the main tectonic joint sets (K1– K5) measured from photogrammetric models, plotted using the Schmidt equal area projection

The sets K1 and K5 are not easily distinguishable in the photogrammetric approach (i.e. using only their orientations), because they are very similar and hence often overlapped on the stereographic plot; this fact makes complex and subjective to trace a sharp boundary between the two joint sets, especially when few poles can be measured. In order to avoid this problem the sets K1 and K5 have been grouped in a new unique set, called again K1 (**Figure 113**).

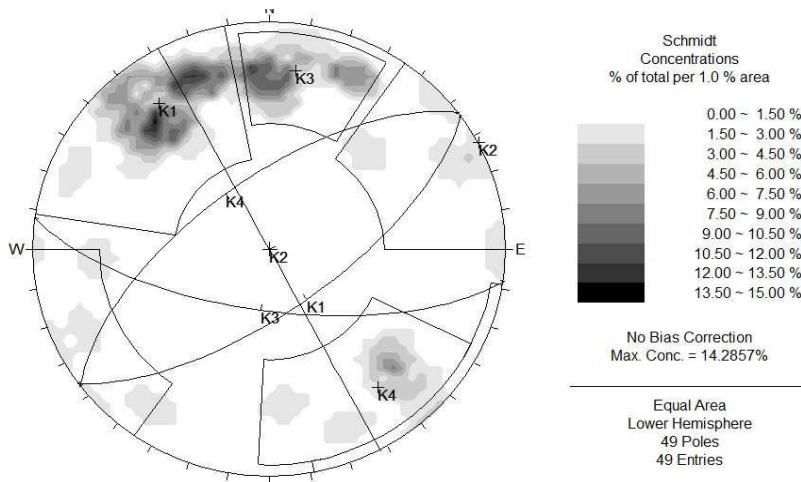


Figure 113 – Counter plot and mean orientations of the main tectonic joint sets (K1– K4) measured from photogrammetric models (the sets K1 and K5 of Figure 72 have been grouped in a unique K1 set)

The new orientations and colours used in figures have been reported in **Table 54**. Some examples of orientations, measured using the photogrammetric approach, have been reported in **Tables 55 and 56**.

| <i>JOINT SET</i> | <i>DIP DIRECTION</i> | <i>DIP ANGLE</i> | <i>COLOUR</i> |
|------------------|----------------------|------------------|---------------|
| K1 | 145° | 69° | red |
| K2 | 242° | 89° | green |
| K3 | 188° | 67° | yellow |
| K4 | 329° | 55° | blue |

Table 54 – Orientations and colours of the four main joint sets obtained through photogrammetry. The new set K1 includes the previous K1 and K5 sets

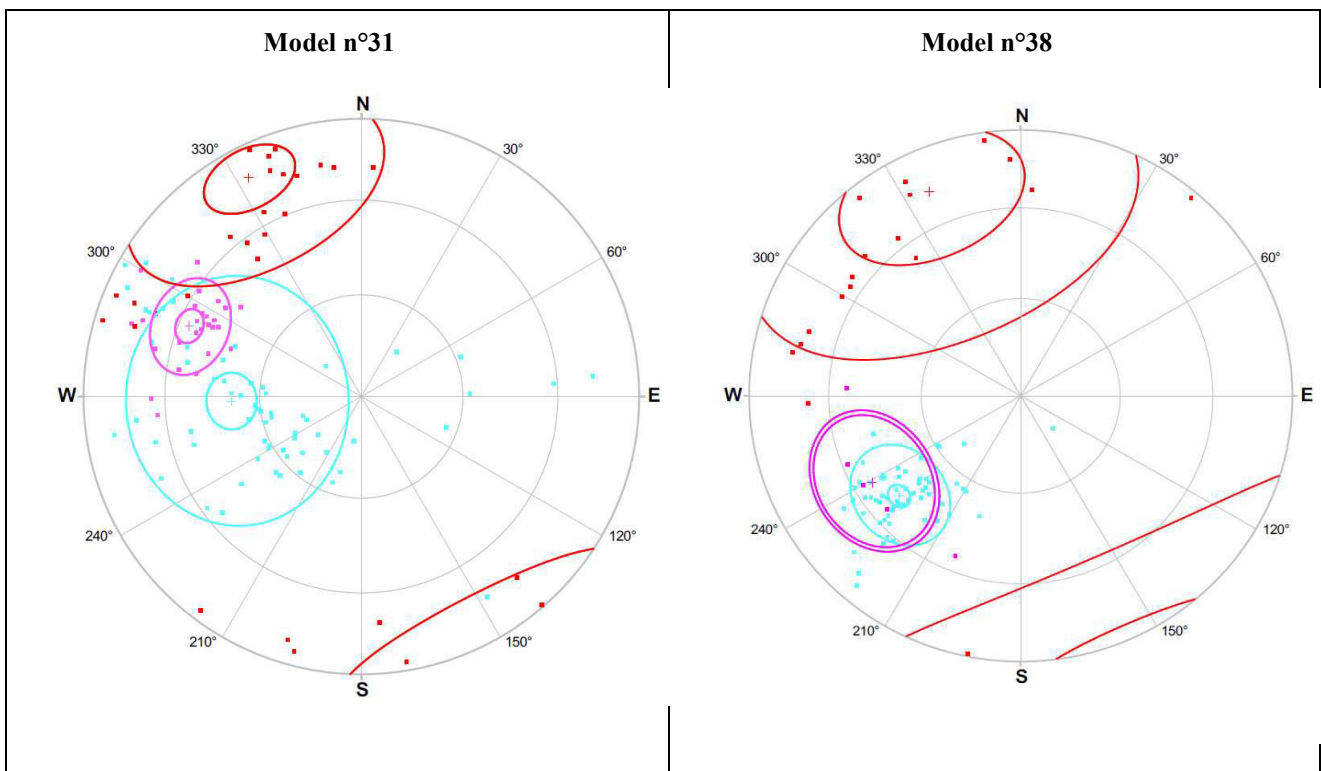


Table 55 - Data of orientations, represented with poles on the stereographic Lambert projection. The “new” joint set K1 is depicted in red, while the exfoliation joints in light blue (for the data collected along the strike) and in pink (for the data collected along the dip direction). The distinction between the joint sets “old” K1 and K5 is difficult and leads to a not significant number of tested discontinuities. For these reasons these two joint sets have been grouped

The new set K1 has been encountered as the prevalent in 21 models, while the tectonic joint set K2 is the prevalent in 5 models and the secondary in 3 photogrammetric models. The tectonic joint set K3 is the prevalent in 12 models and the secondary in only 1 photogrammetric model, finally the set K4 is the prevalent in 4 models and the secondary in 3 photogrammetric models (**Figure 114**).

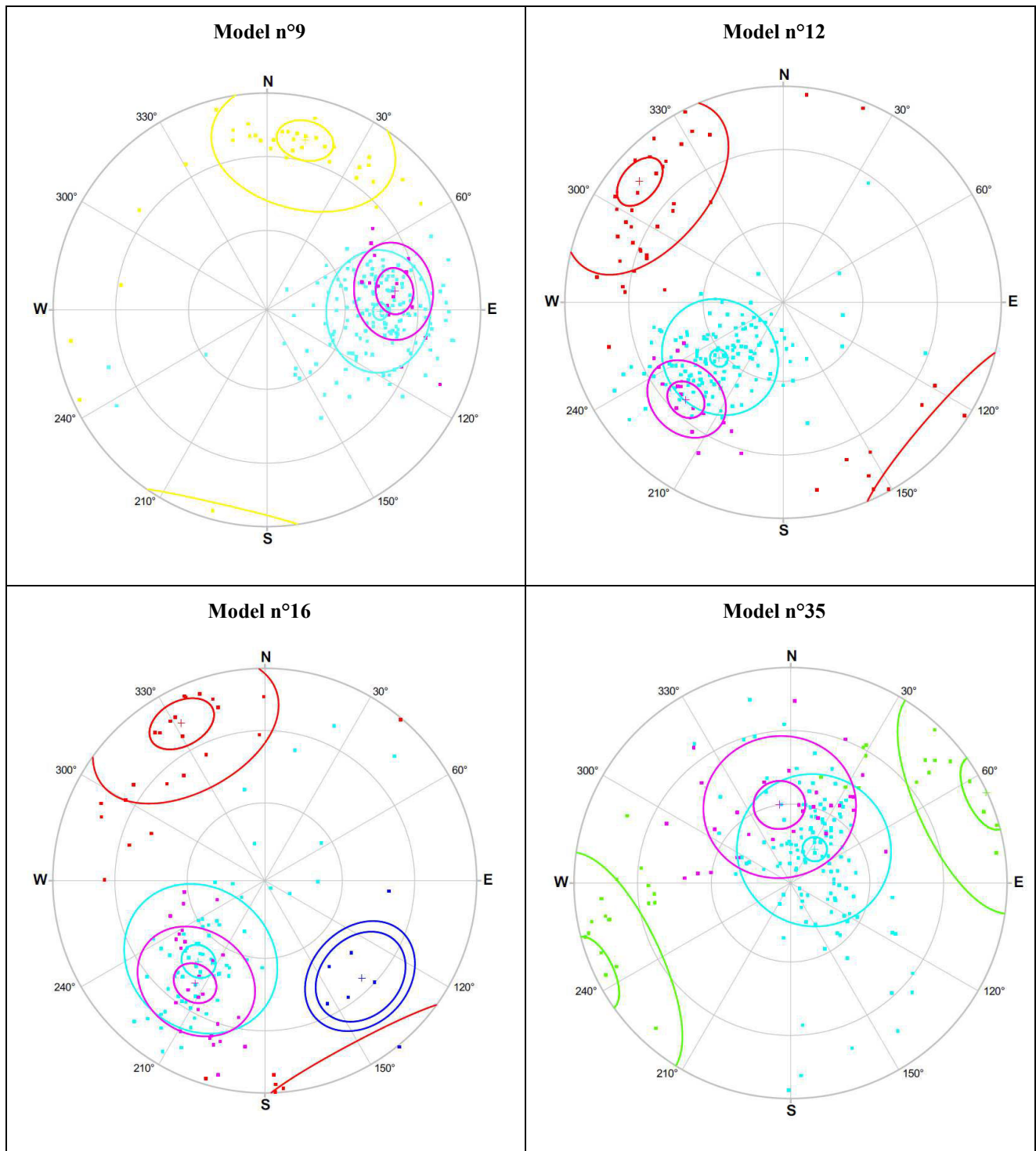


Table 56 - Data of orientations, represented with poles, of the tectonic joint sets K1 (depicted in red), K2 (in green), K3 (in yellow), K4 (in blue) and the exfoliation joints, collected along the strike (in light blue) and dip direction (in pink). In each photogrammetric model the main tectonic joint sets, which are one or sometimes two, have been measured. While the tectonic joint sets have a quite constant orientation in the study area, the orientation of exfoliation joints varies from model to model, according to the topography

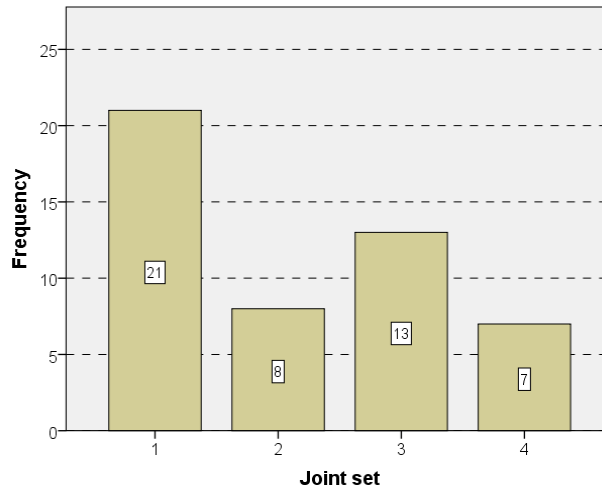


Figure 114 – Frequency histogram of the tectonic joints measured through the photogrammetric approach. In 7 models, beyond the main tectonic joint set, also a secondary joint set has been measured

3.6.2 Trace lengths and terminations

The trace lengths of tectonic joint sets have been measured, tracing out, on each photogrammetric model, the visible trace of each joint, along the real surface of the joint, considering also the roughness. The data have been collected only along the strike.

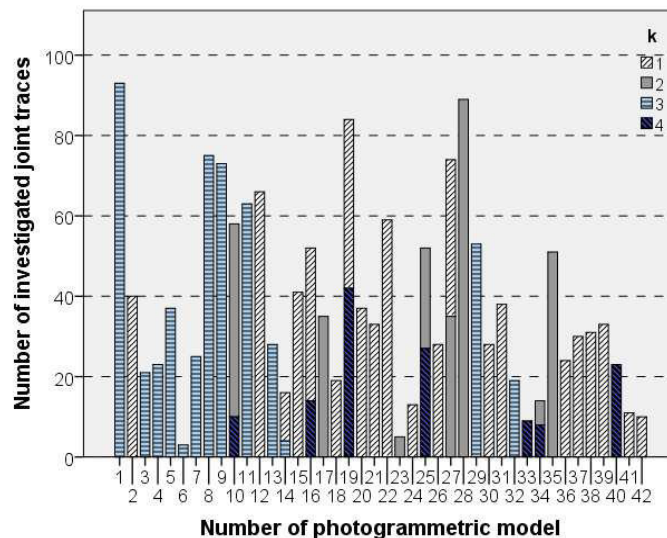


Figure 115 – Frequency histogram of the collected number of trace lengths, for each photogrammetric model, subdivided according to the considered tectonic joint set

The number of sampled trace lengths varies for each model (**Figure 115**), according to the dimension of the investigated area (**Figure 116**): in general bigger the model is, more data can be collected. The clearest dependency between the investigated area and the number of measured trace length, occur for the joint set K1, followed by K4. The set K2 has a slight different trend, because of the photogrammetric model n°28, which allows collecting really an unusual great number of data, respect to the investigated area. Generally, the joint set K3 allows collecting more data that the other sets, and therefore a trend cannot be observed.

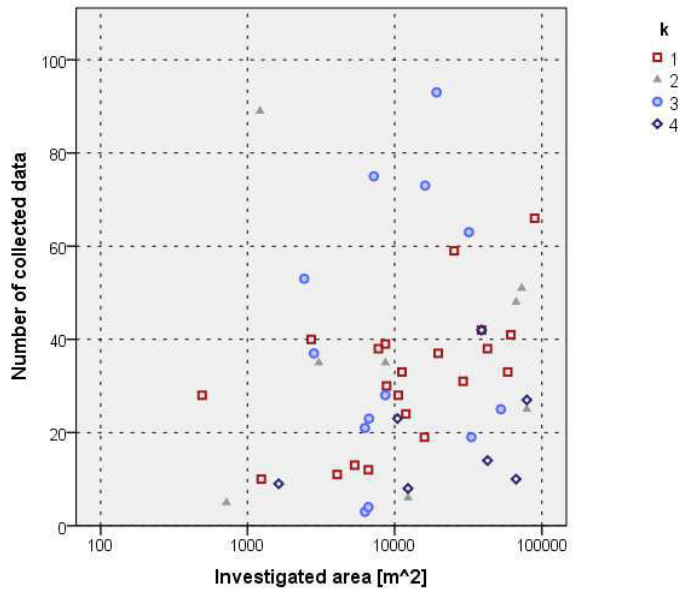


Figure 116 – Relation between the investigated area of photogrammetric model and the number of collected data, subdivided according to the considered tectonic joint set

Considering all the collected data, the minimum, mean and maximum trace lengths, subdivided for tectonic joint set, have been individuated, calculated and reported (Table 57). The mean trace lengths are approximately similar for all the sets, while the minimum and maximum values show a greater variability. The analysis of mean trace length shows that no big differences occur among the different tectonic joint sets: they range from 24.3 metres (for the set K1), to almost 29 metres (K2), and all the median trace length values are between 20 and 26 metres (Figure 117).

| Tectonic joint set | TRACE LENGTH [m] | | |
|--------------------|------------------|------|---------|
| | minimum | mean | maximum |
| K1 | 1.5 | 24.3 | 240.4 |
| K2 | 0.3 | 28.9 | 331.9 |
| K3 | 0.5 | 25.5 | 444.3 |
| K4 | 1.3 | 26.0 | 272.8 |

Table 57 - Values of minimum, mean, maximum and median trace lengths, subdivided for tectonic joint set

The minimum measurable trace lengths are strongly related to the resolution of the photogrammetric model, and so, although the minimum value varies with the set, this is not a good indicator of the joint set.

The maximum trace length values are really long, with values overpassing 200 metres, which of course indicate tectonic lines. The longest measured value reaches almost 445 metres, but it is an extreme outliers. The median of the maximum trace length values ranges from 64 metres (for the sets K1 and K2) to 78 metres (K3), indicating that so high values are not frequent, because the values smaller than 100 metres prevails.

The trace lengths, minimum, mean and maximum, are clearly dependent on the investigated area (Figure 118), with a subsequent size bias. Actually, the real relation between the investigated area and the minimum

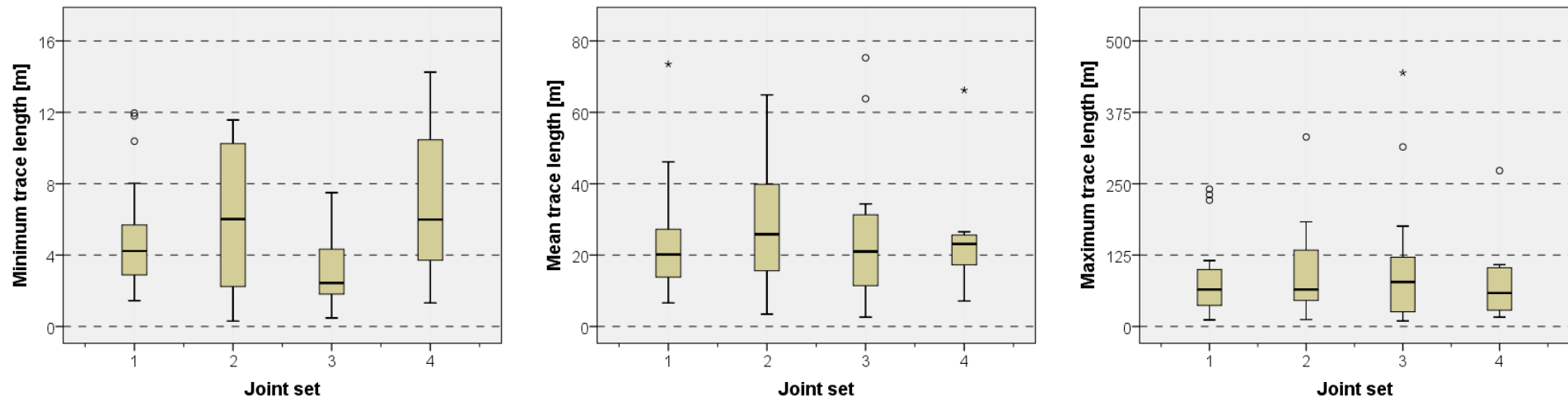


Figure 117 – Box-plots of the minimum, mean and maximum trace lengths (from left to right, respectively), collected from the photogrammetric models, subdivided for tectonic joint sets

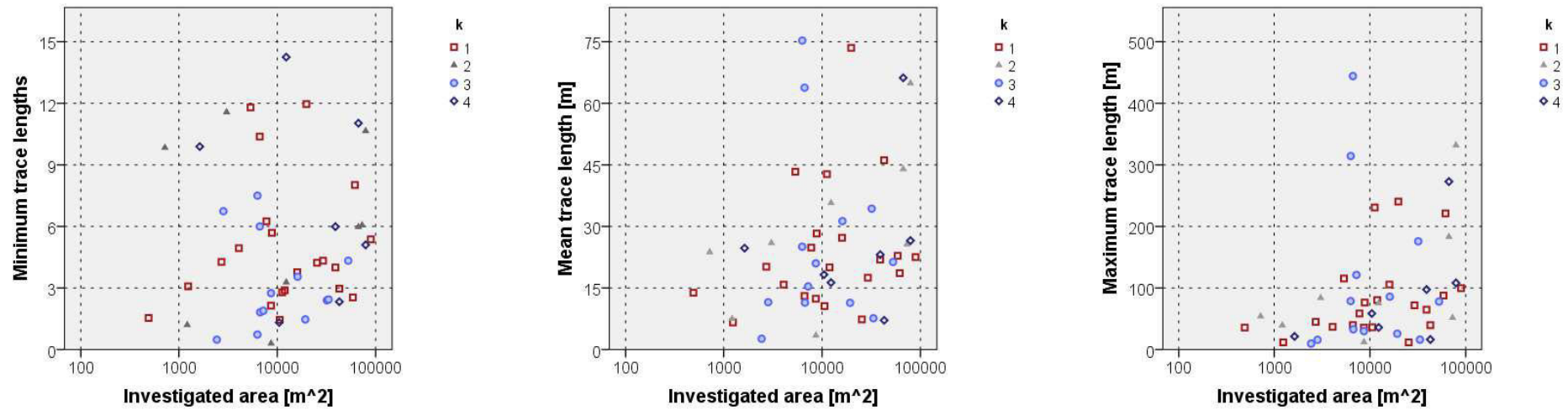


Figure 118 – Relation between the area of the photogrammetric model and the minimum, mean and maximum trace lengths (from the left to the right), subdivided for tectonic joint set

trace lengths cannot be defined, because the minimum measurable value depend on the resolution of the photogrammetric model, leading to a minimum cutoff length which varies changing the considered model. It follows that the truncation bias is not constant in the whole study area.

The measured mean and maximum trace lengths are strongly related to the investigated area; the strongest dependency occur for the tectonic joint set K2, even if the R^2 is always smaller than 0.5. Also the set K4 and K1 exhibit an increase of the measured trace lengths with the investigated area. The joint set K3 has an unusual behaviour with long trace lengths derived from photogrammetric models of medium size. As consequence, the size bias, related to the fact that large joints have higher probability to be sampled than small joints, has been individuated, but it is not removable, due to the reasons which has been already explained in the paragraph 3.4.2.

The censoring bias is related to the fact that the full trace of a joint cannot be measured when the joint is not entirely visible; therefore the trace lengths of joints without both ends observable provide only a lower bound of their length. Therefore, for each sampled trace length, the two tips have been classified as: (i) terminated (Tr) when if the discontinuity ends in rock, (ii) open (Td) if it stops against other discontinuities, and (iii) unknown (Tx) if the real tip of joint is not clearly visible, because it end out from the sampling window or also run off into soil cover, vegetations or shadow and low resolution zones. The number of occurrence of each kind of termination, encountered per each model, has been transformed into percentage, in order to render possible the comparison. The tectonic joints are very long and most of them (between the 70 and 80%) have not clearly visible ends (belonging to the Tx type). The differences in the kind of termination among the different tectonic joint sets are not relevant: the joints with ends of the Tx type prevail, followed respectively by those of Td type, which are less than the 30%, and Tr type, which do not overpass the 5% (**Figure 119**).

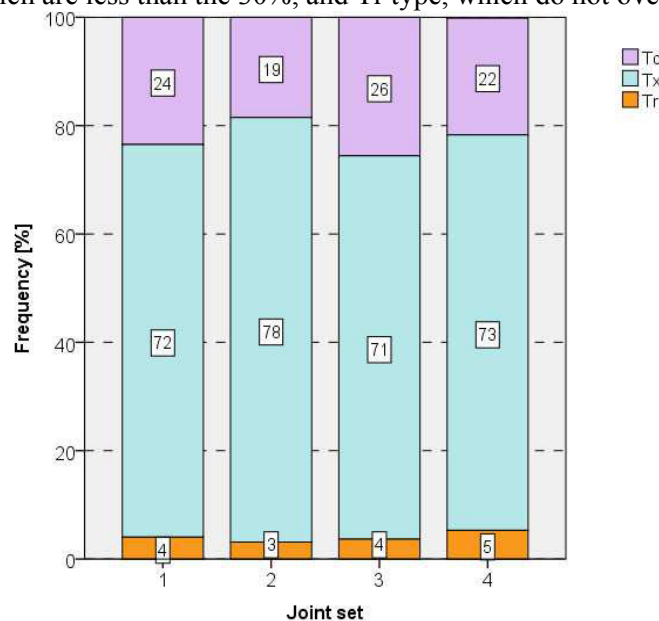


Figure 119 – Kind of terminations, subdivided according to the joint set. Tr, Td and Tx indicate joints ending respectively in rock, against other discontinuities and with a not visible or unclear way

The presence of not visible joint ends leads to the censoring bias, because when at least one tip of the joint is not observable, the real trace length cannot be measured, but only its lower boundary. The true trace length, called real trace length, is therefore visible only for a subset of the joints, those one having both visible ends (i.e. of Tr or Td types). The number of visible terminations is quite variable, even if the models with few visible terminations prevail (**Figure 120**). The joint with both visible terminations are, on average, the 21% for the joint set K1, 7% for K2, 19% for K3 and 14% for K4. The global mean is the 17%.

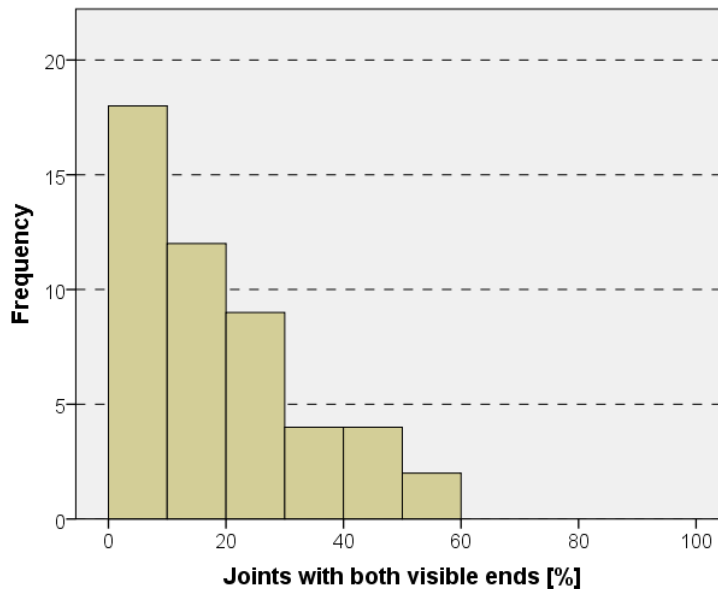


Figure 120 – Histogram of the percentage of joints having both visible terminations

All the joints with one or both not visible ends (i.e. when at least one tip is of the Tx type) have been removed, in order to consider only the real trace lengths. In this way, especially the high values of trace lengths are lost (**Figures 121 and 122**). Comparing the distribution of all data (trace length) with that relative to the only joints without Tx terminations (real trace length), it is possible to observe that the mean and maximum real trace lengths are shorter than the trace lengths (**Table 58**).

| <i>REAL TRACE LENGTH [m]</i> | | | |
|------------------------------|----------------|-------------|----------------|
| <i>Tectonic joint set</i> | <i>minimum</i> | <i>mean</i> | <i>maximum</i> |
| K1 | 4.0 | 17.1 | 131.5 |
| K2 | 0.4 | 12.2 | 42.3 |
| K3 | 0.7 | 13.2 | 59.6 |
| K4 | 3.6 | 27.0 | 75.3 |

Table 58 - Values of minimum, mean, maximum and median real trace lengths, subdivided for tectonic joint set

The minimum values of real trace lengths are a big higher than those of minimum trace lengths, while values of mean and maximum trace lengths are remarkable smaller than those of trace lengths (**Figure 123**). The differences among tectonic sets are now more emphasized: the K4 set has the longest trace lengths, and

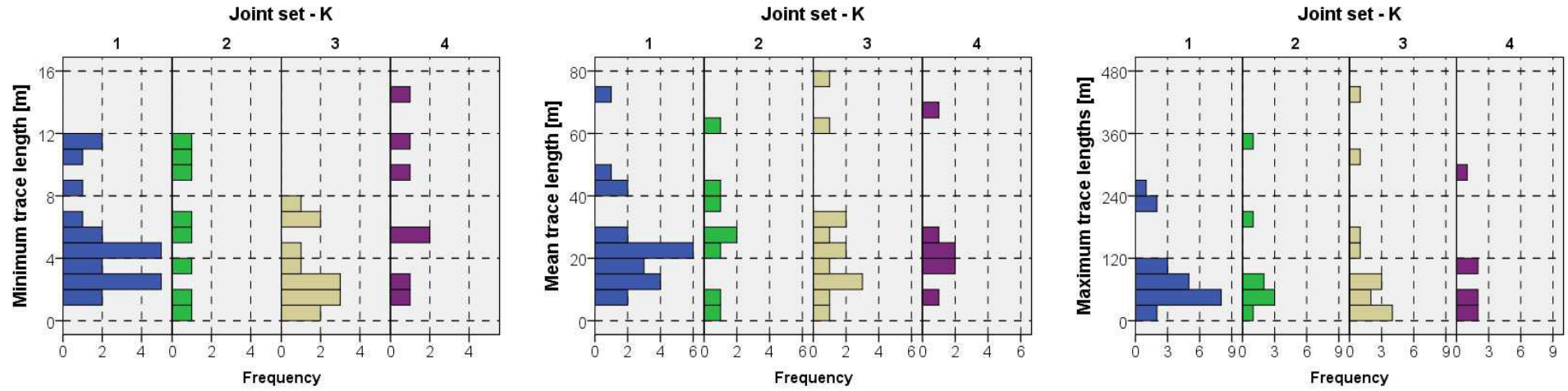


Figure 121 – Frequency histogram of minimum, mean and maximum trace lengths (from left to right, respectively), collected from the photogrammetric models, subdivided for tectonic joint sets

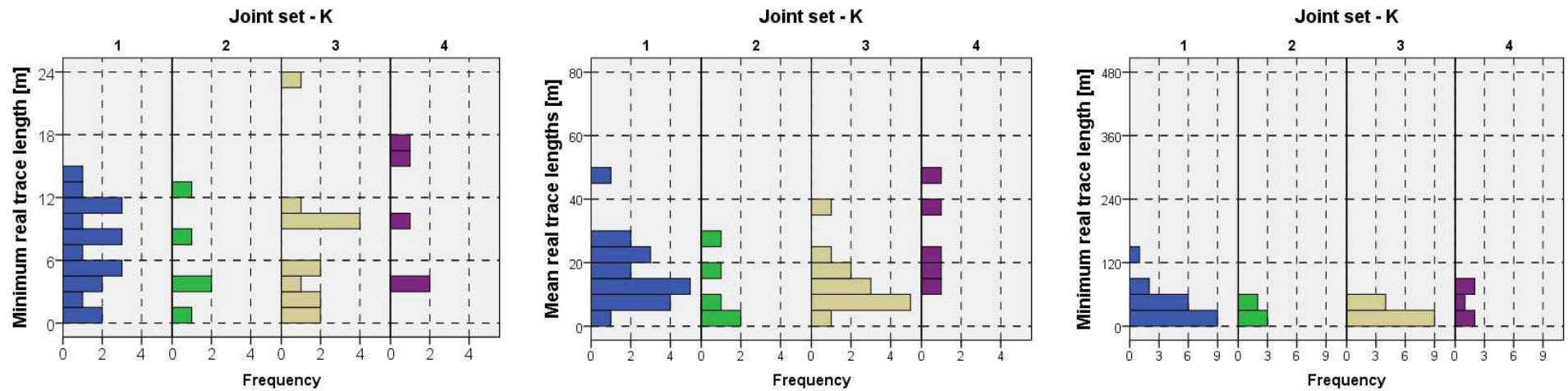


Figure 122 – Frequency histogram of minimum, mean and maximum real trace lengths (from left to right, respectively), collected from the photogrammetric models, subdivided for tectonic joint sets

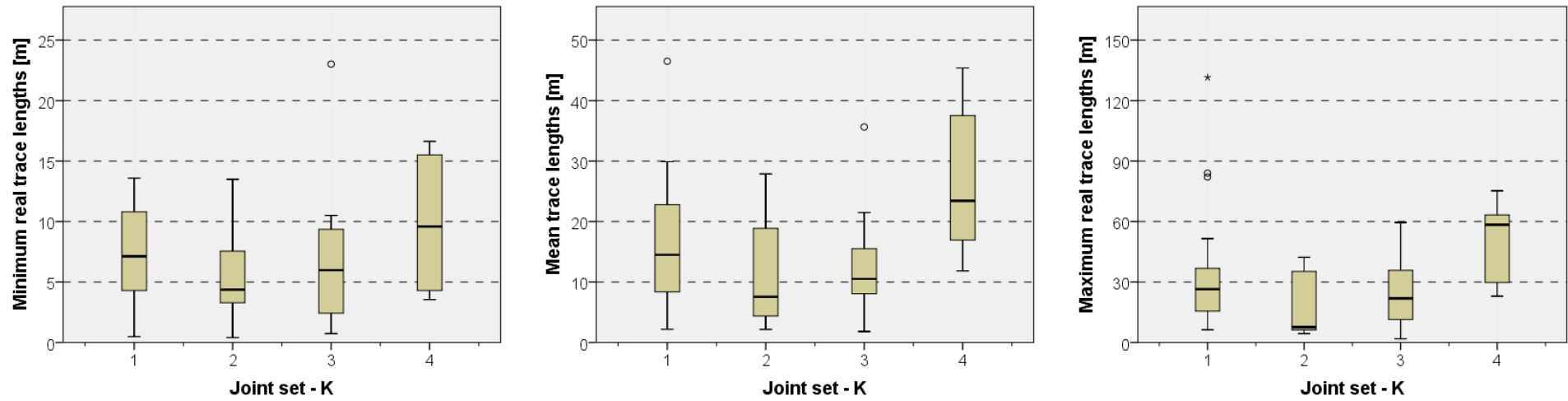


Figure 123 – Box-plots of the minimum, mean and maximum trace lengths (from left to right, respectively), collected from the photogrammetric models, and classified for tectonic joint sets

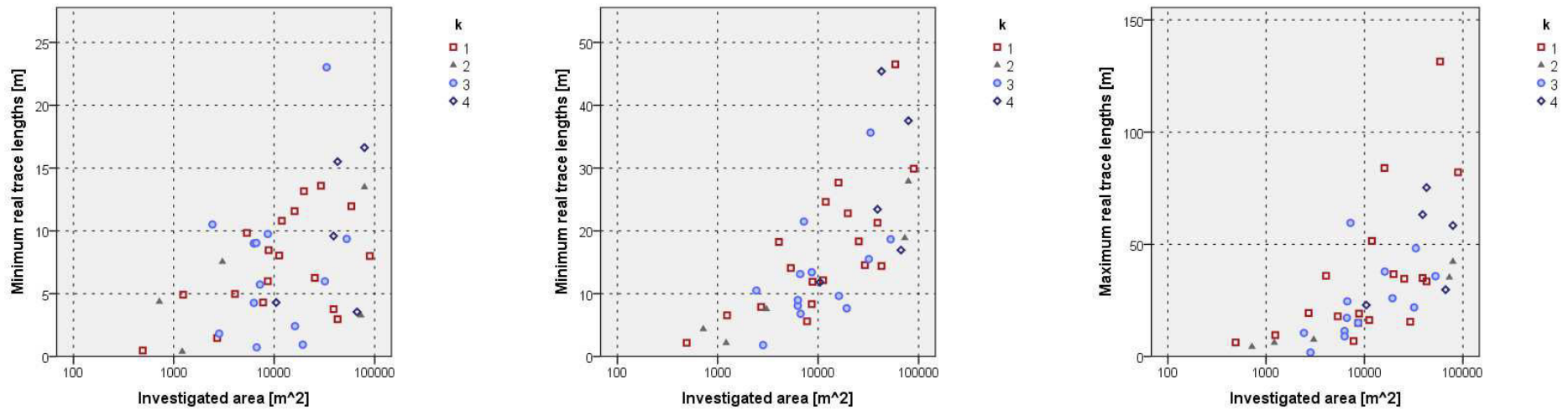


Figure 124 – Relation between the area of the photogrammetric model and the minimum, mean and maximum trace lengths (from the left to the right), subdivided for tectonic joint set

the K2 set the smallest. This fact is respected considering the minimum, mean and maximum trace length values (**Figure 123**).

The frequency distribution of the mean real trace lengths is logarithmic, while those of maximum trace lengths recalls the negative exponential distribution (**Figure 122**). These distributions agree with the literature: the lognormal distributions are the most frequently reported for the trace lengths (McMahon, 1974; Bridges, 1976; Baecher et al., 1977; Barton, 1977; Baecher & Lanney, 1978; Villaescusa & Brown., 1992; Kulatilake et al., 1993; Aler et al., 1996), even if some authors have used exponential distributions (Robertson, 1970; Steffen et al., 1975; Call et al. 1976; Baecher et al., 1977; Cruden, 1977; Priest and Hudson, 1981; Kulatilake et al., 1993; Aler et al., 1996).

The dependency of the measured real trace lengths on the investigated area is very clear, especially for mean and maximum trace lengths (**Figure 124**), which clearly increase with the area. All the joint sets show this strong dependency. The highest R^2 value, equal to 0.96, has been obtained for the maximum real trace length, relative to the K2 set. However, K1 is the most sensitive set to changes in the investigated area.

3.6.3 Rock bridge lengths

Rock bridges between tectonic joint tips are not very common. Actually, the number of discontinuities ending in rock is less than the 5% (**Figure 119**).

How to individuate the rock bridges has been described in the paragraph 3.4.3.

Rock bridges have been encountered only for the joint sets K1 and K3. The rock bridge lengths are always below 6 metres, although rock bridges shorter than 2 metres prevail (**Figure 125**).

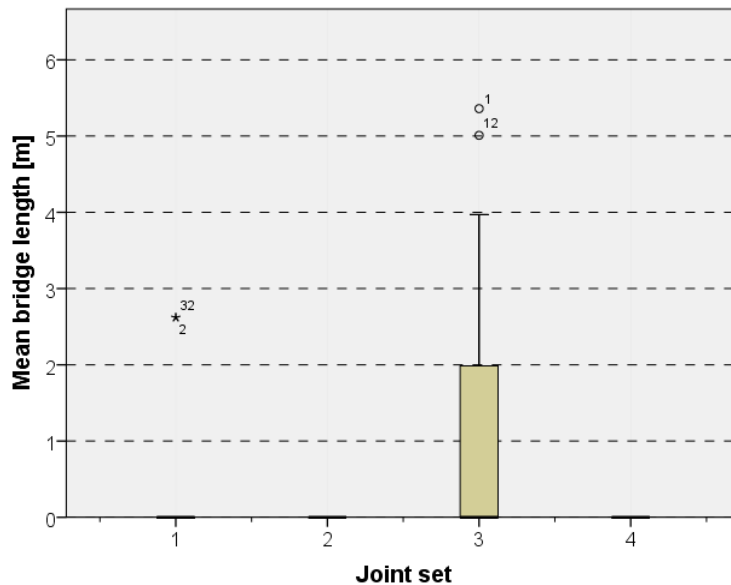


Figure 125 – Box plots of rock bridge lengths, subdivided according to the tectonic joint set

3.6.4 Sinuosity Index

From the trace lengths data, the Sinuosity Index –SI –, defined as the ratio between the real trace length and the Euclidean trace length (i.e. the minimum distance between the tips of the joint) has been computed for each measured tectonic joint. The SI roughly describes the roughness of the joint trace, actually it is equal to 1 for perfectly straight joints.

The SI of tectonic joints is smaller than the SI of exfoliation joints, indicating that the tectonic joints are straighter.

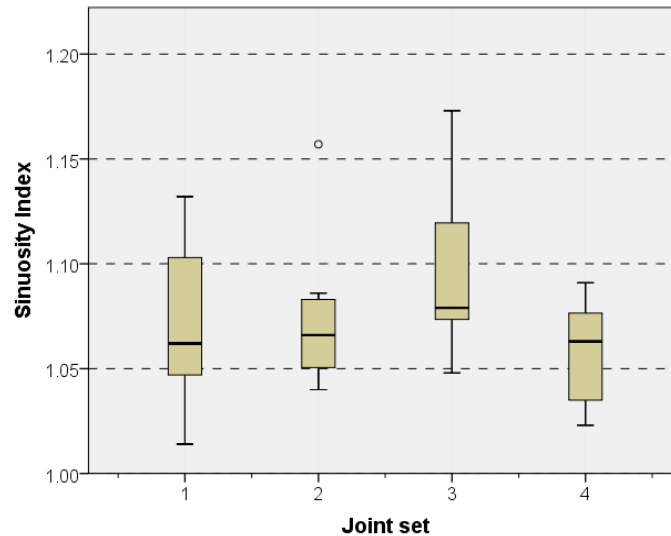


Figure 126 – Box plots of Sinuosity Index values, subdivided according to the tectonic joint set

3.6.5 Spacing

The spacing values have been calculated with the scanline method, previously described in paragraph 3.4.5.

The mean values of joint spacing have been reported in **Figure 127** and in **Table 59**.

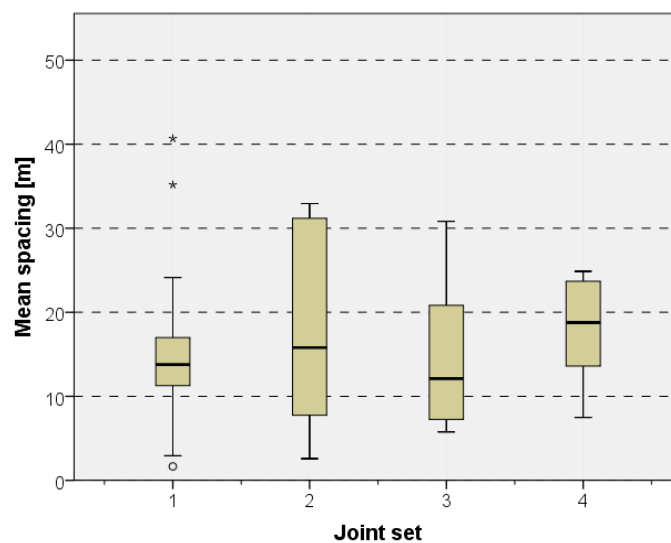


Figure 127 – Box plots of spacing values, subdivided according to the tectonic joint set

The spacing values of tectonic joints are bigger than the spacing values of exfoliation joints. All the tectonic joint sets have similar mean and median values, ranging from 13 to 19 metres. The joint set K1 presents the biggest range, with minimum spacing value of 1.66 metres, and maximum spacing values up to 40 metres. The joint set K4 has the smallest ranges, with a minimum value of 7.50 metres and a maximum one of almost 25 metres. However, the spacing cannot be considered a distinguishing factor for the tectonic joint sets, because all the sets have similar values and distributions.

| <i>MEAN SPACING [m]</i> | | | | |
|-------------------------|----------------|----------------|-------------|---------------|
| <i>Tectonic set</i> | <i>Minimum</i> | <i>Maximum</i> | <i>Mean</i> | <i>Median</i> |
| K1 | 1.66 | 40.68 | 14.57 | 13.78 |
| K2 | 2.58 | 32.94 | 16.40 | 15.80 |
| K3 | 5.77 | 30.82 | 14.52 | 12.31 |
| K4 | 7.48 | 24.88 | 16.65 | 18.78 |

Table 59 – Spacing data, collected from photogrammetric models

Not only the trace length, but also the spacing, can be subjected to some biases:

1. The size bias can be easily recognized plotting the surface of the investigated area against the mean spacing values (**Figure 128**). The relationship is very evident: bigger the model is, bigger the measured spacing value is. The graphs show an exponential relationship for all the sets, this relation is very strong for the set K3 (which provide a R^2 of 0.78), followed by K2 (R^2 of 0.76), K1 (R^2 of 0.63) and finally by K4 (R^2 of 0.03). The R^2 of K4 is so small because there is a small outcrop that allows to measure big spacing values; cutting this outcrop the relationship is clearly exponential also for the set K4.

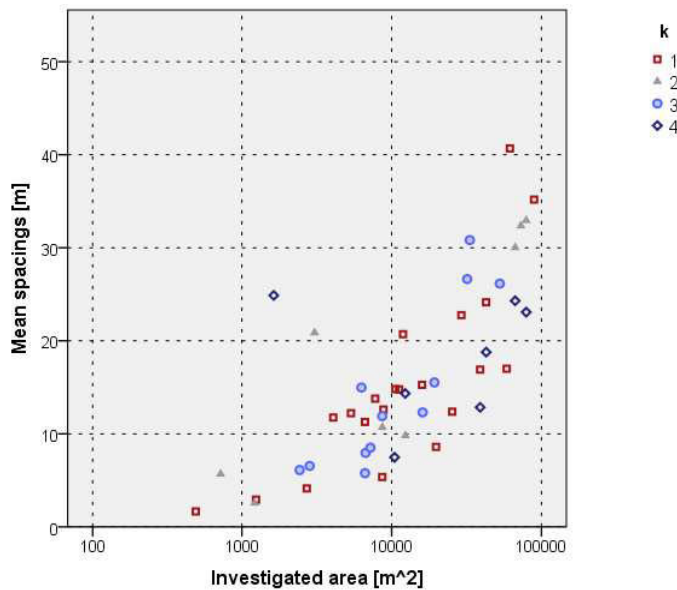


Figure 128 – Relationship between the investigated area of the photogrammetric models and the measured mean spacing values

2. The truncation bias is very variable from photogrammetric model to model; actually, also for the spacing, a constant minimum cutoff equal for all models has not been used, due to the big variations of resolutions among models.
3. The censoring bias does not occur for this kind of measure, indeed the spacing values are always bounded by two observable joints.

A summary table with the mean measured values of tectonic joints has been reported in **Appendix 5**.

3.7 Geostatistical analyses of tectonic joint sets

Some geostatistical analysis, with the almost 3D approach, has been performed also for the tectonic joints. Also in this case, the most reasonable geological approach consists of considering the tectonic joint sets separately.

Data available from photogrammetric models and in situ surveys have been considered, separately, due to scale differences and problems, which have been already described. The locations of photogrammetric models and in situ surveys (carried out from Martin Ziegler) have been reported in **Figure 129**, subdivided for tectonic joint sets.

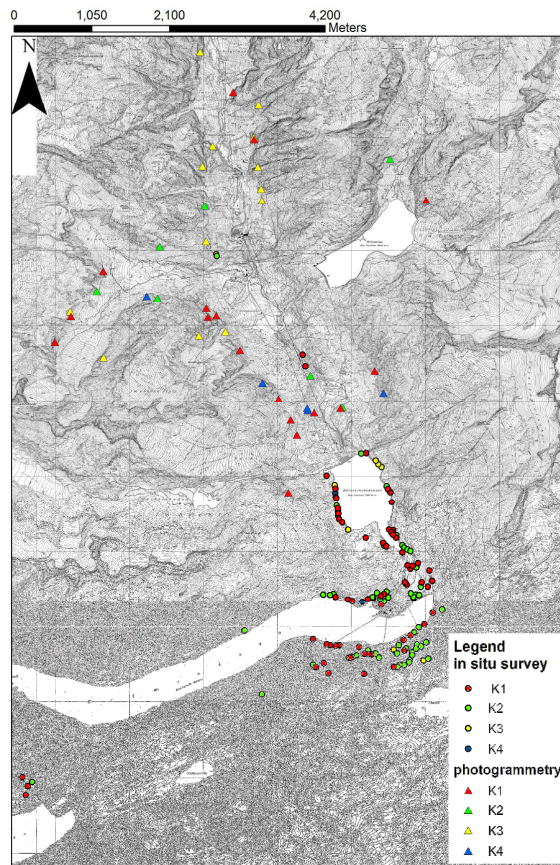


Figure 129 – Locations of sampling points of different tectonic joints sets: K1 set is depicted in red, K2 in green, K3 in yellow and K4 in blue. These data come from photogrammetric models (indicated with triangles) and in situ surveys (indicated with circles)

The map (**Figure 129**) shows that on one hand the K4 set has been observed in not enough locations to carry out a significant geostatistical analysis on this set, on the other hand the set K1 has been frequently recorded, without preferential sampling locations, allowing a significant geostatistical analysis. The situation about K2 and K3 sets is more uncertain; however an attempt can be done. Of sure the photogrammetric models of set K2 are mostly aligned with the direction SW-NE, and therefore a significant result is not expected. The in situ surveys of K2 are more scattered. On the contrary, regarding the set K3, the locations of photogrammetric models are scattered, while the data from in situ surveys are only few, and present a preferential SSE-NNW disposition. As for the exfoliation joints, the properties, which have been studied in the geostatistical analysis, are: the real trace lengths and the spacing. While for the trace lengths data derived both from photogrammetry and in situ surveys are available, the spacing have been measured only on photogrammetric models.

3.7.1 Real trace length

The data of real trace lengths have been subdivided according to the tectonic joint set, transformed through the Gaussian anamorphosis process, and finally used to construct the directional variograms (with an angular tolerance of 22.5°). Initially, the variogram have been constructed, using all the available data (**Table 60**). The lag distance has been assumed equal to 250 metres for data of photogrammetric models and to 100 metres for data of in situ surveys; the linear tolerance has been assumed equal to the semi-lag.

The found maximum correlation directions of set K1 are coherent, despite of the method of data acquisition: for the data coming from the photogrammetrical approach the maximum correlation direction is SSE-NNW, while for the data coming from geomechanical survey the maximum correlation direction is NE-SE. The difference between these two main correlation directions is included in the chosen angular tolerance.

The maximum correlation direction for the K2 and K3 sets, computed respectively from in situ survey and photogrammetric models data, is ENE-WSW, however the variogram of K3 is not very significant.

It is worthy to note that the maximum correlation directions of K1 and K2 are the same of the dip direction of the tectonic joint sets, therefore a geological response for the occurrence of these correlation directions have been found.

The variograms obtained using data of photogrammetric models cannot be used for the modelling and the estimation stages. Actually, the pairs of data involved in the resulting variograms (indicated with a number near to each red cross of the experimental variogram) are not enough to carry out a meaningful estimation.

The obtained using in situ data are decisively better, even if only that one referring to K1 can be used, because the variogram of K2 set has a nugget effect that is too high, respect to the sill value, and cannot be used to model properly the set.

It follows that only the K1 set has been used in the variogram modelling and prediction steps.

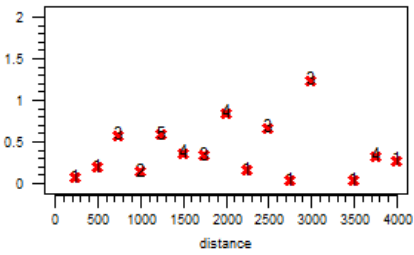
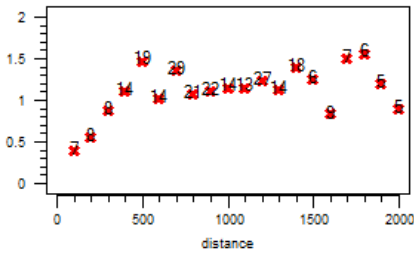
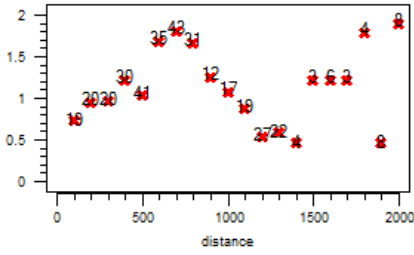
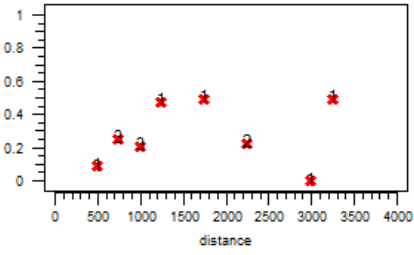
| TRACE LENGTH | Photogrammetric models | In situ survey |
|-------------------------------|---|--|
| <p>K1 145°/69°</p> | <p>157.5°-337.5°</p>  | <p>135°-315°</p>  |
| <p>K2 242°/89°</p> | <p>Data are not enough to find a significant variogram</p> | <p>67.5°-247.5°</p>  |
| <p>K3 188°/67°</p> | <p>67.5°-247.5°</p>  | <p>Data are not enough to find a significant variogram</p> |
| <p>K4 329°/55°</p> | <p>Data are not enough to find a significant variogram</p> | <p>Data are not enough to find a significant variogram</p> |

Table 60 – Directional variograms of real trace lengths, subdivided according to tectonic joint sets and method of data acquisition

The tectonic joint set K1 has been used in the variogram modelling and prediction steps. The main problem is that, once again, the in situ data have been only estimated and not measured. It means that a categorical variable and not a continuous one form the dataset. The data have been therefore reclassified and the indicator variograms computed. However, since the SGS have given the best results in the previous cases, an attempt to treat this variable as a continuous one, considering the mean values of the class, has been done. The in situ data have been reclassified, as follow:

- Class 1: trace length shorter than 2 metres;
- Class 2: trace lengths between 2 and 4 metres;

- Class 3: trace lengths between 4 and 10 metres;
- Class 4: trace lengths longer than 10 metres.

Since the in situ data of trace lengths are 68, about $\frac{3}{4}$ of them (53) have been used to construct the variograms and the remaining $\frac{1}{4}$ (15) for the validation.

The directional variograms (**Table 60**) have been constructed both as a normal variogram, considering the mean trace length value of the class, and as an indicator variogram considering the median class of the trace lengths. In this case, since the number of classes is even, between the classes 2 and 3, the third one has been chosen, because it is the class with the highest number of data (i.e. 32).

| <i>TRACE LENGTH</i> | <i>Maximum correlation direction</i> | <i>Mean correlation direction</i> |
|---|---|---|
| <i>Mean value of trace length class</i> | <p>135°/315°</p> <p>plot 18: variogram - azth=135, dip=0</p> | <p>45°-225°</p> <p>plot 8: variogram - azth=45, dip=0</p> |
| <i>Class n°3</i> | <p>315°/20°</p> <p>plot 16: variogram - azth=135, dip=160</p> | <p>45°-225°</p> <p>plot 8: variogram - azth=45, dip=0</p> |

Table 60 – Theoretical models used to fit the experimental semivariograms of real trace lengths, which have been measured in 53 sampling locations during in situ survey. In the first row there are normal directional variograms, and in the second one there are indicator variograms. The lag distance always is equal to 100 metres

The parameters of models that best fit the experimental variograms have been reported in **Table 61**.

Although the maximum correlation direction is similar, the indicator variogram exhibits a nugget effect, a sill and a range that are significantly smaller than those of the variogram computed using the mean values. Of course the nugget effect and sill are smaller because the variability of binary transformed data is smaller than mean values of the variable.

The model derived from mean trace lengths values and the median indicator variogram model have been used to estimate the real trace length values, through the SGS and the SIS technique, respectively. In order

to guarantee a direct comparison between the two resulting maps (Table 62), also the values of the map obtained with the SGS have been reclassified.

| <i>REAL TRACE LENGTHS</i> | <i>Mean values</i> | <i>Class 3</i> |
|-----------------------------------|--------------------|----------------|
| Kind of model | Spherical | Spherical |
| Nugget effect | 0.2 | 0.06 |
| Sill | 1.3 | 0.30 |
| Maximum correlation direction [°] | 135-315 | 315/20 |
| Maximum range [m] | 800 | 520 |
| Mean correlation direction [°] | 45-225 | 45-225 |
| Mean range [m] | 200 | 200 |
| Minimum correlation direction [°] | 135/90 | 135/70 |
| Minimum range [m] | 40 | 60 |

Table 61 - Values of theoretical variogram models used to fit the experimental variograms of trace lengths

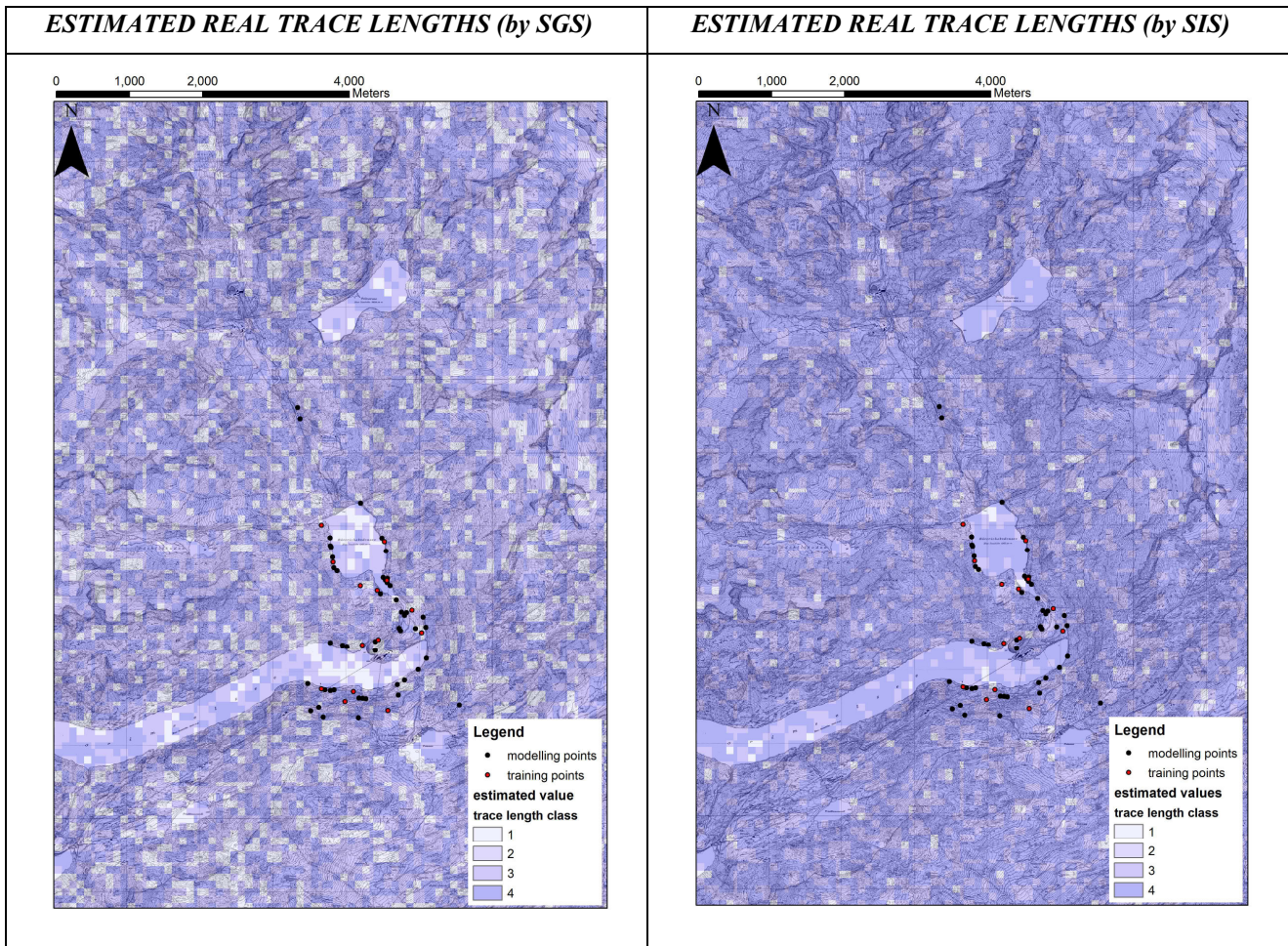


Table 62 – Estimated real trace length classes, obtained through sequential Gaussian simulation (on the left) and Sequential Indicator Simulation (on the right), considering data from 53 in situ surveys (whose locations are reported in black.). The red circles represent the models which have been used in the validation process

The map obtained through the SIS has more values belonging to the third and fourth classes than the map obtained with the SGS, resulting in longer estimated trace lengths.

The validation process has been carried out using 18 in situ survey data and comparing the estimated trace length class in these locations with the measure values (**Figure 130**).

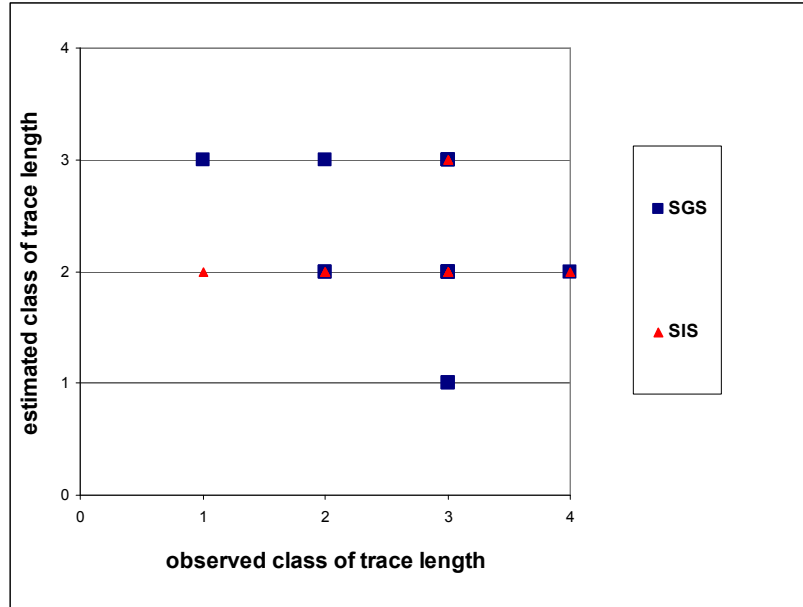


Table 130 – Comparison between observed and estimated real trace length classes, founded applying the Sequential Gaussian Simulation and the Sequential Indicator Simulation approaches

The validation shows that the SIS technique gives the best results, with a mean error of 0.53 and a deviation standard of 0.74. Using the SGS approach the mean error is of 0.47, but with a standard deviation of 1.13.

The comparison between the estimated and observed classes of trace lengths (**Table 63**) shows that however the right class have been estimated only in the 40% of the cases. the method of subdivided the data in classes, without measuring their values, is therefore not recommendable in the estimation process.

| REAL TRACE LENGTHS | SGS | SIS |
|-------------------------------|------------|------------|
| Estimation of the right class | 40% | 40% |
| Overestimation of 1 class | 7% | 7% |
| Overestimation of 2 classes | 6% | 0% |
| Underestimation of 1 class | 27% | 46% |
| Underestimation of 2 classes | 20% | 7% |

Table 63 – Comparison between the validation results of Sequential Gaussian Simulation and Sequential Indicator Simulation

3.7.2 Spacing

The spacing values have been only measured on photogrammetric models and not also in situ.

A directional variogram including all the spacing values (after the Gaussian anamorphosis process), despite of the tectonic joint set, has been constructed (**Figure 131**). It indicates that the spacing can be treated as a

Regionalized Variable, because a significant variogram structure has been found. However the main correlation direction is N-S and indicated the main axis of the Hasli valley, and so reflects the disposition of the photogrammetric models.

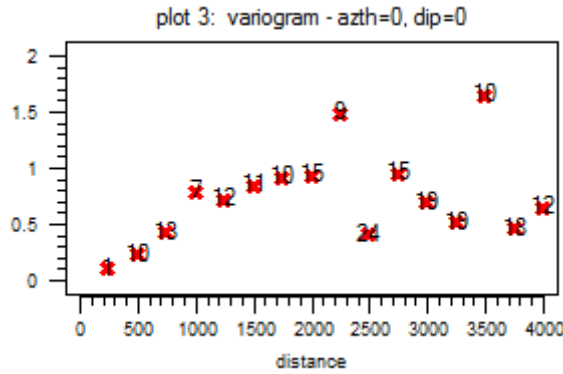


Figure 131 – Variogram including all the mean spacing values measured from photogrammetric models

Afterwards the spacing values have been subdivided according to the tectonic joint set and transformed into a Gaussian standard distribution. K1 is the only joint set recorded in a number of photogrammetric models, which is sufficient to perform both the modelling and the validation. Actually K1 set has been encountered in 21 photogrammetric sampling locations, $\frac{3}{4}$ of them (16 models) have been used in the modelling dataset, with the aim to construct the experimental variograms, and the other $\frac{1}{4}$ (5 models) have been used in the training point dataset, to validate the results.

The directional experimental variograms have been computed using a lag of 250 metres, with a linear tolerance of hal- lag and an angular tolerance of 22.5° (Table 64).

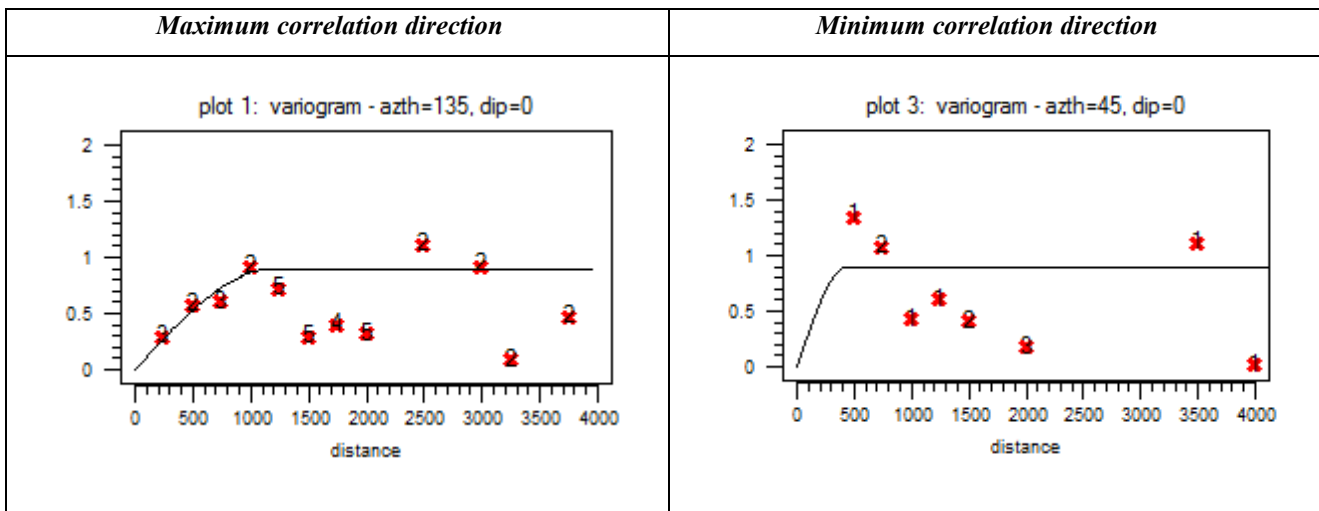


Table 64 – Variogram including all the mean spacing values measured from photogrammetric models

The experimental variograms have been modelled with a spherical model, whose parameters have been reported in Table 65. The maximum correlation direction recalls the dip direction of the joint set K1. The nugget effect is null and the sill is equal to 0.9.

| <i>SPACING</i> | <i>K1</i> |
|-----------------------------------|-----------|
| Kind of model | Spherical |
| Nugget effect | 0 |
| Sill | 0.9 |
| Maximum correlation direction [°] | 135-315 |
| Maximum range [m] | 1200 |
| Mean correlation direction [°] | 45-225 |
| Mean range [m] | 440 |
| Minimum correlation direction [°] | 135/90 |
| Minimum range [m] | 240 |

Table 65 - Values of theoretical variogram models used to fit the experimental variograms of K1 spacing values

The SGS have been performed to estimate the spacing values of K1 on the whole domain (Figure 132).

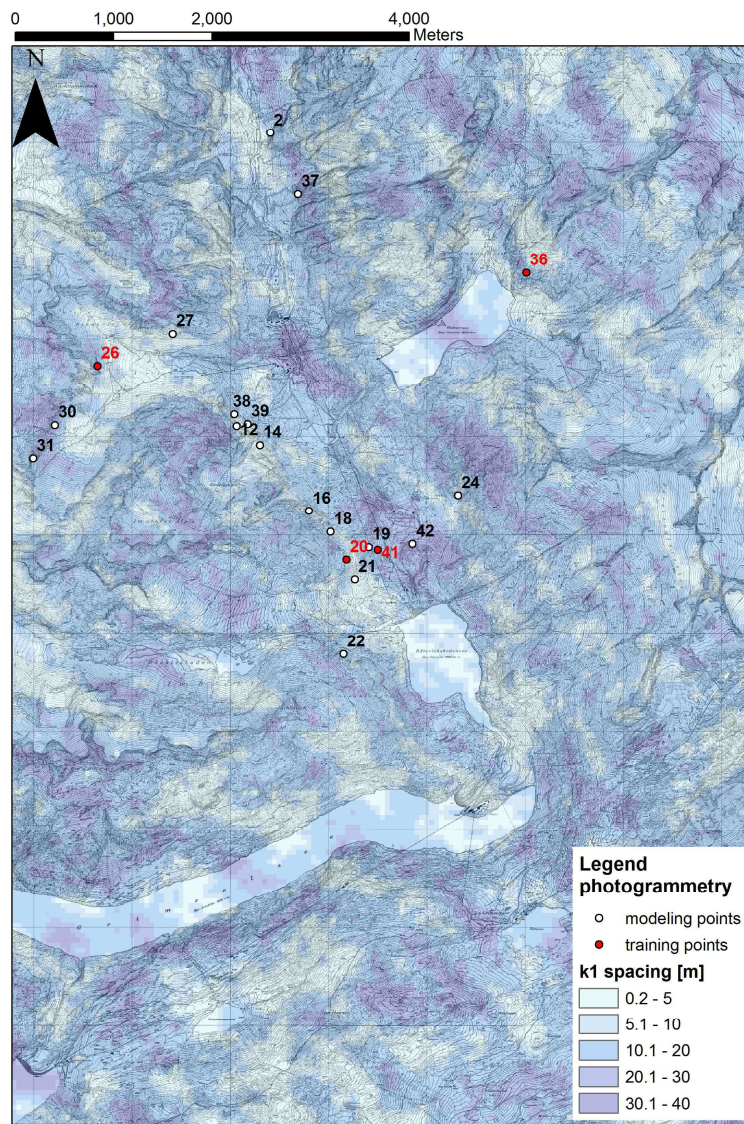


Figure 131 – Variogram including all the mean spacing values measured from photogrammetric models

The validation graph (**Figure 132**) shows a really good agreement between measured and estimated data, even if it has been constructed considering only five models.

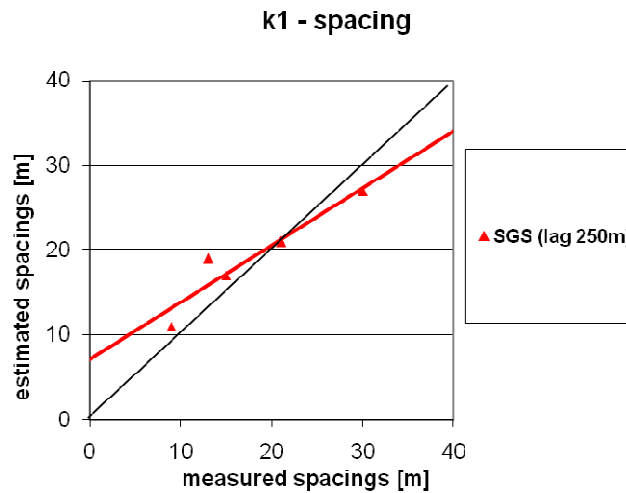


Figure 132 – Validation of K1 spacing values, estimated using the Sequential Gaussian Simulation approach

3.8 Conclusions

Some conclusion can be outlined from the Grimselpass case study.

Trace lengths and spacing, measured from photogrammetric models and observed in situ, have been estimated both from exfoliation joints and tectonic joints, separately. Actually the analysed properties are related to a single joint set and therefore need to be treated independently. Therefore the exfoliation joints have been subdivided, according to their features, into three generations of exfoliation joints (with different age of formation), and the tectonic joints into four main sets, according to their orientations. The study, the individuation, distinction and analysis of exfoliation joints have been done thanks to the essential contribution of Martin Ziegler, Simon Loew and Stephan Bolay of the Engineering Geology group of the ETH (Zuerich, CH).

Regarding the photogrammetric model dataset, the SGS technique, with an almost 3D approach, has been successfully applied for the spacing, considering both exfoliation joints (belonging to the second generation) and the tectonic set K1. For all the other generations and sets the data were not enough to find significant spatial correlations. The main correlation direction of the second generation of exfoliation joints is parallel to the main valley, while the main correlation direction of the joint set K1 is its dip direction. Some problems arise from trace lengths, especially those of exfoliation joints. Actually the computed variograms show a strange behaviour, with some incoherent rotations of the maximum correlation direction, which render impossible to find a significant variogram to model. This could be related to the fact that the exfoliation joints, which formed parallel to the paleo-valley topography, following its curvature, present curvilinear features (parallel to the valley), which cannot be captured using the main geostatistical tool: the variogram. Actually, it describes the dissimilarity of a variable observed at any two spatial locations and hence is not

able to capture mathematically the complexity of curvilinear features, which require at least correlations between three spatial locations at a time. This problem does not arise with the spacing because it is measured perpendicularly to joint traces, and so following straight lines.

In my opinion the main drawback dealing with photogrammetric models is that the dimension of the investigated area varies with the photogrammetric model, and the main problem is that it cannot be normalized (considering only a standard area equal for all the models), because the minimum measurable value is strongly related on the resolution of the model. Although very numerous data have been collected from the photogrammetric model, the use of the mean value for the whole outcrop results to be not significant. Actually an outcrop is a rich source of geological information, providing a lot of data and information, which are lost considering only the mean value. Actually, such amount of information and so the geological heterogeneity cannot be captured using the variogram, which merely describes correlations between only two spatial locations. Yet at the same time, a unified and flexible geostatistical methodology for capturing the geological richness of outcrop data is still lacking.

Regarding the in situ survey data set, kindly permitted by Martin Ziegler, the main problem is that the values have been estimated using some classes and not measured. This fact leads to dealing with discrete (or categorical) variable, which in geostatistics need a binary transformation of the values. With categorical variable the indicator variograms need to be constructed and the Sequential Indicator Simulation –SIS– technique can be applied. This technique revealed to be inadvisable, because it generates maps that are “homogeneously heterogeneous”, being maximally disconnected in the low and high values; hence, these maps are characterized by the maximum entropy property, which does not match with the geological properties of the fractures. It follows that the estimation of classes of values, without measuring them, does not allow a precise estimation of rock mass properties in a wide area. However considering the spacing of the tectonic joint set K1 this approach gives rough but reasonable results.

Another important shortcoming of the application of geostatistical techniques is that these are based, and at the same time limited, by the stationarity assumption, which implies the absence of trends in the data. Actually, in geology, trends are often present: it is well known that the rock mass quality is lower in surface and it improves going in depth, due to increasing of spacing values and, at the same time, the decreasing of persistence and apertures. For instance, at the Grimselpass it has been observed that exfoliation joint spacing increases from less than 1 meter in the near-surface to more than 10 metres at greater depth (Ziegler et al., 2013). Moreover it is well known that exfoliation joints are restricted in occurrence to relatively shallow depths (Gilbert, 1904; Dale, 1923; Jahns, 1943), with typical depths ranging from a few decametres to more than 100 m below the ground surface (e.g., Jahns, 1943; Lewis, 1954). Therefore, the exfoliation joints tend to disappear in depth. Structural data interpretation in subsurface galleries, together with observations from surface outcrops, shows that exfoliation joint maximum depth range between 55 and 180 metres (for a borehole 610 metres deep), and 70 and 260 metres, at different locations, within the Grimsel area (Ziegler

et al., 2013). Therefore, for the exfoliation joint set spacing a trend occur with the depth. It follows that, with the aim to respect the stationarity property, estimation have been performed only near the surface. It could be possible to perform estimation with depth only with the availability of more depth data, which allow subdividing the 3D models in some homogenous portions (i.e. without trend) to treat independently. The only use of superficial data to obtain 3D geostatistical models is meaningless.

4. GENERAL CONCLUSIONS AND FINAL REMARKS

The objective of this thesis consists in the estimation (i.e. the prediction), through geostatistical techniques, of the geomechanical parameters determining the quality of rock masses, starting from punctual and scattered sampling locations.

The main challenge was to understand if geostatistical techniques, which were applied so successfully to local and specific problems, could be applied also at regional scale (i.e. considering very wide portion of territory), finding the best method useful to make estimation of that scale.

Two study areas, both located in the central portion of the Alpine chain, with similar geological history, have been considered in this work: Chiavenna valley and Grimselpass area. In the first case study, data of rock mass properties have been collected directly from geomechanical surveys carried out on the outcropping rock masses. In the second case, data of geometrical rock mass features have been collected indirectly from photogrammetric models, but also direct in situ observations have been independently considered.

In the first case study, global properties of rock mass (i.e. horizontal intercept, Rock Mass Rating and Volumetric Joint Count), which describe the rock mass as a result of all the geological and structural events involved in its history, have been analysed.

In the second study case, properties related to single joint set (trace lengths and joint sets spacing) have been considered; therefore data have been collected subdividing them according to the history and mechanism of formation of discontinuities. Data of the youngest fracture set (the exfoliation joints) have been distinguished and separately analysed from data of older tectonic joint sets. Moreover, the exfoliation joints have been subdivided, according to their relative ages, in four generations, and the tectonic joints in five sets, distinguished according to their orientations.

Each of the global rock mass property (horizontal intercept, Rock Mass Rating and Volumetric Joint Count) has been revealed to be a Regionalized Variable –RV–, and has been successfully estimated over the studied domain. Regarding the properties dependent on a single joint set, the set spacing has been successfully estimated, but not the trace length. This could be related to the fact that the exfoliation joints, which formed parallel to the paleo-valley topography, following its curvature, present curvilinear features (parallel to the valley), which cannot be captured using the main geostatistical tool: the variogram. Actually, it describes the dissimilarity of a variable observed at any two spatial locations and hence is not able to capture mathematically the complexity of curvilinear features, which require at least correlations between three spatial locations at a time. This problem does not arise with the spacing because it is measured perpendicularly to joint traces, and so following straight lines.

The same geostatistical analysis process has been used in both locations. It consists of four main steps:

1. Exploratory Spatial Data Analysis
2. Variogram Analysis
3. Prediction
4. Validation

Since both study cases are located in Alpine areas, the consideration of the elevations, beyond the latitudes and longitudes, plays a key role in the estimation process. The altitude has to be considered during both the semivariogram analysis and the prediction stage, in order to obtain reliable results. This is one of the main innovative results, which has obtained thanks to this thesis.

Regarding prediction technique, both Ordinary Kriging –OK– and Sequential Gaussian Simulation –SGS– have been applied in both study cases, which have shown that the SGS gives the best results when it is performed considering also the elevation. The main shortcoming of OK is that it does not respect the extreme values of the analysed variable, producing a remarkable smoothing effect, which consists on the overestimation of low values and underestimation of high ones. In the second case study, when the data have not been measured, but only estimated in classes, the Sequential Indicator Simulation –SIS– has been applied. This technique revealed to be inadvisable, because it generates maps that are “homogeneously heterogeneous”, being maximally disconnected in the low and high values; hence, these maps are characterized by the maximum entropy property, which does not match with the geological properties of the fractures. It follows that the estimation of classes of values, without measuring them, does not allow the correct estimation of rock mass properties in a wide area. Of course, the observation of rock mass properties, with the subdivision of their values in classes, is important because it allows having a general idea about the rock mass properties, but these classes can be used only as a soft data. They cannot be treated as hard data in geostatistical modelling. To do so it is very important to carry out detailed geomechanical surveys, according to a standard procedure, for instance according to the ISRM suggested method (ISRM, 1978).

The best results come from the Valchiavenna case study, because data have been homogeneously collected, considering rock masses having the same support (i.e. 20 metres length and 2 metres high), and collecting a significant number of data for each property. The geostatistical analysis has been performed on the mean values of each property, which is significant because the considered area is small.

In particular, the RMR estimation gives good results, especially removing the contribution of water, which has not been surveyed with standard climatic conditions in all the geomechanical survey locations. This is another important result, because it demonstrates how a parameters which is given by the sum of more parameters, can be treated as a Regionalized Variable and successfully estimated. The knowledge of RMR values in a whole area can have interesting application in land use planning, such as in the landslide susceptibility mapping, and in the identification of the critical points.

The results of the first case study have been summarized in the following three papers:

- Ferrari F., Apuani T. & Giani, G.P., 2013. Rock Mass Rating spatial estimation by geostatistical analysis. *International Journal of Rock Mechanics and Mining Sciences*, submitted;
- Ferrari F., Apuani T. & Giani G.P., 2012. Analisi spaziale e previsionale delle proprietà geomecniche degli ammassi rocciosi della Val San Giacomo (SO), mediante tecniche geostatistiche. *GEAM – Geoingegneria Ambientale e Mineraria*, n° 1, pag. 21-30;
- Ferrari F., Apuani T. & Giani G.P., 2011. Geomechanical surveys and geostatistical analyses in Valchiavenna (Italian Central Alps). *Proceedings of the 8th International Symposium on Field Measurement in GeoMechanics*, 12-15 September 2011, in Berlin.

In the second study case, the dimension of the investigated area varies with the photogrammetric model, and the main problem is that it cannot be normalized, because the minimum measurable value is strongly related on the resolution (and so to the distance) of the model. Although very numerous data have been collected from the photogrammetric model, the use of the mean value of a whole outcrop result to be not significant, because outcrop data provide a rich source of geological information, which are lost considering only the mean value. Actually, such amount of information and so the geological heterogeneity cannot be captured using the variogram, which merely describes correlations between only two spatial locations. Yet at the same time, a unified and flexible geostatistical methodology for capturing the geological richness of outcrop data is still lacking. Some improvements could be using the multiple-point statistics, which relies on the use of training images, which are essentially a database of geological patterns, from which multiple-point statistics, including the variogram, can be borrowed.

Another important shortcoming of the application of geostatistic techniques is that these are based, and at the same time limited, by the stationarity assumption. Actually, geostatistical algorithms are driven by stationarity assumptions since one relies on the fact the same algorithmic operation can be applied/repeated in every grid cell whose property requires estimation/simulation. The stationarity assumption implies the absence of trends in the data. Actually, in geology, trends are often present: regarding the rock mass properties, it is well known that the rock mass quality is lower in surface and it improves going in depth, due to increasing of spacing values and, at the same time, the decreasing of persistence and apertures. For instance, at the Grimselpass it has been observed that exfoliation joint spacing increases with the depth, until a maximum depth beyond it the exfoliation joints disappear. It follows that, with the aim to respect the stationarity property, estimation can be performed only near the surface. In order to perform estimation with depth, it is necessary to have a lot of numerical depth data, which allowed subdividing the 3D models in some homogenous portions (i.e. without trend) to treat independently. Only in this way it will be possible to construct significant 3D geological models which allow to estimate the rock mass properties also in depth.

5. REFERENCES

- 3G Software & Measurement, 2007. ShapeMetrix3D User Manual 2.0, 97 pp.
- Adler P.M. & Thovert J.F., 1999. Fractures and fracture networks. Kluwer Academic Publishers, Netherlands, 433 pp.
- Agterberg F.P., 1974. Geomathematics: mathematical background and geo-science applications. Elsevier Scientific Publishing Company, Amsterdam, 596 pp.
- Albrecht J., 1994. Geologic units of the Aar Massif and pre-Alpine rock associations: a critical review. The pre-Alpine crustal evolution of the Aar, Gotthard and Tavetsch massifs. Schweizerische Mineralogische und Petrographische Mitteilungen, Vol.74, 5-27
- Aler J., Du Mouza J. & Arnaud M., 1996. Measurement of the fragmentation efficiency of rock mass blasting and its mining applications. International Journal of Rock Mechanics and Mining Sciences & Geomechanics Abstracts, Vol.33, 125-140
- Alikarami R., Torabi A., Kolyukhin D. & Skurtveit E., 2013. Geostatistical relationships between mechanical and petrophysical properties of deformed sandstone. International Journal of Rock Mechanics and Mining Sciences, Vol.63, 27-38
- Alli M.M., Novatzki E.A. & Myers D.E., 1990. Probabilistic analyses of collapsing soil by indicator kriging. Mathematical Geology, Vol. 22 (1), 15-38
- Apuani T., Giani G.P. & Merri A., 2009. Geomechanical studies of an alpine rock mass. Proceedings of III CANUS Rock Mechanics Symposium, Toronto
- Baecher G.B. & Lanney N.A., 1978. Trace length biases in joint survey. Proceedings of the 19th U.S. Symposium on Rock Mechanics, Vol.1, 56-65
- Baecher G.B., 1983. Statistical analysis of rock mass fracturing. Journal of the International Association for Mathematical Geology, Vol.15 (2), 329-348
- Baecher G.B., Lanney N.A. & Einstein H.R., 1977. Statistical description of rock fractures and sampling. Proceedings of the 18th u.S. Symposium on Rock Mechanics
- Bahat D., Grossenbacher K. & Karasaki K., (1999). Mechanism of exfoliation joint formation in granitic rocks, Yosemite National Park. Journal of Structural Geology, Vol.21 (1), 85-96
- Bandis S.C., Lumsden A.C. & Barton N., 1981. Experimental studies of scale effects on the shear behaviour of rock joints. International Journal of Rock Mechanics and Mining Sciences & Geomechanics Abstracts, Vol.18, 1-21

- Bär O., 1957. Gesteinsklüfte und Rundhöcker. Untersuchungen im Aare- und Gotthardmassiv. *Geographica Helvetica*, Vol.12, 1-40
- Barla G., Scavia C., Antonellis M. & Guarascio M., 1987. Characterization of rock mass by geostatistical analysis at the Masua Mine. *Proceedings of 6th ISRM Congress, Montreal*, 777-786
- Barnes R., 2003. Variogram tutorial. Golden, CO: Golden Software
- Barnes R.J., 1991. The Variogram Sill and the Sample Variance. *Mathematical Geology*, Vol. 23 (4), 673-768
- Barton C.A. & Zoback M.D., 1990. Self-similar distribution of macroscopic fractures at depth in crystalline rock in the Cajon Pass scientific drillhole. *Rock Joints*, Balkema, Rotterdam, 163-170
- Barton C.M., 1977. *Geotechnical Analysis of Rock Structure and Fabric in C.S.A. Mine*, Cobar, New South Wales. *Applied Geomechanics Technical Paper*, Vol.24
- Barton N. & Choubey V., 1977. The shear strength of rock joints in theory and practice. *Rock Mechanics*, Vol.10, 1-54
- Barton N., Lien R. & Lunde J., 1974. Engineering classification of rock masses for the design of tunnel support. *Rock mechanics*, Vol.6 (4), 189-236
- Bastante F.G., Ordóñez C., Taboada J. & Matías J. M., 2008. Comparison of indicator kriging, conditional indicator simulation and multiple-point statistics used to model slate deposits. *Engineering Geology*, Vol.98, 50-59
- Bastante F.G., Taboada J., Alejano L.R. & Ordonez C., 2005. Evaluation of the resources of a slate deposit using indicator kriging. *Engineering Geology*, Vol.81, 407-418
- Baudin T.H. & Marquer D., 1993. Metamorphism and deformation in the Tambò nappe (Swiss Central Alps): evolution of the phengite substitution during Alpine deformation. *Schweizer Mineralogische und Petrographische Mitteilungen*, Vol.73, 285-299
- Baudin T.H., Marquer D., Barfety J.C., Kerckhove C. & Persoz F., 1995. A new stratigraphical interpretation of the mesozoic cover of the Tambò and Suretta nappes: Evidence for early thin-skinned tectonics (Swiss Central Alps). *Comptes Rendus de l'Academie des Sciences Paris*, Vol.321 (5), 401-408
- Bieniawski Z.T., 1989. *Engineering rock mass classifications*. Wiley, 251 pp.
- Biino G.G., Marquer, D. & Nussbaum C., 1997. Alpine and pre-Alpine subduction events in polycyclic basements of the Swiss Alps. *Geology*, Vol.25 (8), 751-754

- Billaux D., Chilès J.P., Hestir K., & Long, J., 1989. Three-dimensional statistical modelling of a fractured rock mass - an example from the Fanay-Augères mine. *International Journal of Rock Mechanics and Mining Science*, Vol.26 (3/4), 281–299
- Bohling G., 2005. Introduction to geostatistics and variogram analysis. Kansas geological survey, 20pp.
- Bolay S., 2013. Quantitative Measurements of Exfoliation Joint Spacing in the Central Aar Granites of the Grimsel Area (Central Swiss Alps). Unpublished Master Thesis, Department of Earth Sciences, Geological Institute, ETH Zurich, 77 pp.
- Bouroz C., 1990. Les joints et leur signification tectonique en domaine tabulaire: exemples dans le plateau du Colorado (Utah, Arizona, Nouveau Mexique). Unpublished Ph.D. thesis, Paris
- Bradley W.C., 1963. Large-scale exfoliation in massive sandstones of the Colorado Plateau. *Bulletin of the Geological Society of America*, Vol.74 (5), 519-528
- Bridges M.C., 1975. Presentation of Fracture Data for Rock Mechanics. Proceedings of the 2nd Australian - New Zealand Conference on Geomechanics, Brisbane, 144-148
- Brunner F. & Scheidegger A., 1973. Exfoliation. *Rock Mechanics and Rock Engineering* Vol.5 (1), 43-62
- Bucher S.P. & Loew S., 2009. Talklufte im Zentralen Aaregranit der Schollenen-Schlucht (Kanton Uri, Schweiz). *Swiss Journal of Geosciences*, Vol.102 (3), 403-421
- Caers J. & Zhang T., 2004. Multiple-point geostatistics: a quantitative vehicle for integrating geologic analogs into multiple reservoir models. *American Association of Petroleum Geologists Memoir*, Vol. 80, 383-394
- Caers J., 2005. *Petroleum Geostatistics*. Society of Petroleum Engineers, 88 pp.
- Call R.D., Savely J.P., Nicholas D.E. & Call, P.D., 1976. Estimation of joint set characteristics from surface mapping data. Proceedings of the 17th US Symposium on Rock Mechanics
- Chiessi V., D'Orefice M., Scarascia Mugnozza G, Vitale V. & Cannese C., 2010. Geological, geomechanical and geostatistical assessment of rockfall hazard in San Quirico Village (Abruzzo, Italy). *Geomorphology*, Vol.119, 147-161
- Chiles J.P. & Delfiner P., 1999. *Geostatistics: modeling spatial uncertainty*. Wiley & Sons, New York.
- Chilès J.P., 1988. Fractal and Geostatistical Method for modelling a Fracture Network. *Mathematical Geology*, Vol.20 (6), 631-654
- Choi J.Y. & Lee C.I., 2007. An estimation of rock mass rating using 3D-indicator kriging approach with uncertainty assessment of rock mass classification. Proceedings of the 11th congress of the International Society for Rock Mechanics, Lisbon, Vol.2, 285-288

- Choi Y., Yoon S.Y. & Park H.-D., 2009. Tunneling Analyst: A 3D GIS extension for rock mass classification and fault zone analysis in tunneling. *Computer & Geosciences*, Vol.35, 1322-1333
- Choukroune P. & Gapais D., 1983. Strain pattern in the Aar Granite (Central Alps): orthogneiss developed by bulk inhomogeneous flattening. *Journal of Structural Geology*, Vol.5 (3/4), 411-418
- Ciotoli G. & Finioia M.G., 2005. Dalla statistica alla geostatistica, Introduzione all'analisi dei dati geologici e ambientali. Aracne Editrice, Roma, 239-392
- Clerici A., 2000. Fondamenti di rilevamento geologico-tecnico. Valdina editore, Bergamo, 293 pp.
- Cruden D.M., 1977. Describing the Size of Discontinuities. *International Journal of Rock Mechanics and Mining Sciences & Geomechanics Abstracts*, Vol.14 (3), 133-137
- Dale T. N., 1923. The commercial granites of New England. US Government Printing Office, Vol. 738
- Dantini E.M., Lisardi A. & Raspa G., 1999. Stabilità dei fronti di scavo in relazione alla caduta di cunei rocciosi. Atti del convegno Samoter "Attualità e problematiche degli scavi in gallerie in Italia", Verona, 29-36
- De Poli C., 1987. Studio geologico petrografico della falda Tambò. Tesi di laurea inedita, Università degli Studi di Milano
- Deere D.U. & Miller R.P., 1966. Engineering classification and index properties for intact rock. University of Illinois, 292 pp.
- Dershowitz W.S. & Einstein H.H., 1988. Characterizing rock joint geometry with joint system models. *Rock Mechanics and Rock Engineering*, Vol.21 (1), 21-51
- Deutsch C.V. & Journel A.G., 1992. *GSLIB - Geostatistical Software Library and user's guide*: Oxford University Press, Oxford, 340 pp.
- Deutsch C.V. & Journel A.G., 1998. *GSLIB - Geostatistical Software Library and User's Guide*, second edition: Oxford University Press, New York, 369pp.
- Deutsch C.V., 2002. *Geostatistical Reservoir Modeling*. Oxford University Press, 376 pp.
- Digonzelli E., 1987. Studio petrografico-geochimico dell'ortogneiss del Truzzo in Val San Giacomo (provincia di Sondrio). Tesi di laurea inedita, Università degli Studi di Milano
- Dowd P.A., Xu C., Mardia K.V. & Fowell, R.J., 2007. A Comparison of Methods for the Stochastic Simulation of Rock Fractures. *Mathematical Geology*, Vol.39 (7), 697-714
- Einstein H.H., 2003, Uncertainty in rock mechanics and rock engineering—then and now. X Congress International Society for Rock Mechanics, Technology roadmap for Rock Mechanics, Pretoria, 281-293

- Ellefmio S.L. & Eidsvik J., 2009. Local and Spatial Joint Frequency Uncertainty and its Application to Rock Mass Characterisation. *Rock Mechanics and Rock Engineering*, Vol.42 (4), 667-688
- Escuder Viruete J., Carbonell R., Jurado M.J., Martí D. & Pérez-Estaún A., 2001. Two-dimensional geostatistical modeling and prediction of the fracture system in the Albala Granitic Pluton, SW Iberian Massif, Spain. *Journal of Structural Geology*, Vol.23, 2011-2023
- Escuder Viruete J., Carbonell R., Martí D. & Pérez-Estaún A., 2003a. 3-D stochastic modeling and simulation of fault zones in the Albalá Granitic Pluton, SW Iberian Variscan Massif. *Journal of Structural Geology*, Vol.25, 1487-1506
- Escuder Viruete J., Carbonell R., Martí D., Jurado M.J. & Pérez-Estaún A., 2003b. Architecture of fault zones determined from outcrop, cores, 3-D seismic tomography and geostatistical modeling: example from the Albalá Granitic Pluton, SW Iberian Variscan Massif. *Tectonophysics*, Vol. 361, 97-120
- Esfahani N.M. & Asghari O., 2013. Fault detection in 3D by sequential Gaussian simulation of Rock Quality Designation (RQD). Case study: Gazestan phosphate ore deposit, Central Iran. *Arabian Journal of Geosciences*, Vol.6, 3737-3747
- Exadaktylos G. & Stavropoulou M., 2008. A specific upscaling theory of rock mass parameters exhibiting spatial variability: Analytical relations and computational scheme. *International Journal of Rock Mechanics & Mining Sciences*, Vol.45, 1102-1125
- Exadaktylos G., Stavropoulou M., Xiroudakis G., de Broissia M. & Schwarz H., 2008. A spatial estimation model for continuous rock mass characterization from the specific energy of a TBM. *Rock Mechanics and Rock Engineering*, Vol.41, 797-734
- Ferrari F., Apuani T. & Giani G.P., 2011. Geomechanical surveys and geostatistical analyses in Valchiavenna (Italian Central Alps). *Proceedings of the XIII International Symposium on Field Measurement in GeoMechanics*, Berlin
- Franceschi M., Massironi M., Franceschi P. & Picotti V., 2013. Study of the Early Jurassic Calcarei Grigi carbonate platform (Southern Alps, Italy) integrating 3D-modeling and geostatistics. *Rendiconti Online della Società Geologica Italiana*, Vol. 29, 59-62
- Froitzheim N., Schmid S.T. & Conti P., 1994. Repeated change from crustal shortening to orogenparallel extension in the Austroalpine units of Graubünden. *Eclogae Geologicae Helvetiae*, Vol.87 (2), 559-612
- Gelmetti A., 1988. Studio del basamento cristallino della falda Suretta tra il passo d'Emet e Campodolcino, con particolare riferimento alle rocce metapelitiche (Val S. Giacomo, provincia di Sondrio). Tesi di laurea inedita, Università degli Studi di Milano

- Giani G.P., 1992. Rock slope stability analysis. Balkema, Rotterdam, 361 pp.
- Glacken I.M. & Blackney P., 1998. A practitioners implementation of indicator kriging .The Geostatistical Association of Australasia, Beyond Ordinary Kriging Seminar, Perth, Western Australia, 12 pp.
- Glasser N.F., 1997. The origin and significance of sheet joints in the Cairngorm granite. *Scottish Journal of Geology*, Vol.33 (2), 125-131
- Goovaerts P., 1996. Stochastic simulation of categorical variables using a classification algorithm and simulated annealing. *Mathematical Geology*, Vol.28, 909-921
- Goovaerts P., 1997. *Geostatistics for Natural Resources Evaluation*. Oxford University Press, New York, 443 pp.
- Goovaerts, P., 2001. Geostatistical modeling of uncertainty in soil science. *Geoderma*, Vol.103, 3-26
- Grigarten E. & Deutsch C.V., 2001. Variogram Interpretation and Modelling. *Mathematical Geology*, Vol.33 (4), 507-534
- Grigarten E., 1996. 3-D Geometric Description of Fractured Reservoir. *Mathematical Geology*, Vol.28 (7), 881-893
- Gumiaux C., Gapais D. & Brun J.P., 2003. Geostatistics applied to best-fit interpolation of orientation data. *Tectonophysics*, Vol.376, 241-259
- Hanson G.N., Grünfelder M. & Soptrayanova G., 1969. The geochronology of a recrystallized tectonite in Switzerland - The Roffna gneiss. *Earth and Planetary Science Letters*, Vol.5, 413-422
- Hast N., 1969. The state of stress in the upper part of the earth's crust. *Tectonophysics*, Vol.8 (3), 169-211
- Heim A., 1891. Das Thalgebiet von Schams. *Beiträge zur Geologischen Karte der Schweiz*, Vol.25 (10), 377-407
- Hoek E. & Brown E.T., 1997. Practical Estimates of Rock Mass Strength. *International Journal of Rock Mechanics and Mining Science*, Vol.34 (8), 1165-1186
- Hoerger S.F. & Young D.S., 1987. Predicting local rock mass behaviour using geostatistics. *Proceedings of the 28th Symposium on Rock Mechanics*, Tucson, 99-106
- Holzhausen G. R., 1989. Origin of sheet structure, 1. Morphology and boundary conditions. *Engineering Geology*, Vol.27, 225-278
- Houlding S.W., 2000. *Practical geostatistics: modeling and spatial analysis*. Manual. Springer,
- Huang Q. & Angelier J., 1989. Fracture spacing and its relation to bed thickness. *Geological Magazine*, Vol.126, 355-362

- Huber R.H. & Marquer D., 1996. Tertiary deformation and kinematics of the southern part of the Tambò and Suretta nappes (Val Bregaglia, Eastern Swiss Alps). *Schweizer Mineralogische und Petrographische Mitteilungen*, Vol.76, 383-397
- Huber R.H. & Marquer D., 1998. The tectonometamorphic history of the peridotitic Chiavenna unit from Mesozoic to Tertiary tectonics: a restoration controlled by melt polarity indicators (Eastern Swiss Alps). *Tectonophysics*, Vol.296, 205-223
- Isaaks E.H. & Srivastava R.M., 1989. *An Introduction to Applied Geostatistics*. Oxford University press, New York, 561 pp.
- ISRM – International Society for Rock Mechanics, 1975. Commission on Terminology, Symbols and Graphic Representation: Terminology. International Society Rock Mechanics secretary, Lisbon
- ISRM – International Society for Rock Mechanics, 1978. Suggested methods for the quantitative description of discontinuities in rock masses. *International Journal of rock Mechanics and Mining Sciences and Geomechanics Abstracts*, Vol.15 (6), 319-368
- ISRM – International Society for Rock Mechanics, 1981. *Rock Characterization, Testing and Monitoring, ISRM Suggest Methods*, Pergamon, London
- Jahns R.H., 1943. Sheet structure in granites: its origin and use as a measure of glacial erosion in New England. *The Journal of Geology*, 71-98
- Johnson A.M., 1970. *Physical processes in geology: a method for interpretation of natural phenomena; intrusions in igneous rocks, fractures, and folds, flow of debris and ice*. Freeman, Cooper
- Journel A.G. & Posa D., 1990. Characteristic Behaviour and Order Relations for Indicator Variograms. *Mathematical Geology*, Vol. 22 (8), 1011-1025
- Journel A.G., 1983. Nonparametric estimation of spatial distributions. *Journal of the International Association for Mathematical Geology*, Vol.15 (3), 445-468
- Journel A.G., Huijbregts C., 1978. *Mining geostatistics*. Academic Press, London
- Juang K.W., Chen Y.S. & Lee D.Y., 2004. Using sequential indicator simulation to assess the uncertainty of delineating heavy-metal contaminated soils. *Environmental Pollution*, Vol.127, 229-238
- Keusen H.R., Ganguin J., Schuler P. & Buletti, M., 1989. Grimsel Test Site. *Geology. Technical Report NTB 87-14E*, Nagra, Baden, Switzerland, 120 pp.
- Kieslinger A., 1958. Restspannung und Entspannung im Gestein. *Geologie und Bauwesen*, Vol.24 (2), 95-112
- Kitanidis P.K., 1997. *Introduction to geostatistics: applications in hydrogeology*. Cambridge University Press, Cambridge

- Koike K. & Ichikawa, Y., 2006. Spatial correlation structures of fracture systems for deriving a scaling law and modeling fracture distributions. *Computer & Geoscience*, Vol.32, 1079–1095
- Koike K., Komorida K. & Ichikawa Y., 2001. Fracture-distribution modelling in rock mass using borehole data and geostatistical simulation. *Proceedings of the International Association for Mathematical Geology Conference*, Cancun
- Koike K., Liu C. & Sanga, T., 2012. Incorporation of fracture directions into 3D geostatistical methods for a rock fracture system. *Environmental Earth Sciences*, Vol.66 (5), 1403-1414
- Krige D. G., 1951. A statistical approach to some basic mine valuation problems on the Witwatersrand. *Journal of the Chemical, Metallurgical and Mining Society of South Africa*, Vol.52 (6), 119-139
- Kulatilake P.H.S.W. & Wu T.H., 1984. The density of discontinuity trace in sampling windows. *International Journal of Rock Mechanics and Mining Sciences & Geomechanics Abstracts*, Vol.21, 345-347
- Kulatilake P.H.S.W., Wathugala D.N. & Stephansson O., 1993. Joint network modeling with a validation exercise in Stripa Mine, Sweden. *International Journal of Rock Mechanics and Mining Sciences & Geomechanics Abstracts*, Vol.30, 503-5226
- La Pointe P. R. & Hudson J. A., 1985. Characterization and interpretation of rock mass joint patterns. *Geological Society of America Special Papers*, 199, 1-37
- La Pointe P.R., 1980. Analysis of the spatial variation in rock mass properties through geostatistics. *Proceedings of the 21th Symposium on Rock Mechanics*, Rolla, 570-580
- Lana M.S., Cabral I.E., Gripp A.H. & Gripp M.F.A., 2010. Estimation of potential failure risks in a mine slope using indicator kriging. *International Journal for Numerical and Analytical Methods in Geomechanics*, Vol.34, 1725-1742
- Lilliefors H., 1967. On the Kolmogorov-Smirnov test for normality with mean and variance unknown. *Journal of the American Statistical Association*. Vol.62 (318), 399–402
- Lilliefors H.W., 1967. On the Kolmogorov-Smirnov Test for Normality with Mean and Variance Unknown. *Journal of the American Statistical Association*, Vol.62 (318), 399-402
- Long J.C.S. & Billau D.M., 1987. From Field Data to Fracture Network Modeling: An Example Incorporating Spatial Structure. *Water Resources Research*. Vol.23 (7), 1201-1216
- Marinoni O., 2003. Improving geological models using a combined ordinary-indicator kriging approach. *Engineering Geology*, Vol.69, 37-45

- Marquer D., Baudin T.H., Peucat J.J. & Persoz F., 1994. Rb-Sr mica ages in the Alpine shear zones of the Truzzo granite: Timing of the Tertiary alpine P-T deformations in the Tambò nappe (Central Alps, Switzerland). *Eclogae Geologicae Helvetiae*, Vol.85 (3), 1-61
- Marquer D., Challandes N. & Schaltegger U., 1998. Early Permian magmatism in Briançonnais terranes: Truzzo granite and Roffna rhyolite (eastern Penninic nappes, Swiss and Italian Alps). *Schweizerische mineralogische und petrographische Mitteilungen*, Vol.78 (3), 397-414
- Matheron G., 1971. The theory of regionalized variables and its applications. Ecole de Mines, Fontainebleau, 218 pp.
- Mazzoccola D., 1993. La dinamica dei versanti della media Valchiavenna (SO): analisi geomeccanica dei fenomeni di stabilità in atto e potenziali. Tesi di dottorato inedita, Università degli Studi di Milano
- Mazzoccola D., 1994. Una nuova metodologia classificativa dell'ammasso roccioso per una valutazione preliminare dell'instabilità di versante a grande scala. *Geologica Romana*, Vol.30, 185-196
- McMahon B., 1974. Design of Rock Slopes Against Sliding on Preexisting Surface. *Proceedings of the 3rd International Symposium on Rock Mechanics*, Vol.2B, 803-808
- Merritt A.H. & Baecher G.B., 1981. Site characterization in rock engineering. *Proceedings of the 22nd U.S. Symposium on Rock Mechanics*, 49-66
- Meyer T. & Einstein H.H., 2002. Geologic Stochastic Modeling and Connectivity Assessment of Fracture Systems in the Boston Area. *Rock Mechanics and Rock Engineering*, Vol.35 (1), 23-44
- Milnes A.G. & Schmutz, H.U., 1978. Structure and history of the Suretta nappe (Pennine zone, Central Alps) - A field study. *Eclogae Geologicae Helvetiae*, Vol.71 (1), 19-33
- Minder W., 1932. Beiträge zur Petrographie des mittlern Aarmassivs: tektonisch-petrographische Studien im Zentralgranit des obern Haslitalen. *Schweizer Mineralogische und Petrographische Mitteilungen*, Vol.12, 353-422
- Mullis, J., 1996. P-T-t path of quartz formation in extensional veins of the Central Alps. *Schweizer Mineralogische und Petrographische Mitteilungen*, Vol.26, 159-164
- Narr W. & Suppe J., 1991. Joint spacing in sedimentary rocks. *Journal of Structural Geology*, Vol.13, 1037-1048
- National Research Council, 1996. Rock fracture and fluid flow: contemporary understanding and applications. National Academy Press, Washington, 555 pp.
- Nieto A.S., 1983. Some geologic factors in the location, design and construction of large underground chambers in rock. *Proceedings of Rapid Underground Excavation and Tunnel Conference, AIME*, 569-596

- Nussbaum C., Marquer D. & Biino G.G., 1998. Two subduction events in a polycyclic basement: Alpine and pre-Alpine high-pressure metamorphism in the Suretta nappe, Swiss Eastern Alps. *Journal of metamorphic Geology*, Vol.16, 591-605
- Olea R.A., 1999. *Geostatistics for Engineers and Earth Scientists*. Kluwer Academic Publishers, 303 pp.
- Ozturk C.A. & Nasuf E., 2002. Geostatistical assessment of rock zones for tunnelling. *Tunneling and Underground Space Technology*, Vol.17, 275-285
- Palmström A., 1982. The volumetric joint count: a useful and simple measure of the degree of rock mass jointing. *Proceedings of the IV Congress IAEG*, New Delhi, 221-228
- Palmström A., 1995. Rmi - a rock mass characterization system for rock engineering purposes. Ph.D. thesis, University of Oslo, Norway.
- Palmström A., 2001. Measurement and characterization of rock mass jointing. *In-Situ Characterization of rocks*, Sharma and Saxena Editors, Balkema, 49-97
- Palmström A., 2005. Measurements of and Correlations between Block Size and Rock Quality Designation (RQD). *Tunnels and Underground Space Technology*, Vol.20, 362-377
- Papoulis A. & Pillai S.U., 2002. *Probability, random variables, and stochastic processes*. Tata McGraw-Hill Education
- Pardo-Igúzquiza E. & Dowd P.A., 2004. Normality Tests for Spatially Correlated Data. *Mathematical Geology*, Vol.36(6), 659-681
- Pfiffner O.A., Frei W., Valasek P., Sfauble M., Levato L., DuBois L., Schmid S.M., Smithson S.B., 1990. Crustal shortening in the Alpine orogen: results from deep seismic reflection profiling in the eastern Swiss Alps, Line NFP20-EAST. *Tectonics*, Vol.9, 1327-1355
- Pollard D.D. & Aydin A., 1988. Progress in understanding jointing over the past century. *Geological Society of America Bulletin*, Vol.100 (8), 1181-1204
- Priest S.D. & Hudson J.A., 1976. Discontinuity spacing in rock. *International Journal of Rock Mechanics and Mining Sciences & Geomechanics Abstracts*, Vol.13, 135-148
- Priest S.D. & Hudson J.A., 1976. Discontinuity spacing in rock. *International Journal of Rock Mechanics & Mining Science*, Vol.13 (5), 135-148
- Priest S.D. & Hudson J.A., 1981. Estimation of fracture spacing and trace length using scanline surveys. *International Journal of Rock Mechanics and Mining Sciences & Geomechanics Abstracts*, Vol.18, 183-197

- Rafiee A. & Vinches, M., 2008. Application of geostatistical characteristics of rock mass fracture system in 3D model generation. *International Journal of Rock Mechanics and Mining Science*, technical note, Vol.45, 644–652
- Remy N., Boucher A. & Wu J., 2008. *Applied Geostatistics with SGeMS. A user's guide*. Cambridge University Press, New York
- Ring U., 1992a. The Alpine Geodynamic Evolution of Penninic Nappes in the Eastern Central Alps - Geothermobarometric and Kinematic Data. *Journal of Metamorphic Geology*, Vol.10 (1), 33-53
- Ring U., 1992b. The Kinematic History of the Pennine Nappes East of the Lepontine Dome - Implications for the Tectonic Evolution of the Central Alps. *Tectonics*, Vol.11 (6), 1139-1158
- Rives T., Razack M., Petit J.P. & Rawnsley K.D., 1992. Joint spacing: analogue and numerical simulations. *Journal of Structural Geology*, Vol.14 (8/9), 925-937
- Robertson A., 1970. The Interpretation of Geological Factors for Use in Slope Stability. *Proceedings Symposium on the Theoretical Background to the Planning Of Open Pit Mines with Special Reference to Slope Stability*, 55-71
- Rolland Y., Cox S.F. & Corsini M., 2009. Constraining deformation stages in brittle–ductile shear zones from combined field mapping and $^{40}\text{Ar}/^{39}\text{Ar}$ dating: the structural evolution of the Grimsel Pass area (Aar Massif, Swiss Alps). *Journal of Structural Geology*, Vol.31, 1377–1394
- Rouleau A. & Gale J.E., 1985. Statistical characterization of the fracture system in the Stripa Granite, Sweden. *International Journal of Rock Mechanics and Mining Sciences & Geomechanics Abstracts*, Vol.22, 353-367
- Ruf J.C., Rust K.A. & Engelder T., 1998. Investigating the effect of mechanical discontinuities on joint spacing. *Tectonophysics*, Vol.295, 245-257
- Schaltegger U., 1994. Unravelling the pre-Mesozoic history of Aar and Gotthard massifs (central Alps) by isotopic dating: a review. *Schweizerische Mineralogische und Petrographische Mitteilungen*, Vol.74, 41–51
- Scheiber T., Pfiffner O.A. & Schreurs G., 2012. Strain accumulation during basal accretion in continental collision - A case study from the Suretta nappe (eastern Swiss Alps). *Tectonophysics*, Vol.579, 56-73
- Schmid S.M., Pfiffner O.A. & Schreurs G., 1997. Rifting and collision in the Penninic zone of eastern Switzerland. In: Pfiffner O.A., Lehner P., Heitzmann P., Mueller S. & Steck, A., *Deep Structure of the Swiss Alps: Results of NRP 20*. Birkhäuser Verlag, 160-185
- Schmid S.M., Zingg A. & Handy M., 1987. The kinematics of movements along the Insubric Line and the emplacement of the Ivrea Zone. *Tectonophysics*, Vol.135, 47-66

- Schmidt C., 1891. Gesteine aus dem Thalgebiete von Schams. Beiträge zur Geologischen Karte der Schweiz, Vol.25, 73-76
- Sciesa E., 1991. Geologia della Alpi Centrali lungo la traversa Colico-Passo dello Spluga (Province di Sondrio e Como). Il Naturalista Valtellinese, Atti Museo Civico di Storia naturale di Morbegno, 23-34
- Seifert D. & Jensen J.L., 1999. Using Sequential Indicator Simulation as a Tool in Reservoir Description: Issues and Uncertainties- Mathematical Geology, Vol.3 (5), 527-550
- Sen Z. & Kazi A., 1984. Discontinuity spacing and RQD estimates from finite length scanlines. International Journal of Rock Mechanics and Mining Sciences & Geomechanics Abstracts, Vol.21, 203-212
- Shapiro S.S. & Wilk M.B., 1965. An analysis of variance test for normality (complete samples). Biometrika. Vol.52 (3/4), 591-611
- Sibson R.H., 1985. A note on fault reactivation. Journal of Structural Geology, Vol.7 (6), 751-754
- Snow D.T., 1970. The frequency and apertures of fractures in rock. International journal of Rock mechanics and Mining sciences & Geomechanics Abstracts, Vol.7 (1), 23-40
- Snow, D. T. 1969. Anisotropic permeability of fractured media. Water Resources Research Vol.5(6), 1273-1289
- Stalder H.A., 1964. Petrographische und mineralogische Untersuchungen im Grimselgebiet (Mittleres Aarmassiv). Schweizer Mineralogische und Petrographische Mitteilungen, Vol.44, 187-398
- Staub R., 1926. Geologische Karte des Avers, 1:50000. Beitrage zur Geologischen Karte der Schweiz, Spezialkarte 97
- Stavropoulou M., Exadaktylos G. & Saratsis G., 2007. A Combined Three-Dimensional Geological-Geostatistical-Numerical Model of Underground Excavations in Rock. Rock Mechanics & Rock Engineering, Vol.40 (3), 213-243
- Steffen, O., Kerrich, J.E. & Jennings, J.E., 1975. Recent developments in the interpretation of data from joint surveys in rock masses. Proceedings of the 6th Regional Conference for Africa on Soil Mechanics and Foundations, Vol.2, 17-26
- Steinitz G. & Jäger E., 1981. Rb-Sr and K-Ar studies on rocks from the Suretta nappe; Eastern Switzerland. Schweizerische mineralogische und petrographische Mitteilungen, Vol.61, 121-131
- Sullivan P., 1984. Conditional Recovery Estimation Through Probability Kriging - Theory and Practice. In: Verly G., David M., Journel A. & Maréchal A., Geostatistics for Natural Resources Characterization, Part 1, Reidel Publishing Company, Hingham, 365-384

- Sutter B., 2008. Kluftmuster und Kluftgenese am Grimselpass: Geologisch-geotechnische Eigenschaften und Tiefenentwicklung der Trennflächensysteme. Unpublished Master Thesis, Department of Earth Sciences, Geological Institute, ETH Zurich, 96 pp.
- Taboada J., Vaamonde A., Saavedra A. & Alejano L., 1997. Application of geostatistical techniques to exploitation planning in slate quarries. *Engineering geology*, Vol.47 (3), 269-277
- Tavchandjian O., Rouleau A., Archambault G., Daigneault R. & Marcotte D., 1997. Geostatistical analysis of fractures in shear zones in the Chibougamau area: applications to structural geology. *Tectonophysics*, Vol.269, 51-63
- Terzaghi R.D., 1965. Sources of error in joint surveys. *Geotechnique*, Vol.15 (3), 287-304
- Tsoutrelis C.E., Exadactylos G.E. & Kapenis A.P., 1990. Study of the rock mass discontinuity system using photoanalysis. *Mechanics of Jointed and Faulted Rock*, Balkema, Rotterdam, 103-112
- Villaescusa E. & Brown E.T., 1990. Characterising joint spatial correlation using geostatistical methods. In: Barton N. & Stephansson O., editors. *Rock Joints*, Balkema, Rotterdam, 115-122
- Villaescusa E. & Brown E.T., 1992. Maximum likelihood estimation of joint size. *Rock Mechanics and Rock Engineering*, Vol.25, 67-87
- Voight B., 1966. Beziehung zwischen grossen horizontalen Spannungen im Gebirge und der Tektonik und der Abtragung. *Proceedings of the 1st Congress of the International Society of Rock Mechanics*, Lisbon, Portugal, 51-56
- Voll G., 1976. Recrystallisation of quartz, biotite and feldspars from Erstfeld to the Leventina Nappe, Swiss Alps and its geological significance. *Schweizer Mineralogische und Petrographische Mitteilungen*, Vol.56, 641-647
- Wiederkehr M., Bousquet R., Schmid S. & Berger A., 2008. From subduction to collision: Thermal overprint of HP/LT meta-sediments in the north-eastern Lepontine Dome (Swiss Alps) and consequences regarding the tectono-metamorphic evolution of the Alpine orogenic wedge. *Swiss Journal of Geosciences*, Vol.101, 127-155
- Wilhelm O., 1929. *Geologie der Landschaft Schams*, 1:50000. Geolischen Karte der Schweiz, Spezialkarte, 114 (mit Profilen),
- Wilhem O., 1921. *Geologische Karte der Landchaft Schams und Profile*, 1:50000. *Beitraege zur Geologischen Karte der Schweiz*, Spezialkarte, 114A und B
- Yi H., Choi Y. & Park H.D. Application of multiple indicator Kriging for RMR value estimation in areas of new drift excavation during mine site redevelopment. *Environmental Earth Sciences*, 8 pp.

- You K. & Lee J.S., 2006. Estimation of rock mass classes using the 3-dimensional multiple indicator kriging technique. *Tunnelling and Underground Space Technology*, Vol.21(3/4), 229
- Young D.S., 1987a. Random Vectors and Spatial Analysis by Geostatistics for Geotechnical Applications. *Mathematical Geology*, Vol.19 (6), 467-479
- Young D.S., 1987b. Indicator Kriging for Unit Vectors: Rock Joint Orientations. *Mathematical Geology*, Vol.19 (6), 481-501
- Yu Y.F. & Mostyn G.R., 1993. Spatial correlation of rock joints. *Probabilistic methods in geotechnical engineering*, Balkema, Rotterdam, 241-255
- Ziegler M., Loew S. & Moore J.R., 2013. Distribution and inferred age of exfoliation joints in the Aar Granite of the central Swiss Alp and relationship to Quaternary landscape evolution. *Geomorphology*, Vol.201, 344-362

6. APPENDIXES

6.1 Appendix 1 - Papers about rock mechanics and geostatistics

| <i>Authors</i> | <i>Year</i> | <i>Estimated parameters</i> | <i>Method</i> | <i>Range</i> |
|---------------------------------------|-------------|---|-----------------------|-------------------|
| <i>Barla et al.</i> | 1987 | <i>RQD, n° of discontinuities/m, dip direction, dip angle, conditions of discontinuities, RMR</i> | <i>k</i> | <i><25m</i> |
| <i>Billaux et al.</i> | 1989 | <i>fracture density, persistence, orientation</i> | <i>s</i> | <i><100m</i> |
| <i>Choi & Lee</i> | 2007 | <i>RMR</i> | <i>ik</i> | <i><400m</i> |
| <i>Choi et al.</i> | 2009 | <i>RMR</i> | <i>mik</i> | <i>-</i> |
| <i>Ellefmo & Eidsvik</i> | 2009 | <i>n° of discontinuities/m, RQD</i> | <i>k</i> | <i><400m</i> |
| <i>Escuder Viruete et al.</i> | 2003 | <i>n° of discontinuities/m</i> | <i>sgs</i> | <i><600m</i> |
| <i>Esfahani & Asghari</i> | 2012 | <i>RQD</i> | <i>sgs</i> | <i><80m</i> |
| <i>Exadaktylos & Stavropoulou</i> | 2008 | <i>RMR</i> | <i>k</i> | <i><30m</i> |
| <i>Exadaktylos et al.</i> | 2008 | <i>SE, RMR, Q</i> | <i>k</i> | <i><120m</i> |
| <i>Gumiaux et al.</i> | 2003 | <i>orientation</i> | <i>ok</i> | <i>-</i> |
| <i>Hoerger & Young</i> | 1987 | <i>orientation</i> | <i>k</i> | <i>< 250m</i> |
| <i>Kaewkongkkaeu et al.</i> | 2011 | <i>RMR</i> | <i>ok</i> | <i>-</i> |
| <i>Koike & Ichikawa</i> | 2006 | <i>linear and areal fracture density, strike</i> | <i>sgs</i> | <i><10000m</i> |
| <i>Lana et al.</i> | 2010 | <i>orientation</i> | <i>ik</i> | <i>< 115m</i> |
| <i>Long & Biallux</i> | 1987 | <i>areal fracture density, orientation, length, aperture</i> | <i>s</i> | <i><80m</i> |
| <i>Oh et al.</i> | 2004 | <i>RMR, resistivity</i> | <i>k on residuals</i> | <i>< 40m</i> |
| <i>Ozturk & Nasuf</i> | 2002 | <i>rock compressive strength, RQD, JCS, net cutting rate</i> | <i>k</i> | <i>< 1400m</i> |
| <i>Stavropoulou et al.</i> | 2007 | <i>RMR</i> | <i>ok</i> | <i>< 20m</i> |
| <i>Tavchandjian et al.</i> | 1997 | <i>fracture density for discontinuity set</i> | <i>ik</i> | <i>< 60m</i> |
| <i>Yi et al.</i> | 2013 | <i>RMR</i> | <i>mik</i> | <i>-</i> |
| <i>You & Lee</i> | 2006 | <i>RMR</i> | <i>mik</i> | <i>< 200m</i> |
| <i>Young</i> | 1987 | <i>orientation</i> | <i>ok, ik</i> | <i>< 600m</i> |
| <i>Yu & Mostyn</i> | 1993 | <i>spacing, fracture density, dip direction, RQD, fracture frequency, orientation</i> | | <i>< 100m</i> |

Appendix 1: bibliography relatives to the estimation of rock mass properties. The following abbreviations have been used:

- *for the estimated parameters: RMR is Rock Mass Rating, RQD Rock Quality Designation, Q the Q-system, SE specific energy of Tunnel Boring Machine, and JCS is Joint wall Compressive Strength;*
- *for the estimation method: k is kriging, ok the ordinary kriging, ik the indicator kriging, mik the multiple indicator kriging, s the simulation, and sgs the sequential Gaussian simulation, and mps multiple-point statistics;*
- *for the range: - means not specified.*

6.2 Appendix 2 - Summary of data collected in Chiavenna Valley

| <i>Code of survey</i> | <i>Long GB [m]</i> | <i>Lat GB [m]</i> | <i>Elevation [m.a.s.l.]</i> | <i>Structural unit</i> | <i>Lithology</i> | <i>n° of sets</i> | <i>Horizontal Intercept [cm]</i> | <i>Jv [n°/m³]</i> | <i>GSI</i> | <i>RMR</i> |
|-----------------------|------------------------|---------------------------|---------------------------------|----------------------------|------------------|-----------------------|--|----------------------------------|------------|------------|
| cp01 | 1524217 | 5145342 | 1950 | FTb | pGN | 4 | 41.23 | 26.0 | 63 | 57 |
| cp02 | 1526271 | 5143662 | 1643 | FTc | QZ | 3 | 5.23 | 34.4 | 53 | 58 |
| cp03 | 1524169 | 5145009 | 1957 | FTb | pGN | 4 | 36.42 | 12.3 | 66 | 69 |
| cp04 | 1525391 | 5144879 | 1481 | FTb | pGN | 3 | 21 | 22.6 | 63 | 67 |
| cp05 | 1525173 | 5144409 | 1335 | FTb | pGN | 4 | 15.2 | 15.6 | 65 | 68 |
| cp06 | 1524106 | 5144634 | 1953 | FTb | pGN | 3 | 16.5 | 22.0 | 62 | 62 |
| cp07 | 1525727 | 5144385 | 1606 | FTc | pGN | 4 | 36.3 | 40.8 | 50 | 55 |
| cp08 | 1524787 | 5145514 | 1648 | FTb | pGN | 4 | 36.8 | 46.0 | 58 | 50 |
| cp09 | 1525501 | 5143936 | 1279 | FTb | pGN | 4 | 19.4 | 39.8 | 55 | 58 |
| dm10a | 1527373 | 5137382 | 1121 | FTb | oGN | 3 | -9999 | 13.0 | -9999 | -9999 |
| dm10b | 1528058 | 5135617 | 1093 | FTb | iGN | 2 | -9999 | 30.8 | -9999 | -9999 |
| dm11a | 1527892 | 5136841 | 1526 | FTb | ANF | 3 | -9999 | 9.5 | -9999 | -9999 |
| dm11b | 1528201 | 5135549 | 1205 | FTb | iGN | 3 | -9999 | 42.9 | -9999 | -9999 |
| dm12a | 1525310 | 5138792 | 2003 | FTc | MC | 3 | -9999 | 44.4 | -9999 | -9999 |
| dm12b | 1528283 | 5135553 | 1283 | FTb | iGN | 3 | -9999 | 21.4 | -9999 | -9999 |
| dm13a | 1527049 | 5136746 | 996 | FTb | iGN | 4 | -9999 | 20.8 | -9999 | -9999 |
| dm13b | 1527426 | 5135203 | 991 | FTb | iGN | 4 | -9999 | 50.0 | -9999 | -9999 |
| dm14a | 1528294 | 5134270 | 869 | FTb | oGN | 4 | -9999 | 8.9 | -9999 | -9999 |
| dm14b | 1528527 | 5135498 | 1457 | FTb | iGN | 4 | -9999 | 25.0 | -9999 | -9999 |
| dm15a | 1527410 | 5146478 | 2032 | FTc | FL | 5 | -9999 | 46.1 | -9999 | -9999 |
| dm15b | 1528800 | 5135517 | 1746 | FTb | iGN | 4 | -9999 | 16.0 | -9999 | -9999 |
| dm16a | 1526895 | 5137708 | 1071 | FTb | iGN | 3 | -9999 | 17.1 | -9999 | -9999 |
| dm16b | 1528166 | 5136001 | 1597 | FTb | iGN | 3 | -9999 | 25.0 | -9999 | -9999 |
| dm17b | 1528430 | 5135692 | 1401 | FTb | iGN | 4 | -9999 | 17.8 | -9999 | -9999 |
| dm18b | 1527961 | 5135740 | 1077 | FTb | iGN | 3 | -9999 | 15.8 | -9999 | -9999 |
| dm19b | 1528150 | 5135070 | 1006 | FTb | oGN | 6 | -9999 | 37.5 | -9999 | -9999 |
| dm1a | 1524709 | 5139063 | 1912 | FTc | QZ | 4 | -9999 | 13.1 | -9999 | 62 |
| dm1b | 1528684 | 5135631 | 1695 | FTb | GN | 4 | -9999 | 16.0 | -9999 | -9999 |
| dm20b | 1528801 | 5135222 | 1493 | FTb | pGN | 2 | -9999 | 30.8 | -9999 | -9999 |
| dm2a | 1526307 | 5140231 | 1089 | FTb | pGN | 3 | -9999 | 13.3 | -9999 | -9999 |
| dm2b | 1528078 | 5135239 | 1047 | FTb | oGN | 2 | -9999 | 7.3 | -9999 | -9999 |
| dm3a | 1526153 | 5140181 | 1128 | FTb | pGN | 4 | -9999 | 53.3 | -9999 | -9999 |
| dm3b | 1528216 | 5135167 | 1180 | FTb | oGN | 4 | -9999 | 40.0 | -9999 | -9999 |
| dm4a | 1526906 | 5140395 | 1529 | FTb | pGN | 4 | -9999 | 9.6 | -9999 | -9999 |
| dm4b | 1528426 | 5135138 | 1378 | FTb | oGN | 2 | -9999 | 22.2 | -9999 | -9999 |
| dm5a | 1528405 | 5140522 | 1953 | FSb | pGN | 4 | -9999 | 45.7 | -9999 | -9999 |
| dm5b | 1528608 | 5135197 | 1513 | FTb | GN | 2 | -9999 | 16.7 | -9999 | -9999 |
| dm6a | 1527320 | 5139436 | 1221 | FTb | pGN | 3 | -9999 | 18.8 | -9999 | -9999 |
| dm6b | 1528755 | 5135296 | 1618 | FTb | oGN | 4 | -9999 | 23.5 | -9999 | -9999 |
| dm7a | 1526828 | 5136044 | 1133 | FTb | pGN | 3 | -9999 | 10.3 | -9999 | -9999 |
| dm7b | 1528652 | 5135408 | 1503 | FTb | oGN | 3 | -9999 | 35.3 | -9999 | -9999 |

Chapter 6: Appendixes

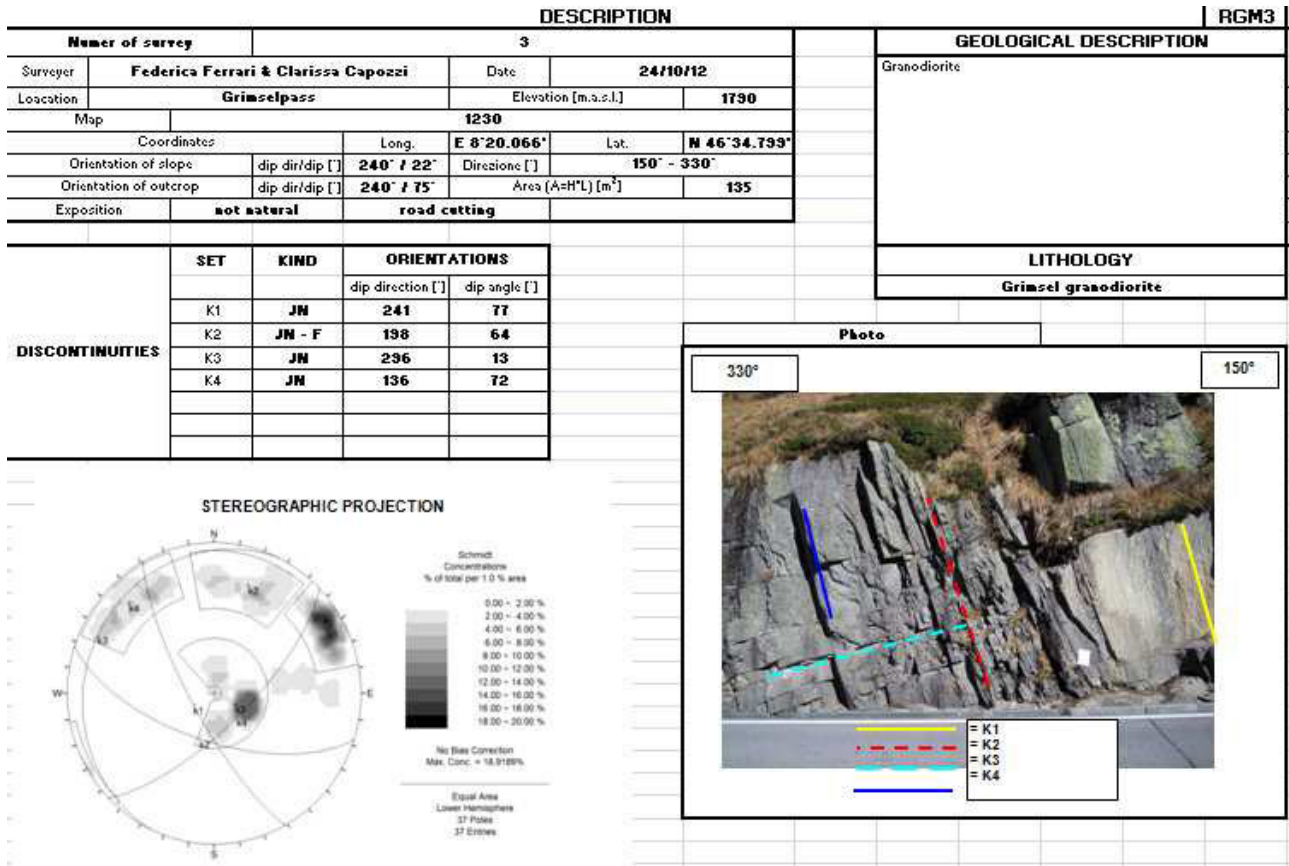
| | | | | | | | | | | |
|-------------|---------|---------|------|-----|-----|---|-------|------|-------|-------|
| dm8a | 1527600 | 5138607 | 1332 | FTb | pGN | 3 | -9999 | 45.8 | -9999 | -9999 |
| dm8b | 1528338 | 5135231 | 1273 | FTb | oGN | 3 | -9999 | 6.7 | -9999 | -9999 |
| dm9a | 1527352 | 5136698 | 1001 | FTb | iGN | 3 | -9999 | 31.7 | -9999 | -9999 |
| dm9b | 1528677 | 5135654 | 1704 | FTb | pGN | 3 | -9999 | 17.6 | -9999 | -9999 |
| fb01 | 1525317 | 5144475 | 1338 | FTb | pGN | 4 | 26 | 30.8 | 50 | 59 |
| fb07 | 1524746 | 5145634 | 1621 | FTb | pGN | 4 | 36.8 | 45.8 | 58 | 57 |
| fb08 | 1525155 | 5144182 | 1373 | FTb | pGN | 4 | 19 | 39.1 | 55 | 60 |
| fb11 | 1526235 | 5140089 | 1148 | FTb | pGN | 4 | 25.9 | 66.6 | 42 | 53 |
| fb12 | 1525856 | 5140073 | 1352 | FTb | pGN | 4 | 19 | 32.9 | 47 | 55 |
| fb13 | 1525204 | 5141558 | 1821 | FTb | pGN | 3 | 13.9 | 44.7 | 50 | 59 |
| fm01 | 1523594 | 5142226 | 1701 | FTb | pGN | 4 | 13.7 | 20.7 | 60 | 60 |
| fm02 | 1523490 | 5142205 | 1647 | FTb | pGN | 4 | 18.7 | 36.2 | 60 | 56 |
| fm03 | 1523490 | 5142127 | 1688 | FTb | pGN | 5 | 9.4 | 41.6 | 50 | 50 |
| fm04 | 1523626 | 5142275 | 1657 | FTb | pGN | 5 | 17.8 | 40.3 | 53 | 53 |
| fm05 | 1523305 | 5141980 | 1742 | FTb | pGN | 4 | 10.3 | 27.0 | 58 | 54 |
| fm07 | 1524415 | 5142894 | 1503 | FTb | pGN | 4 | 13.2 | 17.6 | 63 | 69 |
| fm08 | 1523363 | 5142522 | 1683 | FTb | pGN | 4 | 11 | 21.3 | 55 | 55 |
| fm10 | 1525268 | 5143480 | 1319 | FTb | pGN | 4 | 10.4 | 34.6 | 45 | 61 |
| fm11 | 1523615 | 5142501 | 1550 | FTb | pGN | 5 | 13.2 | 23.8 | 55 | 58 |
| fm12 | 1523615 | 5142729 | 1702 | FTb | pGN | 5 | 10 | 33.2 | 55 | 45 |
| fm13 | 1523918 | 5142850 | 1614 | FTb | pGN | 4 | 7.2 | 42.4 | 58 | 54 |
| fm14 | 1522519 | 5142243 | 1825 | FTb | pGN | 3 | 14 | 30.0 | 50 | 52 |
| fm15 | 1522233 | 5142217 | 1870 | FTb | ANF | 4 | 7.2 | 32.7 | 52 | 62 |
| fm17 | 1522511 | 5141952 | 1791 | FTb | ANF | 5 | 7.8 | 32.1 | 60 | 54 |
| mg01 | 1527393 | 5136377 | 1008 | FTb | pGN | 3 | 32.3 | 6.7 | 50 | 77 |
| mg02 | 1526551 | 5146565 | 1884 | FTb | pGN | 4 | 26.8 | 17.9 | 55 | 60 |
| mg03 | 1525997 | 5147564 | 1998 | FTb | pGN | 3 | 24.6 | 12.2 | 60 | 53 |
| mg04 | 1524683 | 5148513 | 2091 | FTb | pGN | 3 | 33.7 | 10.8 | 57 | 68 |
| mg05 | 1525949 | 5142593 | 1243 | FTb | pGN | 3 | 15.6 | 17.6 | 48 | 59 |
| mg06 | 1524910 | 5150470 | 2239 | FTb | pGN | 3 | 18.4 | 19.9 | 55 | 58 |
| mg08 | 1526071 | 5141350 | 1183 | FTb | pGN | 3 | 20.1 | 13.2 | 50 | 63 |
| mg09 | 1526728 | 5149809 | 2504 | FSb | oGN | 3 | 35.3 | 12.7 | 65 | 69 |
| mg10 | 1528217 | 5147248 | 2211 | FSb | FLq | 3 | 15.8 | 14.1 | 53 | 54 |
| mg11 | 1527558 | 5149593 | 2483 | FSb | oGN | 3 | 30.8 | 10.6 | 68 | 62 |
| mg12 | 1530224 | 5141164 | 2239 | FSb | pGN | 3 | 16.2 | 12.4 | 42 | 66 |
| mg13 | 1528409 | 5148310 | 2346 | FSb | oGN | 3 | 16.9 | 12.1 | 63 | 62 |
| mg14 | 1529912 | 5146870 | 2318 | FSb | MSf | 3 | 40 | 19.2 | 58 | 53 |
| mg15 | 1529270 | 5146684 | 2241 | FSb | oGN | 3 | 36.5 | 9.9 | 67 | 65 |
| mg16 | 1522770 | 5147306 | 2366 | FTb | pGN | 3 | 17.4 | 14.4 | 43 | 61 |
| mg17 | 1528542 | 5140701 | 2019 | FSb | pGN | 3 | 15.9 | 10.4 | 57 | 66 |
| mg18 | 1532404 | 5142538 | 2441 | FSb | pGN | 3 | 20.3 | 14.2 | 49 | 61 |
| mg19 | 1528689 | 5135619 | 1705 | FTb | pGN | 4 | 15.4 | 16.7 | 38 | 56 |
| mg20 | 1526153 | 5138524 | 1596 | FTb | pGN | 4 | 14.1 | 16.2 | 42 | 66 |
| mg21 | 1528751 | 5144404 | 1882 | FSb | oGN | 3 | 18.2 | 11.8 | 61 | 63 |
| mg22 | 1525361 | 5141909 | 1673 | FTb | pGN | 3 | 13.8 | 13.5 | 50 | 56 |
| mg23 | 1525219 | 5138374 | 2009 | FTc | pGN | 4 | 25.2 | 13.3 | 57 | 61 |

| | | | | | | | | | | |
|-------------|---------|---------|------|-----|-----|---|------|------|----|-------|
| mg24 | 1524500 | 5139492 | 1780 | FTc | QZ | 3 | 37.8 | 11.5 | 55 | 70 |
| mg25 | 1525089 | 5140304 | 1750 | FTb | pGN | 3 | 19.4 | 12.2 | 50 | 59 |
| mg26 | 1528945 | 5138657 | 1518 | FSb | pGN | 3 | 17.9 | 15.6 | 45 | 61 |
| rm44 | 1523884 | 5143877 | 1985 | FTb | GN | 3 | 16.5 | 29.1 | 65 | -9999 |
| rm45 | 1524182 | 5143927 | 1874 | FTb | GN | 3 | 10.1 | 36.1 | 65 | -9999 |
| rm46 | 1522510 | 5143050 | 2106 | FTb | GN | 4 | 5.6 | 48.2 | 65 | -9999 |
| rm47 | 1522567 | 5142955 | 2075 | FTb | GN | 3 | 6.7 | 33.4 | 67 | -9999 |
| rm48 | 1522327 | 5142881 | 2061 | FTb | GN | 3 | 5.9 | 38.5 | 55 | -9999 |
| rm49 | 1523083 | 5143854 | 2188 | FTb | GN | 4 | 7.3 | 45.7 | 65 | -9999 |
| rm50 | 1523045 | 5143381 | 2068 | FTb | GN | 3 | 5.7 | 28.6 | 55 | -9999 |

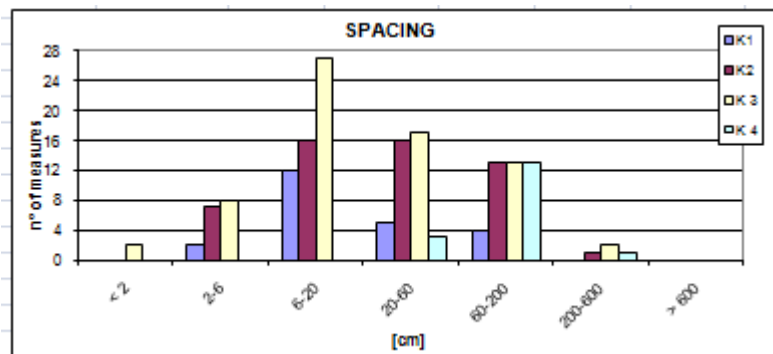
Appendix 2: data collected in Chiavenna Valley. For each geomechanical survey, its code, coordinates (in term of Longitude and Latitude, according to the Gauss-Boaga system), altitude, structural unit, lithology, number of joint sets, mean horizontal intercept, Volumetric Joint count (J_v , computed according to Palmstrom, 1982), GSI and RMR indices are reported. Used abbreviations:

- structural unit:
 - o *FSb* basement of Suretta nappe
 - o *FTb* basement of Tambò nappe
 - o *FTc* cover of Tambò nappe (Spluga Syncline)
- lithology:
 - o *ANF* amphibolite
 - o *FLQ* quartz phyllite
 - o *GN* gneiss
 - o *MS* micaschist
 - o *MSf* phyllitic micaschist
 - o *oGN* orthogneiss
 - o *pGN* paragneiss
 - o *QDI* quartzodiorite
 - o *QZ* quartzite
 - o *ERA* serpentinite
 - o *CL* limestone
 - o *FLc* phyllite cloritica
 - o *DO* dolomite

6.3 Appendix 3 - Recapitulatory sheet of geomechanical survey



| SET | Spacing [cm] | Persistence | Aperture [mm] | Weathering degree | Roughness | | JCS [MPa] | Infilling | Seepage | φ [°] |
|-----|--------------|----------------|---------------|-------------------|------------------|-----------|-----------|----------------|--------------|-----------|
| | | | | | Ondulation | JRC | | | | |
| K1 | 31 | > 30 | 12.00 | WD2 | IV - O SC | 16 | 92 | absent | U III | |
| K2 | 48 | 50 - 30 | 43.28 | WD3 | V - O L | 10 | 76 | cohesiv | U IV | 53 |
| K3 | 44 | 50 - 30 | 8.65 | WD2 | II - G L | 15 | | absent | U II | 68 |
| K4 | 107 | < 50 | 43.28 | WD2 | V - O L | 13 | | absent | U III | |
| | 57 | 50 - 30 | 30 | WD2 | IV - O SC | 13 | 84 | assente | U III | 63 |



Appendix 3: example of final recapitulatory sheet of geomechanical survey. Beyond the information about the site, a summary of all sets features is reported, with the mean value. Each rock mass property has a frequency histogram, reporting all the measures. Here only the spacing histogram has been reported. For each survey carried out in Chiavenna Valley this procedure of data collection has been followed.

6.4 Appendix 4 - Summary of exfoliation joints data collected at Grim-selpass

| <i>n° of model</i> | <i>X mean [m]</i> | <i>Y mean [m]</i> | <i>Z mean [m.a.s.l.]</i> | <i>trace length (s) [m]</i> | <i>trace length (d) [m]</i> | <i>spacing (s) [m]</i> | <i>spacing (d) [m]</i> | <i>bridge length [m]</i> | <i>SI (s)</i> | <i>SI (d)</i> | <i>Generation</i> |
|--------------------|-------------------|-------------------|--------------------------|-----------------------------|-----------------------------|------------------------|------------------------|--------------------------|---------------|---------------|-------------------|
| 1 | 665956 | 165629 | 1231 | 7.90 | 20.4 | 23.27 | -9999 | 2.09 | 1.078 | -9999 | 2 |
| 2 | 666405 | 165101 | 1224 | 5.25 | 12.58 | 3.19 | -9999 | 1.97 | 1.175 | -9999 | 2 |
| 3 | 666681 | 164501 | 1417 | 9.67 | 28.24 | 6.50 | 13.71 | 3.41 | 1.142 | 1.142 | 2 |
| 4 | 666747 | 164928 | 1527 | 8.85 | 26.84 | 7.80 | -9999 | 3.41 | 1.170 | -9999 | 2 |
| 5 | 666127 | 164389 | 1271 | 5.77 | 15.28 | 6.59 | -9999 | 3.01 | 1.075 | -9999 | 2 |
| 6 | 666737 | 164114 | 1429 | 12.53 | 28.51 | 7.17 | -9999 | -9999 | 1.083 | -9999 | 3 |
| 7 | 665988 | 164122 | 1574 | 20.03 | 109.37 | 37.55 | -9999 | 2.33 | 1.164 | -9999 | 2 |
| 8 | 666779 | 163826 | 1447 | 5.38 | 24.77 | 23.99 | -9999 | 2.06 | 1.127 | -9999 | 2 |
| 9 | 666791 | 163670 | 1414 | 7.33 | 15.00 | 7.76 | -9999 | 0.88 | 1.150 | -9999 | 2 |
| 10 | 666023 | 163595 | 1565 | 12.98 | 20.43 | 39.46 | 60.85 | -9999 | 1.193 | 1.051 | 2 |
| 11 | 666040 | 163123 | 1559 | 10.78 | 38.55 | 26.75 | -9999 | -9999 | 1.154 | -9999 | 2 |
| 12 | 666063 | 162111 | 1799 | 17.10 | 19.35 | 52.9 | 78.68 | 3.06 | 1.208 | 1.072 | 2 |
| 13 | 665941 | 161867 | 1922 | 15.03 | 14.75 | 9.35 | 4.69 | 5.74 | 1.192 | 1.096 | 2 |
| 14 | 666301 | 161918 | 1618 | 18.79 | 9.37 | 2.19 | 13.41 | 3.15 | 1.146 | 1.051 | 2 |
| 15 | 666495 | 161679 | 1669 | 15.63 | 18.34 | 35.58 | 59.31 | -9999 | 1.076 | 1.047 | 2 |
| 16 | 666800 | 161248 | 1803 | 11.95 | 21.74 | 42.02 | 15.45 | 2.28 | 1.100 | 1.059 | 2 |
| 17 | 667447 | 161345 | 1581 | 11.97 | 6.95 | 10.96 | 34.41 | -9999 | 1.062 | 1.056 | 2 |
| 18 | 667019 | 161036 | 1870 | 9.90 | 16.20 | 8.13 | 8.06 | 1.97 | 1.112 | 1.035 | 3 |
| 19 | 667409 | 160877 | 1703 | 18.41 | 44.91 | 8.10 | -9999 | -9999 | 1.127 | -9999 | 3 |
| 20 | 667181 | 160751 | 1868 | 8.49 | 38.53 | 14.20 | -9999 | 0.87 | 1.069 | -9999 | 3 |
| 21 | 667265 | 160551 | 1792 | 12.60 | 73.15 | -9999 | -9999 | 5.34 | 1.183 | -9999 | 3 |
| 22 | 667151 | 159788 | 2065 | 9.68 | 36.84 | 9.84 | 5.31 | 3.75 | 1.281 | 1.048 | 3 |
| 23 | 667883 | 160920 | 1646 | 4.13 | 6.51 | 3.82 | -9999 | 1.01 | 1.217 | -9999 | 3 |
| 24 | 668315 | 161407 | 1853 | 10.09 | 12.26 | 8.62 | 19.72 | -9999 | 1.159 | 1.031 | 2 |
| 25 | 668434 | 161116 | 1929 | 26.74 | 27.55 | 33.63 | 10.09 | 6.6 | 1.100 | 1.044 | 3 |
| 26 | 664649 | 162727 | 1916 | 9.47 | 22.53 | 13.80 | 10.54 | -9999 | 1.262 | 1.056 | 2 |
| 27 | 665412 | 163053 | 1818 | 6.47 | 11.15 | 14.92 | 8.91 | 1.33 | 1.104 | 1.071 | 1 |
| 28 | 664563 | 162464 | 1925 | 1.74 | 3.60 | 4.42 | -9999 | 0.45 | 1.173 | -9999 | 1 |
| 29 | 664201 | 162187 | 2103 | 4.78 | 5.60 | 3.24 | 2.73 | 0.74 | 1.267 | 1.048 | 1 |
| 30 | 664213 | 162121 | 2075 | 2.02 | 1.34 | 1.10 | -9999 | -9999 | 1.363 | 1.237 | 1 |
| 31 | 663995 | 161783 | 2173 | 8.68 | 10.90 | 15.38 | 7.57 | 0.91 | 1.118 | 1.099 | 1 |
| 32 | 664653 | 161584 | 2150 | 17.16 | 24.07 | 8.07 | 6.93 | 7.39 | 1.095 | 1.042 | 3 |
| 33 | 665237 | 162397 | 1823 | 10.61 | 7.06 | 2.31 | 4.24 | -9999 | 1.151 | 1.058 | 2 |
| 34 | 665382 | 162370 | 1881 | 14.03 | 16.72 | 2.46 | 4.75 | 6.9 | 1.090 | 1.049 | 2 |
| 35 | 668520 | 164219 | 2046 | 17.86 | 18.32 | 23.30 | 28.12 | 2.71 | 1.144 | 1.06 | 2 |
| 36 | 669010 | 163676 | 2477 | 117.51 | 206.72 | 41.98 | 79.23 | -9999 | 1.203 | 1.021 | 3 |
| 37 | 666687 | 164476 | 1418 | 11.12 | 33.42 | 25.87 | 22.02 | 3.81 | 1.161 | 1.081 | 2 |
| 38 | 666041 | 162230 | 1702 | 11.82 | 12.48 | 12.73 | 10.24 | 3.21 | 1.186 | 1.038 | 2 |
| 39 | 666176 | 162131 | 1621 | 12.10 | 10.09 | 7.92 | 28.46 | 10.07 | 1.142 | 1.070 | 2 |

Chapter 6: Appendixes

| | | | | | | | | | | | |
|----|--------|--------|------|-------|-------|------|------|-------|-------|-------|---|
| 40 | 667404 | 160909 | 1686 | 11.11 | 16.39 | 6.90 | 6.16 | 3.90 | 1.104 | 1.044 | 3 |
| 41 | 667500 | 160849 | 1639 | 10.41 | 17.26 | 3.97 | 6.61 | 3.25 | 1.116 | 1.042 | 3 |
| 42 | 667854 | 160909 | 1654 | 6.07 | 6.37 | 2.75 | 1.94 | -9999 | 1.069 | 1.085 | 3 |

Appendix 4: summary of the data about exfoliation joints collected at Grimselpass from photogrammetric models. The mean values for each model are reported. The number of photogrammetric model is reported, together with coordinates (X and Y), altitude (Z), trace length, spacing, bridge length, Sinuosity Index and generation of exfoliation joints. These abbreviations have been used:

- (s) indicates data collected along the strike;
- (d) data collected along the dip direction;
- -9999 means no data value.

6.5 Appendix 5 - Summary of tectonic joints data collected at Grimselpass

| <i>n° of model</i> | <i>X mean [m]</i> | <i>Y mean [m]</i> | <i>Z mean [m a.s.l.]</i> | <i>Dip direction [°]</i> | <i>Dip angle [°]</i> | <i>Spacing [m]</i> | <i>Trace length [m]</i> | <i>Bridge length [m]</i> | <i>SI</i> | <i>Joint set</i> |
|--------------------|-------------------|-------------------|--------------------------|--------------------------|----------------------|--------------------|-------------------------|--------------------------|-----------|------------------|
| 1 | 665956 | 165629 | 1260 | 190 | 57 | 15.52 | 11.39 | 5.36 | 1.074 | K3 |
| 2 | 666405 | 165101 | 1204 | 154 | 65 | 4.13 | 20.18 | 2.62 | 1.100 | K1 |
| 3 | 666681 | 164501 | 1406 | 181 | 54 | 14.98 | 25.05 | -9999 | 1.141 | K3 |
| 4 | 666747 | 164928 | 1563 | 178 | 62 | 7.95 | 11.42 | -9999 | 1.073 | K3 |
| 5 | 666127 | 164389 | 1259 | 188 | 81 | 6.55 | 11.55 | -9999 | 1.173 | K3 |
| 6 | 666737 | 164114 | 1394 | 172 | 71 | -9999 | 75.28 | -9999 | -9999 | K3 |
| 7 | 665988 | 164122 | 1541 | 183 | 57 | 26.15 | 21.34 | -9999 | 1.048 | K3 |
| 8 | 666779 | 163826 | 1435 | 180 | 65 | 8.51 | 15.39 | 3.97 | 1.067 | K3 |
| 9 | 666791 | 163670 | 1389 | 193 | 69 | 12.31 | 31.30 | -9999 | 1.084 | K3 |
| 10 | 666023 | 163595 | 1572 | 314 | 79 | 24.30 | 66.20 | -9999 | 1.089 | K4 |
| 10 | 666023 | 163595 | 1572 | 87 | 62 | 30.02 | 43.97 | -9999 | 1.049 | K2 |
| 11 | 666040 | 163123 | 1579 | 180 | 66 | 26.63 | 34.33 | 5.01 | 1.074 | K3 |
| 12 | 666063 | 162111 | 1769 | 130 | 75 | 35.18 | 22.53 | -9999 | 1.110 | K1 |
| 13 | 665941 | 161867 | 1946 | 183 | 72 | 11.90 | 21.00 | -9999 | 1.090 | K3 |
| 14 | 666301 | 161918 | 1621 | 113 | 78 | 11.28 | 13.05 | -9999 | 1.103 | K1 |
| 14 | 666301 | 161918 | 1621 | 206 | 72 | 5.77 | 63.81 | -9999 | 1.098 | K3 |
| 15 | 666495 | 161679 | 1645 | 158 | 69 | 40.68 | 18.62 | -9999 | 1.086 | K1 |
| 16 | 666800 | 161248 | 1859 | 152 | 73 | 24.14 | 46.12 | -9999 | 1.084 | K1 |
| 16 | 666800 | 161248 | 1859 | 315 | 55 | 18.78 | 7.13 | -9999 | 1.091 | K4 |
| 17 | 667447 | 161345 | 1560 | 36 | 74 | 20.88 | 25.98 | -9999 | 1.086 | K2 |
| 18 | 667019 | 161036 | 1824 | 134 | 65 | 15.27 | 27.24 | -9999 | 1.026 | K1 |
| 19 | 667409 | 160877 | 1692 | 135 | 56 | 16.90 | 21.92 | -9999 | 1.029 | K1 |
| 19 | 667409 | 160877 | 1692 | 355 | 58 | 12.85 | 23.13 | -9999 | 1.026 | K4 |
| 20 | 667181 | 160751 | 1887 | 142 | 58 | 8.60 | 73.50 | -9999 | 1.032 | K1 |
| 21 | 667265 | 160551 | 1780 | 139 | 59 | 17.00 | 22.84 | -9999 | 1.014 | K1 |
| 22 | 667151 | 159788 | 2072 | 136 | 86 | 12.38 | 7.35 | -9999 | 1.052 | K1 |
| 23 | 667883 | 160920 | 1641 | 243 | 75 | 5.69 | 23.76 | -9999 | 1.157 | K2 |
| 24 | 668315 | 161407 | 1852 | 167 | 73 | 12.22 | 43.33 | -9999 | 1.047 | K1 |
| 25 | 668434 | 161116 | 1878 | 224 | 50 | 32.94 | 64.88 | -9999 | 1.052 | K2 |
| 25 | 668434 | 161116 | 1878 | 315 | 70 | 23.08 | 26.54 | -9999 | 1.023 | K4 |
| 26 | 664649 | 162727 | 1883 | 169 | 63 | 14.81 | 10.60 | -9999 | 1.106 | K1 |
| 27 | 665412 | 163053 | 1843 | 145 | 59 | 5.36 | 12.38 | 2.62 | 1.057 | K1 |
| 27 | 665412 | 163053 | 1843 | 270 | 87 | 10.71 | 3.45 | -9999 | 1.080 | K2 |
| 28 | 664563 | 162464 | 1950 | 227 | 87 | 2.58 | 7.49 | -9999 | 1.040 | K2 |
| 29 | 664201 | 162187 | 2095 | 202 | 75 | 6.11 | 2.63 | -9999 | 1.151 | K3 |
| 30 | 664213 | 162121 | 2068 | 138 | 68 | 1.66 | 13.84 | -9999 | 1.131 | K1 |
| 31 | 663995 | 161783 | 2150 | 153 | 78 | 13.78 | 24.85 | -9999 | 1.103 | K1 |
| 32 | 664653 | 161584 | 2133 | 206 | 73 | 30.82 | 7.62 | -9999 | 1.074 | K3 |
| 33 | 665237 | 162397 | 1818 | 319 | 64 | 24.88 | 24.71 | -9999 | 1.063 | K4 |
| 34 | 665382 | 162370 | 1867 | 310 | 59 | 14.34 | 16.32 | -9999 | 1.064 | K4 |
| 34 | 665382 | 162370 | 1867 | 66 | 74 | 9.82 | 35.72 | -9999 | 1.062 | K2 |

| | | | | | | | | | | |
|----|--------|--------|------|-----|----|-------|-------|-------|-------|----|
| 35 | 668520 | 164219 | 2073 | 245 | 89 | 32.36 | 25.66 | -9999 | 1.070 | K2 |
| 36 | 669010 | 163676 | 2179 | 140 | 87 | 20.71 | 20.02 | -9999 | 1.037 | K1 |
| 37 | 666687 | 164476 | 1429 | 146 | 49 | 12.61 | 28.27 | -9999 | 1.050 | K1 |
| 38 | 666041 | 162230 | 1648 | 156 | 73 | 22.76 | 17.51 | -9999 | 1.062 | K1 |
| 39 | 666176 | 162131 | 1607 | 136 | 70 | 14.78 | 42.73 | -9999 | 1.132 | K1 |
| 40 | 667404 | 160909 | 1691 | 337 | 73 | 7.48 | 18.25 | -9999 | 1.044 | K4 |
| 41 | 667500 | 160849 | 1629 | 159 | 69 | 11.75 | 15.83 | -9999 | 1.058 | K1 |
| 42 | 667854 | 160909 | 1655 | 141 | 81 | 2.93 | 6.60 | -9999 | 1.102 | K1 |

Appendix 5: summary of the data about tectonic joints collected at Grimselpass from photogrammetric models. The mean values for each model are reported. The number of photogrammetric model is reported, together with its coordinates (X and Y), altitude (Z), dip direction, dip angle, spacing, trace length, bridge length, Sinuosity Index and the tectonic joint set. When a photogrammetric model is reports twice is because two main tectonic joint sets have been encountered in that model. -9999 means no data value.